Hybrid Organic/Inorganic Optoelectronics

by

Christopher Kyle Renshaw

A dissertation submitted in partial fulfillment
of the requirements for the degree of
Doctor of Philosophy
(Applied Physics)
in the University of Michigan
2014

Doctoral Committee:

Professor Stephen R. Forrest, Chair
Professor L. Jay Guo
Professor Cagliyan Kurdak
Associate Professor Jamie Phillips
Associate Professor Max Shtein

Acknowledgements

First, I would like to thank my advisor Stephen Forrest for being a compassionate, motivating and inspirational mentor. While under his guidance, I benefitted tremendously from his sage advice, storied career, scientific expertise and high expectations for all of his students. He provided a stimulating learning environment and a rigorous research community in his Optoelectronic Components and Materials Group, affectionately called "OCM".

Next, thank you to all of my colleagues in OCM. Especially my seniors in the group from whom I learned a great deal: Johnny Lunt, Stephane Kena-Cohen, Chris Giebink, Xin Xu, and Mike Arnold. Jeramy Zimmerman was practically a second advisor but my first resource whenever I had a problem, question, or idea to discuss (thank you for staying with OCM for the duration of my tenure!). I am grateful to Brian Lassiter, Greg McGraw, Anurag Panda, Yifan Zhang, and Ning Li for useful discussions and help along the way. I owe a special thanks to Kyusang Lee for teaching me MBE, nanofabrication, growing wafers, and always being helpful and patient. Michael Slootsky and Xiaoran Tong were the best labmates, friends, and roommates I could ever hope for – thank you both.

I would also like to thank the staff of the Lurie Nanofabrication Facility, especially Matt Oonk and Dennis Schweiger, for advice and technical assistance. I benefitted from many useful discussions with Robert Krasny about numerical modeling and simulation. I am grateful to Alex Gaeta and Saikat Ghosh who nourished my interest in scientific research while at Cornell. I

enjoyed many intellectual discussions and life-experiences with my housemate and colleague Franklin Dollar.

I am eternally grateful for the support and encouragement I have received from my family. To my parents, Natalie and Randy Schuldt, I would not have made it this far without your loving support and invaluable life-lessons to guide me. My grandparents, Carrol and Brig Anderson, have also been a tremendous influence in my life. They have always inspired me to learn, to get an education, and to pursue my dreams.

Finally, I would like to thank my wife and my best friend – Amanda. Her strength, focus and drive motivated me throughout graduate school. Meanwhile her love and care supported me, enabling me to finish. Thank you and I love you!

Table of Contents

Acknowledgements .... **ii**
List of Figures .... **vii**
List of Tables .... **ix**
Abstract .... **x**
Chapter 1: Introduction **1**
1.1. Inorganic semiconductors (iSC's) 6
1.1.1. Nature of bonding and crystals 7
1.1.2. Optoelectronic properties 19
1.2. Organic semiconductors (oSC's) 32
1.2.1. Nature of bonding and films 33
1.2.2. Optoelectronic properties 39
Chapter 2: Physics of Organic Photovoltaics **44**
2.1. Background 44
2.2. Absorption in thin film devices 46
2.3. Exciton diffusion 49
2.4. Exciton dissociation at a heterojunction 52
2.4.1. PP formation and the Giebink model 53
2.4.2. Hot charge transfer states 58
2.5. Charge extraction 62
2.5.1. Isotype layers 62
2.5.2. Drift-diffusion equation: $J = 0$ 63
2.5.3. Drift-diffusion equation: $J \neq 0$ 65
2.5.4. Uniform field approximation 67
2.5.5. Ohmic and space charge limited current 67
2.6. Current-Voltage Characteristics 70

Chapter 3: Recombination in Organic Buffer Layers ... 73
3.1. Background ... 73
3.2. Theory ... 77
3.3. Experimental ... 85
3.3.1. Materials ... 85
3.3.2. Device Fabrication and Characterization ... 86
3.3.3. UV Photoelectron Spectroscopy ... 87
3.4. Results ... 88
3.5. Discussion ... 90
3.6. Conclusion ... 97
Chapter 4: Photoconductivity in Organic Photovoltaics ... 100
4.1. Background ... 100
4.2. Theory ... 103
4.3. Experiment ... 110
4.4. Results ... 111
4.5. Discussion ... 113
4.6. Conclusion ... 119
Chapter 5: Excited State and Charge Dynamics of Hybrid Organic/Inorganic Heterojunctions: Theory ... 120
5.1. Background ... 120
5.2. Theory of Conduction for Organic/Inorganic Heterojunctions ... 124
5.2.1. Current Conduction Under Quasi-equilibrium Conditions ... 124
5.2.2. Current Conduction Under Non-equilibrium Conditions ... 140
5.3. Results and Discussion ... 145
5.4. Conclusions ... 155
Chapter 6: Hybrid Organic/Inorganic Heterojunctions: Experiment ... 157
6.1. Background ... 157
6.2. Theory ... 158
6.3. Experiment ... 163
6.4. Results ... 165
6.5. Discussion ... 167
6.6. Conclusion ... 172

Chapter 7: Visible/NIR Hemispherical Array Detector for Imaging 174
7.1. Background.. 174
7.2. Fabricating an Organic Sensor Array 179
7.2.1. Patterning soft materials on a non-planar surface 179
7.2.2. Crosshatch OPD Array 183
7.2.3. OPD Array with Blocking Diode 184
7.2.4. Passive Pixel Sensor 187
7.2.5. A 10×10 PPS Array 194
7.2.6. Scaling to High-Density Arrays 198
7.3. Conclusions 203
Chapter 8: Conclusions and Future Work 205
8.1. Conclusions 205
8.2. OI HJ with crystalline Inorganics 206
8.3. Existence of Charge Transfer State: Monte Carlo Simulation 209
8.4. Hybrid Sensory Array.. 209
8.4.1. III-V Transistor Fabrication.. 210
8.4.2. Array Transfer 213
Appendix 218
Appendix A... 219
Bibliography 222

List of Figures

Figure 1.1 – Electronic Classes of Solids ... 2
Figure 1.2 – Bond Formation ... 9
Figure 1.3 – Cohesive Energy ... 11
Figure 1.4 – Czochralski Process ... 13
Figure 1.5 – Energy Gaps of Inorganic Semiconductors ... 16
Figure 1.6 – MBE Chamber ... 17
Figure 1.7 – Periodic Potential ... 20
Figure 1.8 – Interatomic Coupling ... 21
Figure 1.9 – Band Diagram ... 25
Figure 1.10 – Density of States ... 29
Figure 1.11 – Doping in Silicon ... 30
Figure 1.12 – Organic Transport Levels ... 40
Figure 2.1 – Current Generation in an Organic Photovoltaic Device ... 45
Figure 2.2 – Optical Field Profile in Organic and Inorganic Photovoltaics ... 47
Figure 2.3 – Energy Level Diagram of an Organic Photovoltaic Device ... 50
Figure 2.4 – Giebink Model ... 54
Figure 2.5 – Hot Charge Transfer Exciton Dissociation ... 60
Figure 2.6 – Uniform Field Approximation ... 68
Figure 2.7 – OPV J-V Characteristics ... 71
Figure 3.1 – Reciprocal Carrier Collecction ... 74
Figure 3.2 – Double Diode Model ... 83
Figure 3.3 – Ruthenium Complexes ... 85
Figure 3.4 – Thick RCC OPVs ... 89
Figure 3.5 – Thin RCC OPVs ... 89
Figure 3.6 – Recombination in Inverted Marcus Regime ... 91
Figure 3.7 – Thick RCC OPVs (log scale) ... 91
Figure 3.8 – Energy Levels for Ru Complexes ... 93
Figure 4.1 – Photoconductivity in OPVs ... 101
Figure 4.2 – Onsager-Braun Based Polaron Pair Dissociation ... 105
Figure 4.3 – Effect of Photoconductivity ... 108
Figure 4.4 – Voltage Dependent Photocurrent ... 112
Figure 4.5 – Temperature Dependence of Bilayer OPVs ... 113
Figure 4.6 – SubPc Photoconductance ... 114
Figure 4.7 – Simulated J-V ... 118
Figure 5.1 – Hybrid Organic/Inorganic Model ... 125
Figure 5.2 – Hybrid Charge Transfer Exciton ... 134
Figure 5.3 – Space-charge in an OI Device ... 142

Figure 5.4 – Simulated OI Device 147
Figure 5.5 – Energy Band Diagram for an OI Device 148
Figure 5.6 – OI Simulation Results 149
Figure 5.7 – Simulated Dark Current 150
Figure 5.8 – Varied Electric Field and Recombination Rate 153
Figure 5.9 – Fill Factor and Power Conversion Efficiency 154
Figure 6.1 – Hybrid TiO_2/DBP Device 158
Figure 6.2 – Dark Current of the OI Device 166
Figure 6.3 – Illuminated Curent Density Versus Voltage 167
Figure 6.4 – Excess Forward Bias Current Under Illumination 171
Figure 6.5 – Temperature Dependence of Mobility and Exciton Flux 172
Figure 7.1 – Commercial Cameras 175
Figure 7.2 – Optical Aberrations 177
Figure 7.3 – Stamp Patterning Organics 181
Figure 7.4 – Hemispherical Photodetector Array 182
Figure 7.5 – Pixel with a Blocking Diode 185
Figure 7.6 – Passive Pixel Sensor 188
Figure 7.7 – Passive Pixel Sensor Response 191
Figure 7.8 – OTFT Switching Speed 193
Figure 7.9 – 10x10 Passive Pixel Array 196
Figure 7.10 – Array Response 197
Figure 7.11 – Aligned Stamping 199
Figure 7.12 – 128x128 Passive Pixel Array Design 201
Figure 7.13 – OTFT Array Fabrication 202
Figure 8.1 – Hybrid OI with Crystalline Inorganics 207
Figure 8.2 – Quantum Well at OI Heterojunction 208
Figure 8.3 – Flexible Inorganics 210
Figure 8.4 – InP JFET 211
Figure 8.5 – JFET Design 212
Figure 8.6 – JFET Fabrication 213
Figure 8.7 – Inorganic Array Transfer 214
Figure 8.8 – Patterning PETg 215
Figure 8.9 – GaAs Array Transfer 217

List of Tables

Table 3.1 – Definitions for reciprocal carrier collection.. 78
Table 3.2 – RCC fit results: 95
Table 4.1 – Estimated material properties for typical organic:...................................... 106
Table 5.1 – Definition of variables used... 128
Table 5.2 – Table of parameters used in model OI-HJ calculations............................... 129
Table 6.1 – TiO_2/DBP fit results... 168
Table 7.1 – HARDI Program Metrics.. 179

Abstract

Traditional inorganic semiconductors are the foundation of modern electronics. These materials are widely used in computing and optical devices (such as lasers, LEDs, cameras, etc.), but they are limited in functionality by their particular set of material properties. In particular, traditional crystalline inorganic semiconductors are not well suited for large area or flexible electronics applications. This limitation has driven the development of a new generation of thin-film semiconductor materials.

Thin-film semiconductor materials are ideal for solar energy conversion because they have the potential for cost effective large area fabrication. Promising next generation photovoltaic devices have been demonstrated using organic photovoltaics (OPVs) and dye-sensitized solar cells (DSSCs). OPVs are a promising technology because they are inexpensive, strong absorbers. However, it is challenging to produce efficient OPVs due to the excitonic nature and poor charge transport characteristic of these materials. DSSCs are hybrid devices that combine the strong absorption of organic semiconductors with the good charge transport of inorganic metal-oxide semiconductors.

Devices based on thin-film, low mobility, excitonic materials are governed by fundamentally different physical processes than traditional inorganic devices. In this thesis, we develop physical models to analyze the performance of devices based on organic/organic and hybrid organic/inorganic heterojunctions (HJs). These models are based on interface dynamics at

the HJ and are used to identify the physical processes that limit device performance. Specifically, we extend the interface model to understand: 1) reciprocal carrier collection in OPVs, 2) photoconductivity in OPVs, 3) the adaptation of traditional depletion models to thin-film devices, and 4) space-charge effects in hybrid devices. To model hybrid devices, we introduce a theory that bridges the gap between traditional semiconductor theory and models developed to explain thin-film excitonic systems. Once the important physical processes are understood, we can proceed to design optimized devices.

In the last section we consider the application of organic and hybrid devices for flexible or non-planar devices. Here, we develop technologies to enable the fabrication of high-performance devices and high-density circuits on flexible and non-planar substrates. We then demonstrate an integrated passive pixel photodetector array and discuss the extension to a high-performance hybrid sensor array.

Chapter 1

Introduction

I would like to begin by addressing the most basic questions a casual reader may have while reading my thesis – "What are optoelectronics?" Optoelectronics are a subset of semiconductor based electronics that are used for light generation or absorption – i.e. they are optically active semiconductor devices. As the name implies a semiconductor is a material that has electronic properties in between those of a conductor and an insulator (i.e. not-a-conductor). Summarily, a conductor transports charge easily, an insulator does not transport charge and a semiconductor is conductive or not depending on external controls applied to the material. Figure 1.1 shows the energy levels for electrons in these different classes of materials. Without complicating this picture with details, the Fermi level represents the equilibrium level for electrons in the material and when there are available states near the Fermi level charge is easily conducted through the material. Conversely, if there are no available states near the Fermi level charge conduction is very poor – this is the case for an insulator which has a wide gap of unavailable states and the Fermi level is far from the available states. A semiconductor also has unavailable states but the Fermi level is close enough to the available states that limited charge

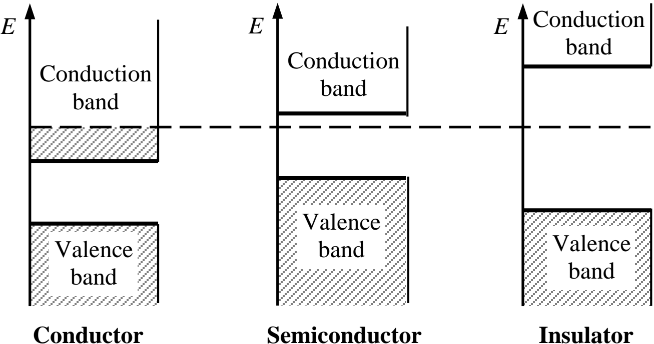

Figure 1.1 - Electronic Classes of Solids: Conductors have an unfilled band that allows electrons o freely move through the solid, 2) Semiconductors have a few thermally excited electrons that allow limited conduction, 3) Insulators have a filled valence band and an empty conduction band with very few thermally generated electrons so that they are very poor conductors.

conduction can occur, but more importantly external controls can move the Fermi level closer or farther from the available states, allowing for tuning of the conductivity of the semiconductor. It is this control over the conductivity of the semiconductor that makes them extremely useful and an essential a building block of our modern society.

Before the development of the semiconductor industry, all electronics consisted entirely of discreet components (resistors, capacitors, inductors, relays, transformers, and vacuum tube devices). This means electronics were bulky, expensive and not practically scalable to complex circuits. With the development of semiconductors and then, naturally, integrated circuits the electronics industry was revolutionized.

Today, the semiconductor industry is based on inorganic semiconductors that are now a well-known and well understood materials system. Over the last 80 years, the theoretical foundations for solid-state physics have been laid and then applied to develop advanced electronic devices which have revolutionized the world that we live in today. These devices have led us into the "Information Age" where the internet, computers and communication devices are a daily part of people's lives, enabling access to zettabytes (~10^{21} bytes) of new digital

information annually. The impact of these semiconductor devices extends far beyond the very visible computing devices – indeed, it impacts nearly every aspect of daily life.

Of course, theoretical foundations alone were not enough to enable this revolution, the proliferation of advanced electronic devices also required major advances in materials science and electrical engineering to enable the fabrication of these devices. For example, the fabrication of nearly perfect single crystal Si boules has grown from 50mm in 1965 to 300mm today and 450mm fabrication facilities are currently under development.[1] Similarly, transistors have been scaled down from 20μm in 1975 to below 32 nm (32×10^{-9} m) today.[2] Such advances in fabrication technology have enabled a wide range of high-tech devices.

Despite their vast capabilities and fantastic optoelectronic performance, traditional inorganic semiconductors are not an ideal platform for some optoelectronic applications. Two important applications for which these materials are not well suited are: 1) non-planar or flexible devices and 2) large-area coverage. Traditional inorganic semiconductors are not good for these applications because they are crystalline materials and are fabricated on flat, rigid and expensive single crystal wafers. Consequently, flexible and non-planar devices cannot be fabricated because the wafer substrate is flat and rigid. Likewise, large area coverage (required for applications such as solar cells) is not economical because the wafer substrate is expensive.

The ability to fabricate non-planar and flexible devices would relax the constraints for device design enabling new applications with novel functionality and performance. For example, non-planar (in particular, hemispherical) optoelectronic devices could dramatically improve compact high-performance imaging systems (c.f. Chapter 7 and Ref. [3]). As another example, flexible displays have already been shown to be much more robust than standard, rigid displays[4]

and they could also be folded or rolled into a compact size[5] offering new convenience and form-factors that are unattainable on rigid substrates. In another example, flexible electronics could revolutionize sensors and transducers used in medical applications,[6,7,8] offering unparalleled performance as the devices can conform to the non-planar shapes found throughout the human body.

There have been various attempts to fabricate flexible or non-planar devices using traditional inorganic semiconductors. One approach is to dice a wafer into small discreet pieces and place them individually onto a flexible substrate.[9] This technique is not practical for high performance devices with a large number and high density of discreet devices. Another approach is to etch through the wafer leaving thin and flexible ribbons of wafer (i.e. mechanical supports) between adjacent devices.[10] This approach utilizes microfabrication techniques enabling parallelized and high-density fabrication, but mechanical robustness and electrical interconnection are major challenges with this technique. Lift-off techniques designed to remove the thin active device from the thick growth wafer and transfer them to a flexible substrate are the most promising method to use inorganic semiconductors for these applications (c.f. Chapter 8 and Refs. [11],[12],[13],[14],[15]). Organic semiconductors are a promising alternative for these applications because they are typically non-crystalline and can be fabricated directly on flexible or non-planar substrates (c.f. Chapter 7 and Refs. [5],[16],[17],[18],[19],[20]).

The economical fabrication of semiconductor devices designed to cover large areas would enable the utilization of one of the very few scalable, environmentally friendly and renewable energy sources that exist – the direct conversion of sunlight into electricity. Photovoltaic cells (PVs), commonly called solar cells, are arguably the most promising option for large scale renewable energy generation. However, after many years of environmental

activism and demands for energy security, renewable sources supply 12% of the energy consumption in the United States in 2012.[21] However, hydropower generation (a stagnant resource that cannot be substantially increased) accounts for 7% of that total, while scalable renewables only account for 5% or our energy supply. Of that 5%, energy generation from our most abundant resource, solar energy via direct PV conversion, contributes less than 0.1%.[21] The challenge to PVs as an energy source is the massive scale of our energy usage combined with the low intensity of solar radiation. To make a non-trivial contribution to global energy consumption, PVs must be deployed to cover square miles, not square centimeters – the more suitable metric for traditional semiconductors. Nonetheless, PVs based on traditional inorganic semiconductors are manufactured, sold and deployed – but are done so at about twice the cost of fossil fuel generation. PVs must become more economical in order to succeed outside of niche markets (space or remote applications), without unsustainable government subsidies, and without economically damaging regulation (Renewable Portfolio Standards). The way to reduce PV cost is through new technologies designed to enable large scale fabrication of large area PVs. These next generation PVs are based on thin film semiconductors deposited onto inexpensive substrates in a high-throughput-compatible manufacturing process.

My thesis work is focused on addressing these two applications where traditional inorganic semiconductors fail – flexible optoelectronics and economical PVs. While these applications are not necessarily related, the solutions we identify are – the solutions require low-temperature-processable and thin-film semiconductors that are compatible with flexible plastic or metal foil substrates. For both applications, we initially investigated solutions consisting entirely of organic semiconductors because they meet these basic requirements. However, we found that a hybrid combination of organic and inorganic semiconductors could provide a synergy that

meets or exceeds the performance of either material alone. I note that none of this work is focused simply on improving device performance or power conversion efficiency. Fine tuning architectures and processing conditions for long-lived, repeatable devices with record breaking performance is a task best suited for industry. Here, I aim to improve our understanding of the physical principles that govern the performance of these devices, and to demonstrate key technologies that enable their fabrication.

The rest of this chapter is intended to provide the reader with important background information concerning the state-of-the-art understanding of these two distinctly different materials systems.

1.1. Inorganic semiconductors (iSC's)

The semiconductor industry began with elemental semiconductors consisting of the Group IV elements Germanium (Ge) or Silicon (Si). Today, Si is the dominant semiconductor material and it is used in almost all electronics applications. However, there are some applications where the optical or electronic properties of Si are not sufficient. For example, Si does not absorb light with wavelengths longer than 1100 nm – so other materials are required in order to make an infrared (IR) photodetector. As another example, the electron mobility in Si at room temperature is μ_e = 1400 cm^2/Vs – higher mobility materials are required in order to make super-high-frequency (3-30 gigahertz) or extremely-high-frequency (30-300 GHz) electronics. Similarly, Si is a very poor light emitter because it has an indirect bandgap so that the lowest energy transition is not optically allowed – for this reason alternative materials are required to make practical light emitting diodes (LEDs) or lasers.

Compound semiconductors were introduced to address the limitations of Si and offer new devices with new functionality in order to expand the range of applications of semiconductor devices. The compound semiconductors are classified as III-V materials (GaAs, InP and more recently GaN based materials) and II-VI materials (CdTe, ZnSe based materials) based on their group numbers in the periodic table. The III-V materials are the most important semiconductor materials after Si – because they are suitable for high-frequency electronics, lasers, LEDs, and IR photodetectors. In fact, nearly 100% of the electronics market was comprised of Si or III-V materials – that is, up until the last few years. Over the last few years, the next generation of semiconductor materials has made it into the market; these materials are based on thin-film technologies and are better suited for large area devices than are the traditional Si and III-V semiconductors.

1.1.1. Nature of bonding and crystals

Traditional inorganic semiconductor materials consist of one or a few elements covalently or ionically bonded together into a robust macroscopic solid. The industry goes to great lengths to fabricate semiconductors into nearly perfect single crystals (typically with less than 1 defect per billion lattice sites). This is because a perfect crystalline structure provides the optimal electronic properties, and the ability to fabricate high quality single crystals was the key to the industry's fantastic success.

1.1.1.1. Bonding in Crystals

Bonding in solids is a complex phenomenon, the details of which depend on the constituent materials. All bonding is ultimately due to electrostatic interactions, but bonding can be grouped into four classes based on the nature of those interactions: 1) covalent bonding, 2)

ionic bonding, 3) molecular bonding and 4) metallic bonding. A thorough and detailed discussion of all of these classes is beyond the scope of this work. Here, I provide only a brief description of covalent and ionic bonding found in inorganic semiconductors in order to compare against the molecular bonding of organic films (cf. Section 1.2.1).

Covalent bonds are strong chemical bonds that are formed by atoms sharing electrons in order to reduce the potential energy of the whole system. The details of chemical bonding can be found in the literature and texts.[22] In short, core electrons are tightly confined to the nucleus, do not contribute significantly to bonding and effectively screen the same number of protons in the atomic nucleus. Then the atom can be thought of as a charged center with N^+ charge surrounded by an electron cloud of sign N^-, where N is the number of outermost electrons (the valence electrons). It is these valence electrons that contribute to bonding because they have the strongest interaction with neighboring atoms. The outer electrons determine the number and type of bonds that the atom will form as well as the orientation of bonds, the crystal structure, and the physical properties of the resulting solid.[23] Suffice it to say, atoms in the p-block of the periodic table seek to satisfy the octet rule when bonding into a solid by sharing electrons with their neighboring atoms so that each atom is surrounded by eight electrons. This configuration fills the atomic S and P valence orbitals and minimizes the energy of the system. For this reason, Si (with four valence electrons) will form four single bonds with four neighboring Si atoms by sharing one valence electron with each of them as shown in Figure 1.2. Si is a perfect example of covalent bonding because the bond energy (or the energy of cohesion) is produced exclusively by the sharing of electrons – there is no charge transfer and no net Coulombic attraction between neighboring Si atoms.

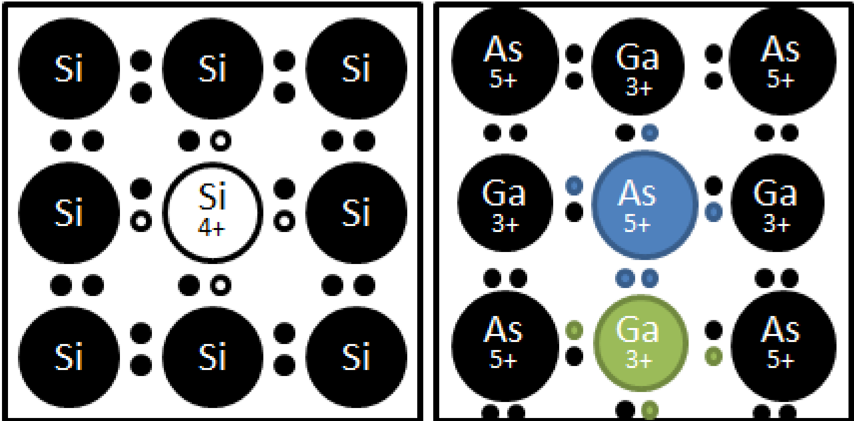

Figure 1.2 - Bond Formation: Silicon forms purely covalent bonds by sharing one electron with each neighbor. It retains its four electrons resulting in a neutral Si atom. GaAs forms mixed covalent and ionic bonds. Arsine transfers one of its five electrons to gallium so that both have four electrons to form covalent bonds with the four nearest neighbors. Arsine has a net positive charge while gallium gains a net negative charge.

Ionic bonds are also strong chemical bonds but they are formed by charge transfer between two atoms. Ionic bonds form between two atoms with largely different electronegativities such as sodium (Na), which has one valence electron, and chlorine (Cl), which has seven valence electrons. The bonds in an ionic solid such as NaCl are formed by the Coulombic attraction of the Na^+ and Cl^- ions that are created when the Na atom transfers its valence electron to the Cl atom. This charge transfer occurs to fill the Cl 3p valence shell while reducing the Na to a filled 2p valence shell, thereby reducing the energy of the system. Such an ionic bond is considered a chemical bond because of the charge transfer between the atoms, however the bond energy is dominated by the attraction of the resulting ions.

For an ionic solid, the cohesive energy per ion pair is a function of ion separation (r) and is dominated by two components as,

$$E(r) = E^{rep}(r) + E^{coul}(r), \tag{1.1}$$

where $E^{rep}(r)$ is the repulsion of the nuclei due to the quantum mechanical Pauli Exclusion Principle and $E^{coul}(r)$ is the Coulombic attraction of the ions.[24] The repulsive term is due to the required reorganization of the electron wave functions in order to satisfy the Pauli Exclusion Principle that two electrons with the same quantum numbers cannot occupy the same state. The functional form of this repulsion requires very complicated quantum mechanical calculations and instead is usually assumed to be of the form $E^{rep}(r) = A/r^m$, where A and m are determined by empirical measurements of the bulk modulus and nearest-neighbor separation of a particular solid. The power m is always large (>6) because it represents a very short range interaction – the nuclear-nuclear repulsion which is a nearest neighbor interaction. Here we will use $m = 12$ to be consistent with the convention used for the Lennard-Jones potential of Sect. 1.2.1.

The Coulombic interaction for isolated point charges is given by $E(r) = e^2/4\pi\varepsilon r$, where ε is the dielectric constant of the medium surrounding the charge. This is a very long-range interaction due to the weak $1/r$ dependence and the energy of a given ion pair in the solid is dependent on the Coulomb interactions with all the surrounding ions within a large distance on the order of micrometers – not simply nearest-neighbor ions. Consequently, the energy per ion pair requires summing up all of these interactions in the solid and this can be done analytically for crystalline solids due to their periodicity. This was famously done by P. P. Ewald in 1921[25] for several crystal structures and demonstrated that this interaction is given by,

$$E^{coul}(r) = -\alpha \frac{e^2}{4\pi\varepsilon r}, \tag{1.2}$$

where α is the Madelung constant which is dependent only on the materials crystal structure, and is typically in the range of 1.5-1.8.

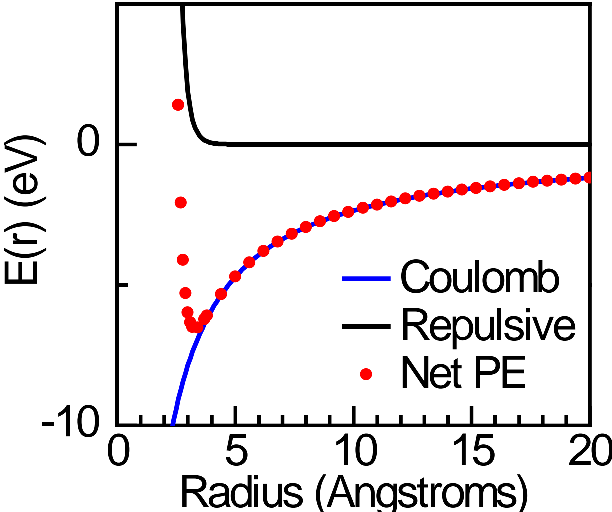

Figure 1.3 – Cohesive Energy: The electrostatic interaction between two ions. The nuclear repulsion raises the potential energy (PE) of the system (black line). The long range attractive Coulomb interaction between ions in an ionic solid is described by the Madelung potential of Eq. 1.2 (blue line). The net potential energy (red circles) has a global minimum at 3.2 Angstroms and this is the equilibrium lattice constant for this simulated solid.

Figure 1.3 shows the resulting cohesive energy (the net potential energy) of the ion pair in an ionically bonded solid with α=1.6381 (corresponding to the Zincblende crystal structure).[24] This cohesive energy is less than zero at large *r*, so it is energetically favorable to form the solid. According to the Second Law of Thermodynamics a system with dissipation (such as heat) will equilibrate to the lowest energy state; consequently, the solid is formed. The cohesive energy is greater than zero at small *r* due to the nuclear repulsive force that stabilizes the solid by preventing the ions from collapsing onto each other. Figure 1.3 shows simply the equilibrium lattice (*a*) constant of the crystal (determined by the minimum energy *r*), the bulk modulus (how much energy is required to compress and expand the solid), and the enthalpy of formation of the crystal from its constituent elements. This shows that a crystal can be formed by enabling the solid to reach the global minimum energy state, where all atoms are separated by *a*.

The compound III-V and II-VI semiconductors, such as GaAs, are in between purely covalent and purely ionic solids. As most materials do, they exhibit partially covalent and partially ionic bonds. As shown for GaAs in Figure 1.2, there is electron transfer from the As to Ga so that each atom has four electrons and this results in an ionic attraction between the As^- and Ga^+ ions. Then those electrons are shared with four nearest-neighbors forming covalent bonds.

This section has discussed how traditional inorganic semiconductors form strong, chemical bonds in the solid phase. This fact has two important consequences for these materials: 1) they form hard, mechanically robust solids, and 2) the constituent atoms are strongly coupled together electronically. The mechanical robustness enables them to withstand a wide range of fabrication processes, while the strong electronic coupling enables their high performance optoelectronic properties (cf. Section 1.1.2).

1.1.1.2. Crystal growth and film deposition techniques

All fabrication and processing for traditional inorganic devices begins with a single crystal semiconductor wafer as a substrate. The wafer is typically 300-500 micrometers (microns or μm) thick for convenient handling, while the devices fabricated on the top surface typically require less than 10 microns of semiconductor material. Essentially 98% of the material is wasted – it is used simply as a mechanical support that is required for the fabrication steps. This is the motivation for developing thin-film semiconductor technologies that do not require the use of a wafer in the fabrication process – cf. Section 1.2. However, this waste of material and the expense of the fabrication processes are offset by the scalability of the fabrication technologies. The fabrication technologies enable devices to be made on a very small area of the wafer (less than 0.5 μm^2 per transistor in the 2008 Intel Quad core i7 CPU and less than 0.1 mm^2 for a

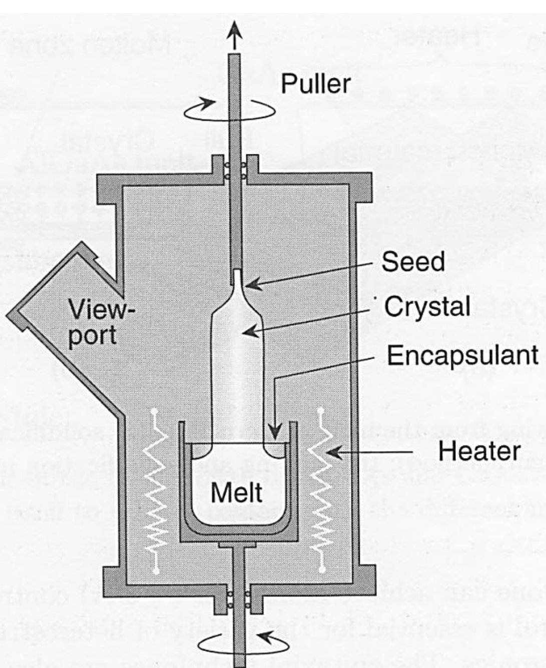

Figure 1.4 - Czochralski Process: Single crystalline boules of inorganic semiconductors are formed using the Czochralski process in a chamber as shown here. Raw material is melted and slowly pulled out of the melt to crystallize extending seed crystal. Reproduced from Ref. 26.

typical diode laser) and to be fabricated in parallel, enabling the production of large numbers of devices simultaneously.

The Czochralski process is the predominant method used to grow a large single crystal boule which is then diced into a large number of wafers. The Czochralski process is shown in Figure 1.4.[26] To begin this process, high purity semiconductor material is melted in a crucible. Dopant impurities (such as boron or phosphorous) can be intentionally added to the melt in precise quantities to dope the material to be either n-type or p-type. A small single crystal seed is dipped into the melt and rotated while it is slowly drawn out. Surface tension in the melt causes some molten semiconductor to be pulled out of the melt by the seed crystal. As this material is pulled from the melt it cools and solidifies while attached to the seed. As the seed crystal is continually drawn farther up, the newly solidified semiconductor draws more molten material

out of the melt which also attaches to the growing solid. By carefully controlling the temperature of the melt, the rotation speed, and the draw rates, the cooling liquid can be given enough time to freeze into the lowest energy state by extending the single crystal of the seed. The pulling rate also determines the boule diameter which is designed for a particular wafer size – Si wafers are fabricated up to 300mm in diameter while 450mm wafer fabrication facilities are being considered.

A benefit of Czochralski process, is that impurities that may exist in the source material at concentrations of 10^{17} cm^{-3} (1 part per million) are filtered by the crystallization process. Typically less than 1% of harmful impurities are incorporated into the crystal. Meanwhile, the materials used for intentionally doping the semiconductor are required to have a high incorporation rate into the crystal, and this restricts the choice of dopant materials.

Once the boule is prepared, wafers are diced from the boule and then polished to provide a nearly atomically flat surface. For most Si substrates this is the final step of the semiconductor fabrication; however, it is followed by numerous processing steps to fabricate devices on the substrate including doping, oxidation, etching and metallization. Additional semiconductor crystal growth is typically performed on top of III-V substrates by epitaxial techniques. Epitaxy is the extension of the substrate crystal by adding material to the surface one monolayer at a time and allowing it to relax into the lowest energy crystal state defined by the substrate.[27] Epitaxial growth allows the fabrication of a heterogeneous crystal composed of layers of different materials. This is a key difference between compound and elemental (Group IV) semiconductors – the use of heterostructures enables new device architectures such as quantum-well based devices[28] (including high performance semiconductor lasers,[29] LEDs,[30] and infrared photodetectors[31]) or a high-electron mobility transistor (HEMT).[32] Presently, the most common

growth techniques used to produce these heterostructures are MOCVD (metal-organic chemical vapor deposition) and MBE (molecular beam epitaxy). Without getting into the details of these growth techniques, I will summarize some of the important concepts used in epitaxial growth in order to arrive at the main conclusion – that these are extremely expensive materials that are only suitable for small area devices such as lasers, LEDs and photodetectors.

Epitaxial growth is performed on a single crystal template – usually a thick wafer grown by the Czochralski process as discussed above. In order to maintain the crystal structure, the deposited materials must have the same lattice constant (a) as the substrate (a_0). If the lattice constant is mismatched, a strain is induced in the film according to

$$\epsilon = (a - a_0)/a_0. \quad (1.3)$$

If the strain energy becomes greater than the bond energy, dislocations will be formed in the crystal to relax the excess strain. This occurs at a critical thickness $t_c \cong a_0/2|\epsilon|$, after this point the crystallinity of the growth is compromised.[30] Occasionally, thin strained layers (< t_c) are intentionally utilized, but typically only materials that are lattice-matched to the substrate are included in the device. For example, GaAs and AlAs can be grown on a GaAs wafer. The ternary material $In_xGa_{1-x}P$ can be lattice matched to a GaAs wafer if $x = 0.49$, where x is the fractional percentage of In versus Ga incorporated into the layer. This value of x is determined by the compositional average of the InP and GaP lattice constants according to:

$$a_{InGaP}(x) = x \cdot a_{InP} + (1 - x)a_{GaP} = a_0, \quad (1.4)$$

where a_{InP} and a_{GaP} are the lattice constants of pure InP and GaP. Similarly, quaternary materials can be grown such as $In_xGa_{1-x}As_yP_{1-y}$ or $In_xGa_yAl_{1-x-y}P$, subject to similar lattice matching requirements and that the composition contains equal amounts of group III and group V

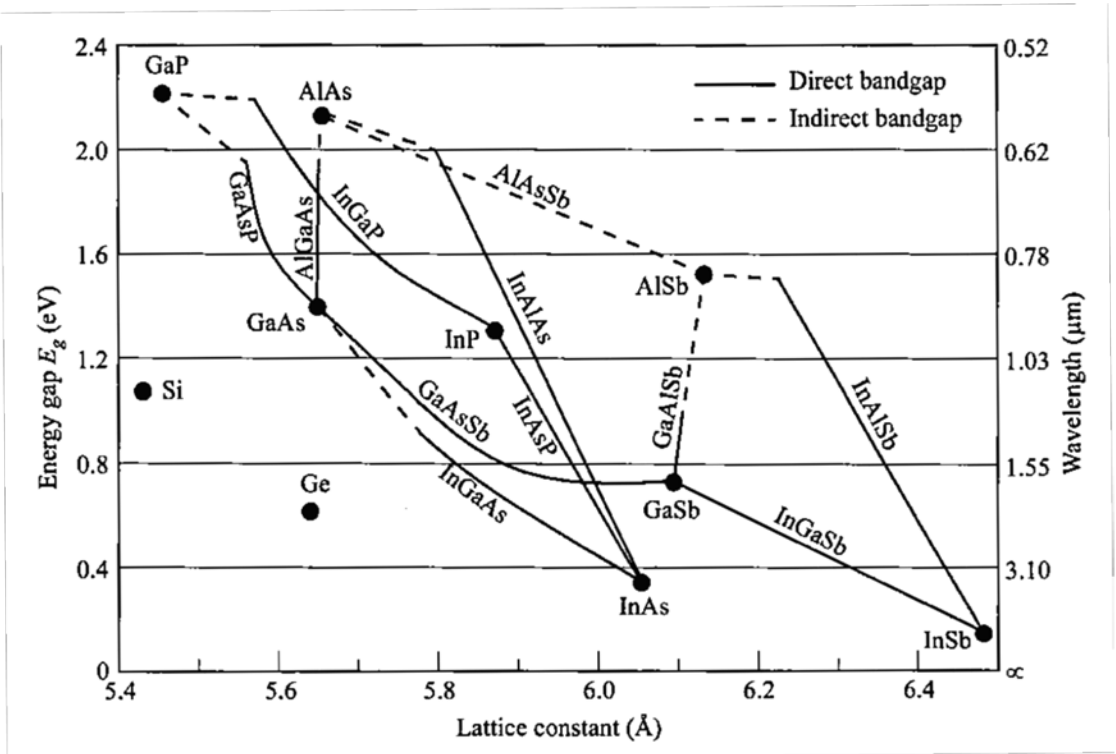

Figure 1.5 - Energy Gaps of Inorganic Semiconductors: Energy gaps and lattice constants of inorganic semiconductors. Lattice constants must be matched for defect free growth of thick crystalline layers. Ternary and quaternary alloys with various energy gaps and lattice constants can be formed within the designated regions connecting the binary alloys. Reproduced from Ref. 26.

elements. The properties of the ternary and quaternary materials, such as lattice constant, dielectric constant and bandgap, are well approximated by the compositional average of the binary compounds. Figure 1.5 shows the lattice constants and bandgaps of most of the relevant binary compounds.[26] A vertical line through GaAs shows the range of bandgaps that can be lattice matched to a GaAs wafer.

An example MBE process chamber is shown in Figure 1.6.[26] In the MBE process, epitaxial growth is performed inside an ultra-high vacuum (UHV) chamber, with a typical base pressure of 10^{-9} Torr, in order to avoid incorporation of unwanted impurities into the crystal. To maintain UHV conditions, a shroud inside the chamber surrounds the growth zone and is

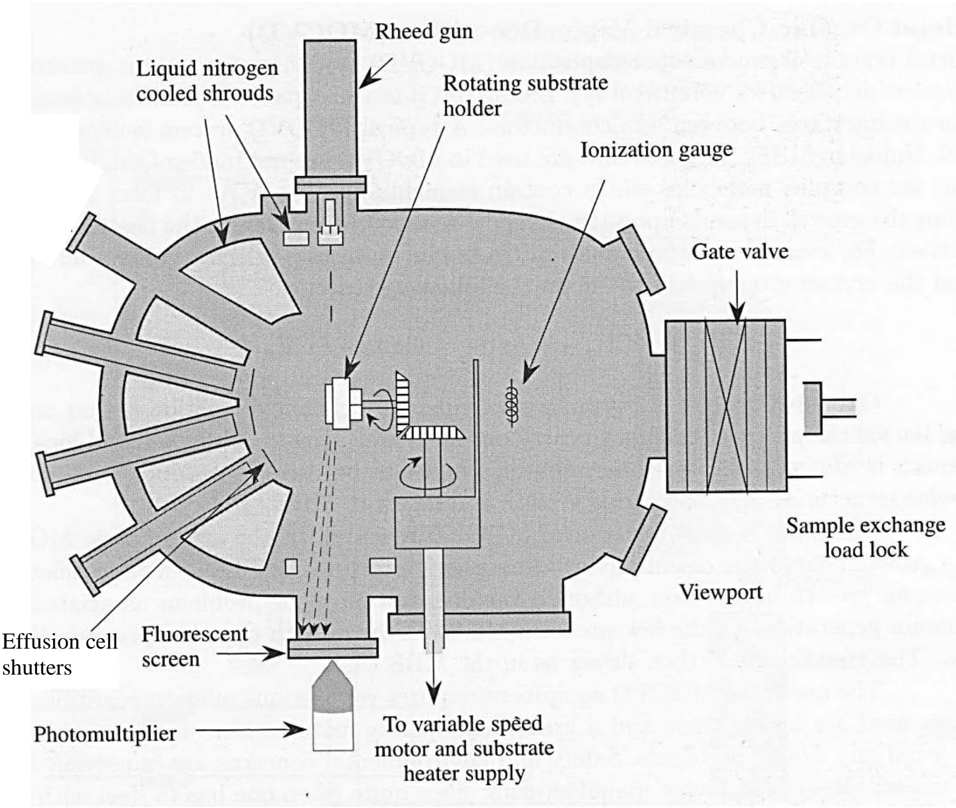

Figure 1.6 - MBE Chamber: Layout of a molecular beam epitaxy (MBE) chamber used for epitaxial crystal growth. Reproduced from Ref. 26.

cryogenically cooled to -196°C with flowing liquid nitrogen (LN_2). The wafer substrate is degassed and the native oxide that forms on the surface is driven off by heating the substrate to ~500°C. The completion of the oxide removal and the recovery of a clean, free surface is verified by identifying the RHEED (reflection high-energy electron diffraction) pattern of the relaxed, free surface.[33] The substrate is maintained at this moderate temperature that is much lower than the wafer's melting point but high enough to allow deposited materials to move on the surface and find low energy equilibrium crystal sites. Growth proceeds by flowing a vapor of elemental materials onto the surface. This vapor is formed by evaporating a solid metallic source material (for solid-source MBE) such as Al by heating it to ~1000°C, or by flowing a gas phase molecule such as phosphine (PH_3) through a ~1000°C heater to break the hydrogen bonds and free the phosphorous (for gas-source MBE). The composition of the resulting film is determined by the

flux of each element onto the substrate surface. These fluxes are precisely controlled by increasing the temperature of a solid source or increasing the flow rate of a gas source. Dopants can be incorporated into the film in an identical fashion.

Careful calibration of a process chamber and growing high-quality material is an art that requires patience, experience and attention to many details that I do not discuss here in sufficient depth. In short, I outline the most basic but important tools used to measure film quality and calibrate growth conditions. Growth rate can be measured in-situ by RHEED intensity oscillations[34] or ex-situ by film thickness verse deposition time. Composition can be measured by x-ray diffraction (XRD),[35] absorption spectroscopy, or SIMS (secondary ion mass spectroscopy).[36] Doping density can be measured by SIMS, Hall-effect[37] and capacitance-voltage measurements.[38] Defect densities can be measured by photoluminescence (PL) yield[39] or viewed under various microscopes.[40]

To summarize, epitaxial growth is a precision process that requires extreme environmental control. UHV chambers, high-temperature sources, LN_2 cooling, lethally toxic materials, slow growth rates and low-throughput process chambers all combine to make epitaxial growth extremely expensive. The substrate wafer alone is also expensive and amounts to roughly a third of the total cost of a completed solar cell. While Si is the most readily abundant material on earth and the price of Si has been dramatically reduced by the economics of scaling, Ga and As are much scarcer resources, and wafers are produced on a much smaller scale so that currently a 4” GaAs wafer costs ~$160 while a 4” Si wafer only costs ~$20. Adding epitaxy and device fabrication costs brings the cost of a completed GaAs wafer upwards of ~$450. This cost is not prohibitive if you dice such a wafer up into 1000 or more laser diodes, but to lay it out in the sunlight and cover 12 square inches in order to generate power would take over 300 years to

pay off the cost of the semiconductor alone (at an energy price of $0.07/kW-hr using a 30% efficient solar cell).

1.1.2. Optoelectronic properties

1.1.2.1. Electronic states and band transport

The theory of quantum mechanics tells us that, when we look closely enough, we can no longer treat an electron as a point charge of infinitely small size; rather an electron is distributed through a small region of space. Indeed it is more appropriate to describe an electron by a charge distribution $|\psi|^2$, where ψ is called the electrons wavefunction. A basic premise of quantum mechanics is that ψ is an eigenstate of the time-independent Schrödinger equation,

$$\hat{H}\psi = \left(-\frac{\hbar^2}{2m}\nabla^2 + U(r)\right)\psi = E\psi, \tag{1.5}$$

where $\hat{H}$ (the Hamiltonian of the system) is an operator that describes the energy of the system. The constant $\hbar$ is the reduced Planck constant and m is the electron mass. The first term in $\hat{H}$ is the kinetic energy of the electron and the second term $U(r)$ is the potential energy of the electron due to external electric fields. Operating $\hat{H}$ on ψ yields the constant energy of the system E.

In a crystal, atoms are fixed at periodically spaced lattice sites. The nucleus is a very small (~1000x smaller than the Bohr radius of the electron) and heavy (~1000x heavier than the electron) positive charge that sits rigidly at these lattice sites, while the valence electrons occupy a much larger volume surrounding the nucleus as shown in Figure 1.7. In the crystal, the nuclei are packed closely together and the valence electron interacts with surrounding nuclei as described in the discussion of bonding above (cf. Sect. 1.1.1.1). However, in the case of a

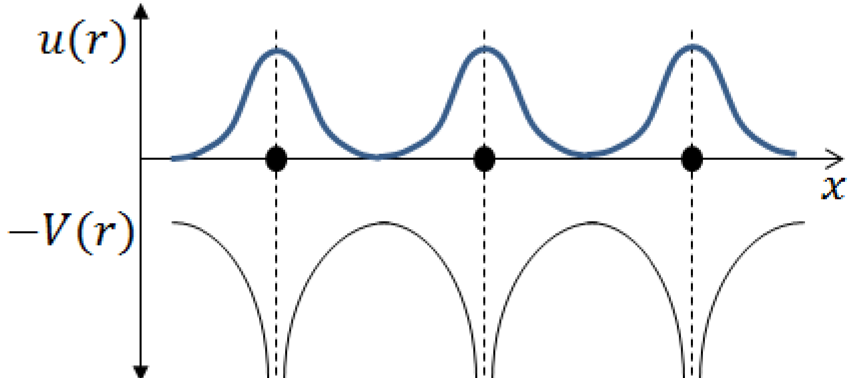

Figure 1.7 - Periodic Potential: The periodic potential of a crystal results in a delocalized electron. The Bloch theorem requires the electronic wavefunction have the same periodicity as the lattice and therefore has a slowly varying envelope u(r).

periodic lattice, the potential energy landscape that the electron experiences is also periodic, and this has a profound effect on the electronic states of the system. In this case, the potential energy has a translational symmetry so that $U(r) = U(r+R)$, where R is any lattice vector. This results in the Bloch theorem which states that ψ can be broken into a plane wave and a slowly-varying periodic function $u(r)$ as

$$\psi_k(r) = e^{ik\cdot r}u(r) \tag{1.6}$$

where k is a wave vector of the electron in the crystal, analogous to the free-electron wave vector. Because $u(r)$ is periodic, the Bloch theorem can be alternatively re-written as $\psi_k(r + R) = e^{ik\cdot R}\psi_k(r)$. This indicates that an electron in this electronic state of the crystal is distributed throughout the crystal, shared equally by the nucleus at each lattice site, and examining the state at any different lattice site (given by the lattice vector, R) simply corresponds to a phase change in the state of $\emptyset = k \cdot R$. This extended or delocalized nature of the electronic states of the crystal yield strong electronic coupling, high charge mobility and good charge transport through the crystal.

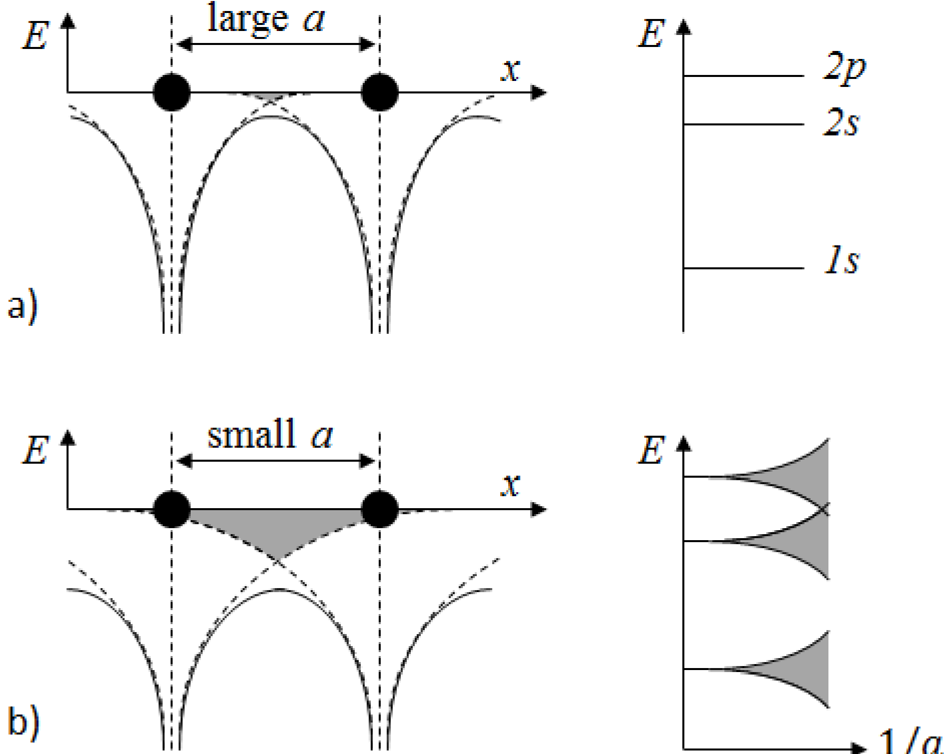

Figure 1.8 - Interatomic Coupling: (a) With a large separation between atoms, the overlap of their electronic potential is very small so that the electronic states are unperturbed from the atomic energy levels. This results in very tight binding of the electron to the atom. (b) When the separation is reduced, overlap of the Coulombic potential of the ion cores is large as indicated by the shaded region. This results in a pronounced deviation of the potential that an electron experiences from the isolated atomic potential shown by the solid line. This electron interacts with neighboring atoms in the crystal, resulting in splitting the atomic energy levels into bands.

The electronic properties of a periodic potential can be demonstrated concisely by the tight-binding method, which gives an intuitive view of the origin of bandstructure in a crystal. The tight-binding method treats the crystal as isolated atoms where each electron is tightly bound to its nucleus. In the extreme case of tight-binding, the electron is so tightly bound that it does not overlap at all with the potential energy of neighboring atoms as shown in Figure 1.8(a) – for example if there is a very large separation between the atoms (a large lattice constant). In this case the electronic energy levels are simply those of the isolated atoms. This is shown in Figure

1.8(a), by the discreet energy levels for a simple, 1-electron atom containing only *s*-orbitals. In this extreme case the Schrödinger equation is simply that of an isolated atom,

$$\widehat{H_{at}}\psi_{n,at} = \left(-\frac{h^2}{2m}\nabla^2 + U_{at}(r)\right)\psi_{n,at} = E_{n,at}\psi_{n,at}, \quad (1.7)$$

where the subscript *at* refers to the wavefunctions and energies of the isolated atoms, and the subscript *n* labels the distinct energy states of the atom. Relaxing the tight-binding condition, for example by reducing the lattice constant, results in a small overlap of the electron with the potential of neighboring atoms in the lattice as shown in Figure 1.8(b). This non-zero overlap indicates that $U(r)$ can no longer be approximated as the pure atomic potential $U_{at}(r)$, and the potential of neighboring atoms must be included in the Schrödinger equation. Because this overlap is small, the potential can be treated as a perturbation to the atomic potential, $U(r) = U_{at}(r) + \Delta U(r)$, and the eigenstates (wavefunctions) and eigenvalues (energy levels) of the new system are expected to be only slightly modified from those of the isolated atoms.

Here I discuss the application of the tight-binding method to the simplest case of a 1-dimensional atomic chain of *N* atoms, with lattice spacing a, total length L=Na, and each atom has only one atomic state which is an *s*-orbital. In this case we drop the subscript *n* and label the atomic state ψ_{at} with energy E_{at}. When there is electronic coupling between the crystal sites, the *N* atomic levels ψ_{at} of the independent atoms are described by *N* crystal states ψ_k that satisfy the Bloch theorem stated above. The crystal state has the form,

$$\psi_k(r) = \sum_R e^{ikR}\psi_{at}\,(r - R), \quad (1.8)$$

where the sum is over all lattice sites R, and there are N states with different $k = 0, 1\frac{2\pi}{Na}, 2\frac{2\pi}{Na}, 3\frac{2\pi}{Na}, \dots, N\frac{2\pi}{Na}$ as determined by Born-von Karman periodic boundary conditions. A complete calculation would acknowledge that $\psi_{at}(r)$ is no longer an eigenstate of the perturbed Hamiltonian $\hat{H} = \widehat{H_{at}} + \Delta U(r)$ and would replace the pure atomic orbitals $\psi_{at}(r)$ by a new function $\varphi(r)$ that is a solution to the new $\hat{H}$. However, to simplify the example we retain $\psi_{at}(r)$; this is reasonable because $\varphi(r)$ is very close to ψ_{at} for small $\Delta U(r)$. For a complete treatment of crystal states and the resulting energy bands, see chapters 8-11 in *Solid State Physics* by N. W. Ashcroft and N. D. Mermin.[24] Next, we calculate the energy of ψ_k by multiplying both sides of the Schrödinger equation by ψ_{at}^* and integrating over all *r* as,

$$\int \psi_{at}^*(r)\left[\left(\widehat{H_{at}} + \Delta U(r)\right)\psi_k(r) = E_k\psi_k(r)\right]dr. \tag{1.9}$$

Substituting in for $\psi_k(r)$ we get

$$\sum_R e^{ikR}\left(E_{at}\int \psi_{at}^*(r)\psi_{at}(r-R)dr + \int \psi_{at}^*(r)\Delta U(r)\psi_{at}(r-R)dr\right) = \tag{1.10}$$

$$E_k\sum_R e^{ikR}\int \psi_{at}^*(r)\psi_{at}(r-R)dr \tag{1.11}$$

This expression simplifies by noting that the overlap of $\psi_{at}^*(r)$ with the nearest neighbor at $\psi_{at}(r \pm a)$ is much greater than the overlap with the sites at distances of *2a* and greater. This is especially true for tight-binding with small $\Delta U(r)$, and we drop all terms except for *R = -a, 0,* or *a*. Next we note that $\int \psi_{at}^*(r)\psi_{at}(r)dr = 1$, and define the constants $\alpha, \beta,$ and γ according to $\alpha = \int \psi_{at}^*(r)\psi_{at}(r \pm a)dr$, $\beta = \int \Delta U(r)|\psi_{at}(r)|^2 dr$, and $\gamma = \int \Delta U(r)\psi_{at}^*(r)\psi_{at}(r+a)dr$.

Note that the *s*-orbitals are symmetric about *r* so that the $+a$ and $-a$ integrals are identical. With these definitions the above equation simplifies to,

$$E_k = E_{at} - \frac{\beta + \gamma\left(e^{ika} + e^{ika}\right)}{1 + \alpha(e^{ika} + e^{ika})} = E_{at} - \frac{\beta + 2\gamma \cos ka}{1 + 2\alpha \cos ka}. \tag{1.12}$$

The resulting energy levels are shown in Fig. 1.9a using $E_{at} = 0$, $\beta = 10$, $\gamma = 5$, and $\alpha = 1$. In general this is referred to as a dispersion relation, and for semiconductors it results in a *band diagram*. Essentially, the energy level E_{at} for the isolated atoms are split into *N* different energy levels corresponding to each wavevector supported by the crystal. Now a range of energy levels exist for an electron corresponding to different *k* values. If the crystal atoms have more than one electronic state, each state is similarly split into an energy band as shown in Figure 1.8(d), and a broad range of electron energies can exist in the crystal. In between the energy bands are energy levels that are not supported by the crystal and an electron cannot exist inside the crystal with these forbidden energies – this gap in the energy states of the crystal is the *bandgap* of the crystal.

It is helpful to note that in a real crystal the atomic spacing is $a \sim 5$Å (which is 0.5 nm or $0.5\text{x}10^{-9}$ m). So a macroscopic crystal that is $(1 \text{ mm})^3$ consists of $N = (L/a)^3 = 8\times10^{18}$ atoms – corresponding to 2 million k states along each axis between $k = 0$ and $k = 2\pi/L$. So far we have referred to *k* as discreet states but they are so closely spaced that they essentially form a continuum of states and we consider *k* to be a continuous variable.

This simple tight-binding example is useful for understanding how energy bands are formed as a result of electronic coupling in a periodic structure. However, real atoms in a crystal have complex energy levels (consisting of numerous electronic levels as in Figure 1.8(b) along

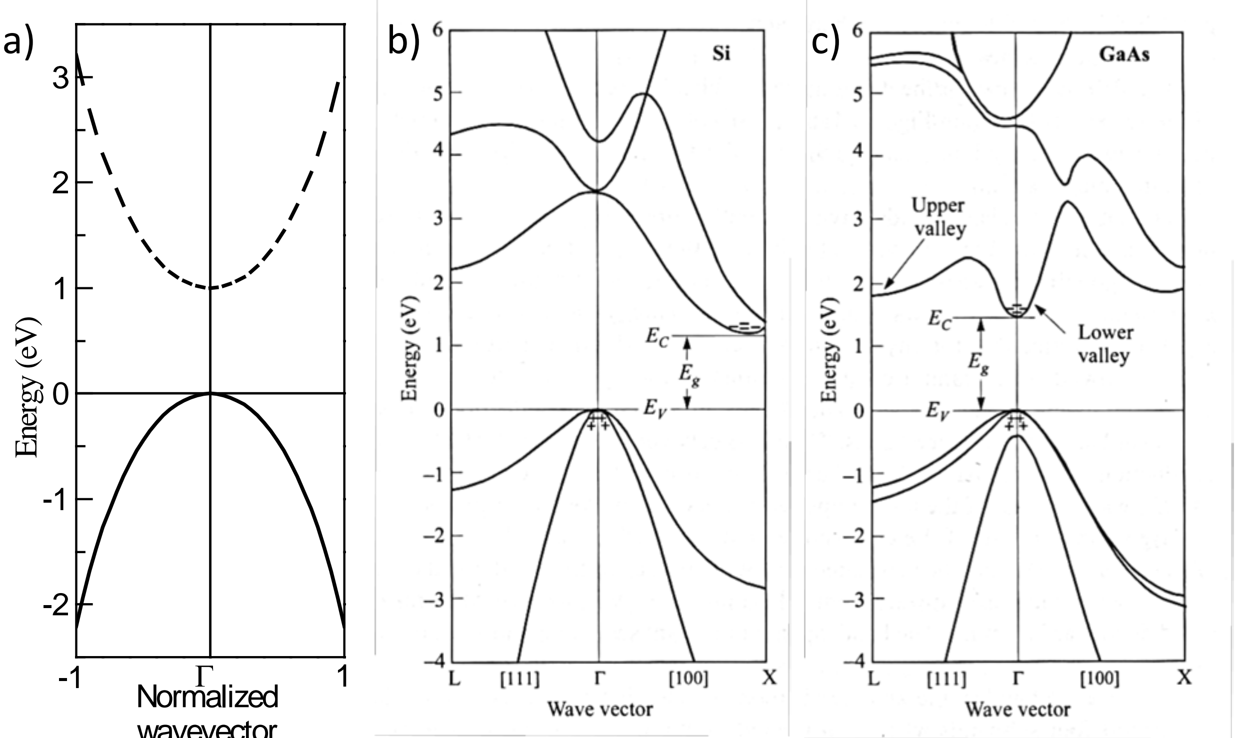

Figure 1.9 - Band Diagram: Energy band diagram for (a) the tight binding model, (b) Silicon and (c) GaAs. The gamma (Γ) point is the k = 0 point. The tight binding model shows the valence s-orbital derived in the text (solid) and a second conduction s-level (dashed). Silicon is an indirect semiconductor because the minimum bandgap is not a vertical transition so it is not an optically allowed transition. GaAs is a direct bandgap material and the minimum energy transition is optically allowed making them useful light emitting materials. Reproduced in part from Ref. 41.

with various electronic spins and the angular momentum states *s-, p-, d-, f-,* and higher orbitals) and can be arranged in complex crystal structures. Calculations of a band diagram is therefore quite complex and there are several methods for doing this – the most important are the orthogonalized plane-wave, the pseudopotential, and the $k \cdot p$ methods. Results of bandstructure calculations[41] for Si and GaAs are shown in Figure 1.9 and show complex dispersion relations along different crystal axes.

Figure 1.9 shows the energy gap E_g for GaAs is located at the Γ-point (which is k=0) and lies between 0 and 1.4eV. As we discussed in relation to Figure 1.1, the Fermi level of a

semiconductor typically lies within E_g. Without any excitation by light or heat (*i.e.* a semiconductor in the dark and at a temperature of 0K), the system is in the lowest energy configuration, *i.e.* the ground state, where all of the states below the Fermi level are filled with electrons and all of the states above the Fermi level are empty (or filled with holes which is a positively charged quasi-particle denoting the lack of an electron).

The most important electronic states are those lying closest to the gap and the filled band below the gap is called the *valence band*, while the empty band above the gap is called the *conduction band*. There is no net charge flow (current) in the conduction band because there are no carriers. Similarly, there is no net charge flow in the completely filled valence band because $E(k) = E(-k)$ along the same crystal axis; there are always the same number of electrons moving in the positive k direction as the negative k direction. Even though the band is full of electrons constantly moving through the crystal, there is no net motion of charge. In fact, charge flow can only occur if an electron is excited from the valence band to the conduction band by light or heat. Once in the conduction band the electron can be driven by an external electric field to produce current. Similarly, when the electron is removed from the valence band, it leaves behind an empty state that can be treated as a positively charged electron – a hole. The hole will respond to an electric field in the same way that an electron does (except with opposite sign) and it can result in current flow due to the valence band.

Energy diagrams as in Figure 1.9 are always drawn with respect to the energy of an electron. This means lower energies are lower energy states for an electron. Hence, when an electron is excited into the conduction band, it will tend to thermalize to the lowest energy state in the conduction band as indicated by charge signs in Figure 1.9. Conversely, the lowest energy

state for a hole is the highest point of the valence band and holes will thermalize to this point, because a hole represents a missing electron.

Near the minimum and maximum of either band, the dispersion relation E versus k can be approximated by a parabolic function as $E \propto k^2$. We can relate the dispersion relation to the free electron case if we write it as $E = h^2k^2/2m^*$, where the constant m^* is the *effective mass* of the electron in the crystal and is determined by the curvature of the energy band. Physically, the effective mass relates how much energy is required to get an electron to move at k. There is an m^* associated with a materials conduction band minimum and valence band maximum. In general the band structure is not symmetric between different crystal axes, so the m^* is a tensor quantity that reflects the band curvature along each crystal axis.

While the m^* is important to understand how charge transports through a semiconductor, it is only part of the story. Charge transport through a crystal in response to an external electric field (F) is described by the mobility (μ) of the material as $v = \mu F$, where v is the velocity of the electron. The mobility is limited by scattering of the electron by impurities /defects in the crystal or by phonons (harmonic lattice vibrations that displace nuclei from their lattice site). Typically the μ is limited by phonon scattering at high temperatures because there are a large number of phonons, but is limited by ionized impurity scattering at low temperature from the intentional dopants in the crystal. A discussion of Boltzman transport and scattering can be found in chapters 4-6 of Ref. [26]. The mobility of inorganic crystals is typically 500-10,000 $cm^2/V \cdot s$.

1.1.2.2. Carrier generation

In the previous section we discussed that there are no carriers above the Fermi level if there were no excitation sources. However, at room temperature there is ambient thermal energy

that can excite electrons and generate an equilibrium density of carriers (*i.e.* electrons in the conduction band or holes in valence band). The Fermi-Dirac probabilities of statistical mechanics determine the probability of an electron being thermally excited to an energy of E above the Fermi level E_F as,

$$f(E) = \frac{1}{1 + e^{(E-E_F)/k_B T}} \approx e^{-(E-E_F)/k_B T} \tag{1.13}$$

where k_B is the Boltzmann constant, T is the temperature, and the approximation is the Maxwell-Boltzmann approximation that is generally valid when E is greater than a few k_BT above E_F (i.e. non-degenerately doped semiconductors). The carrier density is determined from $n(E) = \mathcal{D}(E)f(E)$, where $\mathcal{D}(E)$ is the density of states (each state with distinct k) per unit energy. The conduction band $\mathcal{D}(E)$ in a 3-dimensional crystal is $\mathcal{D}(E) = \sqrt{2}m^{*3/2}\sqrt{E - E_C}/\pi^2\hbar^3$ and increases with E above the conduction band edge E_C; the $\mathcal{D}(E)$ for different dimensional systems (i.e. quantum well, wires and dots) are shown in Figure 1.10. The total number of carriers in the band is found by integrating over all E as,

$$n = \int_{E_F}^{\infty} \mathcal{D}(E)f(E)dE = N_C e^{-(E_C-E_F)/k_B T} \tag{1.14}$$

where α is a proportionality constant that depends on the m^*, and $N_C = 2(2\pi m^* k_B T)^{3/2}/\hbar^3$ is the *effective density of states* of the conduction band. Note that below the conduction band edge the $\mathcal{D}(E) = 0$, so we could change the lower limit of integration in the second equality from E_F to E_C. The last equality results from a simple integration.

For a pure, undoped semiconductor (an *intrinsic* semiconductor) the Fermi level is roughly in the middle of the bandgap. However, dopants are often intentionally incorporated into

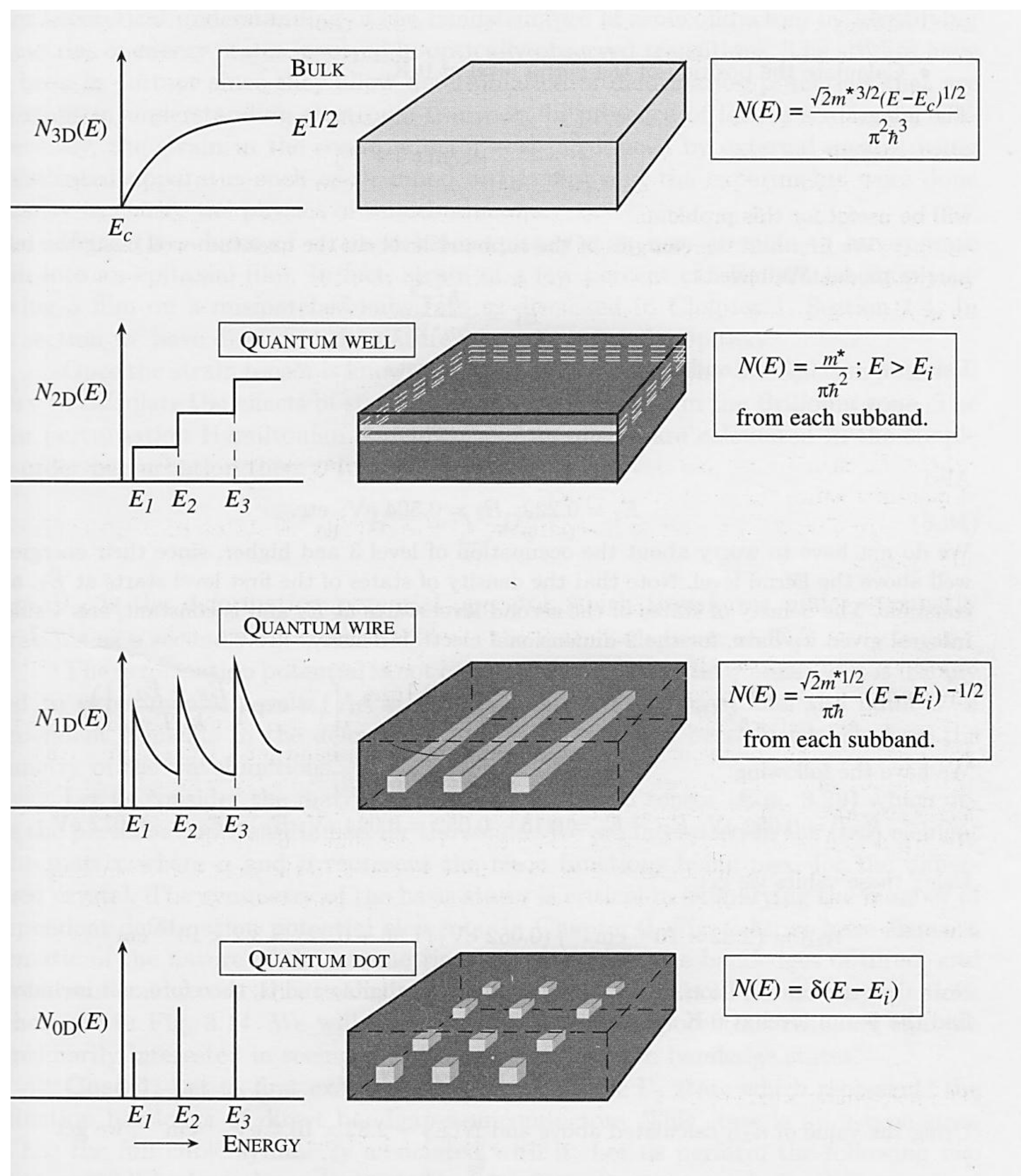

Figure 1.10 - Density of States: Density of states for a semiconductor as a function of dimensionality. In low dimension systems there is a large density of states at the lowest allowed energy level. Reproduced from Ref. 26.

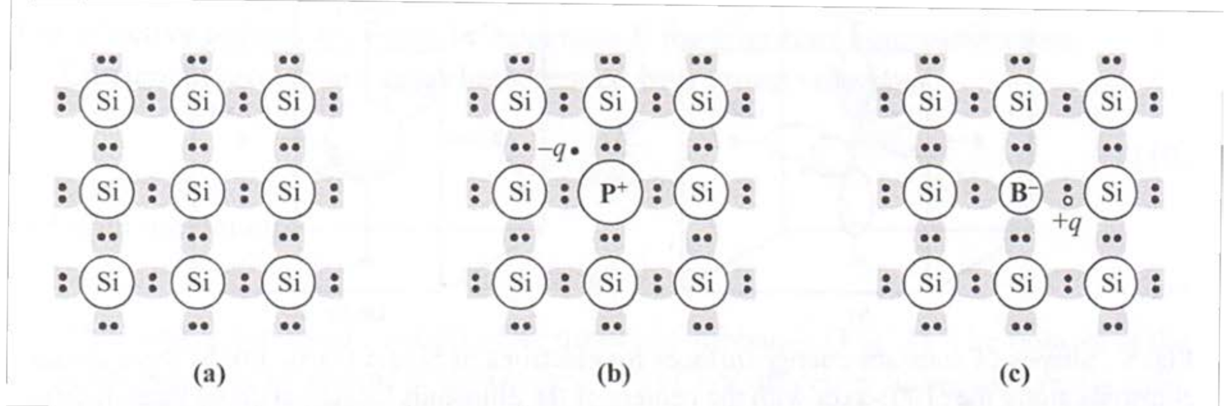

Figure 1.11 - Doping in Silicon: (a) Undoped silicon. (b) Phosphorous (Group 5) doped silicon results in a free electron donated to the crystal. (c) Boron (Group III) doped silicon results in a missing electron called a hole. Reproduced from Ref. 26.

the crystal during growth in order to control the free carrier density. As discussed in section 1.1.1.2, the Group V element P can replace a Group IV Si atom in the crystal resulting in one extra electron in the system as shown in Figure 1.11. This dopant is a perturbation to the crystal, and there is a localized energy level for the extra dopant electron that typically lies within the bandgap. For effective doping, the impurity level is close to the conduction band so that the electron is easily excited into the conduction band by thermal excitation – resulting in an extra free carrier. This doping causes the Fermi level to lie closer to the valence or conduction band so that the carrier density is still given by Eq. 1.14.

A dopant that donates an extra electron to the conduction band is called a *donor*, while a dopant that lacks an electron and can receive an electron from the valence band (thus creating a free hole) is called an *acceptor*. The number of electrons doped into the conduction band is equal to the number of ionized donor atoms and is determined by

$$N_D^+ = \frac{N_D}{1 + 2e^{(E_F - E_D)/k_B T}} \tag{1.15}$$

where N_D is the donor density, E_D is the donor energy level, and the factor of two comes from the spin degeneracy of the electron. In doped crystals, the dopant density is much greater than the intrinsic density so that $n = N_D^+$ and this can be equated with the expression for n above to find the E_F for the doped system.

The thermal equilibrium carrier density is maintained by a balance of thermal generation and recombination of carriers according to the rate equation,

$$\frac{d}{dt}n = G_{th} - R_{th} = 0, \tag{1.16}$$

where G_{th} is a constant thermal generation rate and R_{th} is the carrier recombination rate. This equation describes the average change of carrier density at any location in the semiconductor, and in steady state is identically zero so that at equilibrium $R = G_{th}$. Carrier recombination is a bi-molecular recombination process that scales with the product electrons and holes so $R_{th} = R_0 n_{eq} p_{eq} \equiv G_{th}$, where R_0 is a constant *recombination coefficient*, the subscript *eq* is used to denote these are the carrier densities under equilibrium conditions, and the last equality is due to the steady state condition.

When a semiconductor device is operating, the system is usually perturbed from equilibrium by other processes that must be included in the rate equation – such as electrical injection or photon absorption. A GaAs LED provides an example of how the rate equation can be modified for a device. See *Semiconductor Optoelectronic Devices* by Bhattacharya for details of device operation and design principles. Generally, when an LED is biased by an external voltage, a non-equilibrium carrier density results from electrical injection. Specifically, n and p are increased above their equilibrium values. In this case, $R = R_0 np > G_{th}$ so that electrons and

holes recombine faster than they are thermally generated. The only way this can be maintained as a steady state is to have another charge generation process to maintain the non-equilibrium carrier density. The carrier density is replenished by current injected into the device to sustain the external voltage on the LED. This modifies the rate equation to,

$$\frac{d}{dt}n = G_{th} - R + \nabla \cdot J = 0, \tag{1.17}$$

where $\nabla \cdot J$ is the local change in charge density due to the current *J*.

When electrons and holes recombine, an electron is de-excited from the conduction band back to the valence band. This corresponds to a change in energy approximately equal to the bandgap (~1eV). Conservation of energy requires the simultaneous generation of a large number of thermal phonons (~0.03eV) or a single optical photon (~1eV). For *direct gap* materials (materials with a vertical transition between the conduction band minimum and valence band maximum) such as GaAs as shown in Figure 1.9, *radiative transitions* that generate photons are dominant over *non-radiative transitions* corresponding to phonon generation.

1.2. Organic semiconductors (oSC's)

The term "organic" implies a carbon-hydrogen bond. While most of the materials referred to as "organic semiconductors" do consist of a large number of C-H bonds, some of the most common and important "organic semiconductors" do not meet this technical criterion. Fullerenes (C_{60}), carbon nanotubes, and graphene are some examples that do not have any C-H bonds because they are composed entirely of carbon. Consequently, here (as throughout the field of organic electronics) I use the term organic semiconductor to refer to the broad class of carbon-rich molecular and polymeric semiconductors, regardless of the chemical composition of the

materials. Therefore, the distinction between organic and inorganic semiconductors lies in the nature of the bonding in each material: strong chemical bonding throughout an inorganic solid versus a weak physical bond due to electrostatic coupling in an organic film.

The dramatically different nature of organic semiconductor films yields very different optical and electronic properties than traditional semiconductors. This makes them interesting for extending the range of applications of semiconductor devices. As mentioned above, the big push for these materials is to make inexpensive, large area devices such as solar photovoltaics and large area LEDs. This is driven by the need for clean energy sources and energy efficiency to provide energy security nationally, and environmental sustainability globally. The rest of this chapter describes the properties and fabrication methods of organic semiconductors to illustrate that organics are well-suited for these applications. However, their properties also make them well suited for other applications, such as flexible, transparent, or disposable electronics. Here I reiterate that my interest, and the purpose of this thesis, is to better understand organic semiconductors, how they can be utilized with inorganic semiconductors, and how to bridge the gap between organic and traditional, inorganic theories.

1.2.1. Nature of bonding and films

Organic semiconductors are divided into two classes: small molecules and polymers. Small molecules typically consist of a definite number of atoms (typically between 10-1000 atoms) while polymers are long molecular chains that typically consist of an indefinite number of atoms (typically 10,000 atoms or more). Most of my discussion is equally relevant to both classes, but for simplicity I orient my discussion in regards to small molecules. I will try to highlight any significant differences between the two where applicable.

Many organic semiconductors are strong absorbers with typical absorption coefficients more than 10 times greater than inorganics. This enables the use of thin films (typically 10-100 nm) for optical devices. This thin-film nature requires less material for cost-effective solar cell applications and the non-crystalline, thin-films can be flexible.

1.2.1.1. Van der Waals interactions

Bonding in organic films is different from the strong covalent or ionic bonding of inorganic semiconductors. The isolated molecule is already chemically stable (its valence shells filled, its octet rules satisfied) so that it does not interact chemically with neighboring molecules. The molecule is also neutral so there is no ionic attraction. Instead, bonding occurs by a second order electrostatic effect of dipole interactions. An electrostatic interaction between neutral molecules occurs because the electric field produced by one dipole p_1 is felt by another dipole p_2 and vice-versa. The electric field produced by a dipole is,

$$F = \frac{1}{4\pi\varepsilon_0}\left(\frac{3(\overrightarrow{p_1}\cdot\hat{r})\hat{r} - \overrightarrow{p_1}}{r^3}\right) \equiv \frac{p_1}{2\pi\varepsilon_0 r^3}, \tag{1.18}$$

where ε_0 is the ambient dielectric constant, r is the distance from the dipole and $\hat{r}$ is the unit vector specifying the relative orientation of the dipole. The second equality is the corresponding vector-less expression where *p* is oriented along *r*. The interaction energy of a dipole in this field is therefore,

$$U = -p_2 \cdot F \equiv -\frac{p_1 p_2}{2\pi\varepsilon_0 r^3}. \tag{1.19}$$

Many molecules have a built-in dipole due to their chemical structure. However, even if the molecules do not have a dipole (such as C_{60}), electronic fluctuations randomly form an

instantaneous dipole. This dipole induces a dipole in neighboring molecules according to the molecular polarizability (α) as $p_2 = \alpha F_1$. Consequently, the potential energy of the dipole and induced dipole is $U \propto p_1^2/r^6$. While the time average of the fluctuating dipole p_1 is zero (no net polarization), the potential depends on the square of p_1 which has a non-zero average. This induced dipole attraction is known as a van der Waals force.

Similar to the case of ionic attraction of section 1.1.1.1, when two molecules approach each other there is a repulsive force due to a quantum mechanical interaction. We follow convention and take this repulsive force to be $U = A/r^{12}$. Adding this to the attractive van der Waals potential we arrive at the Lennard-Jones potential,

$$U = \frac{A}{r^{12}} - \frac{B}{r^6}. \tag{1.20}$$

This has a similar profile as Figure 1.3, and the minimum in potential energy determines the separation between molecules in film.

Because the van der Waals interaction is much weaker than chemical bonding (corresponding to a shallow potential well), organic films are mechanically soft and pliable. This makes them compelling candidates for flexible electronics. Also, the target applications of organic semiconductors are for inexpensive high volume applications, so high quality crystals are not needed as with traditional semiconductors. Crystalline films, even single crystals, can be grown as discussed in section 1.2.1.3, but most of the field is based on amorphous or nanocrystalline films with reduced order.

1.2.1.2. Vacuum thermal evaporation

The weak intermolecular interactions not only make the organic materials soft, but it also makes the material easy to evaporate. In contrast to the 800-1000°C evaporation temperature of traditional inorganics, many small molecule organics sublime around 200-400°C before they chemically decompose (by breaking molecular bonds). This low temperature processing combined with the relaxed requirement for crystalline growth, enables the fabrication of films in simple deposition chambers. Consequently, organic films are typically deposited by thermal evaporation in vacuum. In this process organic powder is evaporated from a resistive metal boat in a high vacuum environment of ~10^{-6} Torr. This modest vacuum (relative to UHV conditions of 10^{-9} Torr used in MBE) is easily achieved without cryogenic cooling at the cost of having higher amount of background gas that can be incorporated into the film. Ultimately, this allows for higher throughput and less expensive devices.

Organics are typically deposited onto non-crystalline substrates. This offers dramatic cost savings because materials can be deposited onto any substrate such as glass (much cheaper than wafers), and thin flexible plastics or metal foils (much cheaper than glass). The ability to deposit onto flexible substrates enables the possibility of roll-to-roll processing,[42] which also offers high throughputs and potential cost savings that are ideal for large area coverage.

1.2.1.3. Crystalline growth techniques

Organic films with a high degree of crystallinity and even single crystals have been fabricated by several techniques including: 1) organic molecular beam deposition (OMBD),[43] 2) organic vapor phase deposition (OVPD),[44,45] 3) precipitation out of solution,[46,47] and crystallization from a melt.[48] These efforts have been useful for better understanding the

properties of organic semiconductors, such as identifying the upper limits of mobility[49] and understanding crystal structure. Ultimately, the stringent conditions required for crystal growth poses a challenge for low cost device fabrication.

1.2.1.4. Solution based deposition

The weak bonding in organic solids enables a unique and beneficial method of film fabrication. Because organic solids are bound by relatively weak van der Waals interactions, many of them can be dissolved, or at least dispersed, into solution using organic solvents. The resulting liquid solution can be used to fabricate thin films by spin-casting,[50] drop casting,[51] or inkjet printing[52] techniques.[47] Of these spin-casting is the most common technique and is performed by spinning a substrate at a high rotation rate followed by dropping a small volume of solution onto the substrate. The rotation uniformly disperses the solution across the surface while the volatile solvent evaporates leaving behind a film of the organic semiconductor. Precise control of the film thickness can be achieved by controlling the concentration of semiconductor in the solution, the volatility of the solvent used, and the spin conditions.

The solution deposition techniques available for organic film fabrication are promising new techniques that may facilitate low cost, high volume fabrication of large area semiconductor devices. Most importantly, these processes are amenable to in-line processing that greatly aids high volume fabrication. Roll-to-roll fabrication techniques[53] similar to those used in newspaper printing have already been demonstrated for solution[42] based processing as well as vapor phase[54] based processing. In similar fashion, inket printing[52] of organic device arrays has been demonstrated with high resolution.

1.2.1.5. Doping of organic semiconductors

Electrical doping (doping to generate charge carriers) in organic semiconductors has been performed with limited success.[55,56] Most of the field utilizes pure organic films that are unintentionally doped. There are two major differences between organic and inorganic semiconductors that make electrical doping less useful in organic semiconductors. The first difference is a about a factor of 50 in size. Doping in molecular films is achieved by including a different molecule in the film that has dramatically lower energy level for either an electron or a hole. This dopant can receive an electron or hole from a neighboring neutral molecule; this ionizes the neutral molecule creating a free electron or hole. However, even small organic molecules typically have on the order of 50 atoms comprising the molecule. Consequently the molecular volumes of both the host and the dopant are much larger than size of an atomic dopant incorporated into an inorganic semiconductor. This limits the range of doping to roughly > 0.1 %, whereas doping of inorganic films covers a much larger range, typically 1 part in 10^7 – 10^3, enabling a better range of control. The second major difference is the nature of electronic states (c.f. Sect. 1.1.2 and 1.2.2). Carriers in an inorganic crystal are distributed over a large number of unit cells, so that a moderate amount of doping can be incorporated without perturbing the electronic state because the carrier averages over a large number of unit cells. Doping to a very high level does eventually reduce the carrier mobility by increasing electronic scattering from ionized impurities. In organic films, doping is intrinsically different due to the weak interaction between neighboring molecules that compose the solid. Carriers are localized in the vicinity of a single molecule and transport by hopping through a large number of molecular sites. Consequently, the electronic properties of the dopant can affect charge transport even at relatively low doping densities.

Doping for reasons other than charge generation (neutral doping) has been successfully applied to organic light-emitting diodes (OLEDs).[57,58] In OLEDs, a narrow bandgap dopant is incorporated into a wide bandgap, charge transporting host. The dopant is used as an efficient light emitter. The energy levels of this dopant must lie within the bandgap of the host so that it can capture electrons (holes) that are electrically injected into the charge transport levels of the host. This is similar to the quantum well or quantum dot architecture used in inorganic crystals to localize light emission or absorption. In organics, it is straightforward to fabricate a large density of quantum wells (dopants) distributed throughout the charge transporting host, this provides an ideal platform for light emitting devices. Doped OLEDs have been demonstrated with very high electron to photon conversion efficiencies.[59] OLEDs have already been successfully commercialized into high-performance displays used in cell phones and will soon hit the market in tablet and television size displays.[60]

1.2.2. Optoelectronic properties

1.2.2.1. Electronic states and disorder induced broadening

The weak van der Waals interactions that form an organic solid also result in weak electronic coupling between neighboring molecules. As a result, the electronic states are essentially that of an isolated molecule as shown in Figure 1.12(a) – in stark contrast to the delocalized crystal states of electrons in inorganic semiconductors. The figure shows the two most important *frontier* energy levels of a molecule – the highest occupied molecular orbital (HOMO) and the lowest unoccupied molecular orbital (LUMO). The HOMO is the highest filled state for the neutral, ground state molecule – identical to the lower atomic state that forms the valence band in inorganic crystals. The LUMO is the next energy state that an extra electron

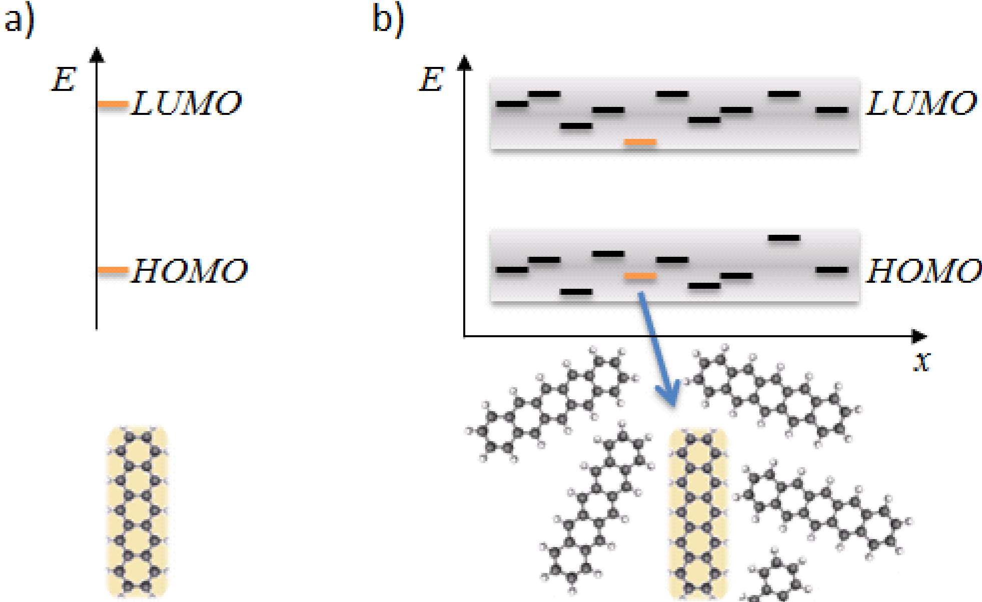

Figure 1.12 – Organic Transport Levels: (a) The highest occupied molecular orbital (HOMO) and lowest unoccupied molecular orbital (LUMO) of an isolated organic semiconductor. (b) In a disordered film, the HOMO and LUMO of molecules are perturbed in a random manner. This results in a distribution of molecule HOMO and LUMO states for different molecules in the film.

would occupy (*i.e.* the molecule would be ionized with a single negative charge if this state were occupied) – this is identical to the higher atomic states that split to form the conduction band in inorganic crystals.

The HOMO and LUMO energies in an organic semiconducting film are analogous to the valence and conduction bands in inorganic crystals. Absorption in an organic film can be thought of as promoting an electron from the HOMO to the LUMO with a bandgap of $E_{gap} = E_{LUMO} - E_{HOMO}$; however, due to the strong electron-hole interaction photon absorption actually results in a bound exciton state so that the optical bandgap is $E_{opt} = E_{LUMO} - E_{HOMO} - E_B$, where E_B is the exciton binding energy (cf. Sect. 1.2.2.3). Conduction occurs between adjacent molecules by electron transport through their LUMO levels. Conduction can only occur in the fully occupied HOMO states if an electron vacancy (a hole) is created in one of the HOMO states. The analogy

between the HOMO/LUMO levels and the valence/conduction band is convenient and allows us to adapt many concepts from traditional semiconductor theory to organic semiconductors.

While the electronic states are very characteristic of the isolated molecule, the molecule is not truly isolated. The molecular state is weakly perturbed by the local potential formed by the electronic landscape of the neighboring neutral molecules. The disorder in the system causes small perturbations in the energy levels of each molecule. A schematic of this random distribution of molecular energy levels is shown is shown in Figure 1.12(b). This disorder broadens the distribution of HOMO/LUMO states giving rise to broadened absorption spectra an d an energetic distribution of transport levels.

1.2.2.2. Charge transport

Unlike the nearly free electrons associated with band transport in inorganics, an electron in the conduction band is localized on a molecule and transports in discreet steps by hopping from one molecule to an adjacent molecule. Because this electron resides on a single molecule, the molecule is ionized, and the electric field from this ion polarizes nearby molecules. This results in a new local potential landscape that perturbs the energy levels of the original neutral molecule. Consequently, this state is not simply an independent electron, and the charged molecule and the electronic reorganization associated with it are collectively referred to as a negative polaron. Similarly, an electron vacancy in a HOMO state is properly called a positive polaron. In the field and in this thesis, this distinction is not generally maintained in the terminology, and *electron* and *hole* are freely applied to refer to the negative and positive polaron.

Because charge transport occurs by hopping between localized sites, the energetic distribution discussed above can have a significant impact on charge transport. Specifically, if a neighboring site is at a lower energy ($\Delta E < 0$), transfer to that site will readily occur. But if that site is a higher energy ($\Delta E > 0$), transfer to that site will occur with lower probability. The model usually applied to describe this transfer rate uses the Miller-Abraham type jump rate and is given by,[61,62,63]

$$k_{et} = \begin{Bmatrix} \upsilon \exp\left(-\frac{\Delta E}{k_B T}\right), & if & \Delta E > 0 \\ \upsilon & & \Delta E < 0 \end{Bmatrix} \tag{1.21}$$

This rate is simply the Maxwell-Boltzmann probability times an attempt frequency factor (υ). From this it is evident that charge transport is a thermally activated process.

The statistics of transport through a gaussian distribution of energy sites (and a gaussian distribution of molecular positions) has been evaluated by Bässler resulting in the gaussian disorder model for charge transport.[64] This model includes the effect of an electric field (F) which modifies the energy of neighboring sites by $\Delta E = FW$, where W is the distance between sites. Other models[65,66,67,68] exist with different functional dependencies on temperature and electric field. It is important to be aware that electron transport is expected to be a function of temperature and field.

1.2.2.1. Excitons in organic semiconductors

Light absorption in inorganic semiconductors directly results in the generation of a free electron and a free hole. There is a Coulombic attraction between the electron and hole, but they easily separate because of the delocalized nature of the carriers and the high dielectric constant of the inorganic crystal. The dielectric constant ($11.9\varepsilon_0$ for Si and $13.2\varepsilon_0$ for GaAs, where $\varepsilon_0 =$

8.85×10^{12} F/m is the dielectric permittivity of free space) results in screening that reduces the Coulomb interaction. In organics, the carriers are localized since the dielectric constant is small (typically $3\varepsilon_0 - 4\varepsilon_0$) so that the Coulombic binding energy (typically $> 0.3eV$) is much larger than thermal energy at room temperature ($k_B T = 26\, meV$). Consequently, light absorption results in a Coulombically bound electron-hole pair called an exciton.

Excitons play a defining and distinctive role in organic devices (such as in organic photovoltaics as described in Sect. 2.3). They can transport through an organic film by nearest-neighbor hopping similar to charge transfer described above. This transfer rate depends on the quantum mechanical overlap of molecular wavefunctions and is described by Dexter transfer.[69,70,71] Unlike charge, excitons can also transport long distances by radiative coupling.[72] This process occurs by radiative relaxation of the exciton causing the emission of a photon, and then reabsorption of the photon by another organic molecule. The photon can travel a great distance before reabsorption, so that the energy can be transferred a great distance in a single step. Closely related to radiative transfer is Förster transfer,[70,71,73] which results from dipole-dipole coupling between molecules that can transfer the excitation a large distance, but is not mediated by emission of a photon. It is closely related not only because it is a long range transfer process, but it is the same dipole oscillator that is coupled in Förster transfer as the oscillator responsible for absorption and emission. The Förster transfer rate is given by:[73]

$$k = \frac{1}{\tau}\left(\frac{R_0}{r}\right)^6 \tag{1.22}$$

Where τ is the exciton lifetime and $R_0 = 9 \cdot \ln(10)\, Q_0 \kappa^2 J / 128\pi^5 n^4 N_A$. Here Q_0 is the fluorescence quantum yield, κ is the dipole orientation factor, J is the spectral overlap integral, n is the refractive index, and N_A is Avogadro's number.

Chapter 2

Physics of Organic Photovoltaics

2.1. Background

Areal power generation from an organic photovoltaic (OPV) device is determined by $P_A = JV$, where J is the current density produced by the device at a voltage V. The power conversion efficiency (η_{PCE}) of an OPV device depends on the maximum product of J and V normalized by the incident optical intensity (I_o) as $\eta_{PCE} = \max(JV)/I_o$. By measuring the J versus V (J-V) behavior, we can directly measure η_{PCE} for a particular device. However, the development of efficient devices is aided if we can accurately predict η_{PCE} for a given device structure.

While the physics of inorganic, crystalline semiconductors is well-established,[38] the physical principles that govern the behavior of organic semiconducting devices is less well understood. The thin-film and amorphous nature of these films presents some challenges to a theoretical treatment of these devices. The standard model for OPV devices consists of a 4 step process to convert sunlight into electrical power as illustrated in Fig. 2.1. The process begins with photon absorption and the absorption efficiency (η_{abs}) of a device can be predicted from an

optical model as outlined in Sect. 2.2. Any absorbed photon generates an exciton that must diffuse to a heterojunction (HJ) as described in Sect. 2.3, and this is characterized by an exciton diffusion efficiency (η_{diff}). After excitons diffuse to the interface they must be separated into free carriers and this occurs with a carrier generation efficiency (η_{cg}) as discussed in Sect. 2.4. Finally, photogenerated carriers must transport through the device to be collected at the contacts, and the carrier collection efficiency (η_{cc}) is addressed in Sect. 2.5.

These four steps determine the photon to electron conversion efficiency defined as the *external quantum efficiency* (η_{EQE}) according to $\eta_{EQE}(\lambda, V) = \eta_{abs}(\lambda)\eta_{diff}\eta_{cg}(V)\eta_{cc}(V)$.[74] Here we have explicitly denoted the wavelength and voltage dependence of the various steps contributing to the η_{EQE}. The η_{PCE} is determined by the J-V which is related to the η_{EQE}. The total current is given by integrating over the spectrum of the incident light intensity as $J(V) = \int \eta_{EQE}(\lambda, V) I_o(\lambda)\, hc/\lambda\, d\lambda$, where h is Planck's constant and c is the speed of light. Given a

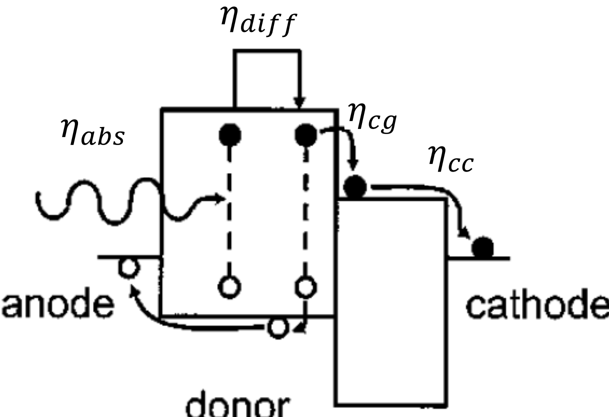

Figure 2.1 – Current Generation in an Organic Photovoltaic Device: A photon is absorbed with efficiency η_{abs}. The photoexcited exciton diffuses to the heterojunction with efficiency η_{diff}. The exciton generates free carriers with efficiency η_{cg}. Free carriers are extracted from the device with efficiency η_{cc}.

model for $\eta_{EQE}(\lambda, V)$, the η_{PCE} can be predicted and used to design optimized devices.

2.2. Absorption in thin film devices

Due to poor charge transport and limited exciton diffusion lengths, efficient organic devices are restricted to using ultra-thin layers – typically less than 100nm. Despite the strong optical absorption for organic materials, these layer thicknesses are shorter than the absorption length. For absorptive devices, incident light propagates through a multitude of layers, and light may be scattered at each of the interfaces between the layers. Consequently, the absorption profile through the device must be modified from the simple expression used for inorganic devices: $I(x) = I_0 \exp(-x/\alpha)$ shown in Fig. 2.2a, where $I(x)$ is the optical intensity at a depth x in the device, I_0 is the incident optical intensity and α is the absorption length.

To determine the optical electric field distribution in thin film devices, reflections from the ultra-thin layers must be treated as coherent reflections. This is compactly done using a transfer matrix formalism.[75,74] Figure 2.2b shows a typical multilayer structure of an organic device, along with a sample field intensity profile. As evident in the figure, the microcavity effects result in constructive and destructive interference effects that produce regions of high and low optical field. Consequently, microcavity effects play a very large role in the performance of optical devices,[75] for example if an OPV has destructive interference where the active materials absorb then very little light will be absorbed resulting in a low power conversion efficiency.

At each interface in the device, part of the optical field is reflected and the rest is transmitted as determined by the Fresnel coefficients according to $r_{jk} = (\overline{n_j} - \overline{n_k})/(\overline{n_j} + \overline{n_k})$ and $t_{jk} = 2\overline{n_j}/(\overline{n_j} + \overline{n_k})$. Here, $r_{jk}$and t_{jk} are the reflection and transmission coefficients of the

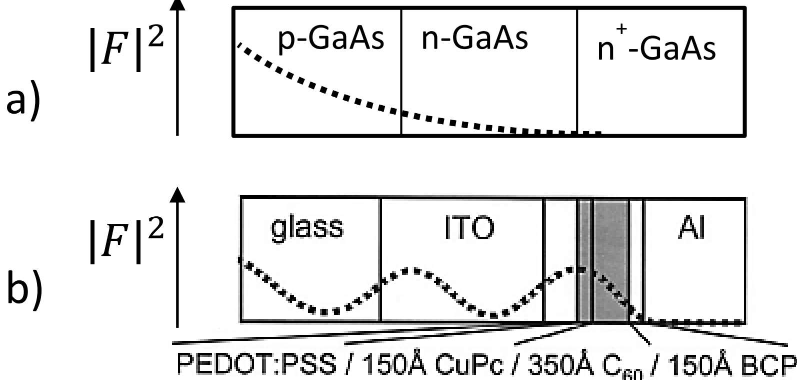

Figure 2.2 – Optical Field Profile in Organic and Inorganic Photovoltaics: (a) Optical electric field intensity (*F*) profile through a thick inorganic active layer. (b) *F* through an organic PV device with thin layers that result in microcavity effects.

optical field travelling from layer *j* to layer k. The $\overline{n_j}$ is the complex index of refraction and is given by $\overline{n_j} = n_j + ik_j$, where n_j is the real index of refraction of the layer, k_j is its absorption coefficient, and both are a function of the wavelength of the optical field λ. The forward (F_j^+) and backward (F_j^-) travelling waves across the (*j,k*) interface are related by the interface matrix I_{jk} given by,

$$\begin{bmatrix} F_j^+ \\ F_j^- \end{bmatrix} = I_{jk} \begin{bmatrix} F_k^+ \\ F_k^- \end{bmatrix} = \begin{bmatrix} 1/t_{jk} & r_{jk}/t_{jk} \\ r_{jk}/t_{jk} & 1/t_{jk} \end{bmatrix} \begin{bmatrix} F_k^+ \\ F_k^- \end{bmatrix}. \tag{2.1}$$

As the field propagates forward or backward through layer *j* with thickness d_j it accumulates a phase shift and absorption described by the matrix L_j,

$$L_j = \begin{bmatrix} e^{-\frac{i2\pi\overline{n_j}d_j}{\lambda}} & 0 \\ 0 & e^{+\frac{i2\pi\overline{n_j}d_j}{\lambda}} \end{bmatrix}. \tag{2.2}$$

Propagation of an incident field through the device with *m* layers can be described by the transfer matrix *S* given by the matrix product,

$$\begin{bmatrix} F_0^+ \\ F_0^- \end{bmatrix} = I_{01} L_1 I_{12} L_2 \dots L_m I_{m(m+1)} \begin{bmatrix} F_m^+ \\ F_m^- \end{bmatrix} = S \begin{bmatrix} F_m^+ \\ F_m^- \end{bmatrix}. \tag{2.3}$$

To simulate absorption inside the device, we must evaluate the field at a layer *j* inside the device. We begin by evaluating the transfer matrix to the left and right of L_j (the matrix corresponding to propagation through layer *j*) according to $S = S_j^- L_j S_j^+$. Then the electric field at any position inside layer *j* of the complete stack can be related to the incident optical field by,

$$F_j(x) = F_j^+(x) + F_j^-(x) = \left(t_j^+ e^{+\frac{i2\pi \overline{n_j} d_j}{\lambda}} + t_j^- e^{-\frac{i2\pi \overline{n_j} d_j}{\lambda}} \right) F_0^+. \tag{2.4}$$

Here t_j^+ corresponds to the net transmission coefficient into layer *j* from layer *j-1* and t_j^- is the transmission of the reverse travelling wave into layer *j* from layer *j+1*. These are given by,

$$t_j^+ = \frac{F_j^+}{F_0^+} = \frac{\frac{1}{S_{j,11}^-}}{1 + \frac{S_{j,12}^- S_{j,21}^+}{S_{j,11}^- S_{j,11}^+} e^{\frac{i4\pi \overline{n_j} d_j}{\lambda}}}, t_j^- = \frac{F_j^-}{F_0^+} = t_j^+ \frac{S_{j,21}^+}{S_{j,11}^+} e^{\frac{i4\pi \overline{n_j} d_j}{\lambda}}. \tag{2.5}$$

The time averaged photon absorption rate is then given by,

$$G_j(x) = \frac{4\varepsilon_0 n_j k_j}{\hbar} \left| F_j(x) \right|^2, \tag{2.6}$$

and the absorbed power is scaled by the photon energy $P_j(x) = (2\pi\hbar c/\lambda) G_j(x)$. The incident field intensity F_0^+ can be related to the incident photon flux by $\phi = c\varepsilon_0 |F_0^+|^2/2$, where ϕ is the number of photons incident on the device per second. Then the absorption efficiency can be calculated by integrating *G* through the device and normalizing by photon flux as,

$$\eta_{abs} = \frac{\int G(x)dx}{\phi}. \tag{2.7}$$

Note that G and ϕ are proportional to $|F_0^+|^2$, so that the absorption efficiency is simply a device property that depends on the optical constants and thicknesses of the layers in the device.

2.3. Exciton diffusion

Light absorption in inorganics directly results in free carriers because the Coulomb attraction is small between the photogenerated electron and hole. This interaction energy is on the order of $E_B \approx 5\ meV$,[24,76] which is less than ambient thermal energy of $E_{th} = k_B T = 26\ meV$, so that the electron and hole easily separate from each other. The energy is small because the electron and hole are delocalized states and the dielectric constant of the material is high $\varepsilon \approx 10\varepsilon_0$, hence the field between the electron and hole are effectively screened. In an organic film, photon absorption results in an electron and hole (more precisely a positive or negative polaron, cf. Sect. 1.2.2) localized on a single molecule or adjacent molecules. Because organics have low dielectric constants, $\varepsilon \approx 3\varepsilon_0$, the Coulomb interaction of an electron and hole is large and can be estimated by a simple point charge approximation,

$$E_B = \frac{q^2}{4\pi\varepsilon a} \sim 0.2 \text{ to } 0.8\ eV, \tag{2.8}$$

where a is on the order of molecular size (5-15 Å). This binding energy is larger than E_{th} so the photoexcited electron and hole are tightly bound; this bound state is treated as a quasi-particle called an *exciton*.

To generate photocurrent after light absorption, the resulting exciton that is generated must be split into free carriers. Excitons can be efficiently dissociated at a heterojunction (HJ) between two different organic materials if they have the appropriate energy levels of a type-II HJ[24] as shown in Fig. 2.3. The energy level requirement is that a *donor* material has a shallow HOMO level corresponding to a low energy state for holes, and an *acceptor* material have a deep LUMO level corresponding to a low energy state for electrons. With this configuration, if an exciton in either material reaches the donor/acceptor (D/A) HJ it will be dissociated by charge transfer of one carrier into the lower energy state of the other material. This is where terminology

Figure 2.3 – Energy Level Diagram of an Organic Photovoltaic Device: Semiconductor bandgaps are indicated by the empty boxes. Shaded region indicates the valence bands that are filled with electrons. Light is absorbed in the active layers, the donor and acceptor. Excitons dissociate at the heterojunction between the donor and acceptor. Blocking layers are sometimes used to maximize exciton collection. A sample exciton density (X) profile is shown in the lower graph.

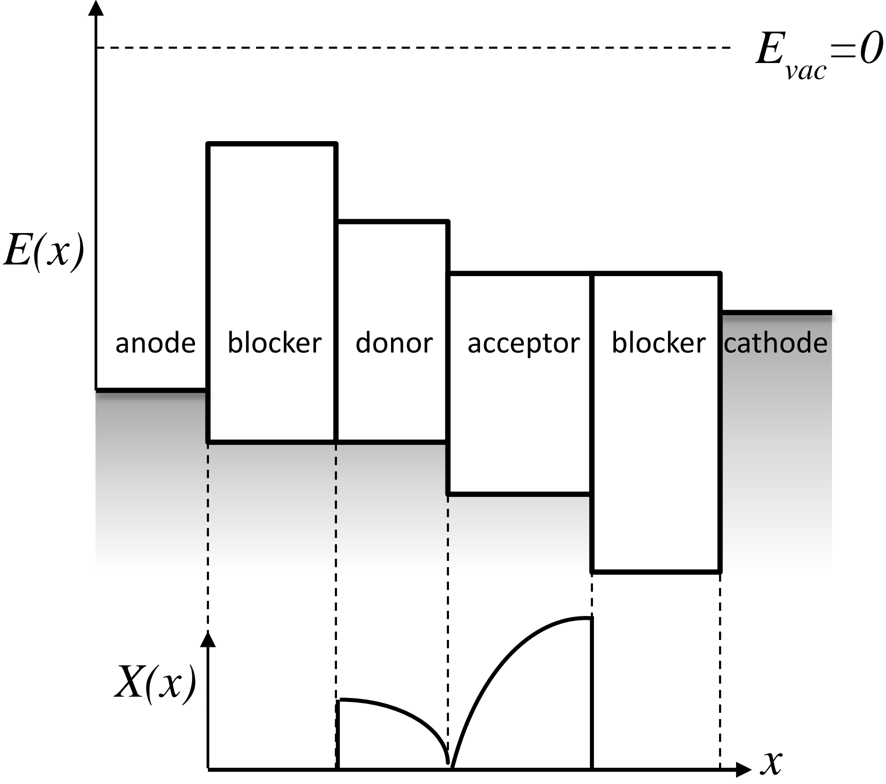

originates, an exciton in the donor dissociates by "donating" an electron to the acceptor which has a lower LUMO energy. Conversely, an exciton in the acceptor dissociates by transferring a hole into the HOMO of the donor – recall that a hole is a quasi-particle representing a missing electron. An electron is transferred from the donor HOMO and is "accepted" by the empty state in the acceptor HOMO.

When the OPV is illuminated, excitons are generated throughout the donor and acceptor layers according to the optical field distribution and the materials absorption coefficients as discussed in the previous section. To dissociate at the D/A HJ, an exciton must first encounter the HJ. Because excitons are a neutral species, they are not affected by a static external field like free carriers – *i.e.* there is no drift component in exciton motion. Instead exciton motion occurs entirely by diffusion. As a result, exciton flow or an exciton current $J_X(x)$ is driven by a gradient in the exciton density as $J_X(x) = -D\nabla X(x)$, where D is the exciton diffusion coefficient and $X(x)$ is the local exciton density. The 1-dimensional rate equation for exciton density is,[74]

$$\frac{d}{dt}X(x) = G(x) - \frac{X(x)}{\tau} + D\frac{d^2}{dx^2}X(x) = 0, \tag{2.9}$$

where τ is the exciton lifetime and $G(x)$ is determined by the optical model. The steady-state exciton profile can be calculated for a device by solving this equation in each layer of the device subject to appropriate boundary conditions. The boundary conditions are either: 1) an exciton at the boundary is quenched resulting in zero exciton population at the boundary (as in the case of a D/A HJ), 2) the exciton is perfectly blocked resulting in a zero change in exciton density at this boundary (for example if the boundary is with a wide bandgap material that the exciton cannot transfer to), or 3) the interface is only partially quenching. The exciton profile of an ideal device

is shown in Fig. 2.3 where the D/A junction is perfectly quenching and transparent, perfectly blocking layers surround the active layers.

Once the boundary conditions and the exciton profile are determined, the exciton flux to the D/A interface ($J_{X,I}$) from each layer can be calculated as,

$$J_{X,I} = \frac{L_D^2}{\tau} \left| \frac{dX}{dx} \right|_{x=x_I} \tag{2.10}$$

where x_I is the position of the interface, and L_D is the exciton diffusion length defined as $L_D = \sqrt{D\tau}$. This flux represents the upper limit to the photocurrent generated by each layer and is equal to the photocurrent from the layer if we have perfect charge collection (*i.e.* no additional losses in the device, such losses are discussed in the following sections). It can be related to the exciton diffusion efficiency as $\eta_{diff} = J_{X,I}/G_T$, where G_T is the total (i.e. integrated over through the layer) exciton generation rate of the layer. Of course, the exciton generation and diffusion equations must be treated for each absorbing layer in a device, and their contributions can be summed to determine the total η_{diff} for the device. In combination with the optical model of Sect. 2.2, the diffusive flux is a useful metric for the design of OPVs.

2.4. Exciton dissociation at a heterojunction

The energy level alignment at a D/A HJ drives the dissociation of excitons that reach the interface. But what happens to the charge immediately after dissociation is still under contention. The two models under debate in the field are: 1) exciton dissociation results in a bound state, called a *polaron pair* (PP) or a *charge transfer* (CT) state, where the electron and hole (though residing in different materials on opposite sides of the interface) are Coulombically

attracted,[77,78,79,80,81,82,83,84,85], or 2) many of the excitons dissociate directly into free carriers while the remainder are lost to geminate recombination.[86,87,88,89,90,91]

2.4.1. PP formation and the Giebink model

The first model for photocurrent generation is based on excitons that dissociate into a bound *polaron pair* (PP) state. This state consists of a hole in the donor (really a positive polaron) that is Coulombically bound to an electron in the acceptor (*i.e.* a negative polaron). The binding energy of this interaction can also be estimated using Eq. 2.7 with an expected size on the order of 5-20 Å. This results in a large binding energy that must be overcome by thermal processes, but also can be aided by a static electric field. In 2010 this model was built into a framework by N. C. Giebink, et al.,[78] and is used to describe the complete current density verse voltage (*J*-*V*) behavior that is characteristic of planar, bilayer OPVs.

The Giebink model is based on an interface state diagram as shown in Fig. 2.4a. As discussed above, photons absorbed in the device generate excitons which reach the interface with a flux of J_X and are dissociated – but they form PPs (with a density labeled as ζ) that are bound at the interface. The PPs are dissociated at a rate k_{PPd} (which depends on temperature and electric field) to form free electrons and holes near the interface in their respective layers. The density of free electrons and holes at the interface are labeled as n_I and p_I. If free electrons and holes encounter each other at the interface, they can relax into the lower energy PP state. This is a bimolecular recombination process and occurs at a rate of $k_{rec}n_Ip_I$. PPs can also recombine to the ground state at a rate k_{PPr} and in this case the energy from the absorbed photon is lost. There is also a thermal generation rate that results in an equilibrium density of PPs, and this rate is

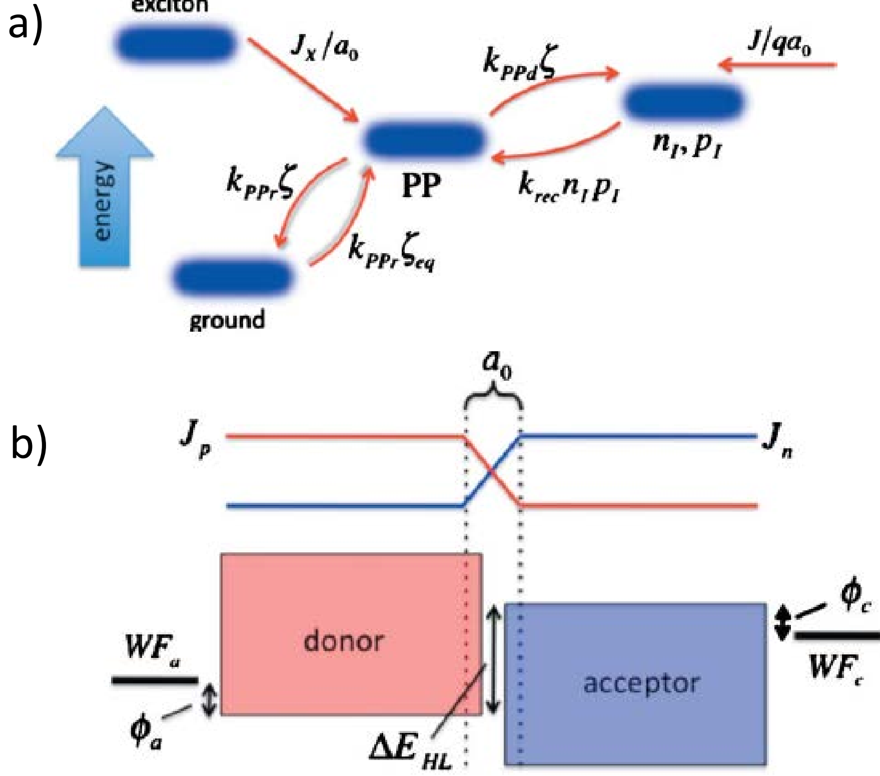

Figure 2.4 – Giebink Model: (a) Interface state diagram and the transitions coupling each state according to the Giebink model. (b) Energy diagram for a simple bilayer organic PV structure. (From Ref. 9)

$k_{PPr}\zeta_{eq}$ as required for detailed balance.[92] Lastly, current flow away from (or toward) the interface will reduce (or increase) the free carrier density.

This state diagram results in the coupled rate equations,

$$\frac{d}{dt}n_I = \frac{d}{dt}p_I = k_{PPd}\zeta - k_{rec}n_Ip_I + \frac{J}{qa_0} = 0, \tag{2.11}$$

and

$$\frac{d}{dt}\zeta = \frac{J_X}{a_0} - k_{PPd}\zeta - k_{PPr}(\zeta - \zeta_{eq}) + k_{rec}n_Ip_I = 0. \tag{2.12}$$

Here, a_0 represents the interface volume, *i.e.* the distance over which PPs are distributed about the interface, and is expected to be roughly 5-20 Å. From the first rate equation, we identify that at equilibrium $J = 0$ and thus $\zeta_{eq} = k_{rec} n_{I,eq} p_{I,eq} / k_{PPd,eq}$, where the subscript eq refers to the equilibrium value of the parameter. Then we can solve the coupled equations to eliminate the PP density and arrive at an expression for current in terms of n_I and p_I as,

$$J = q a_0 k_{rec} \left(\frac{k_{PPr}}{k_{PPd} + k_{PPr}} \right) \left(n_I p_I - \frac{k_{PPd}}{k_{PPd,eq}} n_{I,eq} p_{I,eq} \right) - q J_X \left(\frac{k_{PPd}}{k_{PPd} + k_{PPr}} \right). \quad (2.13)$$

This expression is generally valid as long as the Giebink model expresses all of the physical processes that occur in the device. It could be applied equally well to the case of a bulk heterojunction with nanocrystalline donor and acceptor domains distributed throughought the device volume as to the case of a simple planar HJ. However, for the case of planar DA HJ, it is much easier to analytically solve or numerically simulate the required carrier densities and electric fields (to evaluate k_{PPd}) in the device. Consequently, we consider the case of planar OPVs as shown schematically in Fig. 2.4b.

In a planar device with small currents, the carrier density across each layer can be related to the voltage across the layer by,

$$n_I = n_c \exp\left(\frac{q V_A}{k_B T} \right) = n_C \exp\left(\frac{q \delta_A (V_a - V_{bi})}{k_B T} \right), \quad (2.14)$$

and

$$p_I = p_c \exp\left(\frac{q V_D}{k_B T} \right) = p_c \exp\left(\frac{q \delta_D (V_a - V_{bi})}{k_B T} \right). \quad (2.15)$$

As before, n_I (p_I) is the carrier density at the D/A HJ in the acceptor (donor) layer, n_c (p_c) is the carrier density at the contact in the acceptor (donor) layer, V_A (V_D) is the voltage drop across the acceptor (donor) layer, and δ_A (δ_D) is the fraction of the voltage dropped across the acceptor (donor) layer. These voltages are related to the total voltage dropped across the device by $V_a - V_{bi} = V_A + V_D = (\delta_A + \delta_D)(V_a - V_{bi})$, where it is evident that $\delta_A + \delta_D = 1$. The contact carrier density is given by $n_c = N_{LUMO}\exp(-\phi_c/k_BT)$, with a similar expression for holes.

Substituting Eq. 2.13 and 2.14 into2.12 we arrive at the ideal diode equation for trap-free organics,

$$J = qa_0k_{rec}N_{HOMO}N_{LUMO}(1-\eta_{PPd})\exp\left(-\frac{\Delta E_{HL}}{k_BT}\right)$$

$$\times\left\{\exp\left(\frac{qV_a}{k_BT}\right) - \frac{k_{PPd}}{k_{PPd,eq}}\right\} - qJ_X\eta_{PPd} \tag{2.16}$$

$$= J_{s0}\left\{\exp\left(\frac{qV_a}{k_BT}\right) - \frac{k_{PPd}}{k_{PPd,eq}}\right\} - qJ_X\eta_{PPd},$$

where $\eta_{PPd} \equiv k_{PPd}/(k_{PPd} + k_{PPr})$, and $\Delta E_{HL} \equiv \phi_c + \phi_a + qV_{bi}$ as shown in Fig. 2.4b.

If there is an appreciable density of sub-bandgap traps in either layer of the device, recombination may be mediated by these low-lying states. This is especially relevant for disordered semiconductors which are often characterized by an exponential density of states about the designated HOMO or LUMO level. The Giebink model treats this analytically for the case of an exponential distribution of trap states given by,

$$n_t = H_A\exp\left(\frac{E_{F,n} - E_{LUMO}}{k_BT_{t,A}}\right) \equiv H_A\left(\frac{n}{N_{LUMO}}\right)^{1/l_A}, \tag{2.17}$$

where $l_A = T_{t,A}/T$, and $T_{t,A}$ is the characteristic trap temperature. The second equality is an identity that results from the definition of the quasi-Fermi level (c.f. Sect. 1.2.2.2.2). Considering the recombination of trapped charge in the acceptor with free carriers in the donor (and vice-versa) the ideal diode equation for organics with traps becomes,

$$
\begin{aligned}
J = qa_0(1-\eta_{PPd})\Big\{&k_{rec,n}N_{LUMO}H_D \exp\left(-\frac{\alpha_D}{k_BT}\right)\left[\exp\left(\frac{qV_a}{n_Dk_BT}\right)-\frac{k_{PPd}}{k_{PPd,eq}}\right] \\
&+ k_{rec,p}N_{HOMO}H_A \exp\left(-\frac{\alpha_A}{k_BT}\right)\left[\exp\left(\frac{qV_a}{n_Ak_BT}\right)-\frac{k_{PPd}}{k_{PPd,eq}}\right]\Big\} \\
&- qJ_X\eta_{PPd}
\end{aligned}
\tag{2.18}
$$

$$
= J_{sD}\left\{\exp\left(\frac{qV_a}{n_Dk_BT}\right)-\frac{k_{PPd}}{k_{PPd,eq}}\right\} + J_{sA}\left\{\exp\left(\frac{qV_a}{n_Ak_BT}\right)-\frac{k_{PPd}}{k_{PPd,eq}}\right\} - qJ_X\eta_{PPd}.
$$

where

$$
\alpha_D = \frac{\Delta E_{HL}}{n_D} + \frac{l_D-1}{l_D}(\delta_D\phi_c - \delta_A\phi_a), \qquad \alpha_A = \frac{\Delta E_{HL}}{n_A} + \frac{l_A-1}{l_A}(\delta_A\phi_a - \delta_D\phi_c), \tag{2.19}
$$

and

$$
n_D = \frac{l_D}{\delta_A(l_D-1)+1}, \qquad n_A = \frac{l_A}{\delta_D(l_A-1)+1}. \tag{2.20}
$$

This results in the double exponential behavior often observed in the dark currents of OPVs and provides an explanation as to why the ideality factor in organic devices can be >2 (the upper limit for inorganic diodes based on SRH recombination).

To complete the model, Giebink notes that the PP dissociation rate carries an implicit dependence on temperature and the electric field at the interface so that $k_{PPd} = k_{PPd}(F_I, T)$. This

field and temperature dependence can have a significant effect on the shape of the *J-V* curve, predominantly in the reverse-bias dark current (via $k_{PPd}/k_{PPd,eq}$) and in the photocurrent (via η_{PPd}). The physical behavior of k_{PPd} must be appropriately accounted for in order to calculate accurate *J-V* behavior. As commonly done in the field,[84,85] Giebink suggests modeling k_{PPd} using the Onsager-Braun model for ion dissociation in an electrolyte. While the Onsager formalism[93,94] was rooted in the separation of charge in a liquid electrolyte, the 1984 extension by Braun[95] to solid phase semiconductor systems is widely used.[80,81] It includes the basic physical processes expected to arise in the dissociation of bound charge including 1) field assisted thermal dissociation, 2) screening effects of dielectric medium, and 3) geometrical averaging over the half space of dissociation routes made accessible by the orientation of the electric field. This model predicts k_{PPd} to follow,[95]

$$k_{PPd} = \frac{3}{4\pi a_0^3} k_{rec} \exp\left(-\frac{E_B}{k_B T}\right) \frac{J_1\left[2\sqrt{-2b}\right]}{\sqrt{-2b}}, \tag{2.21}$$

where E_B is the PP binding energy as derived from Eq. 2.7, J_1 is the first order Bessel function, and $b = q^3 F_I/(8\pi k_B^2 T^2)$. If we assume that all the exciton flux (found in Sect. 2.3) dissociates and populates PP states, then the only loss mechanism is PP recombination. Consequently, the carrier generation efficiency is given by k_{PPd} as $\eta_{cg} = \eta_{PPd} = k_{PPd}/(k_{PPd} + k_{PPr})$.

2.4.2. Hot charge transfer states

To describe the second model of charge generation, I use the terminology of charge transfer (CT) state to refer to the bound charge pair at the interface (*i.e.* equivalent to a PP in the Giebink model). Keeping this distinction will be helpful when the two models are compared. This second model for charge generation states that when an exciton dissociates at the interface,

it may transfer to a high-energy (*i.e.* hot) CT state as shown in Fig. 2.5.[86,87] This hot CT state has a reduced binding energy and therefore is easier to thermally dissociate into free carriers. However, if this hot CT thermalizes and relaxes into the ground CT state, it will never be dissociated from this tightly bound state and will ultimately be lost to recombination.

The differences between this model and the Giebink model are subtle and, ultimately, are a matter of semantics. Because it considers a continuum of CT energy states, one can argue that the hot CT model adds more detail to the physical picture of how free charge is generated from a HJ. However, in the Giebink model, the energy of a PP state is simply characterized by an average separation a_0 of the bound charge, and Giebink addresses that one should average over an appropriate distribution of a_0 in order to account for a distribution of PP energy states. In the event that none of the lowest energy CT states are able to generate free carriers (a postulate of the hot CT model), the rate of population of these lowest CT states is simply the k_{PPr} of the Giebink model (i.e. the rate of the loss that reduces the density of CT states that are able to dissociate). In this case, the PP density of the Giebink model corresponds to the density of hot CT states, and any distribution of PP states should reflect the distribution of CT states that are able to be dissociated – ever.

There is only one distinction of importance between the two models, i.e. where these two models represent physically distinct processes. This is in the limit that some excitons populate very high-energy CT states that are automatically dissociated into free carriers. This would require an extra process in the Giebink model of Fig. 2.4a that represents transfer of excitons directly to free carriers. If this is the only way that free carriers are generated (i.e. no PPs ever lead to free carriers), the PP state of the Giebink model is not relevant as it is dynamically identical to the ground state.

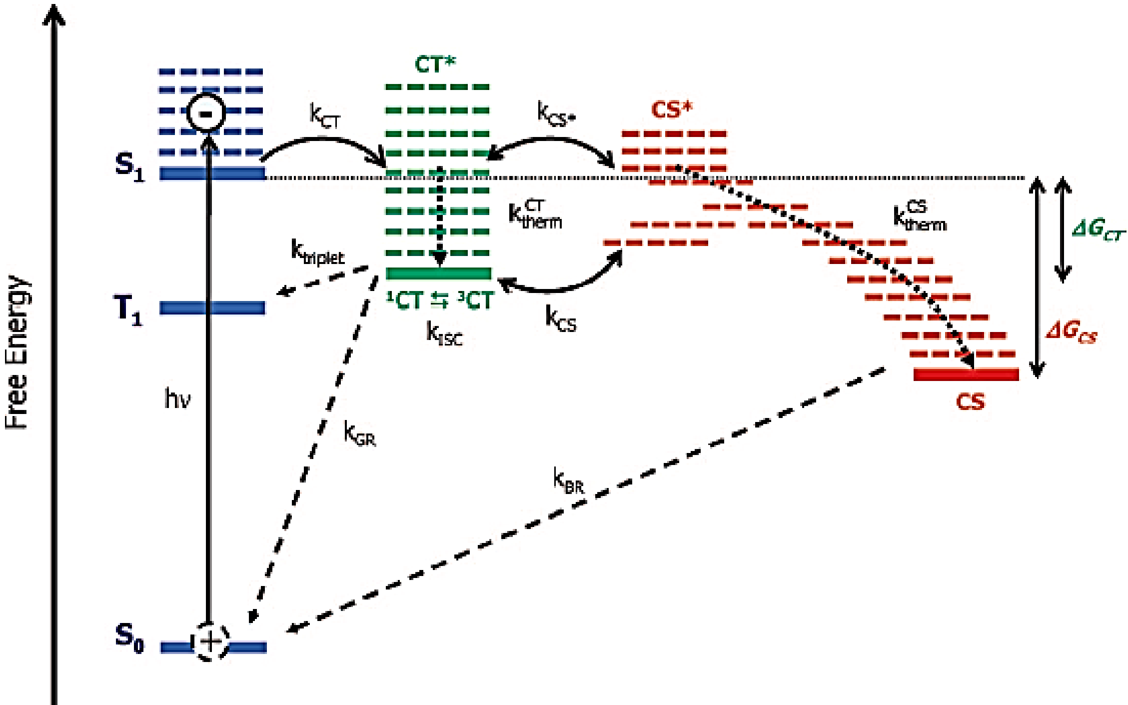

Figure 2.5 – Hot Charge Transfer Exciton Dissociation: Interface state diagram for hot charge transfer. The CT state is equivalent to the PP state of the Giebink model and the CS state is a free carrier state. Figure is reproduced from Ref. 87.

Ultimately, it does not make sense to neglect the possibility of dissociating low energy PPs. Although the binding energy is substantial, the low energy PP state is a stable state that can accumulate a large population density in steady state. A small dissociation probability times a large density can result in a large amount of charge surmounting this barrier – similar to the case of charge emission over a Schottky barrier. Also, while the probability of a single dissociation step succeeding is small due to the large barrier, if a PP dissociation attempt fails it lives to try again. The net dissociation rate is given by,

$$k_{PPd} = N_d e^{-\frac{E_B}{k_B T}} = \frac{1}{k_{PPr} \nu} e^{-\frac{E_B}{k_B T}} \tag{2.22}$$

where ν is the frequency of attempting a single dissociation event and determines the number of attempts N_d that occur before the PP decays. We expect ν to be on the order of phonon

frequencies corresponding to time scales of ~1ps or less. Ultimately, the dissociation efficiency not only depends on the binding energy but also critically depends on the lifetime of the PP state.

On the other hand, charge generated from hot CTs must separate on a very short time scale, because dissociation must occur before the hot CT thermalizes to a stable low energy CT. Because thermalization and dissociation are thermally driven processes, we expect that a single thermalization or dissociation attempt occur on the same time scale, ν. So if we consider a single step process, the hot state has one chance to completely dissociate otherwise it will relax, and then the dissociation probability (i.e. the carrier generation efficiency) is simply,

$$\eta_{cg} = \frac{e^{-\frac{E_B}{k_B T}}}{1 + e^{-\frac{E_B}{k_B T}}} \sim 13\%, \tag{2.23}$$

where we use $E_B = 0.05\ eV$ for the hot CT state and an effective $E_B = 0$ for the energetically driven thermalization probability. A more complete model would consider that there may be many small steps to complete thermalization or complete dissociation; then perform a statistical analysis to calculate the dissociation efficiency when there are many small steps whose probabilities are given by $P^+ = e^{-\Delta E / k_B T}$ or $P^- = 1$ for the upward and downward steps, respectively. I expect the conclusion to be the same, that there is a small likelihood of the hot CT to dissociate rather than thermalize. In contrast, the internal quantum efficiency (neglecting imperfect light absorption) of OPVs can easily be $> 80\%$. Consequently, we will adopt the Giebink model for the following analysis.

2.5. Charge extraction

To arrive at an analytical *J-V* equation, the Giebink model makes two assumptions in regards to charge collection. The first assumption is that the donor and acceptor are *isotype* layers, that is layers that have only one carrier type. – *i.e.* holes in the donor and electrons in the acceptor. The second assumption is that *J* is small so that Eq. 2.13 and 2.14 are valid. These two assumptions have significant implications on the treatment of charge extraction, and I discuss these implications below.

2.5.1. Isotype layers

Although subtle, the assumption of isotype layers is one of the biggest assumption made by Giebink, *et al.*, and it has two physical manifestations in the device model. The first manifestation is that all current injected into the device is completed by recombination (of PPs) *across* the interface. This is in contrast to the inorganic device model where charge is injected by diffusion or thermionic emission over a barrier in the same band (*i.e.* electrons are injected from the conduction band of the n-type material to the conduction band of the p-type material). While bold, this assumption is justified by the introduction of the two ideality factors (via trap states in each the donor and acceptor) commonly observed in OPVs.

A secondary effect of this assumption is that there is zero recombination of charge in the bulk of the organic films. This is forced, because no charge is injected past the interface (i.e. no electrons from the acceptor LUMO are injected into the donor LUMO) and recombination cannot occur without the presence of both charge carriers. Then the only loss mechanism for free carriers is to recombine to form PPs at the interface. Consequently, $\nabla \cdot J = 0$ everywhere in the bulk of the film and the charge collection efficiency is equal to the PP dissociation efficiency,

$\eta_{cc} = \eta_{PPd}$. This is true even given a trap density near the transport levels which simply results in carrier capture and release, corresponding to a mobility reduction but not a loss of charge. In order to evaluate η_{PPd} we need to determine the electric field at the interface, and this is dependent on how charge is extracted through each layer in the device.

2.5.2. Drift-diffusion equation: *J = 0*

The second assumption of the Giebink model is that *J = 0* so that the quasi-Fermi level is flat through each layer. Under this assumption the carrier density at the interface can be directly related to the carrier density at the contact by the voltage across the layer as Eq. 2.13 and 2.14. This analytical relationship enables expressing the *J-V* relation according to Eq. 2.15 or Eq. 2.17 in the case of trap mediated recombination. This is an extremely useful equation because it relates the lump parameters (n, α, J_s) to real physical (*i.e.* knowable) quantities. However, in the case of trap mediated current, evaluation of Eq. 2.17 requires knowledge of the voltage distribution across the device.

The voltage distribution, carrier density, and field distribution in an isothermal device can be related by the homogeneous drift-diffusion (D-D) equation,

$$J = q\mu pF - qD\nabla p = 0. \tag{2.24}$$

Here μ is the hole mobility and D is the hole diffusivity. Generally, $\mu = \mu(F, T)$ may be a function of field and temperature and the diffusivity can be related to μ by the Einstein-Smoluchowski relation as $D = \mu k_B T/q$.[96,97] The first term in Eq. 2.22 accounts for current due to carrier drift, while the second term accounts for diffusion of carriers according to Brownian

motion. At $J = 0$, the drift and diffusion components are equal and the homogeneous D-D equation can be solved analytically.

To solve the homogeneous D-D equation, we also utilize the Poisson equation to describe the relationship between charge and electric field as,

$$\nabla \cdot F = \frac{q(p - p_0)}{\varepsilon}, \tag{2.25}$$

so that charge behaves as an electric field source. Note that the background charge density, p_0 (such as created by doping) does not affect the field because there is a fixed counter charge of the ionized dopant. Here I consider films that are not intentionally doped and expect any unintentional doping to be negligibily small compared to the electrically injected carrier density. Coupling the Poisson equation with the D-D equation results in a second-order non-linear differential equation for F as,

$$F'' = \frac{\mu}{D} F F'. \tag{2.26}$$

Assuming the Einstein-Smoluchowski relation so that $\mu/D = q/k_B T \equiv \beta$, the general solution to this can be evaluated analytically[78,98] and is given by,

$$F(x) = C\left[1 + \frac{2(F_I - C)}{(F_I + C)\exp(-C\beta x) - (F_I - C)}\right], \tag{2.27}$$

$$p(x) = \frac{2\beta\varepsilon}{q} C^2 \exp(C\beta x) \frac{(F_I - C)(F_I + C)}{[(F_I + C) - (F_I - C)\exp(C\beta x)]^2}, \tag{2.28}$$

where C is defined as $C = \sqrt{F_I^2 - 2qp_I/\beta\varepsilon}$. In the special case where $C = 0$, the solution is given by Eq. 2.25 and 2.26 in the limit that $C \to 0$ as,

$$F(x) = \left[\frac{1}{F_I} - \frac{\beta x}{2}\right]^{-1}, \quad (2.29)$$

$$p(x) = \frac{\beta\varepsilon}{2q}\left[\frac{1}{F_I} - \frac{\beta x}{2}\right]^{-2}. \quad (2.30)$$

The constants F_I and C can be determined by imposing appropriate boundary conditions. In the donor for example, at the contact ($x = x_D$, where x_D is the thickness of the donor layer) the charge density p_c is given by $p_c = N_{HOMO}\exp(-\phi_a/k_BT)$, and at the interface (*x=0*) the charge density p_I is given by Eq. 2.14. These equations can be used identically for electrons in the acceptor; then the field and carrier distribution are known everywhere through the device.

2.5.3. Drift-diffusion equation: $J \neq 0$

The previous low current approximation breaks down when the device is under high forward bias or high illumination intensity. In this case a more rigorous device model is required to determine the carrier density and electric field inputs to the Giebink model. The current, carrier density, and field distribution are related by the non-homogeneous D-D equation,

$$J = q\mu pF - qD\nabla p \equiv \mu p\nabla E_{F,p}, \quad (2.31)$$

where $E_{F,p}$ is the hole quasi-fermi level. The second equality is an identity based on the definition of the quasi-Fermi level. This equality indicates that the gradient in $E_{F,p}$ cannot be neglected when large currents flow in a device with low carrier density. In this case, the relation between charge density and voltage given in Eq. 2.14 is not valid, and $p_I(V_D)$ must be determined by coupled solutions to Eq. 2.30 and the Poisson equation. The coupled equations are described by,

$$F'' = \frac{\mu}{D} F F' - \frac{J}{\varepsilon D}. \tag{2.32}$$

As before, this can be uniquely solved by imposing appropriate boundary conditions.

Analytic solutions to Eq. 2.33 are not readily available. It can be reduced to a first order equation ODE by integrating once,

$$F' = \frac{\mu}{2D} F^2 + \frac{J_{ph}}{\varepsilon D} x - C^2, \tag{2.33}$$

as before $C = \sqrt{F_I^2 - 2qp_I/\beta\varepsilon}$. Analytic solutions to this are given in complex Airy functions, and evaluating them with appropriate boundary conditions is very challenging. Alternatively, we can solve this as a power series where $F = \sum_0^\infty a_n x^n$, and if we take $x = 0$ at the interface, this results in,

$$F(x) = F_I + \frac{ep_I}{\varepsilon} x + \left(\frac{J_{ph}}{2\varepsilon D} + \frac{\mu}{2D} F_I \frac{ep_I}{\varepsilon} \right) x^2 + \sum_{n=3}^{\infty} a_n x^n \tag{2.34}$$

where

$$a_n = \frac{\mu}{2Dn} \sum_{m=0}^{n-1} a_{n-1-m} a_m. \tag{2.35}$$

To complete the solution, the charge density can be found by differentiating F as $p(x) = \varepsilon F'/q$. This sum is convergent for sufficiently small F_I, p_I and J_{ph}/D. Outside of this range, there is no solution by the power series method and further solutions can be found by numerically evaluating Eq. 2.33.

2.5.4. Uniform field approximation

It is useful to discuss a further approximation that can be made about the device. If the carrier density through a layer is sufficiently small, then the electric field from the carriers inside the device can be neglected. That is, the effects of the space-charge distributed through the device can be neglected. That is, $\nabla \cdot F$ determined by Eq. 2.25 is small, so that any external field applied across the device is not significantly affected by the carriers inside the device. This is the uniform field approximation (UFA) and results in a simple relationship between voltage and field as,

$$F(x) = F_I = -\frac{V_D}{x_D}, \tag{2.36}$$

where, as before, V_D is the voltage drop across the donor and x_D is the thickness of the donor layer. This approximation is nominally valid for low currents such as low light illumination and when the applied voltage (V_a) is below the built in voltage V_{bi} – i.e. reverse-bias conditions. In this case $V(x) = V_D x / x_D$, so that the energy bands have a constant slope and the charge density exponentially decreases towards the interface as shown in Fig. 2.6.

2.5.5. Ohmic and space charge limited current

The differential equation Eq. 2.31 is greatly simplified if the current in a layer is dominated by drift so that we can neglect the contribution from diffusion. This is generally the case when driving current through a single layer, but is not necessarily true in the case of a heterojunction where there is a barrier for charge that can result in a significant accumulation of carriers at the HJ. Nonetheless, here we consider this useful situation where current is dominated by carrier drift.

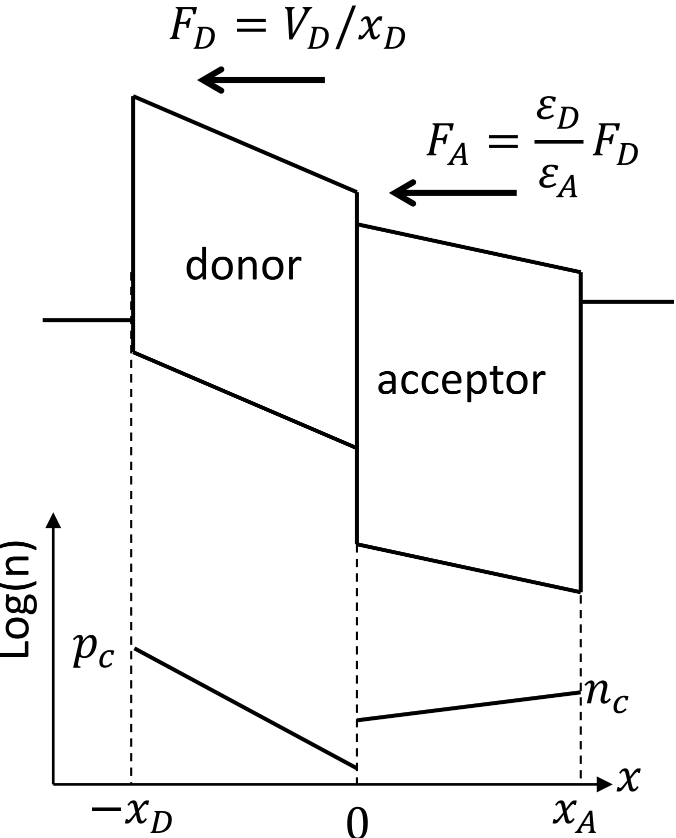

Figure 2.6 – Uniform Field Approximation: Energy band and carrier density diagram in the uniform field approximation. The applied voltage is less than the built-in voltage so that the fields sweep carriers out of the device. The charge density at each contact is determined by an injection barrier.

If there are background carriers in the layer with density p_0 (for example caused by doping or defects), these carriers can conduct a current according to Eq. 2.31 as,

$$J = q\mu p_0 F. \tag{2.37}$$

Note from Eq. 2.25, the background carrier density does not affect the field so that the UFA approximation is rigorously valid and $J = q\mu p_0 V/L$, where L is the layer thickness. This is simple Ohmic conduction and is observed in the low current regime where current is transported by the background carriers.

If a large bias is applied across the layer, carriers are injected into the film from the contact in order to transport the additional current. This results in charging the film, and if there is a large density of these electrically injected carriers they can affect the electric field through the layer. Considering this injected charge, Eq. 2.37 becomes

$$J = q\mu p F = \varepsilon\mu F F', \tag{2.38}$$

where we have used Eq. 2.25 to relate charge density to electric field and assumed p_0 is negligible. This first order non-linear differential equation is separable and is easily solved for *F* as,

$$F = \sqrt{\frac{2Jx}{\varepsilon\mu} - F_0^2}, \tag{2.39}$$

where F_0 is the electric field at the injecting contact. This can be integrated again to find the voltage through the layer,

$$V = \int_0^x F(x')dx' = \frac{\varepsilon\mu}{3J}\left[\left(\frac{2Jx}{\varepsilon\mu} + F_0^2\right)^{3/2} - F_0^3\right] \tag{2.40}$$

And the carrier density is found by differentiating *F* as,

$$p = \frac{\varepsilon\nabla \cdot F}{q} = \frac{J}{q\mu\sqrt{\frac{2Jx}{\varepsilon\mu} + F_0^2}}. \tag{2.41}$$

If we impose a zero electric field at the injecting contact ($F_0 = 0$), then this reduces to the well known Mott-Gurney law for space charge limited current,

$$J = \frac{9\varepsilon\mu V_D^2}{8L^3}. \tag{2.42}$$

The electric field and carrier density are also simplified under this assumption, however, we note that this boundary condition is a mathematical convenience and is not a physical requirement. This condition is violated if there exists a non-zero sheet charge in the contact at the metal organic interface (a condition discussed in Sect. 5.2).

2.6. Current-Voltage Characteristics

The current density versus voltage (*J*-*V*) behavior is the most fundamental characteristic of a device. It indicates how the PV device will perform in the real world. Here I discuss the basic features of and terminology used to describe the *J*-*V* characteristics. Figure 2.7 shows sample *J*-*V* curves for a high and low efficiency OPV. The dark current is the electrical-only behavior of a device (behavior without light) and is a manifestation of the first term in Eq. 2.16 or the first two terms in Eq. 2.18. This is the diode behavior. A high efficiency device will have a sharp diode turn-on that occurs at a high voltage. In forward bias, the electric field is oriented to inject charges which then recombine as described in Sect. 2.4.1. In reverse bias, the field is oriented to extract charge, and the current is low because the charge density and generation rate are small. Little current is injected in reverse bias because the barriers are high (to generate a drift current the anode must inject into the LUMO and the cathode must inject into the HOMO).

When the OPV is illuminated, there is a current source at the D/A HJ. In high reverse bias, the current is efficiently extracted from the device resulting in a saturated photocurrent. In a low resistance device, the photocurrent is efficiently extracted even at $V_a = 0$ (the short-circuit condition) due to the built in field V_{bi} produced by the asymmetric contacts. This is the short-circuit current J_{sc} and is a useful metric that describes the net efficiency of the light absorption and exciton diffusion steps.

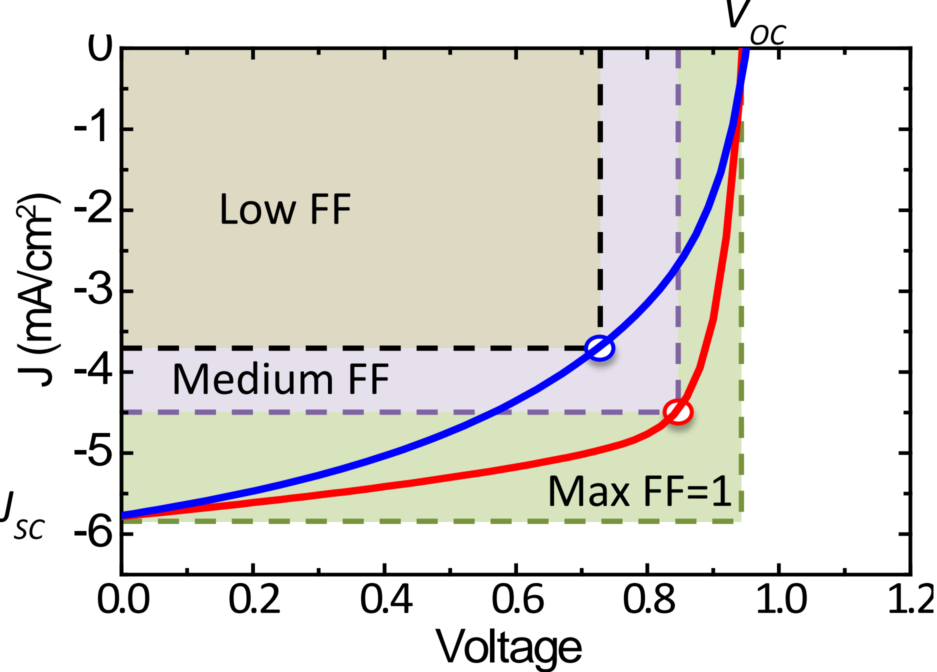

Figure 2.7 – OPV J-V Characteristics: Current density versus voltage characteristics typical of organic photovoltaics. Both devices have the same open-circuit voltage (V_{OC}) and short-circuit current (J_{SC}) but different power conversion efficiencies (PCE). The low fill-factor (FF) device (blue) has a rounded shape resulting in a reduced PCE. The maximum power point (MPP) is indicated by the open circle and the FF is defined as FF = V(MPP) ×J(MPP)/(V_{OC}×J_{SC}). A device with a good FF is shown in red.

Under high forward bias the electrical injection J_{dark} opposes and dominates the photocurrent J_{ph}, and the device becomes an exponential current sink. The current goes to zero when J_{dark} exactly cancels J_{ph} generated in the device, and this occurs at the open-circuit voltage, V_{oc}, that is near V_{bi}. When the device is biased between $V_a = 0$ and $V_a = V_{oc}$, any voltage dependence of the photocurrent (via η_{cg} and η_{cc}) can result in a premature loss of current (before electrical injection turns on and overwhelms the photocurrent). This results in a rounding of the *J-V* curve near the maximum power point, resulting in a loss of η_{PCE}. This effect is quantified by the fill-factor (FF) which relates the η_{PCE} to the J_{sc} and V_{oc} as $\eta_{PCE} = FF \cdot J_{sc} \cdot V_{oc} \cdot A/P_{opt}$, where A is the device area and P_{opt} is the optical power incident on the device. A device with efficient charge transport and low recombination probability can continue to produce most of the

saturated photocurrent as the field in the device is reduced – this results in a nearly "square" *J-V* in the fourth quadrant and a high FF.

Chapter 3

Recombination in Organic Buffer Layers

3.1. Background

Buffer layers are frequently employed between the acceptor and cathode in organic photovoltaic (OPV) devices to improve their power conversion efficiencies (PCE). The layer typically has multiple functions, including as (i) an exciton blocker that prevents quenching at the acceptor-cathode (A/C) interface,[74,99] (ii) a spacer to optimize the optical field at the active donor-acceptor (D/A) junction,[100,101,102] and (iii) a physical buffer to protect the acceptor layer from damage incurred during cathode deposition.[103,104] A commonly used buffer material, bathocuproine (BCP),[99] is effective at suppressing parasitic exciton quenching and protecting the active layers,[104] but its ability to act as an optical spacer is limited due to the thicknesses that can be used. That is, charge transport in this and similar wide energy gap materials depends on introducing charge-conducting pathways through traps induced by damage incurred during cathode metal deposition. Typically, this damage extends only 5-10 nm from the buffer layer surface. This thickness, however, is insufficient to use the layer as an optimal optical spacer that can concentrate the incident field at the active D/A interface.[102,105,106]

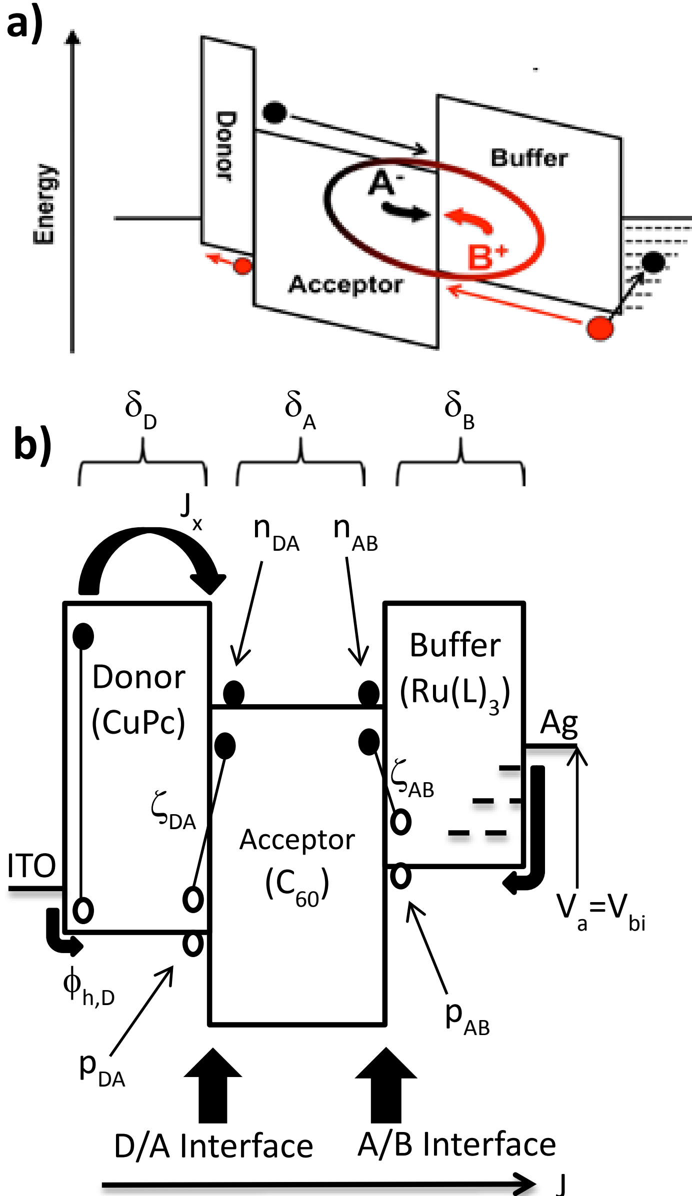

Figure 3.1 – Reciprocal Carrier Collecction: (a) Schematic of the reciprocal carrier collection process. (b) Diagram of the model for reciprocal carrier collection. Exciton flux J_x reaches the donor/acceptor interface (D/A) and creates polaron pairs (PPs) at density, ζ_{DA}. These PPs are in dynamic equilibrium with electrons with density, n_{DA} in the acceptor LUMO, and holes with density p_{DA} in the donor HOMO. Similarly, at the reciprocal acceptor/buffer interface (A/B), there are PPs (density ζ_{AB}) and carriers n_{AB} and p_{AB} in the acceptor LUMO and buffer HOMO, respectively. The interfaces are coupled by n_{DA} and n_{AB} via current density (J) continuity, and whose magnitudes are determined by the voltage drop across the acceptor $\delta_A(V_a\text{-}V_{bi})$. Similarly, p_{DA} and p_{AB} are determined by respective density of states, injection barriers ($\phi_{h,D}$ and $\phi_{h,B}$), and voltage drops (δ_D and δ_B).

Recently, a more thickness-tolerant buffer material, tris(acetylacetonato)ruthenium(III) (Ru(acac)$_3$), was shown to efficiently transport holes along its highest occupied molecular orbital (HOMO) energy level directly to the acceptor, and hence does not depend on the presence of a high density of trap states for conduction.[107] Here, Ru(acac)$_3$ is a ground state neutral metal complex with a low-spin d^5 open shell,[108] leading to efficient hole transport. Figure 3.1(a) depicts the carrier transport mechanism in Ru(acac)$_3$ buffers. Holes are injected from the cathode to the HOMO of the buffer, and then transported to the acceptor-buffer (A/B) interface. Recombination of photogenerated electrons in the lowest unoccupied molecular orbital (LUMO) of the acceptor occurs across the A/B interface with the positive charge in the buffer HOMO.

In this study, a series of tris(β-diketonato)ruthenium(III) analogues bearing various aromatic and electron withdrawing substituents are used as buffer materials in OPV devices. We analyze their current density vs. voltage (*J*-*V*) characteristics based on a model employing geminate polaron-pair (PP) and carrier dynamics (as described in Ref. [78] and outlined in Sect. 2.4.1). The buffer forms a Type-II heterojunction (HJ)[107] with the C_{60} acceptor as shown in Fig. 3.1(b), resulting in two antipolar diodes with the first (forward) diode formed by the donor-acceptor (D/A) junction, and the second (reverse) diode formed by the A/B junction. This arrangement results in an inflection in the *J*-*V* characteristics which is commonly observed in OPVs with non-ideal cathode contacts.[109,110] In previous studies this behavior has been attributed to a reverse-biased diode that inhibits charge collection at one of the contacts[111,112] and has been treated phenomenologically using an equivalent circuit model consisting of two opposing diodes.[113,114] Here the inflection is found to be a fundamental property depending on the energy levels of the buffer, and is related to a reduced polaron pair (PP) recombination rate at the A/B

interface. That is, the A/B junction forms a bottleneck for charge extraction when PP recombination is slow compared to dissociation into free polarons.

We use ultraviolet photoemission spectroscopy (UPS) to measure the energy levels at the A/B and buffer/cathode interfaces, supporting our conclusion that PP recombination at the A/B interface can lead to a divergence from the ideal exponential *J-V* characteristics of a single-junction device.[78] We find that buffer materials yielding the most pronounced inflection have a deeper HOMO level corresponding to a larger A/B interface energy gap (defined as the difference in the LUMO energy of the acceptor and the HOMO energy of the buffer, viz.: $\Delta E_{HL} = E_{LUMO,A} - E_{HOMO,B}$) and a smaller PP recombination rate. The reduction in PP recombination with an increase in ΔE_{HL} suggests that electron transfer between the acceptor and buffer occurs via Marcus transfer in the inverted regime.[67] This indicates that charge extraction and, consequently, the PCE for reciprocal junction devices can be optimized by tuning ΔE_{HL}. The model developed to quantitatively describe the inflected *J-V* characteristics is based on the formalism developed previously by Giebink, et al.,[78] and hence can be generally applied to a range of organic junctions that exhibit reciprocal behavior.

This chapter is organized as follows: In Sect. 3.2 we discuss the theory describing the current in double heterojunctions characteristic of Ru-complex-based buffers used in OPVs. The model is based on exciton, charge and PP dynamics; in Sect. 3.3 we describe the experimental methods for materials synthesis, device fabrication, and measurement; in Sect. 3.4 we provide experimental results; in Sect. 3.5 we fit the experimental data to the model presented in Sect. 3.2 and discuss the physical processes that limit the power conversion efficiency in OPVs; and in Sect. 3.6 we present conclusions.

3.2. Theory

Giebink, et al. have proposed a description of the *J*-*V* characteristics of organic (i.e. excitonic) D/A junctions[78] that balances PP generation, dissociation and recombination at the interface with free polarons injected from, or collected at the contacts. In that model discussed in Chapter 2, excitons with flux, J_x, diffuse to the D/A interface where the bound states are dissociated into PPs. The PPs subsequently recombine to the ground state at a rate, $k_{r,DA}$, or dissociate to form free polarons at a rate, $k_{d,DA}$. Free polarons at the interface (corresponding to a hole density in the donor, p_{DA}, and an electron density in the acceptor, n_{DA}) can recombine by a Langevin process to form PPs at a rate k_{rec}. Here, we assume that there are occupied traps in the donor and acceptor, and that bimolecular recombination is dominated by free polarons recombining with trapped polarons at the interface.[78] This occurs at a rate $k_{rec,n}$ when free polarons in the acceptor recombine with trapped polarons in the donor, $p_{DA,t}$, and $k_{rec,p}$ when free polarons in the donor recombine with trapped polarons in the acceptor, $n_{DA,t}$. The PP density, ζ, is then obtained from:

$$J_x/a_{DA} - k_{r,DA}(\zeta - \zeta_0) - k_{d,DA}\zeta + k_{rec,n}n_{DA}p_{DA,t} + k_{rec,p}n_{DA,t}p_{DA} = 0,$$
$$k_{d,DA}\zeta - k_{rec,n}n_{DA}p_{DA,t} - k_{rec,p}n_{,t}p_{DA} + J/qa_{DA} = 0 \quad (3.1)$$

where the first equation describes the steady-state PP density, and the second gives the balance of charge, also in steady-state. Here, q is the electronic charge, a_{DA} is the width of the D/A junction defined by the spatial extent of interacting PPs, $\zeta_0 = k_{rec,n}n_{DA,0}p_{DA,t,0}/k_{d,DA,0} + k_{rec,p}n_{DA,t,0}p_{DA,0}/k_{d,DA,0}$ is the equilibrium PP density, and $k_{d,DA,0}$ is the equilibrium PP dissociation

Table 3.1 – Definitions for reciprocal carrier collection

Variable		Definition	Units
D/A	**A/B**	**Junction Variables**	
J_x	0	Exciton current density reaching D/A HJ	$cm^{-2}\ s^{-1}$
ζ	ζ_{AB}	Polaron pair density at HJ	cm^{-3}
a_{DA}	a_{AB}	Polaron pair spatial extent	cm
$k_{rec,n}$, $k_{rec,p}$	$k_{rec,AB}$	Free carrier bimolecular recombination coefficient	$cm^{-3}\ s^{-1}$
$k_{d,DA}$	$k_{d,AB}$	Polaron pair dissociation rate	s^{-1}
$k_{r,DA}$	$k_{r,AB}$	Polaron pair recombination rate	s^{-1}
$\eta_{d,DA}$	$\eta_{d,AB}$	Polaron pair dissociation efficiency	
n_{DA}, p_{DA}	n_{AB}, p_{AB}	Free electron and hole densities at the HJ	cm^{-3}
$n_{DA,t}$, $p_{DA,t}$	$n_{AB,t}$, $p_{AB,t}$	Trapped electron and hole densities at the HJ	cm^{-3}
J_{sD}, J_{sA}	J_{sAB}	Saturation current density of HJ	$A\ cm^{-2}$
n_D, n_A	1	Ideality factors due to trap limited recombination	
		Layer Variables	
δ_D, δ_A, δ_B		Fractions of potential dropped across donor, acceptor and buffer layers	
$N_{HOMO,D}$, N_{LUMO}, $N_{HOMO,B}$		Donor HOMO, acceptor LUMO and buffer HOMO densities of states	cm^{-3}
H_D, H_A		Band edge trap densities in the donor and acceptor	cm^{-3}
l_D, l_A		Characteristic temperature ratio for hole and electron trap distributions in the donor and acceptor	
p_{anode}		Density of holes in the donor at the anode	cm^{-3}
ϕ_D, ϕ_B		Hole injection barrier into the donor and buffer	eV
ΔE_{HL}		Interface energy gap at A/B HJ	eV

efficiency. Also, $n_{DA,0}$, $n_{DA,t,0}$, $p_{DA,0}$ and $p_{DA,t,0}$ are the equilibrium free and trapped electron and hole densities at the interface. Important variables used are defined in Table 3.1.

In quasi-equilibrium, the interface polaron densities are related to the charge densities at the contact and the injection barrier following:

$$n_{DA} = n_{cathode} \exp\left(\frac{\delta_A q(V_a - V_{bi})}{k_B T}\right) \approx N_{LUMO} \exp\left(-\frac{\phi_h}{k_B T}\right) \exp(\frac{\delta_A q(V_a - V_{bi})}{k_B T}) \tag{3.2}$$

with a similar expression for holes.[38] Here, T is the temperature, k_B is Boltzmann's constant, $n_{cathode}$ is the carrier density at the cathode, N_{LUMO} is the density of LUMO states in the acceptor, ϕ_e is the electron injection barrier at the contact, δ_A is the fraction of the applied voltage, V_a, dropped across the acceptor layer, and V_{bi} is the built-in voltage given by the difference in the anode and cathode work functions. Now, the trapped electron distribution in organic materials is commonly described by an exponential function:

$$n_t \approx H_A \exp\left(\frac{E_{Fn} - E_{LUMO}}{k_B T_{t,A}}\right) \approx H_A \left(\frac{n}{N_{LUMO}}\right)^{1/l_A} \tag{3.3}$$

with a similar expression for trapped holes. Here, H_A is the total trap density, $T_{t,A}$ is the characteristic trap temperature, and $l_A = T/T_{t,A}$. Then, Giebink, et al. derive the following expression for the current density-voltage characteristics of a D/A junction in the presence of traps:

$$J = J_{sD}\left(\exp\left(\frac{qV_a}{n_D k_B T}\right) - \frac{k_{d,DA}}{k_{d,DA,0}}\right) + J_{sA}\left(\exp\left(\frac{qV_a}{n_A k_B T}\right) - \frac{k_{d,DA}}{k_{d,DA,0}}\right) - q\eta_{d,DA} J_x \tag{3.4}$$

with ideality factors n_D, n_A defined according to Eq. 2.19.

The saturation currents, J_{sD} and J_{sA} are defined as in Ref. [78], $\eta_{d,DA} = k_{d,DA}/(k_{d,DA}+k_{r,DA})$ is the PP dissociation efficiency, and $n_{D(A)}$ is the ideality factor of the recombination processes characteristic of the donor (acceptor) layer.

To apply this model to the case of reciprocal carrier collection as found in Ru-complex (or RuL_3 where L=ligand) buffers, we use a similar approach for both the D/A and A/B interfaces (c.f. Eq. 3.2) by considering the polaron states as shown in Fig. 3.1b. The A/B junction is a reverse-biased diode with respect to the D/A junction, and the two are coupled by current continuity in the acceptor layer. Hence, we write the following to describe polaron recombination at the A/B interface, which is coupled to similar expressions at the D/A junction:

$$\begin{gathered} -k_{r,AB}\left(\zeta_{AB}-\zeta_{AB,0}\right)-k_{d,AB}\zeta_{AB}+k_{rec,AB}n_{AB}p_{AB}=0 \\ k_{d,AB}\zeta_{AB}-k_{rec,}n_{AB}p_{AB}-J/qa_{AB}=0 \end{gathered} \tag{3.5}$$

We have neglected exciton flux as a source of PP generation since the optical field near the contact is small, minimizing exciton generation near this second interface.[74] To further simplify the model, we ignore the presence of traps in the buffer. Traps at this interface could be accounted for in the same manner as at the D/A interface, however, we find that we can accurately fit the *J-V* characteristics by assuming a trap-free junction. Continuity requires that polarons leaving the D/A junction must build up at the A/B interface.

We can solve for polaron, ζ_{AB}, and interface electron densities using Eq. 3.5. As in Ref. [78], quasi-equilibrium for holes at the A/B interface gives the current-dependent interfacial electron density, n_{AB}:

$$n_{AB}=\left(\frac{k_{d,AB}}{k_{d,AB,0}}-\frac{J}{J_{sAB}}\right)n_{AB,0}\exp\left(\frac{\delta_B qV_a}{k_BT}\right)$$

Where,

$$J_{sAB} = qa_{AB}\left(1-\eta_{d,AB}\right)k_{rec,AB}n_{AB,0}p_{AB,0}. \tag{3.6}$$

From the voltage drop across the acceptor δ_A, we can relate the electron densities n_{AB} and n_{DA} via:

$$n_{DA} = n_{AB}\, exp\left(\frac{\delta_A q(V_a - V_{bi})}{k_B T}\right). \tag{3.7}$$

The solution to the double junction then is given by Eq. 12 in Ref. [78] for the D/A junction, and by using Eq. 3.2, 3.6 and 3.7 to evaluate both the free and trapped electron densities in the layers. Thus:

$$J = J_{sD}\left(\left(\frac{k_{d,AB}}{k_{d,AB,0}} - \frac{J}{J_{sAB}}\right)\exp\left(\frac{qV_a}{n_D k_B T}\right) - \frac{k_{d,DA}}{k_{d,DA,0}}\right) + J_{sA}\left(\left(\frac{k_{d,AB}}{k_{d,AB,0}} - \frac{J}{J_{sAB}}\right)^{1/l_A}\exp\left(\frac{qV_a}{n_A k_B T}\right) - \frac{k_{d,DA}}{k_{d,DA,0}}\right) - q\eta_{d,DA}J_x$$

with

$$J_{sD} = qa_{DA}\left(1-\eta_{d,DA}\right)k_{rec,n}n_{AB,0}H_D\left(\frac{p_{anode}}{N_{HOMO,D}}\right)^{1/l_D}\exp\left(-\frac{\alpha_D}{k_B T}\right),$$
$$J_{sA} = qa_{DA}\left(1-\eta_{d,DA}\right)k_{rec,p}p_{anode}H_A\left(\frac{n_{AB,0}}{N_{LUMO}}\right)^{1/l_A}\exp\left(-\frac{\alpha_A}{k_B T}\right). \tag{3.8}$$

The corresponding ideality factors are given by:

$$n_D = l_D/\left(l_D - \delta_D(l_D - 1)\right), \qquad n_A = l_A/\left(l_A - (\delta_A + \delta_B)(l_A - 1)\right),$$
$$\alpha_D = (1 - n_D\delta_B)qV_{bi}/n_D, \qquad \alpha_A = (1 - n_A\delta_B/l_A)qV_{bi}/n_A. \tag{3.9}$$

The performance of OPVs with reciprocal carrier collection are fully described by Eq. 3.8 and 3.9. Note that these expressions are analogous to those for a single junction, but differ primarily in the current-dependent prefactors that result from the dependence of n_{DA} on n_{AB}, (i.e. on current continuity). Also, $\alpha_{D(A)}$ and $n_{D(A)}$ differ slightly from their definitions for a single junction, but have a similar dependence on trap temperature, interface energy gap and the voltage distributions, δ_D, δ_A, and δ_B. The exponent of the second current term in Eq. 3.8 precludes an analytical expression for J.

To elucidate the dominant features leading to reciprocal carrier collection, it is useful to simplify Eq. 3.8. For example, one of the diode terms can be neglected when the J-V characteristics are dominated by a single recombination process – i.e. free electrons in the acceptor recombining with trapped holes in the donor, or free holes in the donor with trapped electrons in the acceptor. Indeed, monopolar recombination is consistent with the analysis of CuPc/C_{60} junctions at room temperature.[78] To be general, we keep the second term of Eq. 3.8 based on free holes recombining with trapped electrons by letting $J_{sD} \rightarrow 0$, but find that fitting this non-analytic equation to our device data yields a trap temperature ratio of $l_A = 0.99 \pm 0.01$. This suggests that recombination occurs via free electrons with trapped holes. In this case we keep J_{sD}, and setting $J_{sA} \rightarrow 0$, linearizing the right-hand side of Eq. 3.8. Additionally, for $V_a < V_{bi}$ where the A/B junction is forward-biased, we retain the zero field dissociation rate for the A/B junction, $k_{d,AB} \approx k_{d,AB,0}$. Equation 3.8 is thereby simplified to:

$$J = \left(J_{sD}(\exp\left(\frac{qV_a}{n_D k_B T}\right) - \frac{k_{d,DA}}{k_{d,DA,0}}) - J_{ph}\right) \Big/ \left(1 + \frac{J_{sD}}{J_{sAB}} \exp\left(\frac{qV_a}{n_D k_B T}\right)\right), \tag{3.10}$$

where the photocurrent density is $J_{ph} = q\eta_{d,DA} J_x$.

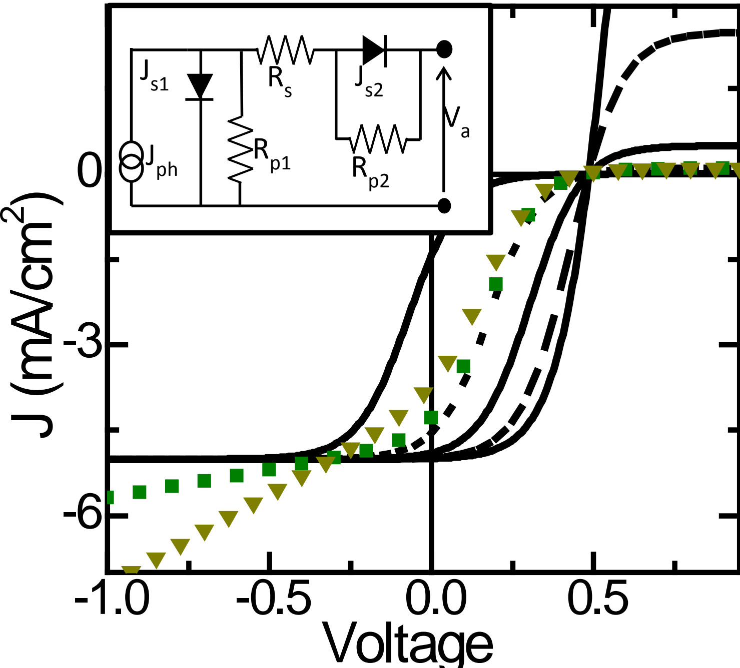

Figure 3.2 – Double Diode Model: Characteristic current density-voltage (*J-V*) curves calculated from the model in text recreate the inflection behavior seen in OPV devices with a charge extraction barrier. For these calculations, we assume $J_{ph} = 5mA$ is the photocurrent, $J_{sD}=10\mu A$ and $n=3$ are the reverse saturation current density and ideality factor of the forward donor/acceptor junction. Solid and broken lines correspond to different saturation currents of the reversed acceptor/buffer junction spanning J_{sAB} = 12.5, 2.5, 0.5, 0.2, and 0.04 mA/cm². Symbols show the reverse bias slope generated by a shunt resistance in the equivalent circuit model, shown in the inset.

In Fig. 3.2 we plot characteristic curves predicted by Eq. 3.10 for several values of J_{sAB}, where we assume $k_{d,DA} = k_{d,DA,0}$ for simplicity. The simulations show that the characteristic "opposing diode" behavior is increasingly apparent at decreasing reverse-diode saturation currents. Furthermore, current saturation occurs in both forward and reverse bias, as rectification

of either the D/A and A/D junction correspondingly limits the total current. The magnitude of the inflection depends on the ratio of J_{sD} to J_{sAB}. The current behaves like a single diode with ideality factor, n_D when $J_{sAB} >> J_{sD}$, or as antipolar diodes with a *J-V* inflection as $J_{sAB} \rightarrow J_{sD}$.

As noted above, the resulting inflection, or 'S' shaped kink, in *J vs. V* near zero bias has

been previously qualitatively attributed to a reverse-biased diode at one of the contacts, and is typically described by an equivalent circuit model as shown in Fig. 3.2, inset.[111,113,114] Both junctions are described by the Shockley Equation modified to include a series (R_s) and junction shunt (R_p) resistance. Only the active junction is forward biased and produces photocurrent; the second junction is reverse biased. In this case, we can write the phenomenological pair of equations:

$$J = J_{s1}\left(\exp\left(\frac{qV_1}{n_1 k_B T}\right) - 1\right) + \frac{V_1}{R_{p1}} - J_{ph}$$
$$-J = J_{s2}\,(\exp\left(-\frac{qV_2}{n_2 k_B T}\right) - 1) - \frac{V_2}{R_{p2}} \qquad (3.11)$$

Here, the subscripts 1 and 2 refer to the D/A and A/B junctions, respectively, and the applied voltage is dropped across the two junctions via, V_a - JR_s = V_1 + V_2. At low current densities, the effect of R_s is small, and hence is ignored. When R_{p2} >> V_2/J, then the coupled equations are reduced to:

$$J = J_{s1}\left(\left(1 - \frac{J}{J_{s2}}\right)^{n_2/n_1} \exp\left(\frac{qV_a}{n_1 k_B T}\right) - 1\right) + \frac{V_a}{R_{p1}} + \frac{n_2 k_B T}{qR_{p1}} \ln\left(1 - \frac{J}{J_{s2}}\right) - J_{ph}. \qquad (3.12)$$

Equation 3.12 has the same form as Eq. 3.8 for a single junction if the shunt current is negligible, i.e. $R_{p1} \rightarrow \infty$. Note that the physical origin of the shunt resistance cannot be understood using the equivalent circuit to fit the large reverse bias slope and simulate the commonly observed deviations from the Shockley Equation. The effect that parallel resistance has on the reverse bias slope is also shown in Fig. 3.2 for R_p=300Ω and 1kΩ. In contrast, the treatment here and in Ref. [78] attribute the reverse bias slope to the field dependence of the PP recombination rate, as described by Onsager-Braun dissociation.[95]

3.3. Experimental

3.3.1. Materials

Preparation of the metal complexes employed the following precursors: ruthenium(III) chloride hydrate (99+%); 1,3-dephenyl-1,3-propanedione (98%); 4,4-difluoro-1-phenyl-1,3-butanedione (97%); 4,4,4-trifluoro-1-phenyl-1,3-butanedione (99%); 4,4,4-trifluoro-1-(2-naphthyl)-1,3-butanedione (99%); 4,4,4-trifluoro-1-(2-thienyl)-1,3-butanedione (99%). Various Ru β-diketonate derivatives were synthesized by the "ruthenium blue" method of Endo, et al.[115] summarized in Fig. 3.3(a). Ruthenium trichloride was refluxed in ethanol under N_2. Excess chelating ligand was introduced, and the liberated H^+ was quenched with multiple fractions of bicarbonate. Complexes were purified over an activated alumina (neutral, Alfa Aesar) column

Figure 3.3 – Ruthenium Complexes: (a) "Ruthenium Blue" process for synthesizing the Ru-based complexes. (b) Molecular structure of the ligand bonded to the Ru core for each buffer layer. Numbers given to each material are ordered by decreasing voltage at the inflection.

with benzene (EMD; 99.92%) as the eluant and recrystallized from ethanol or ethanol/benzene. Ligands were chosen based on their ability to maximize vapor processability, increased intermolecular electronic communication, and the relative HOMO energies of the resulting complex. Depending on the magnitude of the electron withdrawing effects exerted by the β-position substituents[116,117] on the electron density of the chelating oxygen atoms[118] in each ligand, the *d*-orbitals of the metal complexes are progressively stabilized via increasingly electron-deficient chelating atoms. The resulting products were characterized by electron impact ionization mass spectrometry (HP 5973), ultraviolet-visible spectroscopy (Agilent 8453), and solution cyclic voltammetry (EG&G Potentiostat/Galvanostat, Model 283). These results are given in EPAPS.

3.3.2. Device Fabrication and Characterization

Devices were deposited on glass substrates commercially coated with indium tin oxide (ITO with thickness: 1500 ± 100 Å, sheet resistance: 20 ± 5 Ω/sq., transmission: 84% at a wavelength of λ=550 nm). Substrates were solvent cleaned and UV-ozone treated for 10 min prior to loading into a high vacuum deposition chamber (base pressure < $2x10^{-6}$ Torr). All ruthenium analogues, copper phthalocyanine (CuPc from Aldrich; 97%), C_{60} (MER; 99+%), and $Ru(acac)_3$ (Aldrich; 97%) were purified via thermal gradient sublimation (base pressure < $2x10^{-7}$ Torr). Organic and Ag (Alfa Aesar, 99.9999%) layer thicknesses and deposition rates were monitored by a quartz crystal microbalance to yield OPV devices with the structure: ITO/CuPc(400Å)/C_{60}(400Å)/buffer/Ag(1000Å). The *J-V* measurements were performed using a Keithly 2420 SourceMeter® in the dark and under AM1.5G, 1 kW/m^2 white light illumination from a 300W Xe arc lamp, with total power measured using an NREL-calibrated Si photodiode. Fits to the *J-V* data were performed in Matlab using a non-linear, least-squares, trust-region.

3.3.3. UV Photoelectron Spectroscopy

The HOMO energies of the RuL_3 buffer layers on C_{60}/ITO or Ag were measured by UPS. ITO-coated glass substrates with sheet resistance of < 15Ω/sq. were solvent cleaned and UV-ozone treated prior to loading into an ultra-high vacuum (UHV) chamber. Prior to the deposition of a 50 Å thick RuL_3 film: (i) 50 Å thick C_{60} films were deposited onto ITO substrates, or (ii) 300 Å thick Ag films were deposited onto p-type Si. The organic films were deposited by organic molecular beam deposition (base pressure: 10^{-9} torr) from Knudsen cells, while the Ag films were deposited in a separate UHV interconnected chamber by thermal evaporation. Thickness was monitored by an ellipsometrically calibrated quartz crystal microbalance. Following deposition, the samples were immediately transferred under UHV ($< 1 \times 10^{-9}$ Torr) to the UPS chamber. Photoelectron spectra were collected using a Thermo VG hemispherical electron energy analyzer with a pass function full width half maximum of 0.16 eV (calibrated by fitting the Fermi step of a freshly deposited Au film) to filter electrons photoemitted from the sample by a 21.22eV He(I) emission line from a gas discharge lamp. To minimize sample charging, electrical contact to the ITO film was maintained by a metal clip attached to a copper puck and connected to ground. The sample was biased at -9.00 V to ensure that the low kinetic energy electrons pass through the analyzer.

The LUMO energies were estimated by electrochemical methods performed under nitrogen against ferrocene/ferrocenium in dry acetonitrile with tetrabutylammonium hexafluorophosphate as the supporting electrolyte. Silver reference, platinum counter, and glassy carbon working electrodes were used with the potentiostat.

3.4. Results

The RuL_3 complexes investigated, each with a different ligand, L, are shown in Fig. 3.3(b). Each complex was used as a 100Å or 200Å thick buffer layer in the OPV structure of Sect. 3.3. Devices with a 100Å thick buffer layer exhibited similar performance independent of composition, as shown in Fig. 3.4. Power conversion efficiencies range from 1.0% ± 0.3% to 1.4% ± 0.3%, and are comparable to that of an analogous BCP-based device.[74] Since performance is independent of Ru-complex composition, we infer that electron transport through these thin layers occurs via trap states due to damage incurred during cathode deposition, similar to electron transport via BCP traps.

In contrast, devices with 200Å thick buffer layers exhibit performance that is strongly dependent on buffer layer composition. Figure 3.5 shows the *J-V* characteristics for a series of RuL_3-based devices under 1 sun illumination. These same characteristics are replotted in greater detail in the semi-log plot of Fig. 3.6. A current inflection results in a reduction in fill factor and, concomitantly, power conversion efficiency.

We use UPS to characterize the effect of the buffer energy levels on the *J-V* inflection to clarify the conduction mechanisms in RuL_3. Thickness-dependent UPS measurements of the HOMO and vacuum level (E_{vac}) of thin films have often shown that: (1) the Schottky-Mott limit of E_{vac} alignment across an interface is not generally valid due to the presence of an interface dipole, and (2) there can be additional E_{vac} shifts through the bulk due to built-in fields. We measured the HOMO and E_{vac} energies for 50Å thick buffers deposited on C_{60}, with results summarized in Fig. 3.8(a). There is no apparent correlation between the HOMO and LUMO levels and device performance due to band bending between the buffers and C_{60} (observed as a

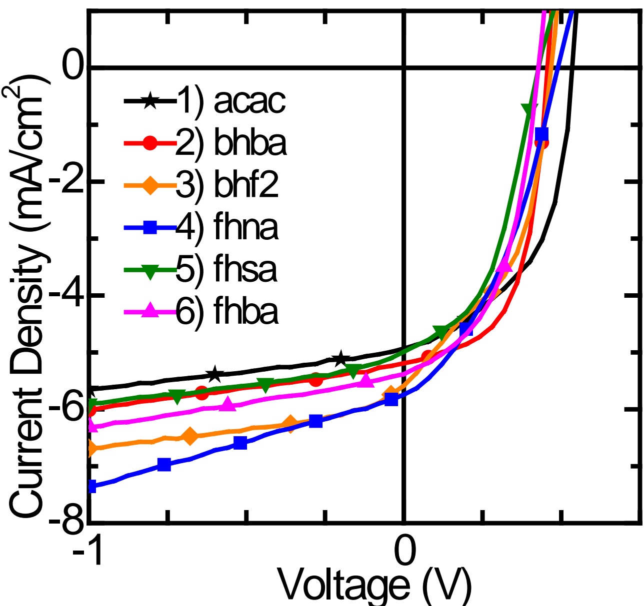

Figure 3.5 – Thin RCC OPVs: Current density vs. voltage (*J*-*V*) characteristics under approximately 1 sun AM1.5G illumination of ITO/copper-phthalocyanine (40nm)/C_{60} (40nm)/buffer (10nm)/Ag (100nm) devices. Data are shown by symbols and lines. Slight differences in photocurrent magnitude from device to device are attributed to small variations in light intensity and device efficiency.

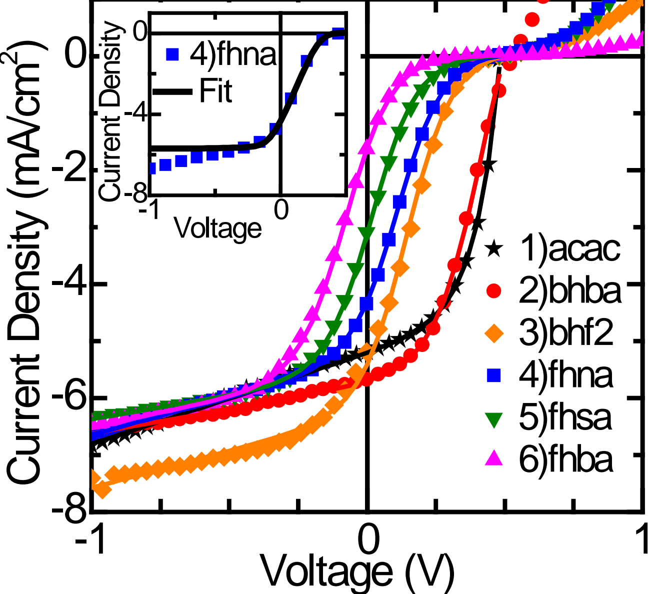

Figure 3.4 – Thick RCC OPVs: Current density vs. voltage (*J*-*V*) characteristics under approximately 1 sun AM1.5G illumination of ITO/copper-phthalocyanine (40nm)/C_{60} (40nm)/buffer (20nm)/Ag (100nm) devices. Data are shown by symbols, and fits to the model in text up to breakdown at ~0.5V are shown by solid lines. Inset: Fit (line) of the measured reverse bias characteristic (symbols) ignoring the voltage dependence of the polaron-pair dissociation rate.

shift in E_{vac}). However, thickness-dependent UPS data for the parent Ru(acac)$_3$ shows that most of this shift occurs over a distance of ~100Å from the interface, and the vacuum levels at the interface are nearly that of C_{60}.[107] This suggests that the interface dipole is small so that the energy level alignment at the A/B interface is independent of the E_{vac} shift through the bulk. In support of this conclusion, we observe a correlation between the HOMO energy and device performance by aligning the vacuum levels at the A/B interface as shown in Fig. 3.8(b). We find that a deeper HOMO (a larger ΔE_{HL}) results in the inflection in the *J-V* characteristic shifted further toward reverse bias.

3.5. Discussion

The *J-V* inflection observed in these reciprocal carrier collection devices is a feature that is frequently found in OPVs, and often results from conditions used in device fabrication.[109,112] In some cases, the inflection can arise from a hole or electron transport layer with poorly matched transport levels.[110,119,120] Applying the model in Sect. 3.2, we find Eq. 3.10 has the functional form to replicate the inflection as shown by the inset of Fig. 3.5, which is a fit to the Ru(fhna)$_3$ device data with all the parameters taken independent of voltage (solid line). This simplified expression fits the inflection but not the reverse bias slope.

The dominant source of reverse voltage dependence of the current is the PP dissociation rate, and therefore also η_d, which is described by Onsager-Braun dissociation.[95] The reverse-biased electric field lowers the barrier for separating Coulombically bound PPs, and increases the dissociation rate following:

$$k_{d,AB} = \frac{3}{4\pi a_{AB}^3} k_{rec,AB} \exp\left(-\frac{E_B}{k_B T}\right)\left(J_1\left(2\sqrt{-2b}\right)/\sqrt{-2b}\right) \tag{3.13}$$

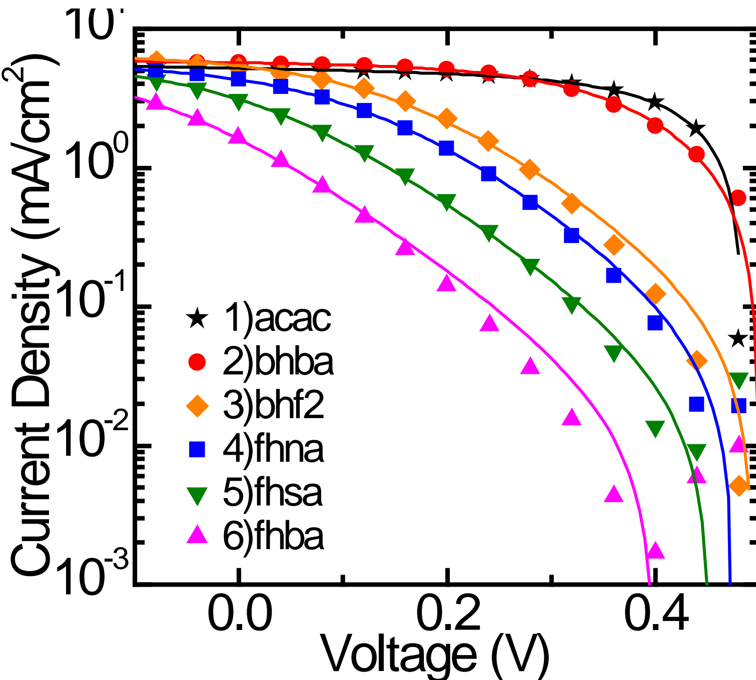

Figure 3.7 – Thick RCC OPVs (log scale): The *J-V* characteristics in Fig. 5 replotted on a semi-log scale. Fits to the data using model in text are shown by lines.

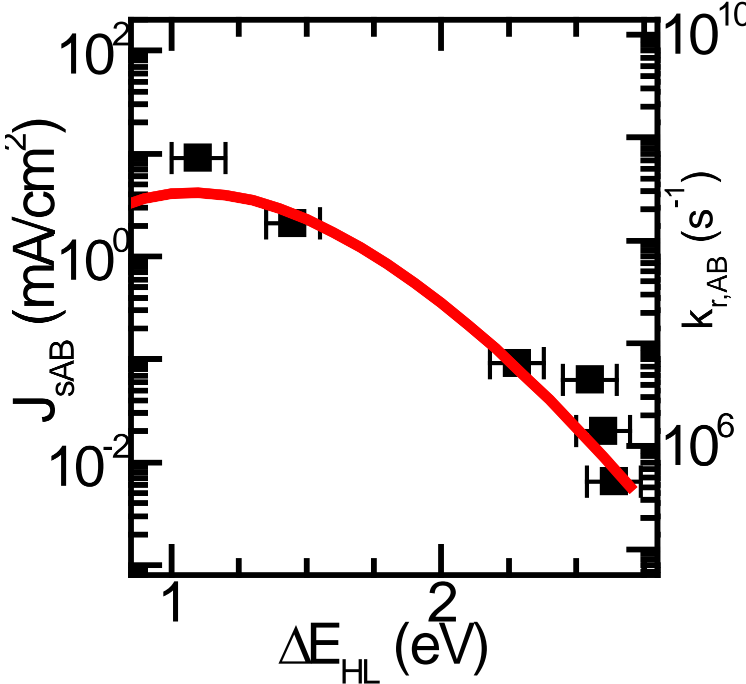

Figure 3.6 – Recombination in Inverted Marcus Regime: Saturation current, J_{sAB}, and polaron pair recombination rate, $k_{r,AB}$, at the acceptor/buffer layer junction compared to the interface energy gap $\Delta E_{HL} = E_{LUMO,A} - E_{HOMO,B}$ for the different buffer compositions. Here, J_{sAB} is obtained by fitting the current density vs. voltage characteristics to the model in text. $k_{r,AB}$ is estimated from J_{sAB} using Eq. 3.6 as described in the text.

with a similar expression for $k_{d,DA}$. Here a_{AB} is the initial PP separation, $b = q^3F_I/(8\pi\varepsilon k_B{}^2T^2)$, E_B is the PP binding energy, F_I is the interface e field, and J_1 is the first order Bessel function. This model applies for fields directed from the acceptor toward the donor where it enhances charge separation – this is the case at the D/A junction when $V_a<V_{bi}$. When a junction is forward biased at $V_a>V_{bi}$, the field is directed from the donor toward the acceptor so that it does not enhance charge separation. As stated previously, this is the case at the reversed A/B junction when $V_a<V_{bi}$, and we retain the zero field dissociation rate $k_{d,AB}\approx k_{d,AB,0}$.

Expanding the Bessel function in Eq. 3.13, and assuming the interface field is linearly dependent on voltage (i.e. the current is sufficiently small to avoid space charge effects), then:

$$k_{d,DA} \approx k_{d,DA,0}(1 - BV_a) \tag{3.14}$$

This rate appears explicitly in Eq. 3.10, and is also present in J_{sD} and J_{ph} via $\eta_{d,DA}$. The large and constant reverse bias slope suggests that $\eta_{d,DA}$ is small over this voltage range, such that $\eta_{d,DA} \approx k_{d,DA}/k_{r,DA}$. Then J_{sD} is constant and the photocurrent is $J_{ph} = qJ_xk_{d,DA,0}(1\text{-}BV_a)/k_{r,DA}=J_{ph,0}(1\text{-}BV_a)$. Then Eq. 3.10 becomes:

$$J = \frac{J_{sD}\left(\exp\left(\frac{qV_a}{n_Dk_BT}\right) - 1 + BV_a\right) - J_{ph,0}(1 - BV_a)}{1 + \frac{J_{sD}}{J_{sAB}}\exp\left(\frac{qV_a}{n_Dk_BT}\right)}. \tag{3.15}$$

These approximations account for the first-order field dependence of PP dissociation, and allow fitting the $Ru(fhna)_3$ data as shown in Figs. 3.5 and 3.6. Note that the data under forward bias do not show the saturation of the second junction, as is apparent in Fig. 3.2. This is attributed to forward biased breakdown of the A/B junction at $V_a\approx 0.5V$ in the devices.

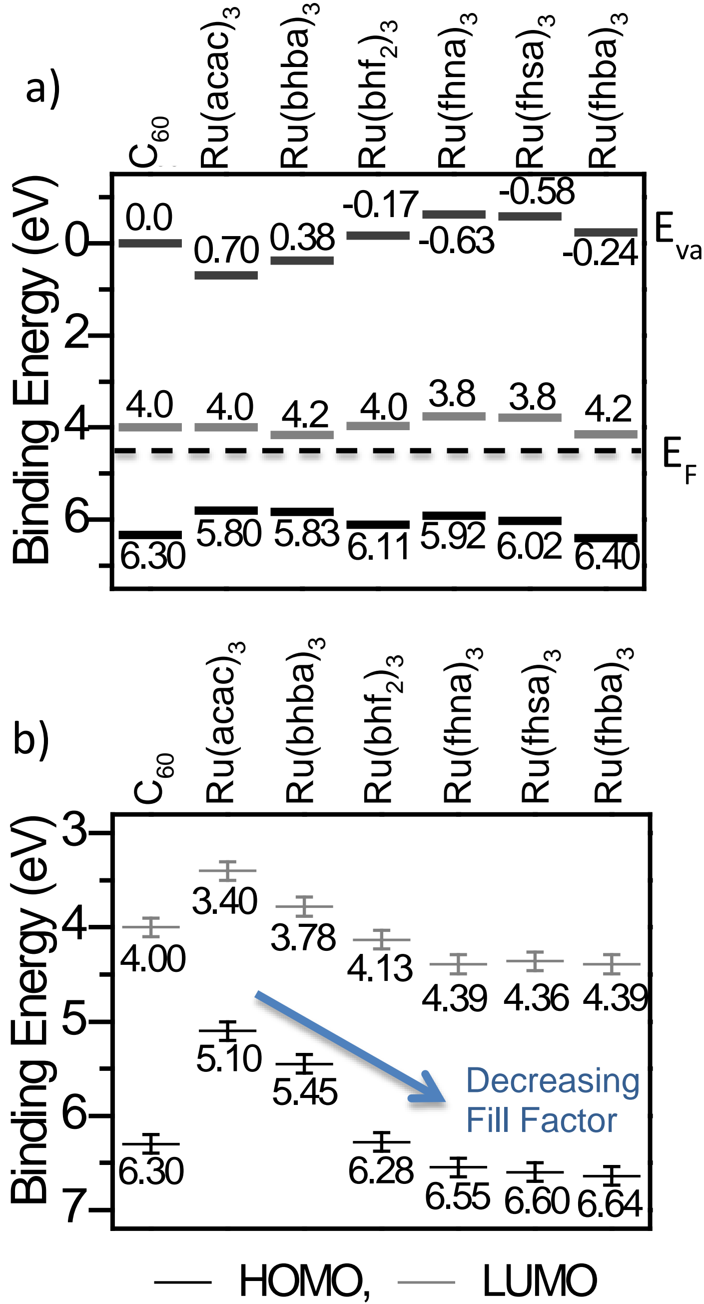

Figure 3.8 – Energy Levels for Ru Complexes: (a) Energy levels measured by a combination of ultraviolet photoelectron spectroscopy (for the highest occupied molecular orbital, HOMO) and cyclic voltammetry (for the lowest unoccupied MO, or LUMO) for 5 nm thick RuL_3 buffer layers on C_{60} (5nm)/ITO. (b) Energy level alignment at the acceptor/buffer interface obtained assuming vacuum level alignment.

Comparing Eq. 3.15 with the equivalent circuit expression of Eq. 3.12, we find the discrepancy between the models is due to the shunt resistance and field-dependent dissociation terms. For typical devices, the natural logarithm term in Eq. 3.12 is negligible, and the reverse bias slope is linear in V_a/R_p. In this case, the equivalent circuit analysis allows R_p to accurately reflect the first-order field dependence of PP dissociation, where R_p is given by:

$$R_p = \frac{1}{\left(J_{ph,0} + J_{sD}\right)B} \tag{3.16}$$

Thus, the phenomenological equivalent circuit model converges to the physical model for back-to-back junctions in OPVs.

The *J*-*V* data can now be fit using Eq. 3.15 with only five parameters n_D, J_{sD}, J_{sAB}, $J_{ph,0}$, and B. This is further simplified since, n_D and J_{sD} depend only on the donor and acceptor, and hence should remain independent of the buffer material, while we expect J_{sAB} to depend only on buffer composition. We also find that B is varied to match the reverse bias slopes of the different devices, as discussed above. In Figs. 3.5 and 3.6 we plot the *J*-*V* data (points) along with the fits (lines). For $V_a > 0.5$V, the current grows exponentially due to breakdown of the reverse-biased A/B junction. The fitting parameters are listed in Table 3.2 and the errors represent a 95% confidence interval for the nonlinear regression fit. Due to the lack of *J*-*V* inflection, the fit only gives a lower limit to J_{sAB} for the $Ru(acac)_3$ device.

The position of the *J*-*V* inflection is determined by J_{sAB}, which varies over three decades for the various RuL_3 buffers studied. Now, J_{sAB} is given in Eq. 3.6, and we expect $p_{AB,0}$ and $\eta_{r,AB} = (1-\eta_{d,AB}) = k_{r,AB}/(k_{r,AB}+k_{d,AB})$ to be dependent on the positions of the buffer HOMO and LUMO energies. We treat the dissociation rate, $k_{d,AB}$, as constant for all buffers since it is a function of

Table 3.2 - RCC fit results: Fit results to the model in text for OPVs with several different RuL3 Buffer composition. Common Parameters: J_{sD} = 16.0 ± 1.5 μA/cm^2, and n_D = 3.31 ± 0.05

Buffer	J_{sAB} (mA/cm^2)	$J_{ph,0}$ (mA/cm^2)	B (V^{-1})
1) Ru(acac)$_3$	9 (+100/-2)	5.2 ± 0.1	0.31 ± 0.01
2) Ru(bhba)$_3$	2.1 ± 0.2	5.7 ± 0.1	0.15 ± 0.01
3) Ru(bhf$_2$)$_3$	(9.2 ± 0.8)x10^{-2}	6.3 ± 0.1	0.19 ± 0.01
4) Ru(fhna)$_3$	(6.4 ± 0.5)x10^{-2}	5.4 ± 0.1	0.23 ± 0.02
5) Ru(fhsa)$_3$	(2.0 ± 0.2)x10^{-2}	5.6 ± 0.1	0.14 ± 0.02
6) Ru(fhba)$_3$	(6.4 ± 0.8)x10^{-3}	5.5 ± 0.1	0.17 ± 0.03

hole mobility and dielectric constant through k_{rec} and E_B[121] in the Onsager-Braun model, which we expect to be reasonably materials independent. Hence, the current inflection is determined either by the carrier density at the *A/B* interface, $p_{AB,0}$, or by the recombination rate, $k_{r,AB}$.

The energies in Fig. 3.8(b) reveal a correlation between device performance and the HOMO position at the A/B interface. However, away from this interface (Fig. 3.8(a)), vacuum level shifts eliminate this consistent variation of device performance with HOMO energy. This suggests that the observed J_{sAB} trend is not dominated by variations in $p_{AB,0} \propto exp(-(E_F-E_{HOMO,B})/k_BT)$, and we do not observe this relationship in J_{sAB}. To simplify the analysis, therefore, we assume that $p_{AB,0}$ and all the other terms in Eq. 3.6 are consistent across this set of devices, varying only the PP recombination rate $k_{r,AB}$.

The *J-V* inflection, therefore, occurs when $k_{r,AB} << k_{d,AB}$, so that $J_{sAB} \propto \eta_{r,AB} \propto k_{r,AB}$. In Fig. 3.7 we plot J_{sAB} verse ΔE_{HL}, and scale the right axis by typical values for the terms in Eq. 3.6 to represent $k_{r,AB}$. We use a_{AB}=1.5nm,[78] μ_A=10^{-2} cm^2/Vs,[122] μ_B=10^{-5} cm^2/Vs, σ_A =8x10^{-7} S/cm,[123] σ_B =2x10^{-7} S/cm,[107] $\varepsilon_A=\varepsilon_B=3\varepsilon_0$,[78] $k_{rec,AB}=q(\mu_A+\mu_B)/\varepsilon$ for Langevin recombination,[38] $k_{d,AB}$=10^9 s^{-1}

from Eq. 3.13 with a PP binding energy of 0.2eV, $p_{AB,0}$=σ_B/qμ_B=10^{17} cm^{-3} and $n_{AB,0}$=σ_A/qμ_A=10^{15} cm^{-3} which are typical of trapped carrier densities that dominate the intrinsic carrier density in equilibrium conditions for disordered organic semiconductors.[124,125] These estimates yield $k_{r,AB}$≈(7x10^{10} cm^2/As)J_{sAB}. This suggests that $k_{r,AB}$ ranges from 6x10^8 s^{-1} to 4x10^5 s^{-1}, which is similar to rates reported for electron transfer from donor to acceptor moieties connected by a steric spacer in solution, and for solid phase Langmuir-Blodgett films of donor-acceptor dyads.[126,127,128]

The variation in recombination rate between the several Ru-complexes studied implies that $k_{r,AB}$ decreases approximately exponentially with increasing ΔE_{HL}. This can be understood in terms of electron transfer from the acceptor LUMO to the buffer HOMO, described by Marcus Theory in the inverted regime.[67] The electron transfer rate can be expressed as $k_{r,AB} = k_{r,AB,0}\exp(-(\lambda - \Delta E_{HL})^2/4\lambda k_B T)$ and in the inverted regime when $\Delta E_{HL} > \lambda$, the molecular reorganization energy, the rate of charge transfer is reduced exponentially with ΔE^2. However, it has been shown for organic molecules with phonon energies > k_BT, that the charge transfer rate can be significantly enhanced by non-adiabatic, phonon-mediated processes.[67,126,129] In this case, one must sum all high energy phonon modes according to their Frank-Condon weighted density of states. For simplicity we use the two parabolic potentials of Marcus Theory, and consider the electron in the acceptor LUMO to be in its vibronic ground state, while we use an average vibronic energy to represent the numerous modes of the buffer molecule. In this case the electron transfer rate is given by:

$$k_{r,AB} = \sqrt{\frac{4\pi^3}{h^2\lambda k_B T}}|M|^2 \sum_{W=0}^{\infty} \frac{e^{-S}S^w}{w!} \exp\left(-\frac{(\lambda - \Delta E_{HL} + whv)^2}{4\lambda k_B T}\right) \quad (3.17)$$

where h is Plank's constant, M is the electronic coupling matrix element, $h\nu = 1500\ cm^{-1}$ is the average phonon energy mode chosen to represent skeletal vibrations, and S is the electron-phonon coupling strength.[126,127]

In Fig. 3.7 we show a fit of Eq. 3.17 to our measured $k_{r,AB}$ verse ΔE_{HL} data, where $\lambda = 0.6eV$, $S = 3.0$, and $M = 0.34\ cm^{-1}$. Errors in our model parameters for calculating $k_{r,AB}$ from J_{sAB} would only result in scaling M with a square root dependence. There are a family of curves described by Eq. 3.17 that fit our data within a 95% confidence interval, given by S=4.1-2.5λ where λ=0.1-1.0 eV. This range is consistent with transfer rates observed in solution.[124,126] Note that J_{sAB} for the Ru(acac)$_3$ device is undefined due to the lack of an inflection; i.e. the absence of a reverse-biased characteristic suggests that J_{sAB} in this case is too large to measure. The point indicated is, therefore, a lower limit for this compound. Additionally, while the assumption that $\eta_{r,AB} = k_{r,AB}/(k_{r,AB}+k_{d,AB}) \approx k_{r,AB}/k_{d,AB}$ is valid for the inflected devices with small J_{sAB}, it is not necessarily accurate for those based on Ru(acac)$_3$.

Our analysis shows that hole-transporting buffer layers can limit the current in OPVs under intense illumination. This effect can be minimized, and under many practical conditions even eliminated if the HOMO-LUMO energy at the A/B interface is minimized, thereby maximizing the PP recombination rate, k_r. In the case of the RuL$_3$ compounds, Ru(acac)$_3$ is an optimized buffer compared to, for example, Ru(fhba)$_3$, where ΔE_{HL} is increased from 1.1eV to 2.6eV with a corresponding increase in k_r which depends exponentially with ΔE_{HL}^2.

3.6. Conclusion

In summary, we synthesized a series of tris(β-diketonato)ruthenium(III) analogues for use as hole transporting buffer layers. The resulting OPV *J-V* characteristics are described in terms of reciprocal carrier collection at the donor/acceptor and acceptor/buffer layer junctions. The material independent performance observed for buffer layer thicknesses <100Å suggests that charge transport in this case is due to damage-induced defects in the RuL_3 complex on metal cathode deposition, similar to that observed for BCP buffers. Incorporating thicker (200 Å) films[107] leads to device characteristics that strongly depend on the composition of the buffer. Specifically, we observe an increasing *J-V* inflection for buffer materials with deeper HOMO energies.

We utilized a detail balance model to describe the observed *J-V* inflection based on free-polaron and PP recombination dynamics, and compared our results to the phenomenological antipolar diode equivalent circuit model that is often applied to OPV devices that exhibit an 'S'-shaped kink in their *J-V* characteristics. The inflection is found to depend strongly on the acceptor/buffer layer saturation current, J_{sAB}, that leads to a barrier to charge extraction. Here, J_{sAB} depends on the material-dependent PP recombination rate, $k_{r,DA}$, and the equilibrium hole density $p_{AB,0}$ at the A/B interface. While a larger buffer HOMO energy would suggest a larger injection barrier from the cathode, and therefore a reduced $p_{AB,0}$, our UPS data suggests the presence of vacuum level shifts that offset the variations in HOMO energies. We find that J_{sAB} varies by several orders of magnitude between the materials studied, and is a function of the HOMO energy of the buffer and hence, the A/B interface energy gap $\Delta E_{HL,AB}$. The behavior of J_{sAB} is understood in terms of non-adiabatic electron transfer in the Marcus inverted regime.

Generally, we have shown that a barrier to charge extraction can dramatically reduce OPV power conversion efficiency, and have demonstrated that free-polaron and PP dynamics

can be used to understand and optimize the choice of buffer. For reciprocal carrier collection devices, device architectures should utilize buffer materials that provide a small ΔE_{HL} and large PP recombination efficiency to optimize power conversion efficiency.

Chapter 4

Photoconductivity in Organic Photovoltaics

4.1. Background

Organic photovoltaic (OPV) cells have been demonstrated with power conversion efficiencies (η) approaching 10%.[130] To reach a high η, considerable effort has been invested to select materials and device architectures that maximize the OPV open-circuit voltage (V_{oc}), short-circuit current density (J_{sc}), and fill factor (FF). Factors that lead to high V_{oc} and J_{sc} are readily understood in terms of the offset of the frontier orbital energies of the donor and acceptor materials, optical absorption, exciton diffusion length, and the recombination dynamics of photogenerated charges within the cell.[74,131] However, the underlying physical processes and materials characteristics that result in a high FF are less well understood. This parameter is frequently treated using an equivalent circuit model for the current density *vs*. voltage (J-V) characteristics, as shown in Fig. 4.1(a). The model may include a second, reverse-biased diode[112,120] to account for an 'S-kink', and a parallel (i.e. shunt) resistance[132,133,134] (R_p) to account for a linear increase of photocurrent with reverse bias. The effect of R_p on the J-V characteristic, and particularly on FF, is shown in the inset, Fig. 4.1(a).

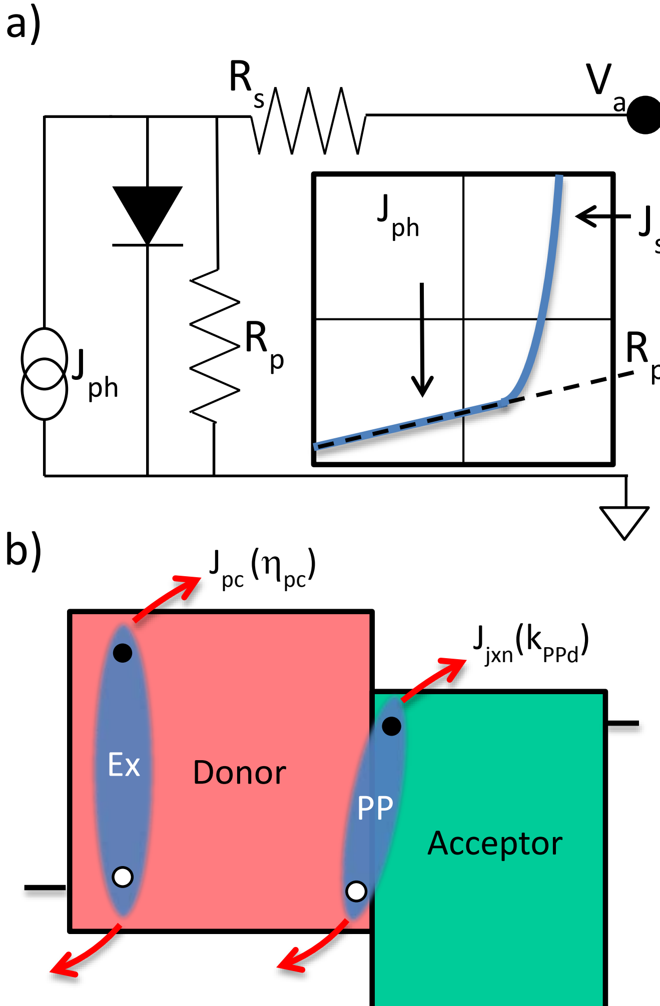

Figure 4.1 – Photoconductivity in OPVs: (a) Equivalent circuit and (inset) the characteristic shape of the current-density *vs*. voltage (*J*-*V*) characteristic for a heterojunction (HJ) organic photovoltaic (OPV) device. The parallel resistance (R_p) is due to photoconductivity and results in a linear slope under reverse bias. (b) Schematic of the OPV device consisting of a donor and acceptor junction. At the HJ, excitons can split into polaron pairs (PPs) that are dissociated at a rate k_{PPd} to generate photocurrent from the junction (J_{jxn}). Photogenerated excitons can also generate free carriers in the bulk of the organic films with a photoconductive efficiency and contribute a current due to photoconductivity (J_{pc}) to the total photocurrent.

Many physical models for the voltage dependence of *FF* consider the electric field dependence of the dissociation of polaron-pairs (PPs) Coulombically bound at the interface. The dynamics of this dissociation process have been described by Onsager[94] and Braun.[95] Subsequently, numerous studies have applied this theory to analyze the voltage dependence of photocurrent in OPVs. [81,135,136,137] Recently, Giebink, et al.[78] developed an analytical formalism describing the *J-V* characteristics of OPVs using a model based on the dynamics of free polarons and polaron-pairs (PPs) as discussed in Sect. 2.4.1. This model provides a physical framework for many common features of the OPV *J-V* characteristics, including the double exponential character of the forward-biased dark current, the heterojunction ideality factor (n), the "S-kink" behavior, and the voltage dependence of the photocurrent (J_{ph}) which leads to a reduced *FF*. In that model, J_{ph} varies with voltage due to the electric field (F) induced polaron-pair dissociation rate (k_{PPd}), which can be described by the Onsager-Braun (O-B)[94,93,95] theory for Coulombically interacting charge pairs in a dielectric medium:

$$k_{PPd} = \frac{3}{4\pi a_0^3} k_{rec} \exp\left(-\frac{E_B}{k_B T}\right) \frac{J_1\left[2\sqrt{-2b}\right]}{\sqrt{-2b}}. \quad (4.1)$$

Here, a is the initial PP separation at the heterointerface, k_{rec} is the Langevin rate for free polarons to form PPs, E_B is the PP binding energy and is approximated by $E_B = q^2/4\pi\varepsilon a$, J_1 is the first order Bessel function of the first kind, $b = -q^3F_I/(8\pi\varepsilon k_B{}^2T^2)$, and F_I is the interface electric field. Also, q is the electronic charge, ε is the material permittivity, k_B is Boltzmann's constant, and T is the temperature. The dissociation leads to a sublinear increase in J_{ph} under reverse bias according to $J_{ph} = J_{jxn} = \eta q J_X$, where J_{jxn} is the photocurrent produced at the donor-acceptor heterojunction (D-A HJ), $\eta = k_{PPd}/(k_{PPd}+k_{PPr})$ is the PP dissociation efficiency, k_{PPr} is the PP recombination rate, and J_X is the exciton flux reaching the HJ that produces PPs. It has been

proposed that the field dependence of k_{PPd} is the underlying physical process that results in a finite R_p commonly observed in OPVs.[78]

Here we show that the observed linear dependence of J_{ph} on voltage can be quantitatively explained by photoconductivity due to exciton generation followed by dissociation in the donor and acceptor bulks, as also identified by W. Jeong, *et al.* This is a significant effect common to many OPVs that often masks the underlying, intrinsic field-dependent dissociation of PPs at the heterojunction.[78,80] In this study we treat the simple case of planar heterojunction OPVs; however photoconductivity is an intrinsic process in all semiconductors. Hence, it is expected to be present even in other OPV device architectures such as bulk heterojunctions (BHJs). In the latter case, PP dissociation depends on the microscopic orientation of D/A domains and charge collection is strongly affected by bimolecular recombination throughout the bulk, which can lead to a more complicated analysis than in simple planar morphologies. We note, however, that whether photoconductivity plays a dominant role compared with other processes such as field-dependent dissociation, or bimolecular charge recombination, depends on the details of the junction morphology in each case. These considerations will be discussed in Sect. 4.4.

4.2. Theory

In excitonic materials where Coulomb interactions between electrons and holes are much larger than the thermal energy, photon absorption generates a bound exciton state that, on dissociation, contributes to the current. Dissociation can be efficient at a D-A HJ when there is an energy offset sufficient to separate the electron and hole[80] into the acceptor and donor layers, respectively. After charge transfer, Coulomb attraction results in a bound PP state at the interface

(see Fig. 4.1(b)). In this case, the current is determined exclusively by PP kinetics at the interface that are described as shown in Sect. 2.4.1 using:

$$J = J_{sD}\left\{\exp\left(\frac{qV_a}{n_D k_B T}\right) - \frac{k_{PPd}}{k_{PPd,eq}}\right\} + J_{sA}\left\{\exp\left(\frac{qV_a}{n_A k_B T}\right) - \frac{k_{PPd}}{k_{PPd,eq}}\right\} - qJ_X\eta_{PPd}. \quad (4.2)$$

Here, J_{sD}, J_{sA}, n_D and n_A are the saturation current densities and ideality factors defined in Ref. [78], V_a is the applied voltage, R_s is the series resistance and $k_{PPd,eq} = k_{PPd}(V_a=0)$ is the equilibrium dissociation rate. Equation 4.2 assumes a separation distance, a, between electron and hole polarons across the interface. To account for the effects of interface disorder, we average over a normal distribution of initial D-A molecular separations using:

$$\langle J \rangle = \int_0^\infty \frac{4}{\sqrt{\pi}a_0^3} a^2 \exp\left(-\frac{a^2}{a_0^2}\right) J(a)\,da \quad (4.3)$$

Here, a_0 is the characteristic initial PP separation.[80] In Fig. 4.2 we calculate the current for various values of k_{PPr} from Eq. 4.1 and using the parameters defined in Table 4.1. Note that it is the *ratio*, $k_{PPd,eq}/k_{PPr}$, that determines the dependence of J_{jxn} on V_a (c.f. Fig. 7, Ref. [78] where $k_{PPd,eq}^{-1}$= 140 ns was assumed), and hence the fill factor of the OPV. For this calculation, we assume $a_0 = 2$ nm and $V_a = 0$ V. Also, when the applied voltage is greater than the built-in potential (i.e. $V_a > V_{bi}$), Eq. 4.1 is no longer valid. Hence, we use the zero-field value, $k_{PPd}(V_{bi})$, for the PP dissociation rate, but add $\delta E = qF_I\left(\sqrt{r_c^2 - a^2\sin^2\theta} - a\cos\theta\right)$ to the binding energy to account for the additional energy needed to separate charge normal to the interface when $F_I > 0$. Here θ is the angle of the PP separation vector relative to the interface normal, $r_C = q^2/4\pi\varepsilon k_B T$ is the Onsager exciton radius,[122] and we average over the half-space, $-\pi/2 < \theta < \pi/2$, of possible PP orientations. With $\varepsilon/\varepsilon_0 = 3$ as in Table 4.1, $r_c \approx 18$ nm >> a_0 and $\delta E \approx qF_I r_C$.

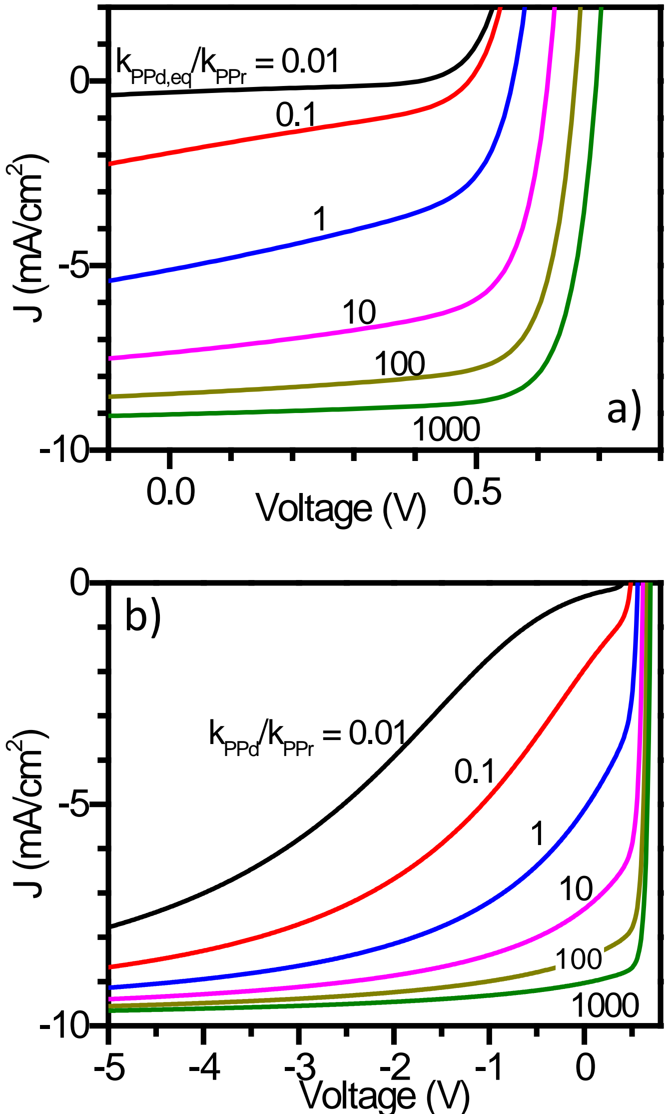

Figure 4.2 – Onsager-Braun Based Polaron Pair Dissociation: (a) Calculated current-density *vs*. voltage (*J*-*V*) characteristics for an organic solar cell according to Eq. 2 in text, with various ratios of the equilibrium polaron pair (PP) dissociation to the recombination rate ($k_{PPd,eq}/k_{PPr}$). (b) The same calculation as in (a) extended to larger reverse bias to emphasize the nonlinear behavior of the O-B process.

Figure 4.2 shows that the shape of the *J*-*V* characteristics and the resulting *FF* are strongly dependent on the recombination rate. In the 4th quadrant (Fig. 4.2(a)), a linear dependence of J_{ph} on V_a was found with the magnitude of the slope dependent on $k_{PPd,eq}/k_{PPr}$. Under these conditions, when $1 < k_{PPd,eq}/k_{PPr} < 100$, the calculated *J*-*V* characteristics following Eq. 4.2 are found to be typical of conventional, planar OPVs. Indeed, this effect has often been

Table 4.1 – Estimated material properties for typical organic: These are the parameters used in the model presented. [a] Model values based on Ref. [79]

Parameter	Value[a]	Definition
d	80 nm	Total thickness of the organic layers
ΔE_{HL}	1.2 eV	Interfacial Energy Gap
V_{bi}	0.8 V	Built-in voltage
$T_{t,A} = T_{t,D}$	1000 K	Characteristic temperature for hole and electron trap distributions in the donor and acceptor
$H_A = H_D$	10^{18} cm^{-3}	Trap densities in the donor and acceptor
$N_{HOMO} = N_{LUMO}$	10^{21} cm^{-3}	Band-edge density of states of the HOMO (donor) and LUMO (acceptor)
δ_A	0.5	Fraction of voltage dropped across the acceptor
a_0	2 nm	Characteristic polaron pair separation
$k_{rec,n} = k_{rec,p} = q\mu/\varepsilon$	$\varepsilon/\varepsilon_0 = 3$, $\mu = 10^{-3}$ cm^2/V-s	Free carrier bimolecular recombination rate
R_s	1 Ω-cm^2	External series resistance
S_{pc}	0.9 mA/V-cm^2	Photoconductance
$\phi_{anode} = \phi_{cathode}$	0.2 eV	Injection barrier at the cathode and anode

explained[132,133] using a parallel resistance (R_p) that serves as a proxy for the underlying physics described by PP dissociation. At higher reverse bias, there is a significant departure from linearity except in the case of very high PP dissociation rates in O-B dominated processes, as shown in Fig. 4.2(b).

In Fig. 4.3(a), we show that the current deviates from a linear dependence on voltage if, in fact, k_{PPd} is determined only by O-B dissociation, as assumed for the analysis in Ref. 78. Additionally, we expect a pronounced temperature dependence in the *J-V* characteristics, since

PP dissociation is a thermally activated process, as also shown in Fig. 4.3(a). In practice, however, OPVs often exhibit a photocurrent, J_{ph} that is linearly dependent on V_a over a large voltage and temperature range, indicating that Onsager-Braun dissociation inadequately describes the observed reverse *J-V* characteristics.

To explain the linear reverse-biased characteristics, we include the effect of direct carrier generation from excitons in the organic semiconductor bulk layers[122,138] by, for example, exciton-assisted polaron detrapping,[139] field-induced barrier lowering,[140] or thermally induced exciton dissociation.[141] Generation of carriers in the bulk can also increase the electron and hole densities, *viz.*: $n=n_0+n_{pc}$ and $p=p_0+p_{pc}$, where n_0 (p_0) is the electron (hole) density in the dark, and n_{pc} (p_{pc}) is the additional photogenerated electron (hole) density. The photocurrent is:

$$J_{pc} = q(n_{pc}\mu_e + p_{pc}\mu_h)F, \tag{4.4}$$

where *F* is the electric field across the layers, and μ_e (μ_h) is the electron (hole) mobility. For sufficiently small carrier densities, Ohmic conduction dominates, in which case the electric field is $F=(V_a-V_{bi})/d$, where the voltage drops across the small internal layer and contact resistances have been ignored. Here, V_{bi} is equal to the offset in anode and cathode contact work functions, and *d* is the sum of the donor- and acceptor-layer thicknesses. This approximation is valid when the applied voltage is more than 0.1 V below V_{bi}, where numerical simulations of the complete device by self-consistently solving the drift-diffusion equations (including PP generation and dissociation into free carriers) indicate that the electric field varies by less than 10% throughout the device. The equilibrium photogenerated electron density is given by $n_{pc}=\eta_{pc}G\tau_e$, with a similar expression for holes. Here, *G* is the exciton generation rate per unit volume, η_{pc} is the photoconductive efficiency given by the fraction of excitons that dissociate

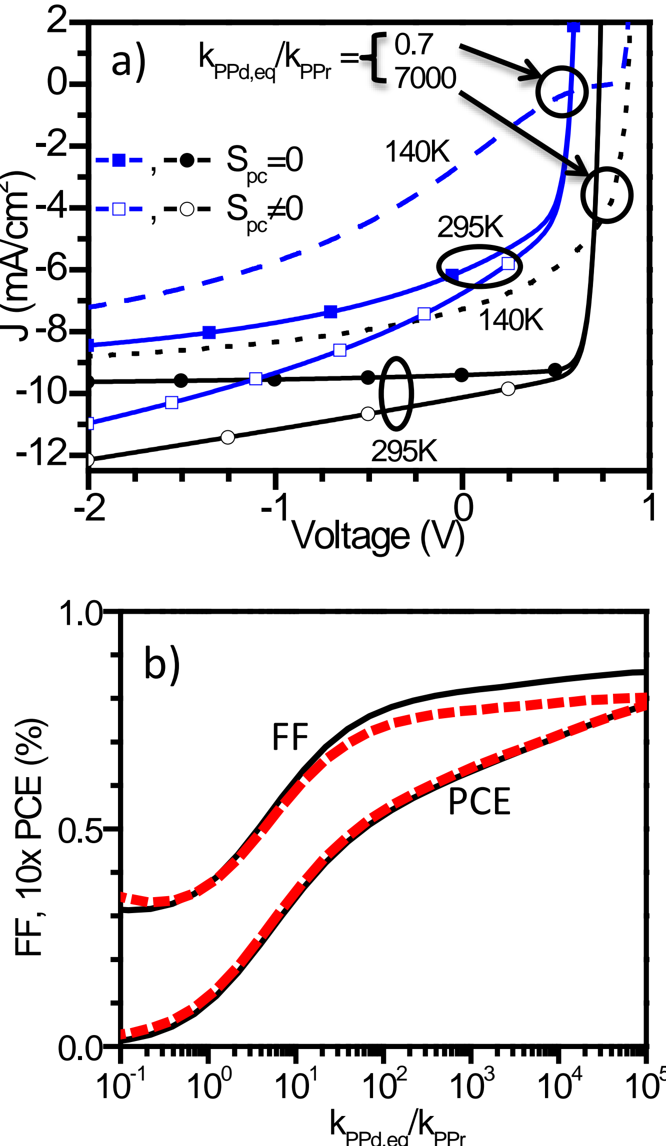

Figure 4.3 – Effect of Photoconductivity: (a) Calculated current-density *vs.* voltage (J-V) characteristics for an organic photovoltaic cell according to Eq. 2 in text, with the ratio of polaron pair (PP) dissociation rate to the PP recombination rate $k_{PPd,eq}/k_{PPr}$ = 7000 (filled circles) and 0.7 (filled squares) at temperature T = 295 K. The same calculation is provided for T = 140K for $k_{PPd,eq}/k_{PPr}$ = 7000 (dotted line) and 0.7 (dashed line). The effect of photoconductivity is shown according to Eq. 6 in text, with S_{pc} = 0.9 mA/V-cm^2 for $k_{PPd,eq}/k_{PPr}$ = 7000(open circles) and 0.7 (open squares). (b) The dependence of the fill-factor and power conversion efficiency on $k_{PPd,eq}/k_{PPr}$, including (dashed lines) and excluding (solid) the effects of photoconductivity.

into free carriers in the bulk, and τ_e (τ_h) is the smaller of the electron (hole) lifetime or transit time. This yields a current of:

$$J_{pc} = q\eta_{pc}G(\tau_e\mu_e + \tau_h\mu_h)(V_a - V_{bi})/d = S_{pc}(V_a - V_{bi}), \tag{4.5}$$

where S_{pc} is the effective photoconductance.

Photoconductivity is a linear process that can result in a corresponding linear slope in the *J-V* characteristic under reverse bias. That is, referring to Fig. 4.1(a), we infer that $R_p = 1/S_{pc}$ when photoconductivity dominates over field-induced PP dissociation (c.f. Eq. 4.1). Photocarrier generation is added to the total photocurrent, $J_{ph} = J_{jxn} + J_{pc}$, yielding a modified ideal diode equation:

$$J = J_{sD}\left\{\exp\left(\frac{qV_a}{n_D k_B T}\right) - \frac{k_{PPd}}{k_{PPd,eq}}\right\} + J_{sA}\left\{\exp\left(\frac{qV_a}{n_A k_B T}\right) - \frac{k_{PPd}}{k_{PPd,eq}}\right\} - J_{jxn} + S_{pc}(V_a - JR_s - V_{bi}). \tag{4.6}$$

In Fig. 4.3(a) we plot *J vs. V* according to Eq. 4.6, with S_{pc} = 0.9 mA/V-cm^2 for both $k_{PPd,eq}/k_{PPr}$ = 0.7 and 7000. Omitting the effects of photoconductivity, k_{PPr} is overestimated to fit the voltage dependence of J_{ph}. Figures 4.2 and 4.3(a) show that J_{jxn} has a nonlinear voltage dependence consistent with the O-B process. In contrast, J_{ph} is linear, as consistent with its photoconductive origin. Including photoconductivity results in a reduced estimate for k_{PPr} inferred from the 4th quadrant *J-V* characteristics, leading to a saturation in J_{jxn} even at low fields (open circles, Fig. 4.3(a)).

In Fig 4.3(b), we calculate *FF* and power conversion efficiency (*PCE*) as functions of $k_{PPd,eq}/k_{PPr}$, both including (dashed) and excluding (solid) the effects of photoconductive charge

generation in the layer bulks. In both cases, FF saturates for $k_{PPd,eq}/k_{PPr}$ > 100 due to efficient PP dissociation and saturation of J_{jxn}. The reduced FF in the presence of photoconductivity is due to the increased J_{sc}; however PCE is not affected since J_{pc} is negligible at the OPV maximum power point (i.e. $MPPT=J_m V_m$, where J_m is the current density at $MPPT$) of operation.

4.3. Experiment

Organic photovoltaic devices were fabricated on 1500 Å thick indium tin oxide (ITO) films patterned into 1 mm wide stripes on a glass substrate. The ITO surface was prepared by solvent cleaning, followed by 10 min exposure to UV-ozone to lower its work function.[142] Prior to use, donor and acceptor source materials were purified once by vacuum thermal-gradient sublimation. The substrate was loaded into a high vacuum thermal evaporator (base pressure < 2×10^{-7} Torr) to deposit the organic layers. Following organic layer deposition, the cathode was patterned by deposition of Ag through a shadow mask with 1 mm wide stripes, and positioned on the film surface inside a glove box filled with ultrahigh purity N_2 to prevent exposure to air during sample preparation. Devices were fabricated with the structure: ITO/boron subphthalocyanine chloride (SubPc) (130 Å)/C_{60} (400 Å)/bathocuproine (BCP) (80 Å)/Ag (1000 Å). A planar device architecture was chosen for this study because it offers a simple geometry for modeling the device. Here, BCP was employed as an exciton blocking layer and optical spacer to improve device efficiency. Layer thicknesses were chosen to yield high efficiency devices. Devices were characterized at various light intensities using illumination from a solar simulator filtered to approximate an AM1.5G spectrum. The temperature-dependent J-V characteristics in the dark and under illumination were obtained using a liquid N_2 cryostat and a 1000 W Oriel solar simulator.

Single layer, photoconductor devices were similarly fabricated, but with the structure: ITO (1500 Å)/SubPc (600 Å)/Ag (1000 Å) and ITO (1500 Å)/C60 (600 Å)/Ag (1000 Å). This architecture was chosen to remove the D/A HJ and enable the direct measurement of photocurrent generated in the bulk of the organic films. The organic layer thickness was chosen to be similar to that used in the OPV devices. Synchronous measurements using a lock-in amplifier in conjunction with incident light from a 100 mW/cm^2 solar simulator, an Argon laser at a wavelength of λ=514 nm, and a diode laser at λ=409 nm chopped at 200 Hz were used for voltage-dependent photocurrent measurements. Speed of response measurements were performed using a 1 ns pulse width, 5 nJ pulsed nitrogen laser at λ=337 nm.

4.4. Results

Figure 4.4 shows the *J-V* characteristics of a SubPc/C_{60} OPV as a function of illumination intensity. There is a linear response of J_{ph} with voltage at $V_a < 0.5$ V. The photocurrent *vs*. light intensity has a slope of m = 15.7 ± 0.6 μA/mW-V and intercept of $S_{pc,0}$ = 0.6 ± 0. 5 μA/V-cm^2 (inset, Fig. 4.4). Figure 4.4(b) shows the linear behavior of the illuminated *J-V* characteristic over a large range of reverse bias. The maximum reverse voltage applied is limited by dielectric breakdown of the organic layers. Figure 4.5 shows the *J-V* characteristics at 1-sun illumination as a function of temperature. Here, S_{pc} has a weak temperature dependence; at 100 mW/cm^2 it decreases from 1.25 ± 0.01 mA/V-cm^2 at T = 300 K, and saturates to 1.11 ± 0.01 mA/V-cm^2 at 217 K. We also studied photoconductor devices to quantitatively understand the origin and magnitude of S_{pc}. Figure 4.6 shows the voltage and light intensity-dependent photocurrent for an ITO/SubPc/Ag photoconductor illuminated using a solar simulator. We find that V_{bi} = 0.8 V, indicated by the voltage where $J_{ph} = 0$, due to the difference in work functions of ITO (5.1 eV)

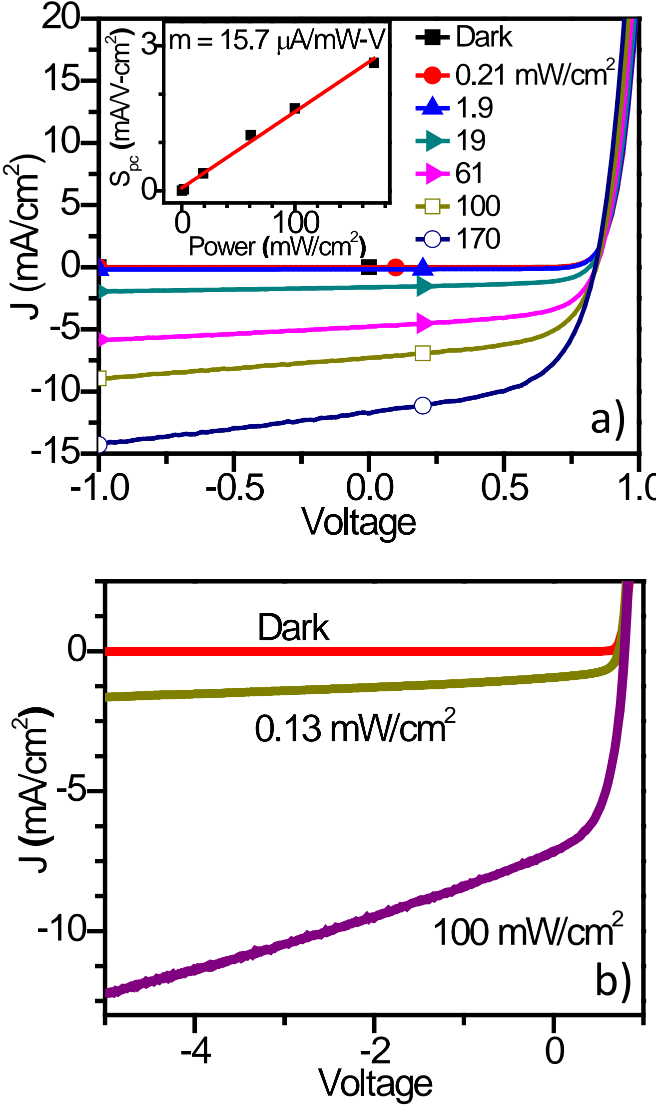

Figure 4.4 – Voltage Dependent Photocurrent: (a) Current density *vs.* voltage (*J*-*V*) characteristics of an ITO (1500 Å)/SubPc (130 Å)/C_{60} (400 Å)/BCP (80 Å)/Ag (1000 Å) organic photovoltaic cell at various AM 1.5G spectral illumination intensities from a solar simulator. The photoconductance is determined by the linear slope at reverse bias, and is plotted in the inset as a function of incident power. The fit shows a linear photoconductive response of 15.7 ± 0.6 μA/mW-V. (b) The linear voltage dependence of the photocurrent is shown over an extended voltage range.

and Ag (4.3 eV). As expected for a photoconductor, J_{ph} shows a linear dependence on applied bias and light intensity. Here, S_{pc} = 0.40 ± 0.04 mA/cm^2-V at a light intensity of 66 mW/cm^2 simulated AM1.5G spectrum. The response increases with light intensity, with a slope of m =

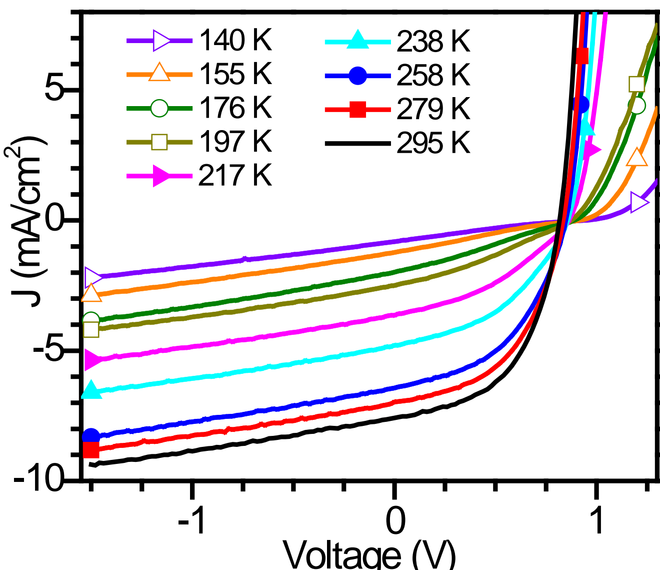

Figure 4.5 – Temperature Dependence of Bilayer OPVs: Temperature dependence of the current density vs voltage (*J*-*V*) characteristics of an ITO (1500 Å)/SubPc (130 Å)/C_{60} (400 Å)/BCP (80 Å)/Ag (1000 Å) organic photovoltaic cell. The photoconductance (S_{pc}), as apparent in the slope of the reverse biased characteristic, is almost independent of temperature, and ranges from 1.25-1.1 mA/V-cm^2.

5.7 ± 0.2 μA/mW-V and intercept of $S_{pc,0}$ = 0.01 ± 0.01 mA/V-cm^2 as shown in the inset, Fig. 4.6. Measurements of an ITO/C_{60}/Ag device shows a similar linear response, with a S_{pc} = 0.82 ± 0.05 mA/cm^2-V at 100 mW/cm^2. We observed a weak temperature dependence of photoconductivity in the Ag/C_{60}/Ag device over the range 140 K < T < 295 K, with an activation energy of ΔE_{pc}=15 ± 3 meV. This behavior is similar to that of S_{pc} for the OPV, where ΔE_{pc}= 6.8 ± 0.7 meV.

4.5. Discussion

The linear dependence of the illuminated *J*-*V* characteristics over a large reverse bias and temperature range indicates that photoconductivity plays a significant role in bilayer OPVs. In contrast, the photocurrent in excitonic BHJs often has a non-linear reverse-biased voltage dependence,[84,143] particularly near 0V. This suggests that field-induced dissociation of PPs, or

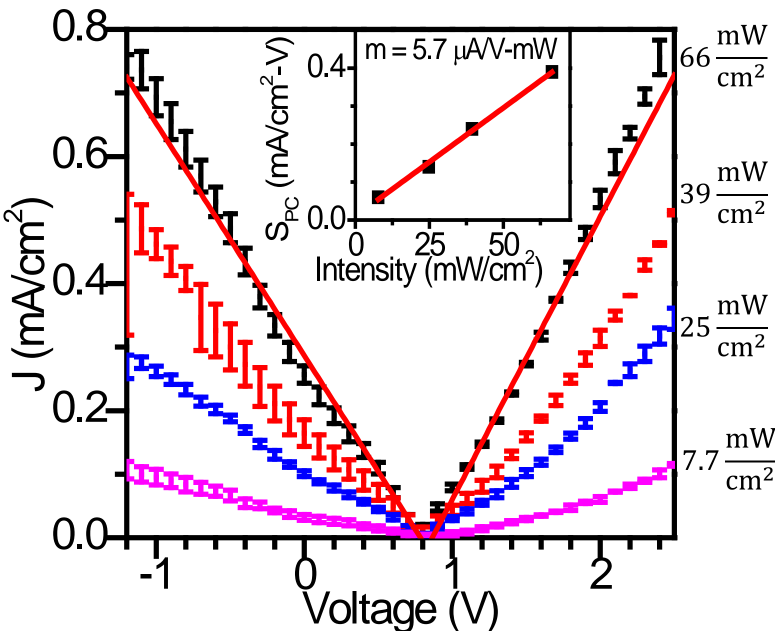

Figure 4.6 - SubPc Photoconductance: Photocurrent density *vs.* voltage characteristics of an ITO (1500 Å)/SubPc (600 Å)/Ag (1000 Å) photoconductor measured by synchronous illumination from a solar simulator. The inset shows that the photoconductance has a linear response with incident power of 5.7 ± 0.2 μA/mW-V, similar in magnitude to the photoconductive effects of the OPV devices in Fig. 5.

bimolecular recombination may dominate the photocurrent characteristics in those cases where charge trapping among the high density of bottlenecks and cul de sacs found in BHJs strongly influences transport and series resisitance.[85] In the case of bilayer HJs, however, there are large regions of homogenous composition through which excitons must diffuse to arrive at a HJ to dissociate. This provides ample opportunity for excitons to first encounter a trap site, a high energy phonon, or defect that enables bulk dissociation resulting in free carrier generation. Hence, while we expect that photoconductivity will be less prevalent in BHJ nanomorphologies compared with bilayer planar HJs studied here, the process itself is of a fundamental origin and hence is anticipated to be present although not necessarily the dominant source of reverse-biased slope. Indeed, such a linear dependence even in polymer BHJs has been observed although it remains an open issue whether its source is of photoconductive origin.[144]

As apparent in this work, photoconductivity in bilayer HJs can potentially mask the effects of thermally-activated and field-dependent PP exciton dissociation at the interface (J_{jxn}) as predicted by O-B in Eq. 4.1. This linear behavior begins when $V_a \approx V_{bi}$-0.5V, suggesting $k_{PPd} >> k_{PPr}$ and very inefficient PP back transfer in SubPc/C_{60} heterojunctions, consistent with previous results.[79] Hence, J_{jxn} reaches a maximum (i.e. saturation) at relatively small electric fields (~10^4-10^5 V/cm). Indeed, in Fig. 4.3(a) we show that in the case of $k_{PPd}/k_{PPr} >> 1$, photoconductance can account for almost all of the observed linearity of J under reverse bias. In Fig. 4.4(b), we observe that the linearity of J_{ph} extends to $V_a < -5$ V, supporting that photoconductivity dominates the reverse bias J_{ph}.

The temperature-dependent J-V characteristics indicate that J_{jxn} is thermally activated due to the temperature dependence of both J_x and the PP dissociation efficiency, $\eta = k_{PPd}./(k_{PPd} + k_{PPr})$. Exciton diffusion lengths have been shown to be temperature dependent;[145,146] this generates an increased J_x and a voltage independent increase in J_{ph} at high temperature. This is the dominant effect observed in Fig. 4.5. The temperature dependence of η is observed at $V_a >$ 0.5 V where the J-V characteristic develops an 'S-kink' when k_{PPd} is reduced with temperature.[78] This is qualitatively similar to the reduction in current at low temperature shown in Fig. 4.3(a), although J_{jxn} reaches saturation at a lower reverse bias than predicted by the O-B model.

From Eq. 4.1, an equilibrium PP dissociation rate of $k_{PPd,eq}^{-1} = 50$ ns is obtained for $a_0 =$ 2 nm. Since it is the *ratio* of $k_{PPd,eq}/k_{PPr}$ that determines J_{jxn} in Figs. 4.2 and 4.3, we infer that $k_{PPd,eq}/k_{PPr} > 10^2$ (i.e. $k_{PPr}^{-1} > 5\mu s$) required for J_{jxn} to saturate and photoconductivity to dominate the voltage dependence of J_{ph} as in Fig. 4.3(a). Now, the PP lifetime, given by $\tau_{PP} = (k_{PPd}+k_{PPr})^{-1} \approx k_{PPd}^{-1}$, must be shorter than the device response time of approximately 1 ns.[147]

However, $k_{PPd,eq}^{-1}$ = 50 ns predicted by the O-B theory is at least 50 times *larger* than the measured device response time. To correct for this discrepancy both k_{PPd} and k_{PPr} must be scaled by the same factor to maintain the same *J-V* characteristics, according to Fig. 4.2. Hence, we infer that k_{PPr}^{-1} > 100 ns to be consistent with the lower value of $k_{ppd,eq}^{-1}$, and hence the linearity of the reverse *J-V* characteristics is not explained by the PP recombination dynamics in this case.

Figure 4.3(b) shows the dependence of *FF* on $k_{PPd,eq}/k_{PPr}$ in the presence (dashed line) and absence of photoconductivity (solid line). Here, *FF* reaches saturation for $k_{PPd,eq}/k_{PPr} > 100$, where PP back transfer or recombination across the HJ is minimal. Thus, for a physically reasonable $k_{PPd,eq}^{-1}$ = 1 ns, we require that k_{PPr}^{-1} > 100 ns to yield a *FF* > 0.7. This value of k_{PPr} is consistent with the rate measured from the phase change observed by intensity modulated photocurrent spectroscopy of similar SubPc/C_{60} HJ OPV devices.[79] Including the contributions of photoconductance of S_{pc} = 0.9 mA/V-cm^2, the maximum *FF* obtained for a practical D-A HJ with $k_{PPd,eq}/k_{PPr} > 100$ is reduced by approximately 10% due to an increase in J_{sc} (dashed line, Fig. 3b). However, the *PCE* of the OPV with and without the presence of photoconductivity is unchanged at the maximum power point, which is close to $V_a = V_{bi}$, where $J_{pc} \to 0$. Note, however, that the PCE can be increased due to photoconductance if the OPV is operated at voltages less than that corresponding to its value (V_m) at the *MPP*.

The effect of photoconductance on the OPV can be understood by identifying the contributions of J_{jxn} and J_{pc} to the *J-V* characteristics. Using data from the photoconductor devices as in Fig. 4.6, we can simulate J_{pc} by first rewriting Eq. 4.5 as:

$$\frac{J_{pc}d}{qG(V_a - V_{bi})} = \eta_{pc}(\tau_e\mu_e + \tau_h\mu_h) = \frac{S_{pc}d}{qG} \equiv \eta_{pc}\tau\mu, \qquad (4.7)$$

where $\tau\mu = (\tau_e\mu_e + \tau_h\mu_h)$. Now, $\eta_{pc}\tau\mu$ characterizes the photoconductive sensitivity of the layers comprising the OPV. We determine $\eta_{pc}\tau\mu$ from the photoconductor device data for both the donor and acceptor, using an optical model that includes optical interference effects to calculate the local, wavelength-dependent exciton generation rate, $G(x,\lambda)$,[75] in the organic layers. The calculation employs the measured (by spectroscopic ellipsometry) wavelength-dependent complex refractive indicies, $\tilde{n} = n + ik$. Integrating over the total active layer thickness and at all wavelengths measured, we obtain $\eta_{pc}\tau\mu$ = (2.2 ± 0.3)x10^{-7} cm^2/V for SubPc, and (4.0 ± 0.2)x10^{-7} cm^2/V for C_{60}. We next use $\eta_{pc}\tau\mu$ to determine the carrier generation in each layer to calculate the S_{pc} = 0.90 ± 0.07 mA/V-cm^2 for the OPV. Here, we fit the dark current to Eq. 4.2 with $J_{jxn} = 0$, and obtain J_{sA} = (1.0 ± 0.8)x10^{-9} mA/cm^2, J_{sD} = (4.7 ± 1.6)x10^{-5} mA/cm^2, R_S = 3.7 ± 0.5 Ω-cm^2, and ideality factors of n_A = 1.6 ± 0.1, and n_D = 5.9 ± 0.7. These parameters, along with the calculated photoconductive response assuming V_{bi} = 0.8 V then provide a simulation of the illuminated *J-V* data. To highlight the relative importance of J_{pc} *vs*. J_{jxn}, in Fig. 4.7 we plot the experimental data (symbols) *vs*. the calculated *J-V* characteristics with (solid line) and without photoconductance (dashed line) assuming $k_{PPr} \rightarrow 0$, and $J_{jxn} = qJ_X$ = 5.8 mA/cm^2. Excluding photoconductance, we identify the photocurrent generated only by dissociation of PPs at the heterojunction (dashed line). By including the additional current due to photoconductivity, the simulation and the device data under illumination are in agreement over the entire range of data fit, indicating efficient PP dissociation and the importance of photoconductivity in these archetype OPV structures.

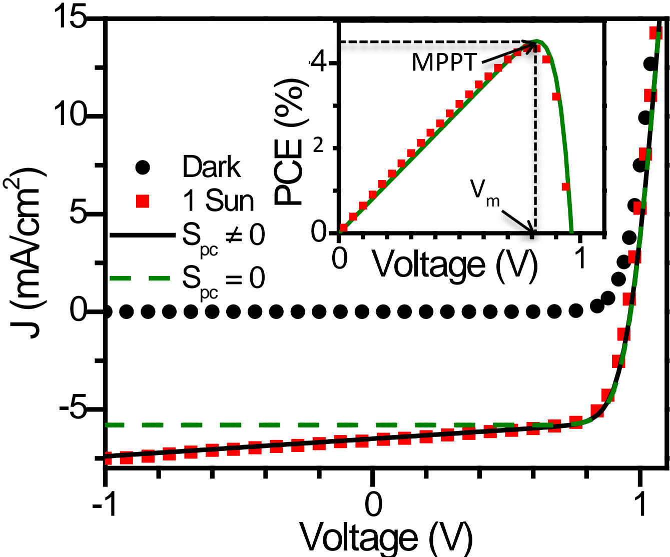

Figure 4.7 – Simulated J-V: Current density *vs.* voltage characteristic (*J-V*) of an ITO (1500 Å)/SubPc (130 Å)/C_{60} (400 Å)/BCP (80 Å)/Ag (1000 Å) organic photovoltaic cell in the dark (black squares) and at 1 sun intensity simulated solar illumination (red circles). Simulated current calculated using Eq. 6 (solid line) with a constant photocurrent and photoconductance of Spc = 0.9 mA/cm^2-V for OPV. Simulated current given by Eq. 2 with a constant photcurrent and no photoconductance (green dashed line). Inset: Power conversion efficiency (PCE) under 1 sun, AM1.5G illumination *vs.* voltage for the simulated (line) and experimental (squares) data.

The presence of photoconductance results in an increase in J_{sc} by 15% in the SubPc/C_{60} devices. The *PCE vs V* is plotted in the inset of Fig. 4.7, and shows that photoconductivity can result in an increase in power generation over much of the 4th quadrant of the *J-V* characteristic. As noted above, however, the presence of photoconductivity cannot increase the $PCE = 4.4 \pm 0.1\%$ at the *MPPT* corresponding to $V_m=0.82 \pm 0.01$ V. The presence of photoconductivity in the active layers, however, does limit the maximum attainable fill factor to:

$$FF_{max} = 1 - \frac{S_{pc}}{J_{sc}} V_{oc}, \tag{4.8}$$

which corresponds to FF_{max}=0.79 for a SubPc/C_{60} HJ OPV. The *FF* is further limited by the diode ideality (Eq. 4.6) based on the ratio of $k_{PPd,eq}/k_{PPr}$, as shown in Fig. 4.3(b).

4.6. Conclusion

In conclusion we have shown that the parallel resistance commonly observed in the J-V characteristics of organic heterojunction devices is due to exciton generation followed by dissociation in the bulk of the constituent donor and acceptor layers. Photoconductivity in the organic layers describes the observed linear increase in current under reverse bias, the temperature dependence and the magnitude of the measured R_p. Since photoconductivity accurately describes the observed linear dependence of J_{ph} on V_a, the junction photocurrent $J_{jxn} = \eta q J_X$ is found to saturate to qJ_x when V_a is only a few hundred millivolts less than V_{OC}. This suggests that the polaron pair dissociation efficiency is large, indicating that $k_{PPr}^{-1} > 100\ k_{PPd,eq}^{-1}$. While photoconductance adds to the short circuit current density, it also leads to a reduced maximum fill factor, and hence imposes a constraint on the maximum power conversion efficiency when photoconductivity is significant in OPVs.

Chapter 5

Excited State and Charge Dynamics of Hybrid Organic/Inorganic Heterojunctions: Theory

5.1. Background

The classical description of inorganic semiconductors based on charge recombination at, and diffusion to p-n junctions has resulted in the so-called "ideal diode", or Shockley equation[148] that, with many subsequent extensions and modifications, has served as the foundation of semiconductor device physics over the past six decades. More recently, Giebink, et al. have extended this analysis to include excitonic semiconductors,[78,79] a large and important class of materials exemplified by organic materials now achieving widespread use in a range of electronic and optical applications.[149] The differences in properties between organic and inorganic semiconductors, that ultimately originate from their vastly different bond energies (i.e. organics are bonded by weak van der Waals forces whereas inorganic semiconductors are bonded by a combination of covalent and ionic forces) requires a significantly different physical description. For example, inorganic semiconductors are characterized by their hardness, ready

formation of crystalline structures, a high charge mobility (μ~10-10,000 cm^2/V-s) and dielectric constant (ε_r~10-100), and the ability to be doped to increase conductivity by several orders of magnitude.[38] In contrast, excitonic materials tend to be relatively soft forming a range of crystalline, nanocrystalline and amorphous morphologies, low mobility[64,150] (μ~10^{-6}-5 cm^2/V-s) and dielectric constant[151] (ε_r~1.5-4), and their relative inability to achieve high conductivities through the introduction of extrinsic dopants.[152,153] Furthermore, the low carrier mobilities of organic materials results in charge self-trapping, thereby generating high effective mass "polarons",[122] whereas the low effective mass of inorganics leads to extensive delocalization of charge.[24] Hence, the dynamics of excitons (i.e. excited states) and charges demand a different physical description than that developed by Shockley.

Intermediate between pure excitonic and inorganic semiconductors is the combination of these two materials, forming a hybrid organic/inorganic heterojunction (OI-HJ) at their point of contact. Indeed, many promising technologies employ OI-HJ's as their charge-separating interface, including sensitive OI photodiodes[154] and solar cells,[155,156] dye-sensitized solar cells (DSSCs),[157,158] colloidal quantum dot solar cells and light emitting devices,[159,160,161] and nanoparticle/organic solar cells.[162] Furthermore, there have been numerous recent studies of hybrid polaritons and other structures that have potential for use in lasers and in the study of non-linear optical phenomena such as hybrid polaritons in optical microcavities.[163,164,165] Finally, metal oxide semiconductor-organic thin film heterojunctions are finding widespread application in high intensity, stacked organic light emitting devices (OLEDs) and tandem organic photovoltaic (OPV) cells, and hence their detailed characterization is essential for their optimization for these device applications.[166,167,168]

While there have been many examples of devices that exploit OI-HJs, a comprehensive understanding of their influence on charge generation, recombination and extraction has yet to be developed. Previous models have primarily relied on an "equivalent circuit" description of the HJs to model their current density vs. voltage (*J-V*) characteristics, both in the dark and under illumination.[169,170] These models have variously considered the organic-inorganic contacts to be equivalent to Schottky-type metal-semiconductor junctions[155,171] or more accurately as HJs,[169,172,173] give a reasonable phenomenological description of the observed characteristics, they fail to provide a fundamental physical understanding of the dynamics of hybrid state formation and dissociation that governs the properties of the OI-HJ.

In this work, we derive a first-principles physical model that describes the dynamics of charge and excited state transport to the interface of a hybrid OI-HJ. The model is based on the photo- or thermal generation of charge in the inorganic semiconductor and Frenkel excitons in the organic layer that migrate to the interface where an unstable hybrid charge transfer exciton (HCTE), analogous to a polaron-pair state at an excitonic junction, rapidly dissociates into free charges. We consider the behavior of this dynamical system both in the presence and absence of interface traps. The model is developed for an example n-P anisotype Type II staggered[38] OI-HJ. Here, the lower case "n" refers to the majority carrier type of the inorganic semiconductor, and the upper case "P" refers to the relative position of the Fermi energy/highest occupied molecular orbital or HOMO, of the organic semiconductor relative to that of the inorganic material. As is often the case, the organic material is assumed to be undoped. The junctions are dominated by interface recombination at low current and by carrier transport properties of the contacting semiconductors at higher currents. The model is general, in that it can be easily modified for application to isotype junctions (e.g. n-N and p-P) as well as to Type I (nested) HJ energy level

offsets. These generalizations are treated in Appendix A. The model is based on the existence of the HCTE state bound at the interface that subsequently dissociates into free carriers that are collected at external (ohmic) contacts. The analysis leads to a rigorous description of the *J*-*V* characteristics of the hybrid structure, both in the dark and under illumination. At low currents (corresponding to reverse bias or at small forward voltage), we observe ideal diode behavior reminiscent of both Shockley p-n and excitonic junctions. At high currents, the diode characteristics are dominated by space-charge effects due to transport through the low mobility organic semiconductor, as previously observed by Forrest, *et al.*[155,169,170]

While the model reduces to an analytical form at low current densities, its evaluation at high *J* (i.e. under significant departures from equilibrium under forward bias) requires numerical solution. In the companion Chapter 6, we apply the model to the specific cases of hybrid devices utilizing a thin-film inorganic TiO_2 layer that is relevant[174] to DSSCs, and InP that is useful in solar cells and photodetectors. [12,156] The HJ between an inorganic metal-oxide and an organic semiconductor also plays an important role as a charge generation layer in OLEDs, and as a buffer layer for hole extraction in OPVs.[166,167,175]

This chapter is organized as follows: The theory of OI-HJs is described in Sect. 5.2. Specifically, Sect. 5.2.1 details the physical processes that occur at the OI heterointerface under near-equilibrium (i.e. low voltage and current) conditions. The dynamics of charge carriers and HCT exciton states[170] are included in the current model describing an “ideal” n-P junction. We intentionally exclude the effects of charge extraction barriers, injection barriers or bulk recombination that can be included into the model using procedures analogous to those employed to describe non-idealities in inorganic and excitonic junctions. Section 5.2.2 combines calculations of the electric field distribution with interfacial charge recombination to obtain the

charge density and voltage distribution across the contacting layers under non-equilibrium (i.e. high voltage and current) conditions. Section 5.3 applies these results to an example pentacene/n-Si OI-HJ, and details its implications on power generation in OI-HJs used in solar electricity generation. Conclusions are presented in Section 5.4. In the Appendix A, we extend the model to several different OI-HJs where both carrier type and relative energy level offset arrangements are different from the archetype n-P OI-HJ that is the subject of this chapter. In Chapter 6, we apply the model to a TiO_2 / tetraphenyldibenzoperiflanthene (DBP) OI device to test its validity under illumination, in the dark, and as a function of temperature.

5.2. Theory of Conduction for Organic/Inorganic Heterojunctions

The physical distinction between an OI-HJ and that of either inorganic or excitonic junctions is the formation of the HCTE state at the organic-inorganic interface that is the quasi-particle intermediate between free charge and the photogenerated state in either of the contacting materials. In considering the processes leading to dark and photocurrent generation, therefore, the physical properties of the HCTE and its recombination kinetics must be considered. We, therefore, divide this section into a discussion on near- (or quasi-) equilibrium conditions where the stability of the HCTE at the HJ determines the rate at which photocarriers are generated, and on non-equilibrium conditions where charge mobility and other bulk thin film processes dominate.

5.2.1. Current Conduction Under Quasi-equilibrium Conditions

In Fig. 5.1(a) we show the simple case of an n-P OI-HJ in the absence of interface defects or traps. In neglecting deep traps, we ignore loss due to minority carrier recombination which is equivalent to assuming defect states at the inorganic surface are inactive or non-existent. Indeed,

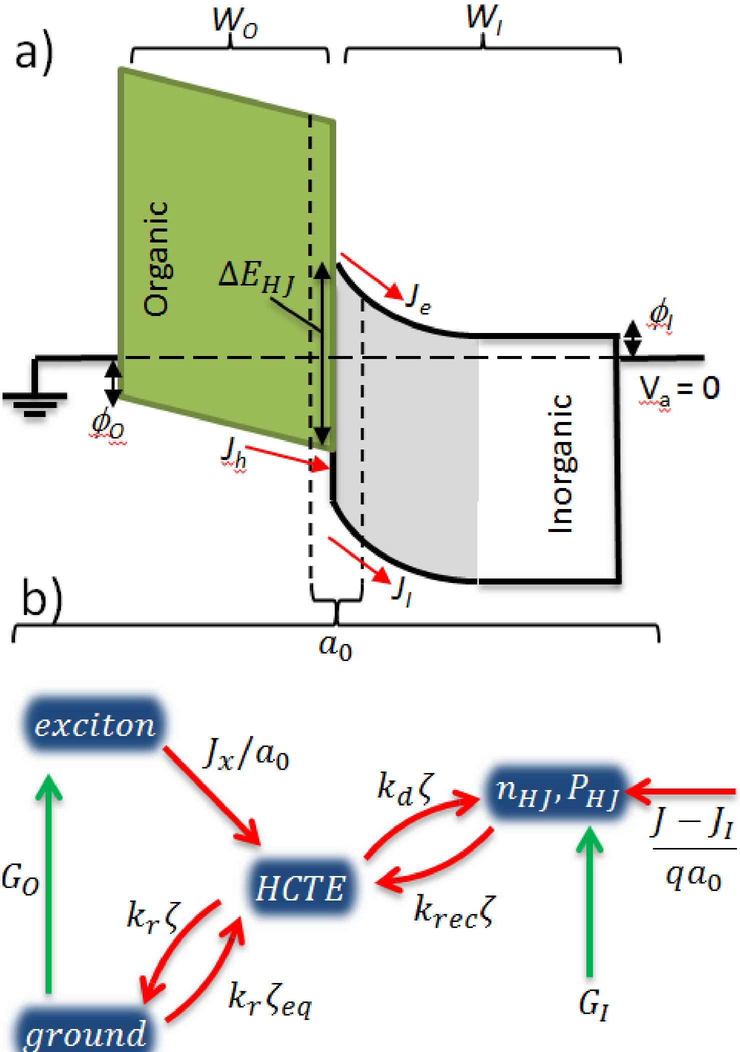

Figure 5.1 – Hybrid Organic/Inorganic Model: (a) Equilibrium energy level diagram for a hybrid organic/inorganic n-P heterojunction. The depletion region formed in the inorganic is indicated in gray and has a width of W_I. The Fermi level in the inorganic is at ϕ_I below the conduction band edge. The organic layer thickness is W_O, and ϕ_O is the barrier for injecting holes into the organic highest occupied molecular orbital from the anode. The interface energy gap is ΔE_{HJ}. Charge generation and recombination at the interface occurs in a region of width, a_0, around the interface according to the state diagram (b). Excitons from the organic dissociate at a rate J_X/a_0 to form hybrid charge transfer excition states (HCTEs). The HCTE recombines and dissociates at rates k_r and k_d, respectively. Carriers at the interface (n_{HJ} electrons in the inorganic and P_{HJ} holes in the organic) recombine to form HCTEs and are populated by current flowing to the interface. Minority carriers generated in the inorganic are extracted through the organic and populate P_{HJ} at a rate J_I/qa_0. Here, J_I is the current density from holes that are photogenerated in the inorganic and subsequently extracted through the organic. J_e is the electron current density in the inorganic and $J_h = J$ is the hole current density flowing in the organic.

it has been shown that, in some cases, the presence of the organic layer can passivate the inorganic surface.[156,176,177] Nevertheless, there is also ample evidence that in other cases, interface states play a dominant role in determining the photoresponse[156] of the OI-HJ. Hence, this latter case will also be considered in this section.

Photocarrier generation can occur via two mechanisms: (i) direct band-to-band absorption of a photon in the inorganic semiconductor that results in minority carrier diffusion to the OI-HJ with an interface energy gap of ΔE_{OI} (see Fig. 5.1(a)), or (ii) photon absorption in the organic leading to exciton generation and diffusion to the junction (with an exciton current of J_X). In either case, once the photoexcited species migrates to the HJ, a HCTE state forms by Coulomb attraction across the interface. The HCTE is a generally unstable precursor to bimolecular recombination to the ground state or, alternatively, to dissociation by generating free charge at the OI heterojunction (n_{HJ}, P_{HJ}) in the inorganic and organic layers, respectively. Figure 5.1(b) shows the interface state diagram for the processes leading to charge generation. The free carriers, n_{HJ} and P_{HJ} are captured at a rate of $k_{rec}n_{HJ}P_{HJ}$ to form HCTEs with a density, ζ, and with a characteristic diameter between the electron and polaron, $\langle a \rangle$, across the interface, thereby defining the "active interfacial volume". The corresponding rate equations for ζ, n_{HJ}, and P_{HJ} as functions of time, t, are given by:

$$\frac{d}{dt}\zeta = -k_r(\zeta - \zeta_{eq}) - k_d\zeta + k_{rec}n_{HJ}P_{HJ} + \frac{J_X}{\langle a \rangle} = 0, \tag{5.1}$$

$$\frac{d}{dt}n_{HJ} = -k_{rec}n_{HJ}P_{HJ} + k_d\zeta + \frac{J_e}{q\langle a \rangle} = 0, \tag{5.2}$$

and

$$\frac{d}{dt}P_I = -k_{rec}n_{HJ}P_{HJ} + k_d\zeta + \frac{J_h - J_I}{q\langle a\rangle} = 0, \tag{5.3}$$

where the final equality holds for steady-state conditions. Here k_r and k_d are the rates that HCTEs recombine to the ground state and dissociate into free carriers, respectively. The thermal generation rate of HCTEs is $k_r\zeta_{eq}$, where ζ_{eq} is their equilibrium density given by $\zeta_{eq} = k_{rec}n_{HJ,eq}P_{HJ,eq}/k_{d,eq}$. Equilibrium corresponds to an external voltage, $V_a = 0$ in the absence of illumination. Tables 5.1 and 5.2 provide definitions of all major variables used.

Minority carriers photogenerated in the inorganic must be extracted through the organic layer, and these carriers populate P_{HJ} at a rate J_I. Also, J_e and J_h are the electron current in the inorganic and the hole current in the organic, respectively. Typically in organic materials, the large bandgap and significant asymmetries in the mobilities of electrons and holes suggests that the current is primarily carried by only one charge species. In our case, we assume that the hole density and mobility are much greater than the electron density and mobility in the organic, and hence $J_h \equiv J$, although this theory is easily modified for an electron current in the organic that is comparable to or greater than, J_h. Continuity demands that $\nabla \cdot J = 0$ everywhere in steady-state. At the interface, this implies that $J_e + J_I = J_h \equiv J$. Hence, Eqs. (5.2) and (5.3) are identical, resulting in perfect coupling between n_{HJ} and P_{HJ}.

In steady-state, the rate equations can be solved to eliminate ζ so that the current is given by:

$$J = qa_0k_{rec}(1-\eta_d)\left(n_{HJ}P_{HJ} - \frac{k_d}{k_{d,eq}}n_{HJ,eq}P_{HJ,eq}\right) - J_{ph}, \tag{5.4}$$

Table 5.1 – Definition of variables used

Variable		Definition	Units
Organic	Inorganic	**Layer Properties**	
P_{HJ}	n_{HJ}	Carrier density at the OI interface	cm^{-3}
P_c	n_c	Carrier density at the contact	cm^{-3}
V_O	V_I	Voltage across each layer	V
δ_O	δ_I	Fraction of voltage dropped across each layer	-
qJ_X	J_I	Photocurrent generated by each layer	A/cm^2
W_O	W_I	Active layer thickness	cm
ϕ_O	ϕ_I	Injection barrier at the contacts	eV
Q_O	Q_I	Net space-charge accumulated (or depleted)	cm^{-2}
$E_{f,p}$	$E_{f,n}$	Quasi-Fermi level for holes and electrons	eV
a_O	a_I	Width of HCTE in each layer	cm
		Interface Properties	
$\langle a \rangle$		Characteristic width of HCTE at the OI interface	cm
$\langle \varepsilon_r \rangle$		HCTE effective dielectric constant	-
ζ		HCTE density	cm^{-3}
E_B		HCTE binding energy	eV
ΔE_{OI}		Interface energy gap at the OI heterojunction	eV
η		HCTE dissociation efficiency	-
k_r, k_d		HCTE recombination and dissociation rate	s^{-1}
k_{rec}		Bimolecular recombination rate	$cm^3 \cdot s^{-1}$
V_a $[V_{bi}]$		Applied [built-in] voltage	V

Table 5.2 – Table of parameters used in model OI-HJ calculations

Organic [Inorganic]	Definition	Value	Units
ε_O [ε_I]	Relative dielectric permittivity	4 [11.9]	-
μ_O [μ_I]	Hole [electron] mobility	10^{-4} [1500]	cm^2/Vs
$E_{g,O}$ [$E_{g,I}$]	Bandgap energy	2.1 [1.12]	eV
E_{LUMO} [E_c]	Electron affinity	2.8 [4.05]	eV
E_{HOMO} [E_v]	Ionization energy	4.9 [5.17]	eV
N_{HOMO} [N_v]	HOMO [valence band] effective DOS	10^{21} [9.8×10^{18}]	cm^{-3}
N_{LUMO} [N_c]	LUMO [conduction band] effective DOS	10^{21} [2.8×10^{19}]	cm^{-3}
P_D [N_D]	Doped carrier density	10^{14} [10^{16}]	cm^{-3}
H_O [H_I]	Characteristic trap density	10^{18} [10^{18}]	cm^{-3}
$T_{t,O}$ [$T_{t,I}$]	Characteristic trap temperature	600 [2000]	cm^{-3}
W_O [W_I]	Active layer thickness	20 [1000]	nm
ϕ_O [ϕ_I]	Injection barrier into the organic [inorganic]	0.2 [0.2]	eV
a_O [a_I]	Radius of the HCTE in the organic [inorganic]	1 [6]	nm
m^*	HCTE effective mass	$0.19m_0$	kg
k_r	HCTE recombination rate	10^9	s^{-1}

where $J_{ph} = qJ_X\eta_d - J_I$ is the total photocurrent which is the sum of the exciton current generated in the organic and the direct carrier generation current in the inorganic. Here, J_I <0 by convention and J_X>0, resulting in J_{ph} > 0. Also, $\eta_d = k_d/(k_d + k_r)$ is the HCTE dissociation efficiency. If J is sufficiently small so that the electron and hole quasi-Fermi levels ($E_{f,n}$ and

$E_{f,p}$) are flat throughout the respective inorganic and organic layers,[154] then the interface carrier densities are given by:

$$n_{HJ} = N_c \exp\left(-\frac{\phi_I}{k_B T}\right) \exp\left(\frac{qV_I}{k_B T}\right) = n_c \exp\left(\frac{qV_I}{k_B T}\right) \quad (5.5)$$

and

$$P_{HJ} = N_{HOMO} \exp\left(-\frac{\phi_O}{k_B T}\right) \exp\left(\frac{qV_O}{k_B T}\right) = P_c \exp\left(\frac{qV_O}{k_B T}\right). \quad (5.6)$$

Here, N_{HOMO} and N_c are the effective densities of states of the HOMO of the organic and at the conduction band minimum of the inorganic, ϕ_O and ϕ_I are the injection barriers into the organic (from the anode) and inorganic (from the cathode) shown in Fig. 5.1(a), and V_O and V_I are the voltages dropped across the organic and inorganic layers, respectively. In the case of a thick inorganic layer where the depletion width does not extend to the contacts, then $\phi_I = E_c - E_{f,n}$ in the undepleted equilibrium region, where E_c is the energy of the conduction band minimum and $E_{f,n}$ is the electron quasi-Fermi level. In this case, n_c is the electron density at equilibrium as determined by the ionized dopant density (N_D). Also, P_c is the hole density in the organic at the anode contact. Note that due to the very low organic layer conductivity, an equilibrium region comparable to that in the inorganic layer does not exist; that is the entire organic layer is depleted of free carriers and hence the field across it is uniform.

Using these definitions and following a procedure analogous to that of Giebink, *et al.*,[78] we obtain:

$$J = q\langle a\rangle k_{rec} N_{HOMO} N_c (1-\eta_d) \exp\left(-\frac{\Delta E_{OI}}{k_B T}\right)\left(\exp\left(\frac{qV_a}{k_B T}\right) - \frac{k_d}{k_{d,eq}}\right) - J_{ph}. \quad (5.7)$$

Here $\Delta E_{OI} = V_{bi} + \phi_O + \phi_I$ as defined in Fig. 5.1(a), and V_{bi} is the built-in voltage determined by the inorganic Fermi level and the anode work function (modified by energy level shifts, such as those due to interface dipoles).[178] The applied voltage is related to the voltage dropped across each layer and the built in voltage by: $V_a = V_O + V_I + V_{bi}$.

Next we consider the case where there is an exponential density of traps in the organic. Then the trapped hole density is given by:

$$P_t = H_O \exp\left(\frac{E_{HOMO} - E_{f,p}}{k_B T_{t,O}}\right) = H_O \left(\frac{P}{N_{HOMO}}\right)^{1/l_O}. \tag{5.8}$$

The trap density, H_O, the characteristic trap temperature, $T_{t,O}$, and the normalized trap temperature, $l_O = T_{t,O}/T$, can be used to fully describe the trap distribution in the organic film. This treatment is valid for disordered organic films that lack a sharp band edge due to disorder-induced transport level broadening.[64,179] Indeed, in organic films, the conduction level density of states itself is often treated by an exponential distribution of site energies, or as a Gaussian distribution that is approximated by an exponential near the energies of the frontier orbitals. For generality, we use a similar trap profile near the *inorganic* conduction band minimum where H_I, $T_{t,I}$, and l_I describe the trapped electron density in the inorganic. This approximation has been shown to be a suitable distribution for disordered inorganics.[180,181] In principle, however, the ensuing analysis applies to any trap distribution, and we will also discuss the case for crystalline inorganics that are typically characterized by a discreet trap level where $n_t = H_I \exp\left(-\frac{E_C - E_{f,n} - E_t}{k_B T}\right)$, and E_t is the trap energy.[38,182]

We assume that interface recombination is dominated by the recombination of a free carrier with a trapped charge, thereby resulting in:

$$J = q\langle a\rangle(1-\eta_d)\left[k_{rec,n}\left(n_{HJ}P_{HJ,t} - \frac{k_d}{k_{d,eq}}n_{HJ.eq}P_{HJ,t,eq}\right)\right.$$
$$\left. + k_{rec,p}\left(n_{HJ,t}P_{HJ} - \frac{k_d}{k_{d,eq}}n_{HJ,t,eq}P_{HJ,eq}\right)\right] - J_{ph}. \tag{5.9}$$

Here $k_{rec,n}$ and $k_{rec,p}$ are the recombination rates for a free electron with a trapped hole, or a free hole with a trapped electron. Further, $P_{HJ,t}$ and $n_{HJ,t}$ are the trapped carrier densities at the HJ, and can be determined using Eq. (5.8). This expression assumes that $n_{HJ}P_{HJ,t}$ and $n_{HJ,t}P_{HJ}$ are greater than either $n_{HJ,t}P_{HJ,t}$ or $n_{HJ}P_{HJ}$, such that J is dominated by free carrier recombination with trapped carriers. Using Eqs. (5.5) and (5.6), the current can be rewritten as:

$$J = q\langle a\rangle(1-\eta_d)\left[k_{rec,n}N_cH_O\exp\left(-\frac{\alpha_O}{k_BT}\right)\left(\exp\left(\frac{qV_a}{n_Ok_BT}\right) - \frac{k_d}{k_{d,eq}}\right)\right.$$
$$\left. + k_{rec.p}N_{HOMO}H_I\exp\left(-\frac{\alpha_I}{k_BT}\right)\left(\exp\left(\frac{qV_a}{n_Ik_BT}\right) - \frac{k_d}{k_{d,eq}}\right)\right] - J_{ph} \tag{5.10}$$

Here:

$$\alpha_O = \frac{\Delta E_{OI}}{n_O} + \frac{l_O - 1}{l_O}(\delta_O\phi_I - \delta_I\phi_O), \tag{5.11}$$

$$a_I = \frac{\Delta E_{OI}}{n_I} + \frac{l_I - 1}{l_I}(\delta_I\phi_O - \delta_O\phi_I), \tag{5.12}$$

$$n_O = \frac{l_O}{\delta_I(l_O - 1) + 1}, \tag{5.13}$$

and

$$n_I = \frac{l_I}{\delta_O(l_I - 1) + 1}. \quad (5.14)$$

Now $\delta_O = V_O/(V_a - V_{bi})$ and $\delta_I = V_I/(V_a - V_{bi})$ are the fractions of the applied voltage dropped across the respective organic and inorganic layers. Contrary to the trap-free case, the voltage distribution across the layers affects the current even in the near-equilibrium approximation used here. This is important due to the asymmetry of the electronic properties of the organic and inorganic layers, as discussed in Sect. 5.2.2. Note that in the case of discrete traps in the inorganic semiconductor, Eqs. (5.12) and (5.14) must be modified such that $\alpha_I = -E_t$ and $n_I = 1$.

Due to the high dielectric constant and delocalized nature of carriers in the inorganic semiconductor, the HCTE binding energy (E_B) is much smaller than the polaron pairs characteristic of purely excitonic heterojunctions, and in some cases $E_B/k_BT \leq 1$ such that the interface state may be unstable at room temperature. To estimate E_B, the HCTE can be thought of as a hybrid of a Frenkel and Wannier-Mott exciton bound to the heterojunction, as illustrated in Fig. 5.2(a). In this example, the hole is localized to within ~1 nm from the interface; while the electron tunnels into the inorganic forming a delocalized density extending ~6 nm over many atomic sites. The charge comprising the exciton immediately dissociates into an electron on the inorganic semiconductor conduction band that is bound to the hole polaron localized at the OI-HJ, thereby forming the HCTE. The HCTE then can be dissociated either by thermal excitation or by the internal junction field that forces the electron to drift toward the bulk, freeing the hole polaron from the interface. As will be shown below, the HCTE dissociation is also very rapid, depending strongly on the applied bias and temperature.

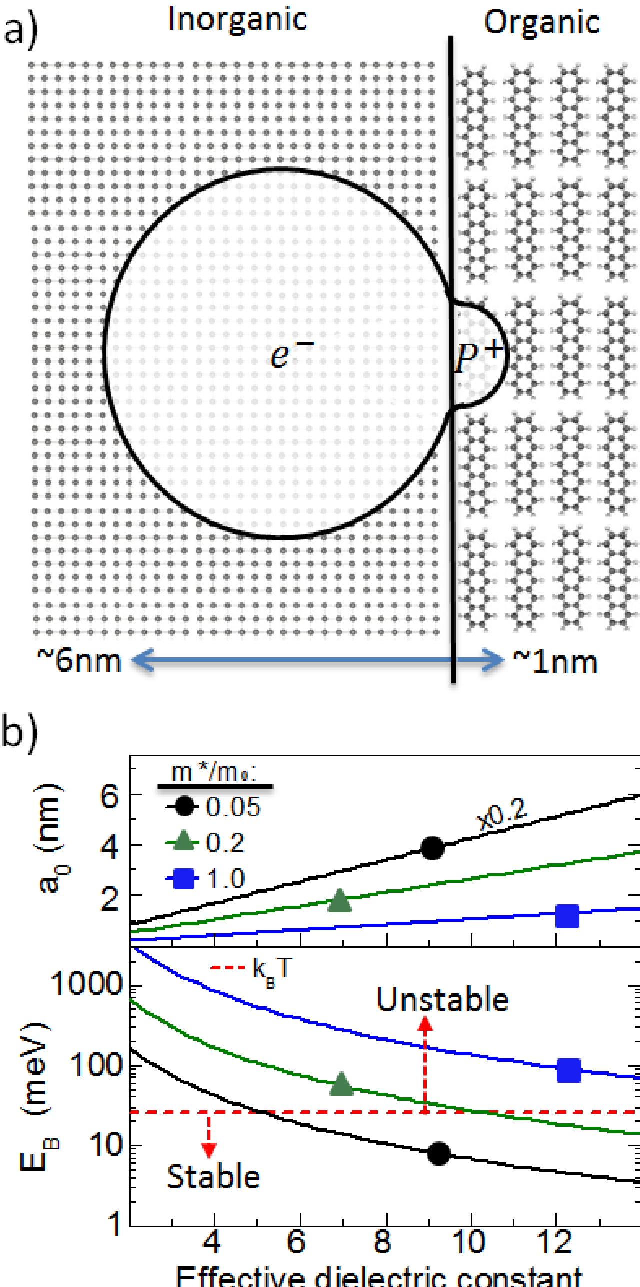

Figure 5.2 – Hybrid Charge Transfer Exciton: (a) Conceptual illustration of the hybrid charge transfer exciton (HCTE) state. The electron in the inorganic is delocalized over a large number of lattice sites due to the relatively large dielectric screening, similar to the case of a Wannier-Mott exciton. This electron is Coloumbically bound to a positive polaron (hole) in the organic that is localized on one or a couple molecules at the interface, analogous to a Frenkel state. The arrows at the bottom note typical extent of these states into the respective materials. (b) Binding energy (E_B) and characteristic radius a_0 of an exciton as a function of effective dielectric constant according to the theory in the text. E_B and a_0 are plotted for the effective mass $m^* = 1m_0, 0.2m_0,$ and $0.5m_0$. The dashed line indicates the thermal energy at room temperature (k_BT) that demarks regions of HCTE stability ($E_B > k_BT$) and instability ($E_B < k_BT$).

While this is an admittedly over-simplified semi-classical picture of the coupled state bound at the interface that can only be accurately understood from a full quantum mechanical description, it nevertheless provides a useful starting point for understanding the charge transfer process.

Following Onsager theory, the radius[93] for the hole in the HCTE is $r_c = q^2/4\pi\langle\varepsilon_r\rangle\varepsilon_0 k_B T$, where ε_0 is the dielectric permittivity of free space, $\langle\varepsilon_r\rangle$ is the effective dielectric constant given by $\langle\varepsilon_r\rangle = (\alpha_I\varepsilon_I + a_O\varepsilon_O)/(a_I + a_O)$, and a_I (a_O) is the extent of the HCTE into the inorganic (organic) layer. To estimate E_B as a function of $\langle\varepsilon_r\rangle$ we follow the Wannier-Mott analysis[24,183] and use the Bohr model to estimate the size of the interacting electron and hole as,

$$\langle a\rangle = a_I + a_O = \frac{8\pi\langle\varepsilon_r\rangle\varepsilon_0\hbar^2}{m^* q^2}, \tag{5.15}$$

where the reduced effective mass is $m^* = 1/(1/m_I + 1/m_O)$, and $\hbar$ is Planck's constant divided by 2π. Note that typically, the electron mass in the inorganic, m_I, is much less than the hole mass in the organic, m_O, in which case $m^* \approx m_I$. This corresponds to a binding energy of:

$$E_B = \frac{q^2}{8\pi\langle a\rangle\langle\varepsilon_r\rangle\varepsilon_0}. \tag{5.16}$$

Figure 5.2(b) shows the exciton binding energy and characteristic exciton radius as a function of the effective dielectric constant for electron effective masses of $m^* = 1m_0, 0.2m_0$ and $0.05m_0$ (typical of the range for inorganics), where m_0 is the mass of a free electron. This model assumes that the electronic states are extended, and that a localized electron is formed by a wavepacket whose motion can be characterized by the effective mass, m^*. The direct extension of m^* to disordered organics is not rigorous, but it has been estimated that for

most small molecule crystalline organic semiconductors, m^* ranges from $0.2m_0$ to $10m_0$, depending on how tightly adjacent molecules are stacked.[184,185,186] However, this semiclassical approximation is not expected to be accurate for large effective masses and highly localized charges; a rigorous calculation of the binding energy once again requires a fully quantum mechanical approach.

For simplicity, we assume that the field dependence of the dissociation rate of the HCTE state is described by the Onsager-Braun (OB)[93,95] model, *viz.*:

$$k_d = A_{OB} k_{rec} \exp\left(-\frac{E_B}{k_B T}\right) \frac{J_1\left[2\sqrt{-2b}\right]}{\sqrt{-2b}} = k_{d,0} \frac{J_1\left[2\sqrt{-2b}\right]}{\sqrt{-2b}}. \quad (5.17)$$

Here, J_1 is the first order Bessel function, $b = q^3 F_{HJ}/8\pi\langle\varepsilon_r\rangle\varepsilon_0 k_B^2 T^2$, and F_{HJ} is the electric field at the interface on the organic side of the HJ, $k_{d,0}$ is HCTE dissociation rate at $F_{HJ} = 0$. This model is valid for low mobility semiconductors where the mean free path is much less than r_c. In the case of a single mobile carrier considered here, the field dependence of k_d may be larger than that predicted by OB yet it nevertheless serves as a first order approximation. The prefactor, ${A_{OB}}^{-1}$, is assumed to be the volume of an ion pair of radius, a,[95] i.e. $A_{OB} = 3/4\pi\langle a\rangle^3$. In the case where the HCT is expected to have a partial Wannier-Mott character, we use $A_{OB} = (m^* k_B T/3\pi\hbar^2)^{3/2}$ where m^* is the effective mass of the electron in the inorganic semiconductor.

The bimolecular recombination rate for low mobility solids is expected to be diffusion-limited, and therefore follows Langevin recombination where $k_{rec} = q\langle\mu\rangle/\langle\varepsilon_r\rangle\varepsilon_0$ and the effective mobility is $\langle\mu\rangle = \mu_I + \mu_O$.[95] In the case of a highly mobile electron in the inorganic semiconductor, $k_{rec} = v_{th}\sigma$, where $v_{th} = \sqrt{3k_B T/m^*}$ is the thermal velocity of the electron and $\sigma = \pi r_c^2$ is its trap capture cross-section. Here we assume that electric field screening in the

high-dielectric constant inorganic semiconductor allows for neglect of the effects of the electrostatic potential[187] on the capture rate.

If the HCTE binding energy is small compared to k_BT (which can occur for low T and/or ε_r for the inorganic) the bound state is readily dissociated, resulting in a large k_d. In the limit that $E_B/k_BT \rightarrow 0$, the HCTE state is coupled to the bath of free-carriers, such that $k_d = k_{rec}/A_{OB}$ is a constant, and $\zeta \approx A_{OB}n_{HJ,eq}P_{HJ,eq} + J_X/k_d\langle a \rangle$. In this case Eqs. (5.2) and (5.3) reduce to:

$$\frac{dn_{HJ}}{dt} = -k_{rec}\left(n_{HJ}P_{HJ} - n_{HJ,eq}P_{HJ,eq}\right) + \frac{qJ_X + J - J_I}{q\langle a \rangle} = 0, \tag{5.18}$$

with a similar expression for P_{HJ}. As expected, this is equivalent to an interface model in the absence of HCTEs, where the excitons dissociate directly into free carriers that subsequently recombine to the ground state. Following the above analysis, this can be reduced to the following expressions for J:

$$J = q\langle a \rangle k_{rec}N_{HOMO}N_c \exp\left(-\frac{\Delta E_{OI}}{k_BT}\right)\left(\exp\left(\frac{qV_a}{k_BT}\right) - 1\right) - J_{ph} \tag{5.19}$$

for the trap-free case, and:

$$\begin{aligned} J = q\langle a \rangle \Bigg[& k_{rec,n}N_cH_O \exp\left(-\frac{\alpha_O}{k_BT}\right)\left(\exp\left(\frac{qV_a}{n_Ok_BT}\right) - 1\right) \\ & + k_{rec.p}N_{HOMO}H_I \exp\left(-\frac{\alpha_I}{k_BT}\right)\left(\exp\left(\frac{qV_a}{n_Ik_BT}\right) - 1\right)\Bigg] - J_{ph}. \end{aligned} \tag{5.20}$$

for the case of an exponential trap distribution in each layer. These expressions are nearly identical to Eqs. (5.7) and (5.10), although they are independent of HCTE dissociation, and

ultimately are the limiting case of the model that includes HCTE dissociation with an efficiency $\eta_d \to 1$. Note that $k_{rec}(1-\eta_d)$ reduces to $A_{OB}k_r$ in the limit that $k_d = k_{rec}/A_{OB} \gg k_r$.

Now, defining a saturation current density of $J_S = q\langle a\rangle k_{rec}N_{HOMO}N_c\exp\left(-\Delta E_{HJ}/k_BT\right)$, then Eq. (5.19) simplifies to the familiar form of the ideal diode equations analogous to those derived by Shockley[148] and Giebink, *et al.*[78]:

$$J = J_S\left(\exp\left(\frac{qV_a}{k_BT}\right)-1\right)-J_{ph}. \tag{5.21}$$

In a similar fashion, an interface with traps yields the current:

$$J = \left[J_{SO}\left(\exp\left(\frac{qV_a}{n_Ok_BT}\right)-1\right)+J_{SI}\left(\exp\left(\frac{qV_a}{n_Ik_BT}\right)-1\right)\right]-J_{ph}, \tag{5.22}$$

making the appropriate substitutions for the saturation currents for the organic, J_{SO}, and inorganic semiconductors, J_{SI}, by comparison to Eq. (5.20).

As OI-HJs often find application in solar cells,[156,168] it is interesting to determine the device open circuit voltage (V_{OC}) in the cases of both stable ($E_B > k_BT$; Eqs. (5.7) and (5.10)) and unstable ($E_B < k_BT$; Eqs. (5.19) – (5.22)) HCTEs. Here, V_{OC} is determined by setting J=0 in the presence of a photocurrent, with $J_{ph} >> J_S$.

In the case of the stable HCTE, the derivation of the open circuit voltage is analogous to that of an excitonic junction as described by Giebink, *et al.*[78] That is, the trap free case is based on Eq. (5.7), *viz.*:

$$qV_{OC} = \Delta E_{OI} - k_BT\ln\left(\frac{k_r}{k_r+k_d}\frac{q\langle a\rangle N_{HOMO}N_ck_{rec}}{J_{ph}}\right). \tag{5.23}$$

Substituting Eqs. (5.15) and (5.17) in the low field limit, which is consistent with $V_a=V_{OC}$, and with $k_d \gg k_r$ we have:

$$qV_{OC} = \Delta E_{OI} - E_B - k_B T \ln\left(\frac{1}{2}\frac{q^3 N_{HOMO} N_c k_r}{4\pi\varepsilon_0 \langle\varepsilon_r\rangle E_B A_{OB} J_{ph}}\right). \quad (5.24)$$

For trap-mediated recombination, one of the exponentials in Eq. (5.10) is usually dominant at high currents. In the case where the first exponential is dominant, and assuming that the contact potentials are equal (i.e. $\phi_O \approx \phi_I$):

$$qV_{OC} \approx \Delta E_{OI} - n_O E_B - n_O k_B T \ln\left(\frac{1}{2}\frac{q^3 H_O N_c k_r}{4\pi\varepsilon_0 \langle\varepsilon_r\rangle E_B A_{OB} J_{ph}}\right). \quad (5.25)$$

If the second exponential in Eq. (5.10) is dominant, the subscripts "O" and "I" are reversed and $N_c \to N_{HOMO}$. Thus, while the binding energy of the HCTE is smaller than that of excitonic junctions, it nevertheless can lead to a decrease in V_{OC} as T is increased since it appears in the argument of the logarithm, along with the related variables of $<\varepsilon_r>$ and the effective mass, m^*. The treatment for an unstable exciton is nearly identical, although in this case $E_B << kT$ and the second term in Eq. (5.24) vanishes. Hence:

$$qV_{OC} = \Delta E_{OI} - n k_B T \ln\left(\frac{k_r}{k_r + k_d}\frac{q\langle a\rangle N_{HOMO} N_c k_{rec}}{J_{ph}}\right). \quad (5.26)$$

In all cases, V_{OC} ultimately depends on the recombination rate, k_r, of the HCTE, resulting in photocurrent loss. The probability of recombination in OI-HJs, however, is significantly lower than in fully excitonic junctions. In OI-HJs, the internal field at the interface rapidly separates charges following migration to the interface (i.e. $k_d >> k_r$); hence there is little opportunity for reactions at rate k_r in Fig. 5.1(b). Thus, the maximum open circuit voltage is:

$qV_{OC}^{max} \approx \Delta E_{OI} - nE_B$, independent of the details of morphology or other factors that influence V_{OC} in excitonic junctions.[78]

5.2.2. Current Conduction Under Non-equilibrium Conditions

The voltage distribution in the device becomes important when traps are present at the interface, or when the small current approximation is no longer valid. For example, it has been found that a high forward voltages, OI-HJ current is typically limited by space charge effects in the organic.[169] In this case, the high current regime is reached at the voltage when the space charge current (e.g. $J = (9/8)(\varepsilon\mu_O V^2/d^3)$ for the trap-free case[179,188]) is equal to that determined by the diode Eq. (5.19).

Due to the radically different electrical properties (*i.e.* mobility and carrier concentration) of the organic and inorganic layers, we expect the voltage distribution to be asymmetric under applied voltages and currents that are large, *i.e.* that are far from equilibrium. To determine the voltage distribution which sets the ratio, δ_O/δ_I from Eqs. (5.11)-(5.14), we must first understand the distribution of charge across all of the layers and contacts. Coupling this electrostatic solution with the dynamical model for the interface then provides a complete, semi-classical physical picture for conduction across OI-HJs under all practical bias conditions.

As noted above, organic films are typically undoped, and even when they are intentionally doped, the maximum free carrier concentration rarely exceeds two orders of magnitude above the adventitious (background) concentration of the as-grown organic.[189,190] As a result, the existence of a background carrier density is due to unintentional doping such as by chemical impurities or oxygen incorporation,[191,192] and is expected to be relatively small. For example, an organic film with a background hole density of $P_D = 10^{15}$ cm^{-3} and $V_{bi} = 0.5\ V$ (of

which half is dropped across the organic), the depletion width[38] is $W_O = \sqrt{2\varepsilon_o(V_{bi}/2)/qP_D} \approx 300\,nm$, *i.e.* larger than the thickness of a typical organic film used in an OI-HJ. With this in mind, the organic layer is assumed to be fully depleted for $V_a < 0$. The resulting energy level diagrams and charge distributions across the OI-HJ under both reverse and forward bias are schematically illustrated in Figs. 5.3(a) and 5.3(b), respectively. These are similar to the distributions in a conventional metal-insulator-semiconductor device,[38] where we have replaced the "perfect" insulator with a leaky organic semiconductor, thereby permitting the existence of a hole current.

The voltage dropped across the inorganic layer, V_I, results in a net space charge, Q_I, given by:[38]

$$Q_I = \mp\sqrt{2k_BTq\varepsilon_I}\sqrt{p_c\left(\exp\left(-\frac{qV_I}{k_BT}\right)+\frac{qV_I}{k_BT}-1\right)+n_c\left(\exp\left(\frac{qV_I}{k_BT}\right)-\frac{qV_I}{k_BT}-1\right)}, \quad (5.27)$$

where $p_c = N_v\exp(-(E_{gap}-\phi_I)/k_BT)$ is the equilibrium minority carrier (hole) density in the inorganic, N_v is the valence band effective density of states in the inorganic, and E_{gap} is its bandgap energy. Under forward bias, $V_I > 0$, and the second exponential dominates, resulting in electron accumulation at the OI heterointerface. Under moderate reverse bias, $V_I < 0$, such that $n_c \cdot qV_I/k_BT$ dominates, resulting in charge depletion. Under large reverse bias ($V_I \ll k_BT/q \cdot \ln(n_c/p_c) \sim 1.5V$), the first exponential dominates, corresponding to carrier inversion. This regime is not reached because the limited hole conductivity of the organic allows the injected charge to be extracted by the contacts before a large inversion voltage can be established.

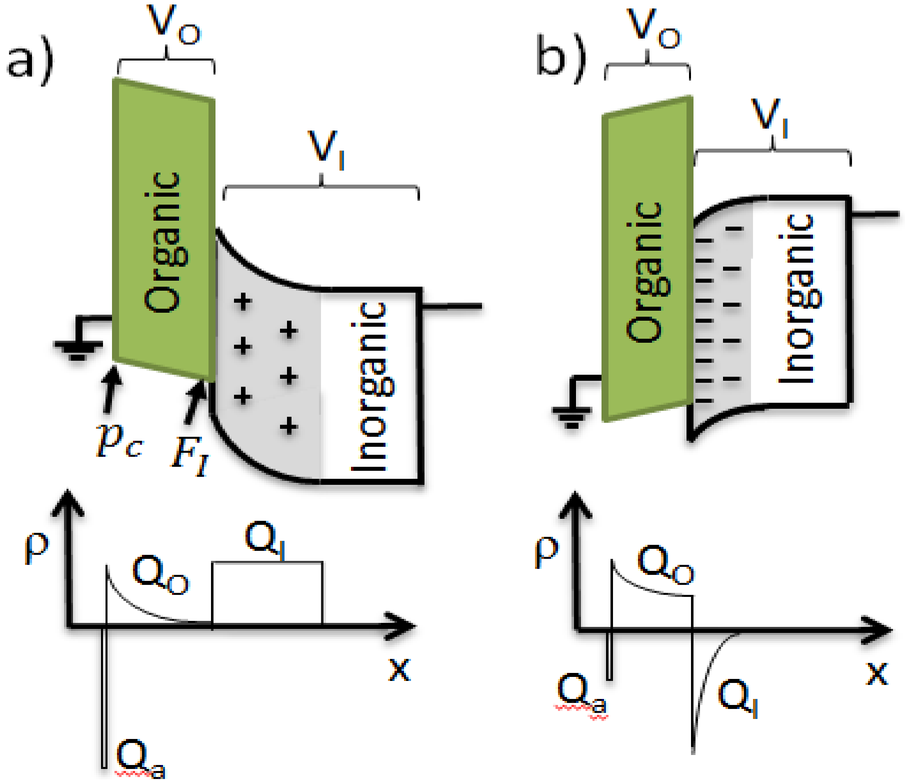

Figure 5.3 – Space-charge in an OI Device: (a) Schematic of a n-P organic-inorganic heterojunction (OI-HJ) under low or reverse bias ($V_a < V_{bi}$, where V_a and V_{bi} are the applied and built-in voltages, respectively). The n-type inorganic is in depletion mode resulting in a positive space-charge (Q_I). The organic is reverse biased; hence, the electric field sweeps holes out of the organic layer resulting in a low charge density (Q_O) and uniform field in the organic layer. Excess charge (Q_a) depleted from the inorganic layer is accumulated at the anode-organic interface. (b) Forward bias condition for the OI-HJ. Electrons accumulate in the inorganic at the OI-HJ such that $Q_I < 0$. The electric field is oriented to force injection of holes into the organic layer that accumulate at the OI-HJ, resulting in a large Q_O. The charge in the anode is determined by charge conservation, i.e. $Q_a = -(Q_I + Q_O)$.

The space-charge in the inorganic results in an electric field at the OI-HJ on the organic side given by:

$$F_{HJ} = -\frac{Q_I}{\varepsilon_O}, \tag{5.28}$$

where we have used the Poisson equation, $\nabla \cdot F = \rho/\varepsilon$ in the inorganic, and $\nabla \cdot (\varepsilon F) = 0$ across the OI-HJ. To ensure that the electric field vanishes at the metallic anode, charge conservation implies that F_{HJ} is terminated by the charge in the organic layer (Q_O) and/or a sheet charge (Q_a) induced at the organic/anode interface. Hence, $Q_I + Q_O + Q_a = 0$.

Under reverse bias ($V_a < V_{bi}$), holes are swept out of the organic layer so that a uniform field approximation can be used. Consequently, $F_{HJ}$is terminated primarily by sheet charge induced at the anode, and the organic behaves as an insulator that capacitively couples the anode to the inorganic semiconductor. In contrast, under forward bias the electrons accumulate at the OI interface thereby drawing holes into, and electrostatically doping the organic layer. The induced hole density can be large, resulting in space-charge screening of the electric field across the layer.

To determine the voltage distribution, we solve the drift-diffusion equation, viz.:

$$J = q\mu_O PF - qD\nabla P, \tag{5.29}$$

With,

$$\nabla \cdot F = \frac{q(P - P_D)}{\varepsilon_o}. \tag{5.30}$$

Here, μ_O is the hole mobility and D is its diffusivity. In the absence of intentional doping, the background carrier density, P_D, is negligible compared to the electrically injected carrier density determined by ϕ_O, J and $V_O(x)$. Equations (29) and (30) are subject to the boundary conditions: $F(W_O) = F_{HJ}$ and $P(0) = P_c = N_{HOMO}\exp(-\phi_a/k_BT)$, where W_O is the organic layer thickness, the OI-HJ is located at $x = W_O$, and P_c is the hole density in the organic at the anode contact

located at $x = 0$. It is useful to assume that μ_O is independent of electric field and that $D = \mu_O k_B T/q$. If we also assume that P_D and J are small, Eqs. (5.29) and (5.30) can be solved analytically,[78] yielding the dependence of V_O on F_{HJ}.

When J is non-zero, Schottky[38,193] demonstrated that Eqs. (5.29) and (5.30) can be solved within the framework of the depletion model by utilizing the resulting analytical electric field profile. Without such a profile, the solution is given by complex Airy functions or by a conditionally convergent power series. Their complexity suggests that numerical simulations of the drift-diffusion equation is a more practical route to calculating the OI-HJ J-V characteristics under non-equilibrium conditions. Numerical simulation also eliminates the need for many explicit assumptions about μ_O, D, and P_D.

Under significant departures from equilibrium, expressions for P_{HJ} and n_{HJ} given by Eqs. (5.5) and (5.6) are no longer valid. That is, when $|J| \gg 0$, the quasi-Fermi level is no longer flat, in which case the hole density at the interface is given by:

$$P_{HJ} = P_c \exp\left(\frac{qV_O - \Delta E_{f,p}}{k_B T}\right), \tag{5.31}$$

where $E_{f,p}(x)$ is the local hole quasi-Fermi level, and $\Delta E_{f,p} = E_{f,p}(W_O) - E_{f,p}(0)$ is the total change across the organic film determined by:

$$\Delta E_{f,p} = \frac{J}{\mu_O} \int_0^{W_O} \frac{1}{P(x)} dx. \tag{5.32}$$

Solution of Eq. (5.32) requires knowledge of $P(x)$ obtained from the numerical solution of the coupled drift-diffusion and Poisson equations described above. The current is then obtained from

Eqs. (5.7) and (5.10) using the transformation $V_a \rightarrow V_a - \Delta E_{f,p}$, or it can be calculated from the carrier densities of Eqs. (5.4) and (5.9).

Thus far, we have only discussed the implications of $J \neq 0$ with respect to the organic layer. In contrast, the majority carrier quasi-Fermi level in inorganic semiconductors is always assumed to be flat – *i.e.* it changes by a negligible amount throughout the depletion region. The reason for the difference between the treatment of the quasi-Fermi levels for organic and inorganic layers is evident from Eq. (5.32), where $\Delta E_{f,p}$ depends inversely on carrier density and mobility. While the background carrier density in organic films is low, P in Eq. (5.32) includes doping due to the electrically injected carriers, which depends on ϕ_O, V_O, and J. Indeed, local electrically induced doping is often comparable to, or larger than carrier densities in doped inorganic layers. Instead, the quasi-Fermi level gradient in the organic[169] results from mobilities that are $10^3 - 10^8$ times lower than in crystalline inorganic semiconductors.

5.3. Results and Discussion

We applied the theory in Sect. 5.2 to simulate the field distributions and *J-V* characteristics of an example hybrid pentacene/Si OI-HJ shown in Fig. 5.4(a). For these calculations, we use the materials properties listed in Table 5.2. The resulting *J-V* characteristics in the trap-free case are shown in Fig. 5.4(b) in the dark and under illumination as a function of temperature. This device is characterized by a diode behavior that rolls off at high currents due to space-charge effects in the organic. Note that at low forward bias, there is a single exponential increase. This is in stark contrast to the behavior of excitonic heterojunctions, where an inflection in the forward characteristic occurs at ~1V due to a sharp change in ideality factor as the voltage distribution shifts from one side of the HJ to the other.[78,194]

The characteristics under illumination assume balanced charge generation of $qJ_X = J_I = 1\, mA/cm^2$ at the interface. This results in unity dissociation of the bound HCTE, yielding a saturated photocurrent at $V_a < 0.2\, V$. In addition, under reverse bias, the *J-V* characteristics are nearly saturated, which also differs from the excitonic junction due to the instability of the HCTE that almost immediately ionizes upon formation. In the excitonic case, the tightly bound Frenkel state requires significant field to force its ionization, hence resulting in a small increase in *J* with increasing reverse bias.

The energy band diagrams, charge and field distributions are shown in Figs. 5.5 and 5.6 at various current densities under forward biased conditions. Note that under reverse bias and low forward bias (and hence, small *J*), the frontier orbital (HOMO and lowest unoccupied molecular orbital, or LUMO) energies in the organic have a nearly constant slope, indicating that the uniform field approximation is indeed valid. However, under large forward bias (corresponding to large *J*), a significant amount of charge is injected into the film that results in a non-uniform field and curvature in the frontier orbital energies. In this case, the large current leads to a pronounced slope in the quasi-Fermi level across the organic layer, characteristic of non-equilibrium conditions.

If traps lead to significant recombination in either layer, the current is given by Eq. (5.20) and the ideality factor is no longer unity. The trap temperature characterizes the depth that trap states penetrate into the energy gap; for example, $T_{t,O}$ increases with disorder that broadens the density of trap states. These energy gap states result in statistics similar to that of Shockley-Read-Hall recombination. In Fig. 5.7(a) we show the effect of traps in the *J-V* characteristics at various temperatures for $H_O = H_I = 10^{18}\, cm^{-3}$ and $T_{t,O} = 600\, K, T_{t,I} = 2000\, K$. Here, we

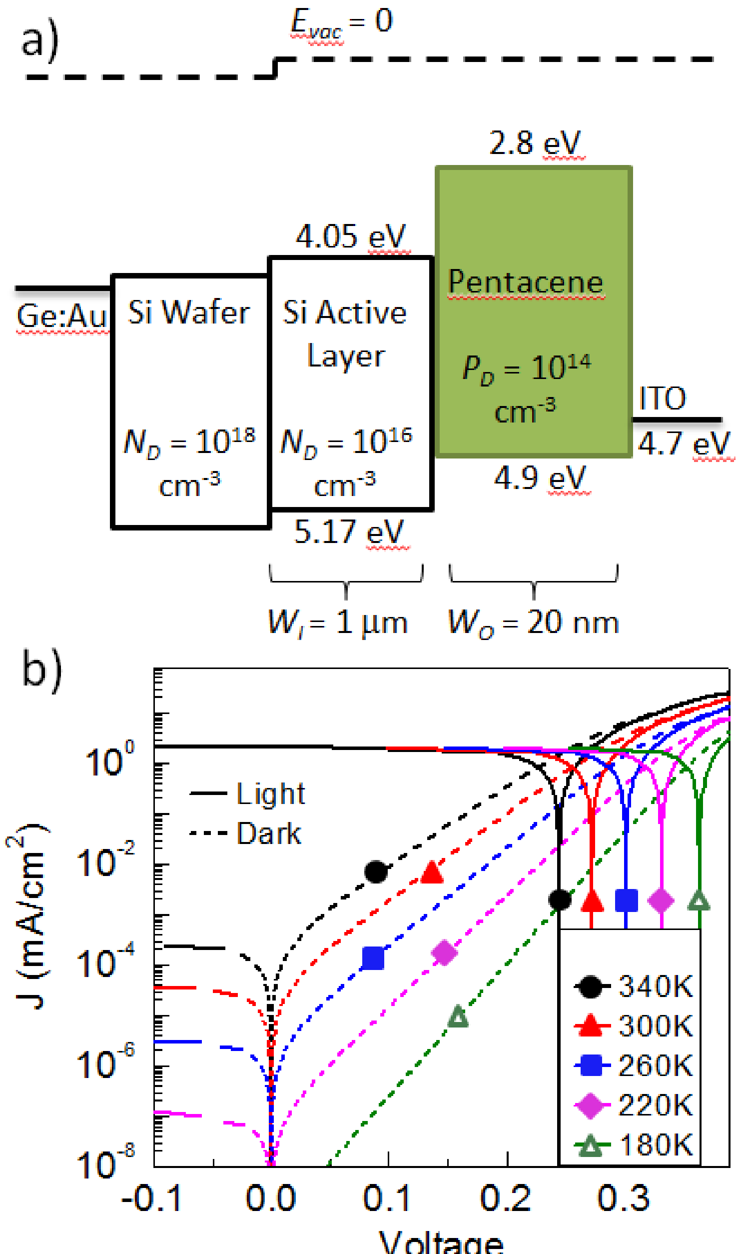

Figure 5.4 – Simulated OI Device: (a) Energy level diagram of an archetype pentacene/Si n-P organic-inorganic heterojunction (OI-HJ). The Si active layer is $W_I = 1\mu m$ thick, and is doped at $N_D = 10^{16}\ cm^{-3}$. The pentacene layer is $W_O = 20nm$ thick and has a low P-type background doping of $P_D = 10^{14}\ cm^{-3}$. The anode contact is assumed to be transparent (i.e. consisting of a transparent conducting oxide such as indium tin oxide (ITO)). A zero vacuum level (E_{vac}, dashed line) offset between the organic and inorganic indicates there is no interface dipole at the heterojunction. (b) Dark (dashed lines) and illuminated (solid lines) current density versus voltage (J-V) characteristics of the OI-HJ at different temperatures. The simulations assume a trap-free interface and an illumination that produces $J_I = qJ_X = 1mA/cm^2$, where J_I is photocurrent generated by the inorganic and qJ_X is Frenkel exciton flux from the organic layer to the organic/inorganic interface.

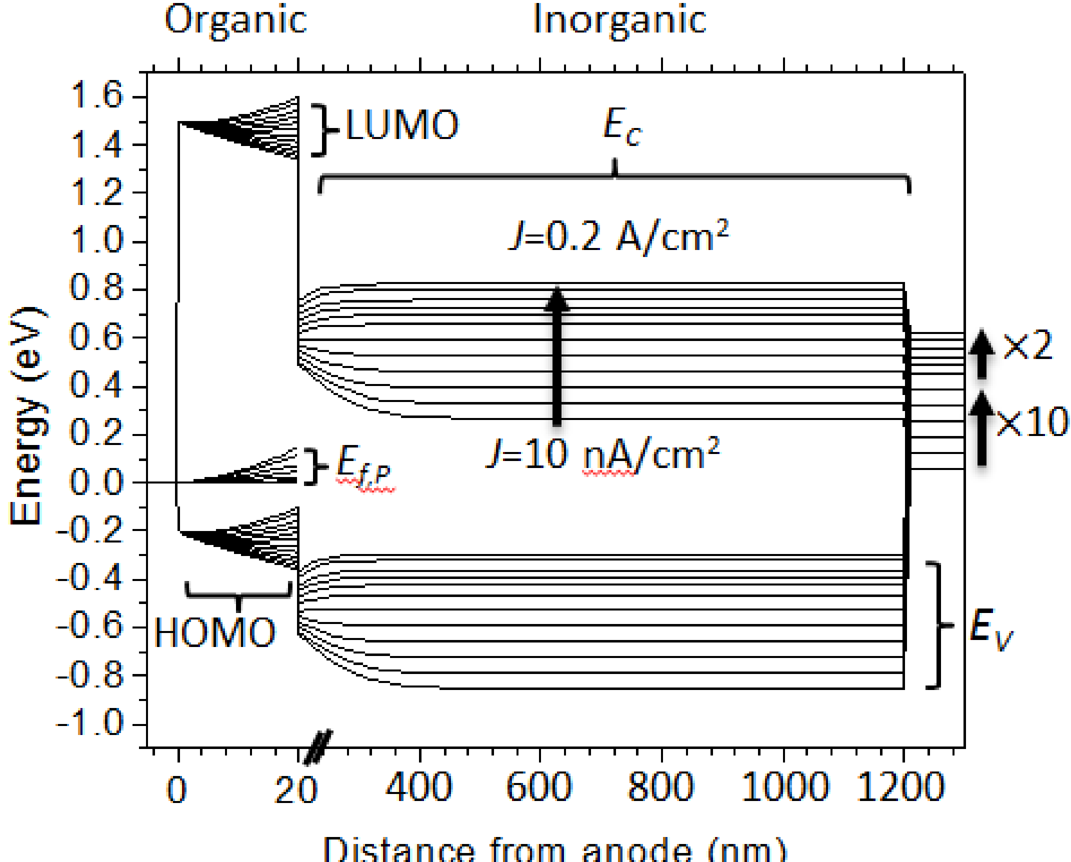

Figure 5.5 – Energy Band Diagram for an OI Device: The valence band (E_v) and highest occupied molecular orbital (HOMO) energy and conduction band (E_c) and lowest unoccupied molecular orbital (LUMO) energy levels are shown for the inorganic and organic layers. The anode contact is shown at zero volts, while the forward voltage required to drive various current densities ($J = 10^{-8}, 10^{-7}, 10^{-6}, 10^{-5}, 10^{-4}, 10^{-3}, 10^{-2}, 0.025, 0.05, 0.1,$ $0.2\ A/cm^2$) is applied at the cathode. The hole quasi-Fermi level ($E_{f,P}$) deviates significantly from its equilibrium value at high currents due to the large density of holes injected from the contact.

observe an inflection in the forward characteristics at low temperatures that is reminiscent of excitonic junctions, but clearly departs from expectations for a conventional p-n junction described by the Shockley equation. Figure 5.7(b) shows the temperature dependence of n_O at various $T_{t,O}$. The increase in ideality factor with increasing $T_{t,O}$ and decreasing ambient temperature is also analogous to that observed for fully excitonic junctions,[78] but the ideality

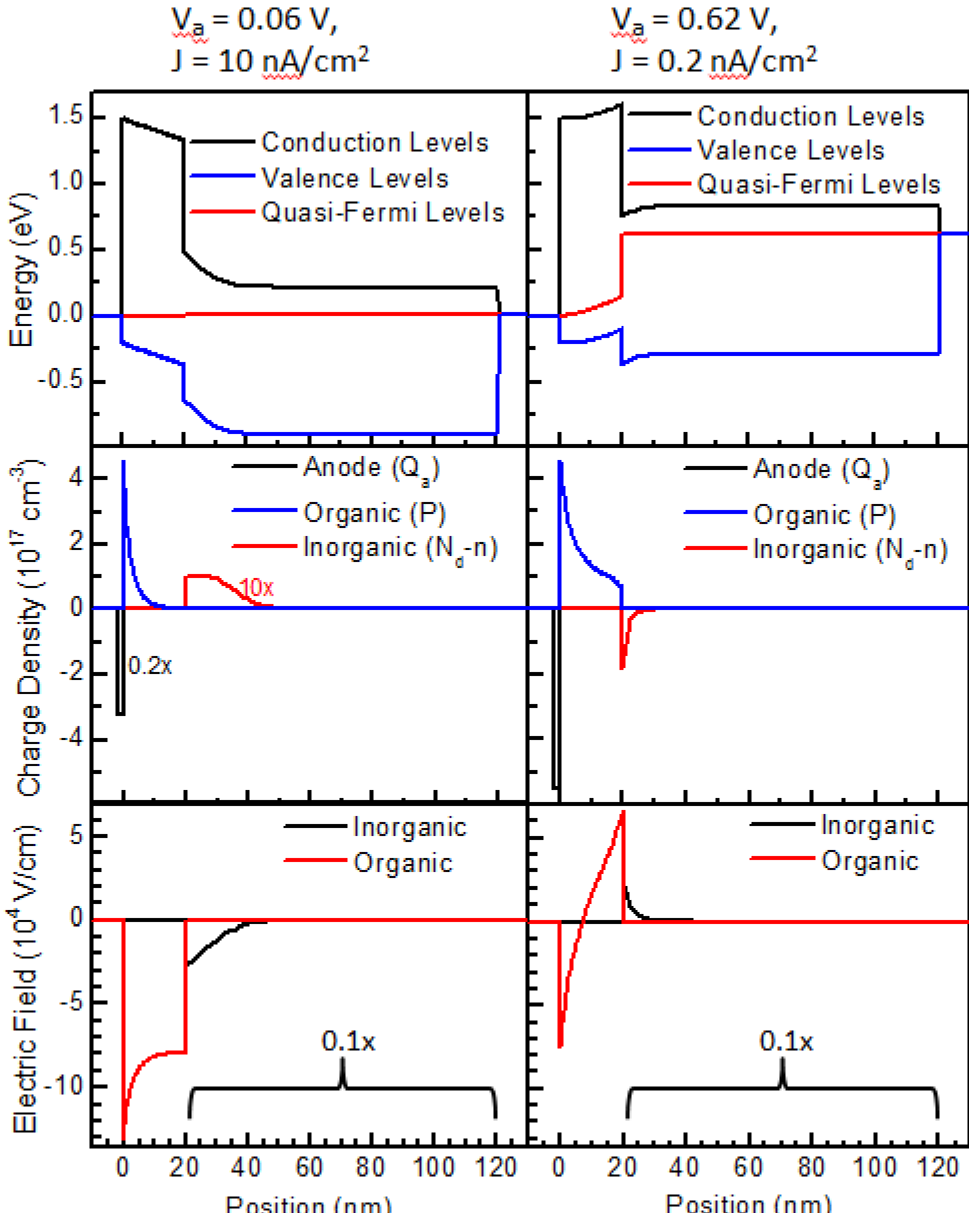

Figure 5.6 – OI Simulation Results: Energy band diagram, total charge density, and electric field distributions through the device with an applied bias of 0.06 V and 0.62 V. At small voltages (also for reverse bias) the inorganic semiconductor has a depletion region resulting in a positive space charge (scaled by 10x for visibility) in the inorganic at the OI-HJ. Most of the depleted charge is accumulated in the anode (Q_a, scaled by 0.2x) at the anode/organic interface. This results in a large electric field (lower panel) in the organic, sweeping holes away from the OI-HJ. When the device is forward biased, electrons are accumulated in the inorganic at the OI-HJ, and a large density of holes are injected into the organic film resulting in space-charge effects. Note that the x-axis is scaled by 0.1x in the inorganic.

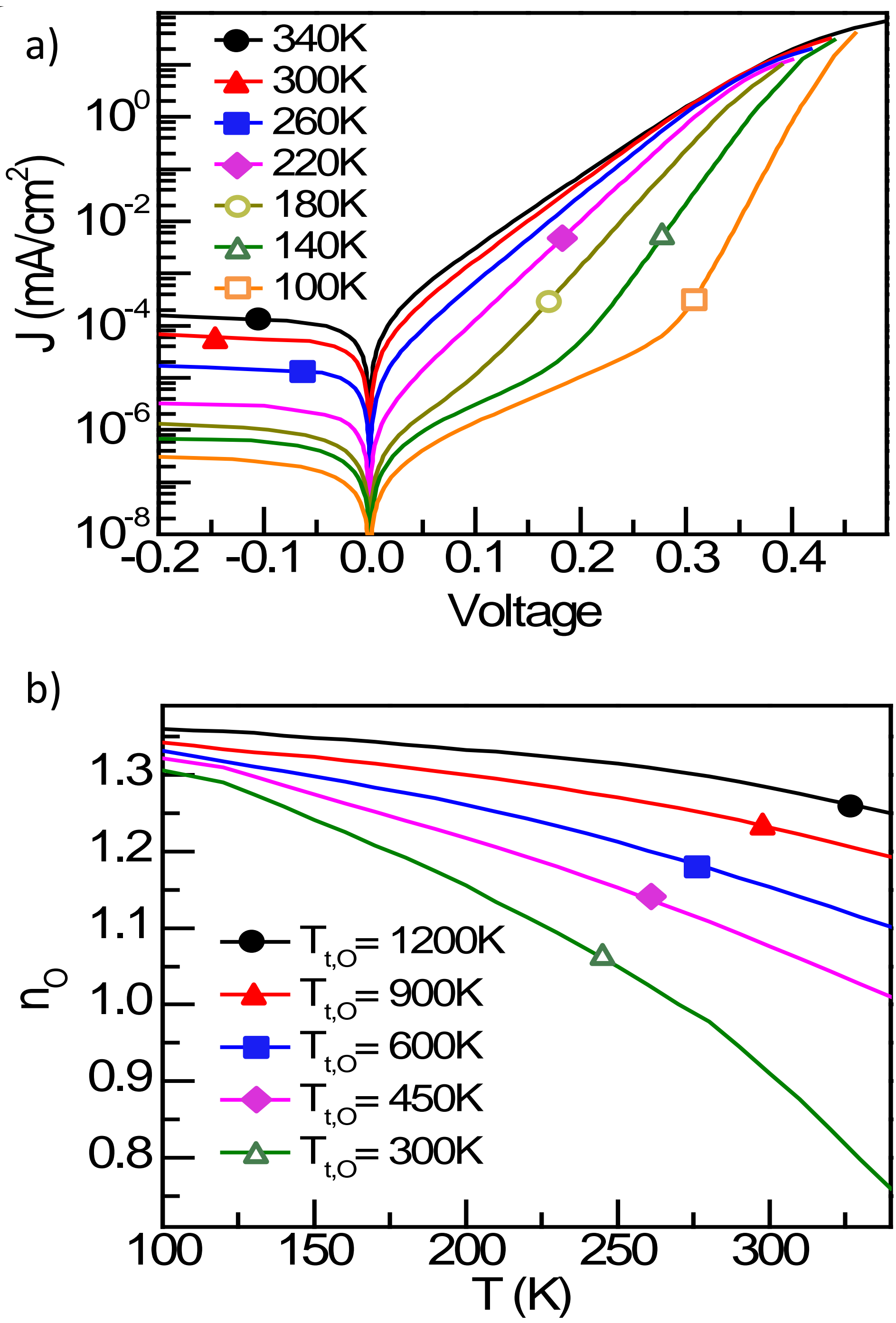

Figure 5.7 – Simulated Dark Current: (a) Current density versus voltage (*J-V*) characteristics of the device in Fig. 5.4(a). Here an exponential density of traps is assumed for both the organic and inorganic layer resulting in two exponential regions that are apparent at low temperature. Calculations based on a pentacene/Si device with material properties given in Table 5.2. (b) The variation in ideality factor (n_O) as a function of temperature with different characteristic trap temperatures ($T_{t,O}$) for the organic layer.

factor is significantly smaller in the case of OI-HJs due to the larger voltage drop across the inorganic layer (c.f. Eq. (5.13)).

In Fig. 5.8(a) we plot the dark *J-V* characteristics as a function of the ratio of the HCTE recombination to its dissociation rate, $R = k_r/k_{d,0}$, which is varied from 1 to 10^{-6}. It is assumed that HCTE dissociation is very efficient due to its low binding energy along with the comparatively high electron mobility characteristic of inorganic semiconductors. Using values in Table 5.2, Eq. (5.17) suggests that the HCTE dissociation rate is $k_d \sim 10^{13}\ s^{-1}$, which is much larger than the natural lifetime of a typical singlet exciton (corresponding to a recombination rate of $k_r \sim 10^9\ s^{-1}$). Indeed, the HCTE recombination rate is reasonably expected to be in the range of $R = 10^6\ s^{-1}$ to $10^{12}\ s^{-1}$, and may vary significantly for different material combinations. As expected, the reverse dark current scales linearly with k_r; the higher recombination rates result in an increase in the rate of charge excitation from the ground state into the various transport bands (c.f. Fig. 5.1(b)).

While k_d follows Eq. (5.17), we assume that k_r is independent of electric field. In this case, Fig. 5.8(b) shows the HCTE dissociation efficiency, η_d, as a function of field for various values of R. We observe that HCTE dissociation is very efficient except for large k_r or large forward bias (corresponding to $F > 0$) where the electric field opposes carrier dissociation. Figure 5.8(c) shows the reduction in η_d at low temperatures, and η_d reaches 100% at a low reverse-bias (or built-in) field. The small HCTE binding energy and large inorganic carrier mobility make the OI interface an efficient site for charge dissociation. Hence, it is useful for photocurrent generation in such devices as dye-sensitized solar cells,[157] and as inter-element charge generating layers in stacked OLEDs[167] and tandem OPVs.[168] Furthermore, the OI

interface can be used to efficiently generate photocurrent originating in organic layers by dissociating the tightly bound organic excitons produced following photon absorption.

Similar to excitonic photovoltaic junctions, losses in an OI solar cell[156] are incurred when HCTE dissociation is inefficient (i.e. $\eta_d < 1$). This occurs when there is strong interface recombination (i.e. R large). However, in the OI solar cell η_d only affects the organic contribution to the photocurrent (*viz.* $J_{ph} = q\eta_d J_X - J_I$), and this results in a loss in fill-factor (FF). Figure 5.9(a) shows the dependence of FF on R for various trap temperatures in the organic. In all cases, HCTE dissociation is efficient when R is small resulting in a high FF. However, when R becomes large (i.e. $k_r \to k_d$), FF decreases due to enhanced interface recombination. This FF loss is more pronounced when $T_{t,O}$ is large due to the increase in midgap states available to enhance interface recombination.

Now V_{OC} (see Eq. (5.25)) is also reduced with increasing R, as shown in Fig. 5.9(b). Since the solar cell power conversion efficiency (PCE) is given by $PCE = FF \times V_{OC} \times J_{SC}/P_{OPT}$, where J_{SC} is the short-circuit current and P_{OPT} is the incident optical power, then the trends in PCE follow closely those of V_{OC} and to a lesser extent, FF. For the calculation of V_{OC}, we have assumed 60% external quantum efficiency at a monochromatic incident illumination wavelength of 650nm. Note that an accurate calculation of V_{OC} and PCE require consideration of response across the entire solar spectrum and the corresponding optical absorption model[74,75] at each wavelength.

Throughout this treatment, we have assumed that the contact barrier at the anode, ϕ_O, is constant. In fact, its value is determined by the difference in anode work function and the HOMO level if the work function lies within the organic energy gap. Interface dipoles

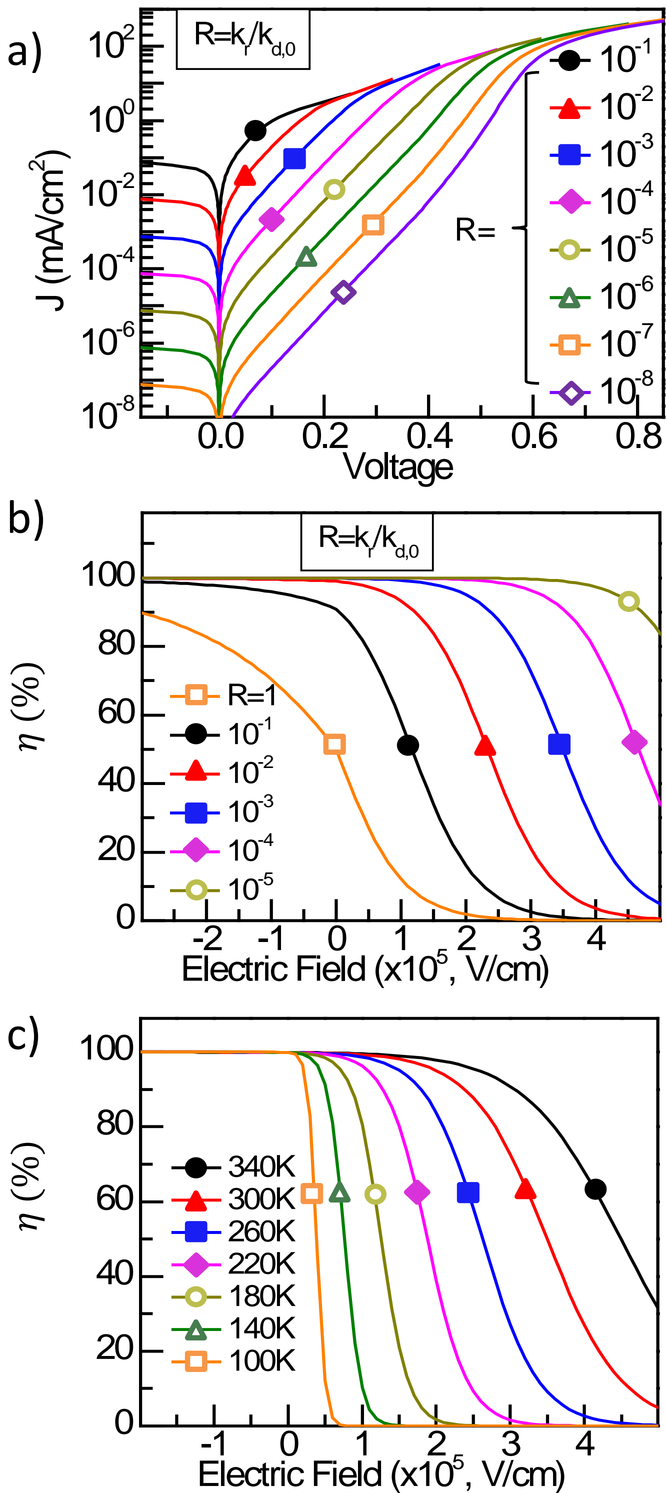

Figure 5.8 – Varied Electric Field and Recombination Rate: (a) Simulated device characteristics for various interface recombination rate ratios $R = k_r/k_{d,0}$, where $k_{d,0}$ is the hybrid charge transfer (HCTE) state dissociation rate at zero electric field. (b) The efficiency of HCTE dissociation ($\eta_d = k_d/(k_r + k_d)$) as a function of electric field and R. For most values of R, the dissociation is efficient when the electric field is less than zero. (c) HCTE dissociation efficiency verse electric field and temperature. At high temperature, η_d is large even for electric fields greater than zero.

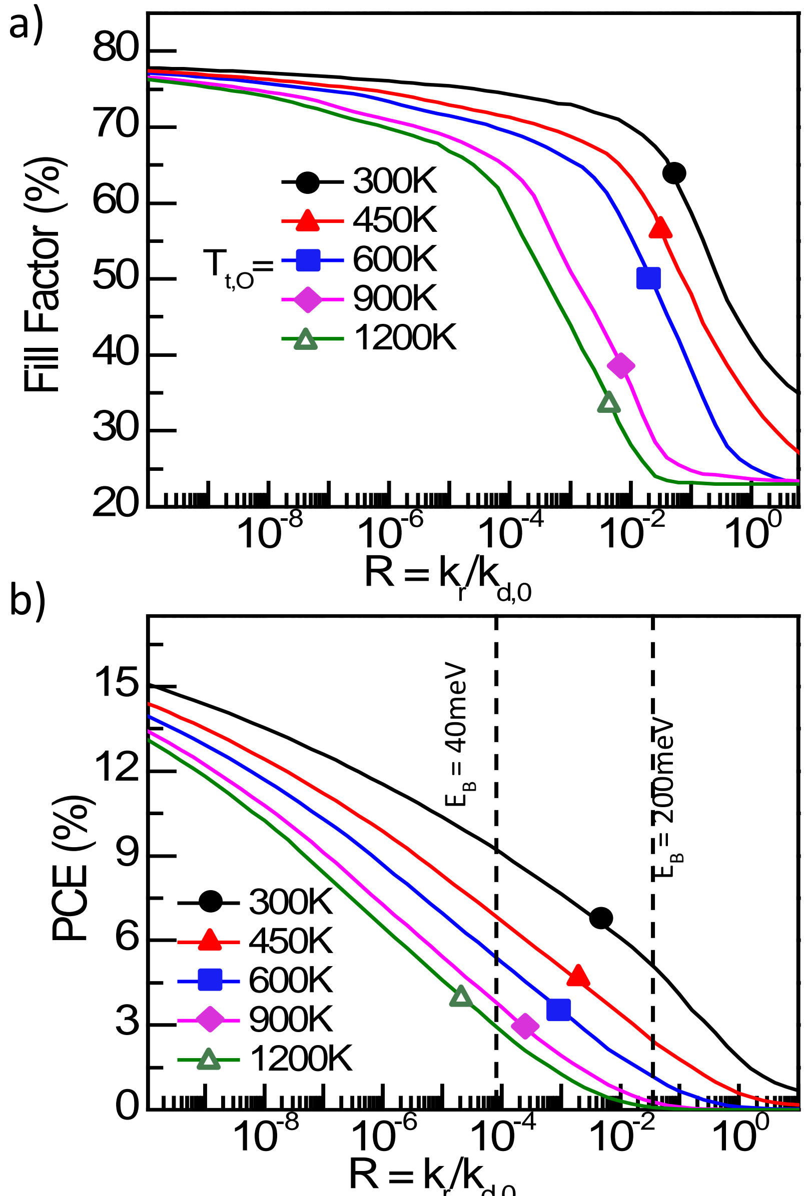

Figure 5.9 – Fill Factor and Power Conversion Efficiency: (a) Dependence of fill-factor (*FF*) on the ratio $R = k_r/k_{d,0}$, of the OI-HJ in Fig. 5.4, where k_r is the recombination rate of the hybrid charge transfer exciton (HCTE) and $k_{d,0}$ is its dissociation rate at zero electric field. Here, *FF* is plotted for various characteristic temperatures of the trap distribution in the organic layer ($T_{t,O}$). In all cases the *FF* is reduced when $R \rightarrow$ large due to enhanced HCTE recombination. (b) The open circuit voltage (V_{OC}) of the OI-HJ in Fig. 5.4 as a function of *R* for various $T_{t,O}$. The V_{OC} increases with reduced *R* due to the increased *FF* and increased open-circuit voltage (c.f. Eq. (5.25)). Vertical lines show values of *R* corresponding to HCTE binding energies E_B = 40 and 200 meV for $k_r = 10^9$ s^{-1}.

commonly observed at the organic/metal interface, however, will result in a corresponding shift in ϕ_O.[195] As shown by Greiner *et al.*,[196] a large work function energy may result in Fermi level pinning at a few tenths of an electron volt above the organic HOMO. We expect this to be the case at small *J*, where ϕ_O is determined by the energy level alignment between the anode and the organic. We show in Chapter 6 that this assumption may not be valid at high currents, particularly when the OI-HJ is in the space-charge regime, far from equilibrium.

Finally, we point out that exciton generation in the organic layer may not always result in photocurrent generation in the OI-HJ diode. For example, extremely rapid thermalization of excitons at the inorganic interface, or lack of energetic resonances that allow for dissociation of the HCTE into free charges on both sides of the HJ can significantly reduce the photocurrent contribution from the organic layer. Indeed, in Chapter 6 we will show that, although significant photogeneration from the organic occurs in wide band gap, TiO_2-based junctions, we do not find evidence for similar contributions in OI-HJs based on the much narrower band gap InP. Hence, which materials combinations are optimal for exciton transport to, and dissociation at organic/inorganic junctions remains an open question.

5.4. Conclusions

We have presented a comprehensive, first principles model for both energy (i.e. exciton) and charge transport dynamics at hybrid organic-inorganic heterojunctions. This model couples the descriptions of the current-limiting processes at the interface with the charge distribution across the entire structure. The model is characterized by a significant asymmetry in materials properties between the contacting materials. The primary outcome of our analysis is the derivation of an ideal diode equation that describes the current-voltage relationship of junctions

in the presence or absence of interface trap states. A new quasi-particle, the hybrid charge transfer exciton whose properties are determined by the characteristics of both the organic and inorganic materials, is found to transfer energy from across the interface. This state is highly unstable (compared to the Frenkel or charge transfer species characteristic of fully excitonic junctions) and hence provides efficient transfer of energy as often observed in photonic devices such as dye sensitized solar cells, stacked OLEDs and OPVs.

Our model can be used to accurately simulate OI-HJ device behavior such as *J*-*V* and capacitance-voltage characteristics. The model can be used to identify those physical processes that dominate in the dynamical properties of the HJ. In the subsequent Chapter 6 we apply the model to understand thin-film hybrid OI-HJs, and find that the relatively low hole mobilities in the organic layer as compared to the charge mobilities in the inorganic semiconductor result in an inflection in the 4th quadrant of the *J*-*V* characteristics, along with a reduction in fill-factor and power conversion efficiency. Similarly this model can be used to understand photocurrent generation processes at the OI interface including the binding energy of a HCTE state.

Chapter 6

Hybrid Organic/Inorganic Heterojunctions: Experiment

6.1. Background

In the companion Chapter 5, we presented a theoretical model for hybrid organic and inorganic heterojunctions (OI-HJs). There we presented a comprehensive model based on charge and exciton dynamics at the OI-HJ. We demonstrated that the model can be used to simulate *J*-*V* curves that are characteristic of hybrid devices based on thick, crystalline inorganics. Here we apply that model to a thin-film TiO_2 / tetraphenyldibenzoperiflanthene (DBP) photovoltaic device with the structure shown in Fig. 6.1. The thin-film nature of this device allows a minor simplification of the complete model presented in Chapter 5 for devices utilizing thick, crystalline inorganics. Here TiO_2 is an electron conductor, while the organic donor is a hole conductor. We choose this materials system for its relevance to solid-state dye-sensitized solar cells (DSSCs). Unlike standard DSSCs that use a distributed bulk-like heterojunction, we fabricate a simple planar bi-layer structure that is easy to describe with a one dimensional (1-D) physical model. This 1-D device is considered here for computational convenience, yet the

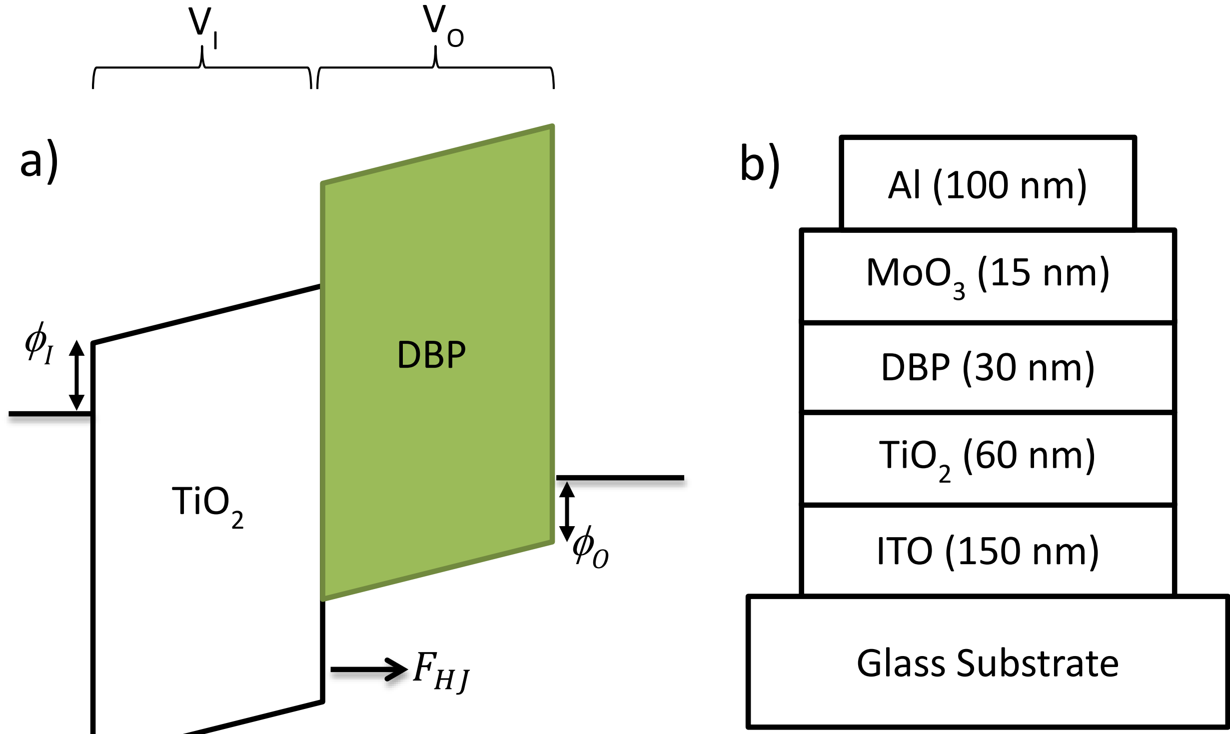

Figure 6.1 – Hybrid TiO_2/DBP Device: (a) Energy level diagram for the thin-film TiO_2 / tetraphenyldibenzoperiflanthene (DBP) hybrid photovoltaic device. V_I and V_O are the voltages dropped across the inorganic and organic layer, respectively. ϕ_I and ϕ_O are the injection barriers into the inorganic and organic layers from their respective contacts. F_{HJ} is the electric field at the organic/inorganic heterojunction. (b) The complete structure of the TiO_2 / DBP device.

model of Chapter 5 can readily be extended to devices with complex morphology that must be modeled in three dimensions. By applying this model to the current density versus voltage (*J*-*V*) characteristics, we can identify the physical processes that dominate charge generation and power generation.

6.2. Theory

To apply the model presented in Chapter 5 to the thin-film TiO_2 / DBP device, it is important to note some fundamental differences between the thin TiO_2 film used here and a bulk inorganic crystal. First, the TiO_2 film is basically amporphous. Even for nanocrystalline TiO_2

used in DSSCs, the electron mobility (~1 cm^2/Vs)[197,198,199] is much lower than that of single crystal inorganics,[38] and the mobility of the film used here is expected to be even lower. Second, the TiO_2 is not intentionally doped, and while background doping can occur by oxygen deficiency during deposition,[200] the carrier density is expected to be lower than that of intentionally doped inorganics. Last, the TiO_2 film used here is 60 nm thick, much thinner than the bulk inorganics considered in Chapter 5. This is important because the TiO_2 film is thinner than the depletion region of a lightly doped inorganic, so we expect that it is fully depleted similar to the case of the thin, lightly doped organic layer. Because it is fully depleted there is not an equilibrium region established in the semiconductor and the voltage through the thin-film also depends on an external field created by charge accumulated in the adjacent metal contact.

Due to the thin-film nature of this TiO_2 layer, we can no longer use the metal-insulator-semiconductor model presented in Chapter 5. Instead we must adapt the electrostatic model to this thin-film system. A rigorous treatment would simultaneously solve the coupled drift-diffusion and Poisson equations on both sides of the device, as done for the organic layer in Chapter 5. However, we find it more illustrative to reduce this system down to an analytical *J-V* relationship by making some simple assumptions.

First we assume that the mobility in TiO_2 is still large enough that we can use the flat quasi-Fermi level assumption as we did for the crystalline inorganic in Chapter 5. That is, we only consider the quasi-Fermi level gradient in the low mobility organic layer. This should be a reasonable assumption because while the TiO_2 mobility may be < 1 cm^2/Vs, we expect it to be considerably larger than the DBP mobility which is likely on the order of 10^{-5} cm^2/Vs. With this assumption we still can describe the electron density at the OI interface (n_{HJ}) as in Chapter 5 by,

$$n_{HJ} = n_c \exp\left(\frac{qV_I}{k_B T}\right), \tag{6.1}$$

where V_I is the voltage dropped across the inorganic layer and n_c is the electron density at the cathode contact. While n_c was determined by the electron density in the equilibrium region for a bulk crystalline inorganic (i.e. the ionized dopant density), here it is determined by an injection barrier at the cathode (ϕ_I) according to $n_c = N_c \exp(-\phi_I / k_B T)$, where N_c is the effective conduction band density of states.

Next we assume that at high currents, we can neglect the diffusion current[155] in the organic layer. While this is less rigorous than the treatment in Chapter 5, it allows us to develop an analytical model for the device. By neglecting diffusion at high currents, we can use a space-charge model to determine the quasi-Fermi level, $E_{f,p}$, through the organic. To do this we combine the zero current solution with a space-charge model for the organic. Then we treat the interface hole density and voltage across the organic as

$$P_{HJ} = P_{HJ}^0 + P_{HJ}^{sc} \tag{6.2}$$

and

$$V_O = V_O^0(x) + V_O^{sc}(x) \tag{6.3}$$

where P_{HJ}^{sc} and V_O^{sc} are the interface hole density and voltage across the organic at large currents due to space charge limited current. While P_{HJ}^0 and V_O^0 are the interface hole density and voltage across the organic at zero current and are related by (c.f. Chapter 5),

$$P_{HJ}^0 = P_c \exp\left(\frac{qV_O^0}{k_B T}\right). \tag{6.4}$$

Here P_c is the carrier density in the organic layer at the anode contact given by $P_c = N_{HOMO}\exp(-\phi_O/k_BT)$, where N_{HOMO} is the effective density of states of the highest occupied molecular orbital of the organic and ϕ_O is the injection barrier at the contact.

The space charge model is derived from the drift current given by $J = q\mu_O PF = \varepsilon_O\mu_O FF'$, where the current is constant through the layer. The second equality comes from the relation between P and F given by the Poisson equation as $\nabla \cdot F = qP/\varepsilon_O$, which assumes a low density of intrinsic carriers. Here ε_O is the dielectric permittivity of the organic and the organic mobility (μ_O) is assumed to be independent of electric field. Then the drift equation can be directly integrated once for the electric field, twice for voltage and the field can be differentiated to find the carrier density. These are given by

$$F(x) = \sqrt{\frac{2Jx}{\varepsilon_O\mu_O} + F_c^2}, \tag{6.5}$$

$$V_O(x) = \frac{\varepsilon_O\mu_O}{3J}\left[\left(\frac{2Jx}{\varepsilon_O\mu_O} + F_c^2\right)^{3/2} - F_c^3\right], \tag{6.6}$$

and

$$P(x) = \frac{J}{q\mu_O}\frac{1}{\sqrt{\frac{2Jx}{\varepsilon_O\mu_O} + F_c^2}}. \tag{6.7}$$

Where F_c is the electric field at the injecting contact. This reduces to the Mott-Gurney law $J = 9\varepsilon_O\mu_O V_O^2/8W_O^3$ when $F_c = 0$. However, F_c is not required to be zero when we allow the existence of a sheet charge in the contact as discussed in Chapter 5.

With this model for space-charge limited current, Eq. 6.2 can be used to relate P_{HJ} to the change in quasi-Fermi level across the organic layer $\Delta E_{f,p}$ as,

$$P_{HJ} = P_{HJ}^{0} + P_{HJ}^{sc} \equiv P_c' \exp\left(\frac{qV_O}{k_BT}\right) \exp\left(-\frac{\Delta E_{f,p}}{k_BT}\right). \tag{6.8}$$

Where P_c' is the hole density at the anode when $J \neq 0$ and is related to P_c (the value at $J = 0$) by $P_c' = P_c + J/q\mu_O F_c$. This is a requirement for this model to be self-consistent, and is a deviation from the simulations of Chapter 5 where we assumed that P_c and the injection barrier ϕ_O (which determines P_c) were both constant. Eq. 6.8 can be inverted to give an analytical expression for $\Delta E_{f,p}$ as,

$$\Delta E_{f,p} = V_O^0 + V_O^{sc} - \frac{kT}{q} \ln\left[\frac{P_{HJ}^{sc}}{P_c'} + \frac{P_c}{P_c'} \exp\left(\frac{qV_O}{kT}\right)\right]. \tag{6.9}$$

Now we can use the interface model presented in Chapter 5 to describe the current. Specifically we consider the low-binding energy case for the hybrid exciton and trap-mediated interface recombination[196] (Eq. 5.20 in Chapter 5) so that the current is given by

$$\begin{aligned} J = q a_0 \Big[& k_{rec,n} N_c H_O \exp\left(-\frac{\alpha_O}{k_BT}\right)\left(\exp\left(\frac{qV_a - \Delta E_{f,p}}{n_O k_B T}\right) - 1\right) \\ & + k_{rec.p} N_{HOMO} H_I \exp\left(-\frac{\alpha_I}{k_BT}\right)\left(\exp\left(\frac{qV_a - \Delta E_{f,p}}{n_I k_B T}\right) - 1\right)\Big] - qJ_X \\ & + J_I. \end{aligned} \tag{6.10}$$

As in Chapter 5, a_0 is the interface volume, $k_{rec,n}$ and $k_{rec,p}$ are the carrier recombination rates, N_{HOMO} and N_c are the organic and inorganic effective density of states, H_O and H_I are the organic and inorganic trap densities, J_X is the exciton flux from the organic layer to the OI-HJ, and J_I is the photocurrent injected from the inorganic valence band into the organic layer. The voltage applied to the device (V_a) is related to the voltage dropped across each layer and the built-in (V_{bi}) voltage by $V_a = V_O + V_I + V_{bi}$. The V_{bi} is determined by the difference in work functions between the anode and cathode (modified by any energy level shifts, such as due to

interface dipoles).[195] The ideality factors (n_O and n_I) and activation energies (α_O and α_I) are defined according to Eqs. 5.11-5.14 in Chapter 5. These terms depend on trap temperatures ($T_{t,O}$, $T_{t,I}$), energy level alignment ($\Delta E_{OI},\ V_{bi},\ \phi_O,\ \phi_I$), and voltage distribution ($\delta_O,\ \delta_I$) as described in Chapter 5.

It is useful to simplify Eq. 6.10 by lumping some of the many material and interface properties into a single lump saturation current prefactor. So we rewrite Eq. 6.10 as,

$$J = J_{s1} \exp\left(-\frac{\alpha_O}{k_B T}\right)\left(\exp\left(\frac{qV_a - \Delta E_{f,p}}{n_O k_B T}\right) - 1\right) + J_{s2} \exp\left(-\frac{\alpha_I}{k_B T}\right)\left(\exp\left(\frac{qV_a - \Delta E_{f,p}}{n_I k_B T}\right) - 1\right) - qJ_X + J_I. \tag{6.11}$$

Where J_{s1} and J_{s2} are independent of voltage. However, the saturation currents contain k_{rec} and the bimolecular recombination rate for low mobility systems is expected to be limited by Langevine recombination[38,95] and depend on carrier mobility as $k_{rec} = q\mu/\varepsilon$. We expect mobility to be temperature dependent and therefor expect J_{s1} and J_{s2} to have the same thermal activation.

6.3. Experiment

We fabricate hybrid OI photovoltaic devices on a 150 nm thick film of Indium Tin Oxide (ITO) patterned into 1 mm wide stripes on a glass substrate. The complete device structure is ITO (150 nm) / TiO_2 (60 nm) / DBP (30 nm) / MoO_3 (15 nm) / Al (100 nm) as shown in Fig. 6.1(b). This is inverted from a typical organic/organic device structure because we deposit TiO_2 by DC reactive sputtering and cannot deposit it on top of the organic donor. Due to the inverted structure we include a MoO_3 hole transport layer as a buffer layer. Without MoO_3 the metal deposition damages the organic resulting in a dramatic reduction in photocurrent generation due

to exciton quenching. We expect that MoO_3 determines the hole injection barrier into the organic donor[196] (rather than the low work function of Al) and find that the MoO_3/Al forms a good hole injection contact.[201,202,203]

We solvent clean the ITO/glass substrate prior to TiO_2 deposition. The TiO_2 film is formed by sputtering from a Ti target with 6 sccm of O_2 flow,[204] while maintaining the chamber pressure at 5.5 mTorr. This O_2 flow rate is at the threshold of complete target oxidization determined by the increase in sputtering voltage at a fixed 300W of DC power.[205] The substrate is heated to 300C to promote formation of a dense conductive TiO_2 film, and the resulting film is determined to be nearly stoichiometric by x-ray photoelectron spectroscopy. The deposition rate under these conditions is 0.33 Å /s.

Next we deposit DBP, MoO_3 and Al by thermal evaporation at 1 Å/s in a high vacuum evaporator with a base pressure of $1x10^{-6}$ Torr. The Al anode is deposited across the ITO stripes through a shadow mask with 1 mm stripes to define a 1 mm x 1mm device area. After TiO_2 deposition the device is not exposed to air during any fabrication steps, including masking which is performed in a dry N_2 environment.

The device is briefly exposed to air to load into an open-cycle liquid N_2 cryostat for temperature dependent *J-V* measurements. The cryostat is then evacuated to < 10 mTorr for the duration of testing. Inside the cryostat, the device is illuminated at 1-sun intensity of 100 mW/cm^2 of AM1.5G light from a solar simulator. The device is alternatively illuminated by a HeNe laser at 632nm, where the HeNe intensity is set to simulate the net absorption from 1-sun by matching the 1-sun photocurrent at short circuit conditions. We find that the *J-V* characteristic is similar in both cases at room temperature and low temperature. We primarily use the HeNe

source for the long temperature dependent measurements due to its long life and stable output power.

We first cool the sample down to low temperature and measure the dark and illuminated current at 20K steps. We allow 20 minutes for thermal stabilization at each temperature step to allow the thermally insulating substrate to equilibrate. At very low currents we find the *J-V* measurement is influenced by a long time constant associated with capacitive effects from traps in device. To mitigate this influence, we use a 5 second delay at each voltage before sampling the dark current and a 1 second delay for the illuminated current. To minimize heating from light absorption, the device is only illuminated while measuring the illuminated J-V response.

6.4. Results

The dark *J-V* characteristics are shown in Fig. 6.2(a) and exhibit a pronounced space charge roll-off from ideal diode behavior that occurs at a lower current threshold at lower temperatures. The earlier onset of space-charge effects at low temperature is indicative of a thermally activated mobility, as expected in organic films where conduction is based on hopping transport between discreet sites with energetic disorder. [64,206] At very low currents there is a plateau region that resembles a second diode with a very high ideality factor (>30). This may be associated with the second exponential term in Eq. 6.10, while the first exponential gives the dominate behavior observed everywhere except for the smallest currents. However these currents are so small (< 100 pA) that they are easily influenced by measurement artifacts such as the long time constant for trapped carriers or dielectric leakage in the probes contacting the device. Nonetheless, we still use the second exponential of Eq. 6.10 to describe this region reasonably well, but we do not consider this region to be of physical interest.

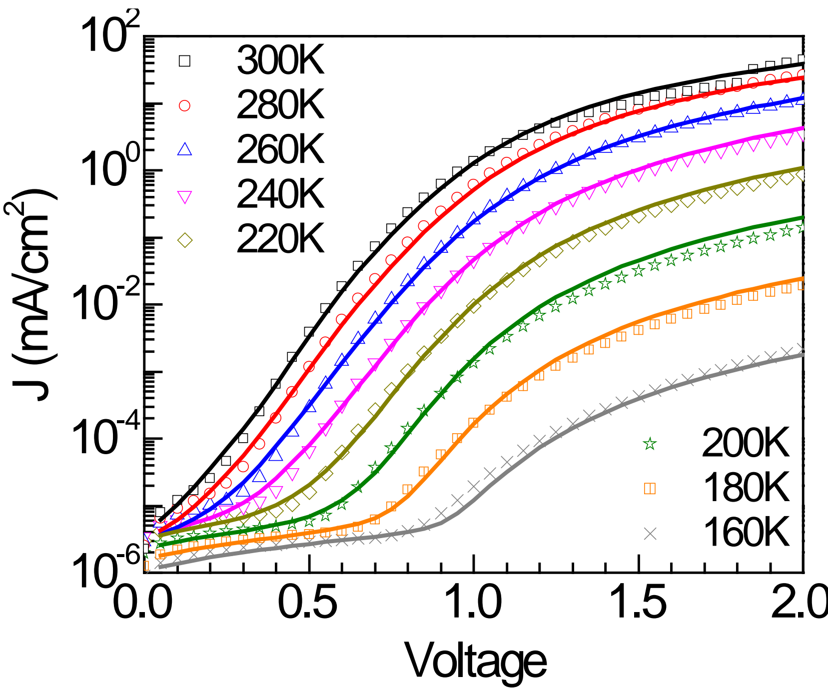

Figure 6.2 – Dark Current of the OI Device: Dark current density versus voltage characteristics of the TiO_2 / tetraphenyldibenzoperiflanthene (DBP) device at various temperatures. Device data is shown by symbols while fits according to the model in the text are shown by solid lines.

The illuminated *J-V* characteristics are shown in Fig. 6.3. The forward biased data (> 0.6 V) exhibits a reduction in current with temperature similar to the dark current, consistent with a thermally activated mobility indicated by the dark current. The fill-factor and power conversion efficiency are also reduced with temperature due to a reduction in photocurrent in the 4th quadrant. The saturated photocurrent at large reverse bias is also thermally activated as it is reduced with temperature. There is a linear slope on the photocurrent that is independent of temperature and is due to photoconductivity of the DBP film.[207]

The external quantum efficiency (EQE) for the device is shown in the inset of Fig. 6.3(b). The photoresponse is entirely due to DBP because the absorption from wide bandgap TiO_2 cuts off above 350 nm. The EQE is relatively low for DBP[175], due to the non-ideal inverted structure of the device. The DBP layer is too close to the reflective Al contact to efficiently absorb the

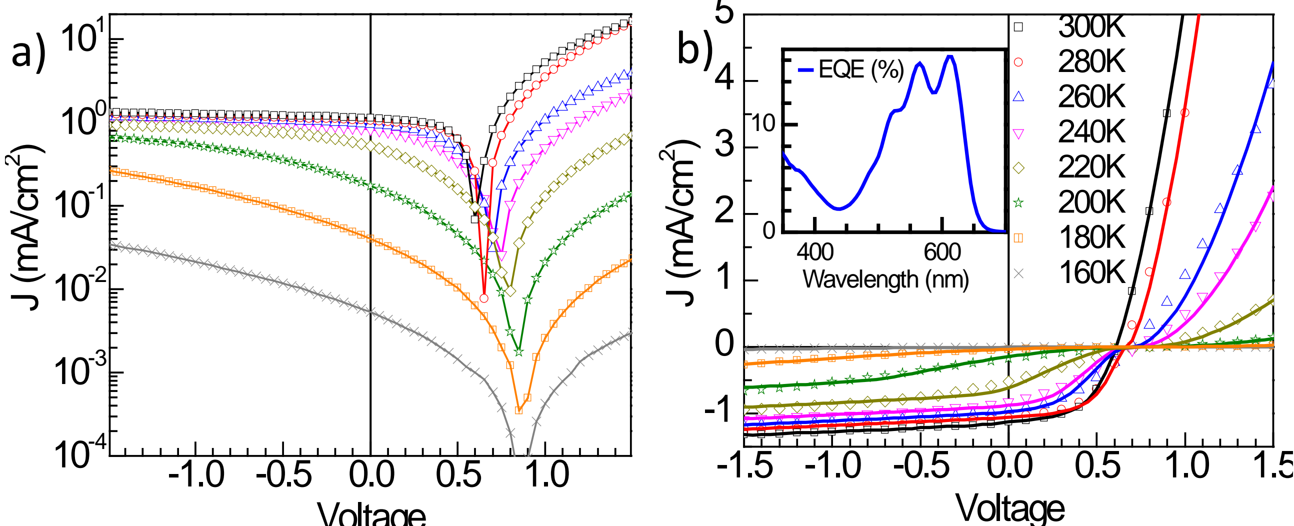

Figure 6.3 – Illuminated Curent Density Versus Voltage: (a) Current density versus voltage (*J*-*V*) characteristics of the TiO_2 / tetraphenyldibenzoperiflanthene (DBP) device at various temperatures while illuminated at 100 mW/cm2 of AM1.5G from a solar simulator. (b) Illuminated *J*-*V* data (symbols) on a linear scale with fits according to the model in the text (solid). Inset: External quantum efficiency of the TiO_2 / DBP device.

incident light. With these considerations, the 15% peak EQE demonstrates that the TiO_2 /DBP interface efficiently dissociates the DBP excitons.

6.5. Discussion

We use Eq. 6.11 to fit the dark characteristics in Fig. 6.2(a). To do this we note that n_O and α_O are implicitly functions of temperature and depend on l_O and δ_I. We assume that δ_I is constant and then V_O in Eq. 6.9 is given by $V_O = (1 - \delta_I)(V_a - V_{bi})$. Assuming that δ_I is constant is a departure from the rigorous model of Chapter 5, but works quite well for the thin-film device. As mentioned above, space-charge roll-off indicates that the carrier mobility is thermally activated. This must be accounted for in order to fit the device data over temperature. We use an Arrhenius activation for the organic mobility as $\mu_O = \mu_\infty \exp(-E_\mu / k_B T)$ which is characteristic of trap and release transport from shallow traps. Then using Eq. 6.11 we can fit the

Table 6.1 – TiO_2/DBP fit results

Parameter	Value	Parameter	Value
δ_i	0.22 ± 0.04	$J_{s1}(dark)$	8 ± 4 A/cm^2
$T_{t,o}$	710 ± 80 K	E_{Js1}	0.19 ± 0.01 eV
μ_∞	6 ± 4 cm^2/Vs	$J_{X,\infty}$	5.2 mA/cm^2
E_μ	0.33 ± 0.06 eV	E_{ph}	40 meV
		$J_{s1}(light)$	80 mA/cm^2

dark current from 160K-300K as shown in Fig. 6.2(a) using $J_{s1}, \delta_I, l_O, \mu_\infty$, and E_μ. The fit results are shown in Table 6.1, where we have used $\varepsilon_O = 4\varepsilon_0$, $V_{bi} = 0.5\,V$, $\phi_I = 0.2\,eV$, and $\phi_O = 0.2\,eV$ in the calculation. Here, the mobility is coupled with the fitting of the illuminated current discussed below. Note that we have left the parameters for the second diode unconstrained so that the low current region does not adversely affect the fitting statistics. As mentioned above, we don't infer any information from this region because it is likely influenced by effects beyond the scope of this model.

To verify that the space-charge roll off is due to DBP as opposed to TiO_2, we fabricated a control device by replacing TiO_2 with a thin C_{60} layer. The structure of the organic PV control was ITO (150 nm) / C_{60} (10 nm) / DBP (30 nm) / MoO_3 (15 nm) / (Al 100nm). Here we used a very thin C_{60} film which has a much higher mobility than typical organic donors. We expect any space-charge effects to be exclusively due to the DBP film. This device exhibits a similar thermal activation for the space-charge roll off as the TiO_2 device, indicating that the space-charge effects are indeed due to DBP.

An initially surprising result from the dark current fitting is the low value of δ_I. While the TiO_2 layer is twice as thick as the organic layer, less than a quarter of the voltage is dropped

across it. We can understand this with a uniform field approximation for both sides of the device. We expect this approximation to be accurate below V_{bi} because both layers have a low intrinsic carrier densities. This is not necessarily accurate when the device is under large forward bias, but this returns to the approximation that δ_I is constant. In the uniform field approximation, the voltage across the organic is $V_O = F_{HJ}W_O$. The boundary condition for the electric field requires that $\nabla \cdot (\varepsilon F) = 0$ at the OI interface. Consequently, the electric field in TiO_2 is F_{HJ} scaled by $\varepsilon_O/\varepsilon_I$ so that the inorganic voltage is $V_I = \varepsilon_O F_{HJ} W_I/\varepsilon_I$. For this device geometry and $\varepsilon_O = 4\varepsilon_0$, this requires that $\varepsilon_I \approx 35\varepsilon_0$. This high dielectric constant is in the range of dielectric constants reported for TiO_2 which vary based on deposition conditions anywhere from 15-250.[208,209,210] In these situations the TiO_2 film is optimized as a high K dielectric constant material. To test the dielectric constant of the reactively sputtered TiO_2 thin-film, we fabricate a thin-film capacitor consisting of ITO (150 nm) / TiO_2 (60 nm) / Au (100 nm). The capacitance exhibited a weak frequency dependence but was in the range of 20-100 nF corresponding to $\varepsilon_I/\varepsilon_0 \approx 30 - 100$, so that our fitted $\delta_I = 0.19$ is reasonable.

To fit the illuminated *J-V*, we consider the two effects observed in the photocurrent of Fig. 6.3. First, there is a reduction in the saturated photocurrent at large reverse bias. This is due to a reduction in the exciton diffusion length $L_D = \sqrt{D\tau}$, so that as we reduce temperature fewer excitons reach the OI interface and are dissociated to contribute to J_X. Generally, reducing temperature reduces non-radiative recombination pathways resulting in a longer exciton lifetime (τ) as indicated by an increase in photoluminescence efficiency. This would indicate a larger J_X, however the increased lifetime is in competition with a reduced exciton diffusivity determined by the dominant exciton transfer mechanism (i.e. either Forster or Dexter transfer). To account

for the reduced photocurrent, we use a simple Arrhenius activation for the photocurrent and assume $J_X(T) = J_{X,\infty}\exp(-E_{ph}/k_B T)$.

The second important effect observed in the photocurrent is the reduction of fill factor with temperature. Initially we expect this to be due to a reduction in the dissociation efficiency of a bound hybrid state at the interface. As discussed in Chapter 5, this dissociation is a thermally activated, field-enhanced process that would require more electric field to efficiently dissociate at lower temperatures (note that the minimum field is ~V_{bi} near the open-circuit voltage). However, we recall that we assumed a negligible binding energy in order to write Eq. 6.10. With this assumption, the bound state can't be the cause of the loss of fill-factor. Nonetheless, $E_B \approx 0$ seems like a valid assumption having identified a high dielectric constant for TiO_2 (c.f. Fig. 5.2(b) in Chapter 5). How can this model account for the loss in fill-factor?

The answer becomes more evident by examining the photocurrent on a log scale as shown in Fig. 6.3. At lower temperatures there is a surprising symmetry in the current centered about the open-circuit voltage. In other words, if the photocurrent doesn't saturate (i.e. we don't efficiently extract all of the photogenerated charge), then the current is symmetric about zero. It doesn't matter which direction the current is going, the voltage required to drive a given current is the same (relative to the open-circuit voltage). We have already discussed that the forward biased current is due to a thermally activated space-charge limited current flow through the organic film, and fit this model to the dark current. So we expect that the fill-factor loss is also due to space-charge effects due to the reduction in mobility. However, the orientation of the space-charge current is reversed when the current becomes negative as the photocurrent from the OI HJ begins to dominate over the injected dark current. In this case, the sign of Eq. 6.9 is reversed and the field at the contact F_c is replaced by the field at the interface F_{HJ}.

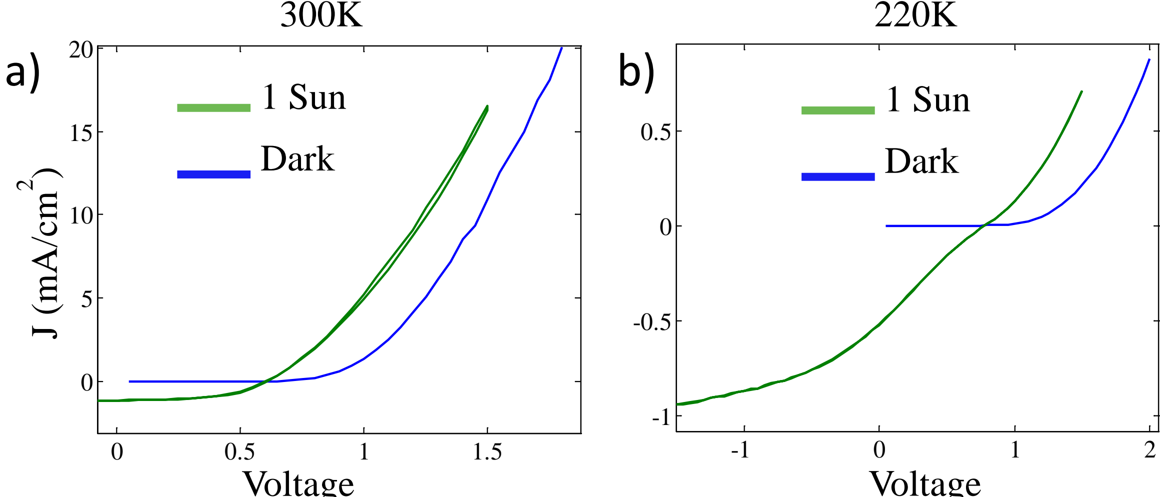

Figure 6.4 – Excess Forward Bias Current Under Illumination: Illuminated and dark current density versus voltage characteristics of a TiO_2 / tetraphenyldibenzoperiflanthene (DBP) device at a temperature of 300K (a) and 220K (b).

To show that this is the case, we make one more important observation. Comparing the illuminated current to the dark current, we notice that the forward biased current increases relative to the dark current as shown in Fig. 6.4. At room temperature, it is even increased by more than the saturated photocurrent of $\sim 1.4\ \mathrm{mA/cm^2}$. In order to fit both the dark and light currents, we have to use a different saturation current prefactor J_{s1} between the light and dark data. In Fig. 6.3, we fit the illuminated *J*-*V* data to Eq. 6.11. Unlike the dark current, we find that J_{s1} is not temperature dependent. For these fits we allow μ_O and J_X to vary freely with temperature, and plot the resulting values in Fig. 6.5. There is a clear Arrhenius activation in both cases with an activation energy of $E_\mu = 0.45\ eV$ and $E_{ph} = 0.04\ eV$. The fit results for both the dark and illuminated data are summarized in Table 6.1.

It is surprising that the fits require a different saturation current between the illuminated and dark data. Even more surprising is that the two cases have a different functional form: J_{s1} in the dark has the same thermal activation as the organic mobility, while J_{s1} in the light is independent of temperature. None of the terms in the prefactor are intuitively light-dependent. A

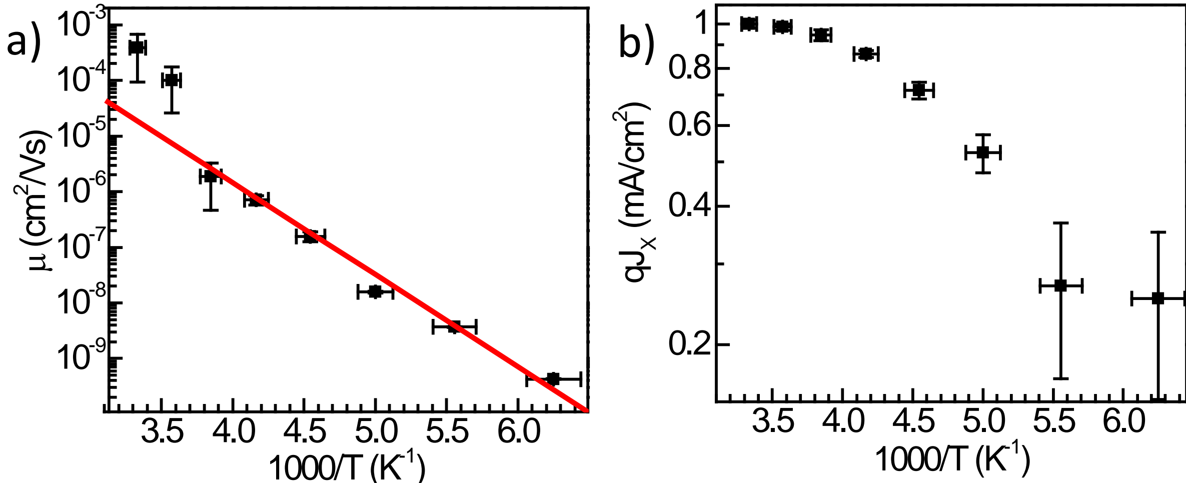

Figure 6.5 – Temperature Dependence of Mobility and Exciton Flux: (a) Arrhenius plot of the temperature dependence of the mobility of tetraphenyldibenzoperiflanthene (DBP). (b) Temperature dependence of the photocurrent generated by exciton diffusion to the TiO_2 / DBP interface.

possible explanation for this is that the bimolecular recombination is indeed limited by Langevine recombination in the dark and therefore k_{rec} and J_{s1} are proportional to mobility. That is, in the dark bimolecular recombination is limited by the rate at which carriers can encounter each other via the carrier mobility. However, when the device is illuminated, the interface carrier density is significantly larger so that k_{rec} is limited by a fixed natural lifetime rather than Langevine recombination.

6.6. Conclusion

The complete device model presented in Chapter 5 and implemented here can be used as a framework to better understand the operation of general hybrid organic and inorganic devices. This work is an attempt to bridge the gap between the traditional inorganic semiconductor theory and the established theories for organic devices. The complete model considers both the interface dynamics of the device but also charge transport to the interface. The general theory in Chapter 5 described the behavior of junctions formed between thick crystalline inorganic layers and thin organic semiconductors. In this highly asymmetric system, we rigorously consider charge

transport through the organic film in order to determine the charge and voltage distribution in the device and here we fit the *J-V* characteristics of an example Si / Pent OI-HJ.

In this chapter, we also adapt the model to a hybrid device using a thin-film inorganic layer. This fully depleted layer is similar to the organic in that a proper depletion model cannot be applied. In this case we consider the additional field due to charge accumulated in the contact and find that the device is well described by a constant voltage distribution between the layers – both in reverse and forward bias. Then we reduce the model to an analytical *J-V* relationship by accounting for the quasi-Fermi level gradient through the organic when $J \neq 0$. We proceeded to show that the roll-off in both forward current and fill-factor are due to space-charge effects due to the reduction in mobility with temperature. Fits to the *J-V* characteristics over a wide range of temperature and light intensity suggests that the mechanism for bimolecular recombination changes when the device is illuminated. Simplifications were made on both sides of the device to present a concise model for the physical phenomenon observed in this particular device. However this framework can easily be extended to include additional processes such as the field-dependence of mobility in the organic, Shockley-Reed-Hall generation in the depletion region of the inorganic or surface-state recombination at the interface.

Chapter 7

Visible/NIR Hemispherical Array Detector for Imaging

7.1. Background

Today's digital consumer cameras come in the three basic formats shown in Fig. 7.1: 1) miniature cameras, 2) point-and-shoot cameras, and 3) single lens reflex (SLR) cameras. Miniature cameras are smaller than $1cm^3$ and are included as extra features in most cell phones and computers. These miniature cameras offer unparalleled convenience but at the cost of poor imaging performance. A step up in camera quality is the point-and-shoot camera, which is the common stand-alone camera with a built-in lens system and few manual controls. These cameras are typically around $100cm^3$ in volume, 100 grams in weight and offer high quality imaging performance that is satisfactory for most people. The best cameras on the market are SLR cameras and are used by all professional photographers. These large cameras with independent lens systems provide the best imaging performance but are typically larger than $1000cm^3$ and weigh more than 1000 grams. Their characteristic feature is a large, bulky, interchangeable lens

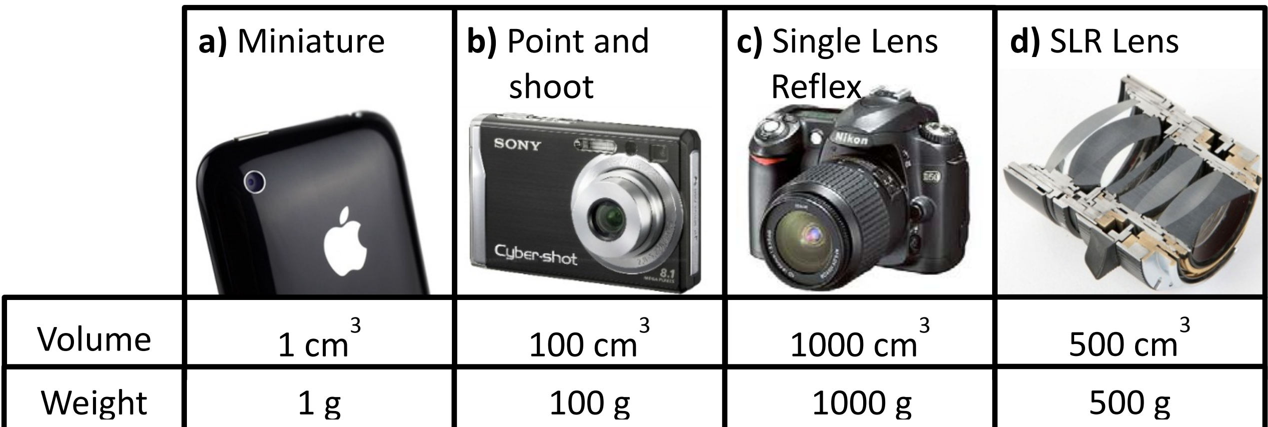

	a) Miniature	b) Point and shoot	c) Single Lens Reflex	d) SLR Lens
Volume	1 cm^3	100 cm^3	1000 cm^3	500 cm^3
Weight	1 g	100 g	1000 g	500 g

Figure 7.1 – Commercial Cameras: Size and weight comparison of the three classes of commercial cameras. (a) Low cost miniature cameras are found in laptops and a cell phones. (b) Mid level point-and-shoot camera. (c) High-end single lens reflex (SLR) camera with lens. (d) Bulky lens of an SLR camera.

system that can be swapped for lenses with different optical properties (such as focal length, field of view, aberration correction). Unlike the simpler camera systems, the bulky lens of an SLR is a complex optical system typically consisting of 7-15 optical components.

The complex imaging system of an SLR camera is designed to produce the best possible image on the camera sensor by maximizing light throughput while minimizing optical aberrations. The most important aberrations to consider are: 1) chromatic aberrations, 2) spherical aberrations and 3) Petzval field curvature. These aberrations are shown in Fig. 7.2. Chromatic aberrations are a manifestation of dispersion from the lens material. Dispersion occurs due to a non-uniform index of refraction at different wavelengths. Most materials exhibit "normal dispersion" over the entire optical spectrum, which is defines as an increase of the refractive index with wavelength. As the refractive index changes, the focal length of a lens also changes with wavelength – consequently when one color in an image is properly focused on the camera sensor, other colors are slightly out of focus due to chromatic aberrations. The effects of this are mitigated in SLR lenses by using achromatic doublet (or triplet) lenses. An achromatic

lens uses multiple elements with different dispersion properties and shapes to minimize chromatic aberrations, for example, by designing the lens so that red and blue have the same focal length. Spherical aberrations are a result of the fact that a lens with spherical curvature is not a very good lens; however, they are easier and cheaper to make than a better lens with an aspherical shape. Spherical aberrations are produced because light rays passing near the perimeter of a spherical lens are focused at a different distance than light passing through the center of the lens. To mitigate this effect, optical systems either 1) only use the middle ~50% area of the lense, 2) use a special combination of concave and convex lenses, or 3) use an aspherical lens. Aberrations due to Petzval field curvature are a result of focusing to an image *plane* – required for planar digital sensors. In a perfect lens, all rays from the object distance (S_1) are focused to an image distance (S_2) from the lens, where S_1 and S_2 are determined by the focal length according to: $1/f = 1/S_1 + 1/S_2$. Objects infinitely far from the lens are focused to an image hemisphere of radii S_2 rather than an image plane. This is also true for most cases in photography and imaging, as long as the object plane $S_1 >> f$, the object plane will be focused to a hemisphere of radii S_2.

Chromatic and spherical aberrations are lens problems that can be mitigated simply by using better lenses, at the expense of increased cost. On the other hand, Petzval field curvature affects the design of the whole camera system – the lenses, the aperture and the sensor. The system is designed to cope with a flat image sensor because all digital image sensors are planar – simply due to limitations in fabrication technology. The result of imaging with such planar sensors is that the camera only takes a small slice of the image hemisphere near its pole – where the plane can sample the largest area of the hemisphere while keeping the image approximately in focus. This is the fundamental limitation to a camera's field of view (FOV) – the portion of

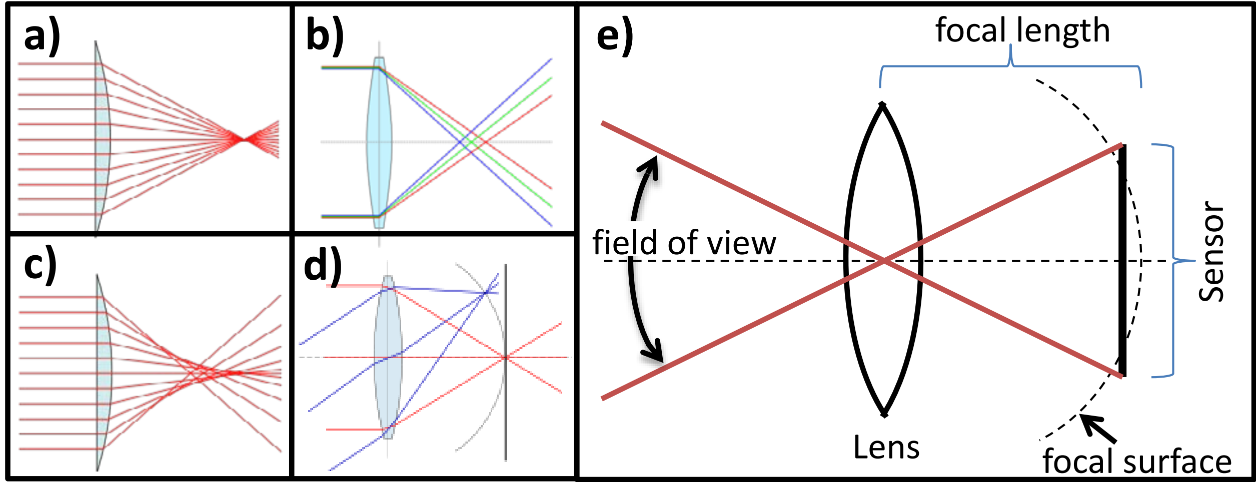

Figure 7.2 – Optical Aberrations: (a) Ideal lens focuses every wavelength of light to a single point. (b) Chromatic aberrations exist if the focal length changes with wavelength. (c) Spherical aberrations occur due to a variation in the focal length of a lens when light is incident at different distances from the axis of the lens. (d) Petzval curvature occurs even in a perfect lens. When light is incident at different angles it does not share a common focal plane. (e) The field of view of an imager is determined by the focal length and size of the sensor.

the object plane that is recreated on the image sensor. The FOV is characterized by the angle that encompasses this portion of the object plane. For a planar sensor the FOV is determined by the size of the sensor and the focal length of the lens according to $FOV = 2\tan^{-1} {}^{w}/_{2f}$, where *w* is the width of the image sensor. Ultimately, the size of the sensor is designed with Petval field curvature in mind so that a lens with the smallest desired focal length will be able focus acceptably across the whole sensor.

Biological systems have developed an imager that is dramatically different from the modern camera systems described above. For example, the human eye is a fantastic imager with a high dynamic range, high sensitivity, > 150 degree FOV, and very high resolution – with a pixel density in the fovea corresponding roughly to a 25 megapixel camera. This performance comes in a very compact package with a volume of 6 cm^3 and weight of < 10 grams. Such

compact performance is achieved by using a hemispherical imaging sensor (the retina) in conjunction with a single lens element.

Looking at the human eye as an exemplary imaging system, the paradigm of imager design changes dramatically when the planar image sensor is replaced by a hemispherical one. Such a sensor mitigates Petval field curvature, and a full 180 degree FOV can be recreated on the image sensor, without loss of image quality. At the same time, a small focal length system can be designed while maintaining this large FOV. Ultimately this enables very good image quality and very large FOV in a compact imaging system.

In this chapter, we develop fabrication techniques to enable the fabrication of a high-performance, hemispherical imaging sensor. The project was funded by DARPA (Defense Advanced Research Projects Agency) as part of the HARDI (Hemispherical ARray Detector for Imaging) program, but is often referred to as the artificial eye due to the imager's resemblance to the human eye. The final goal of this project is to fabricate a 1 megapixel imaging array on a 1cm radius hemisphere with high sensitivity (a specific detectivity, $D^* > 10^{12}$ Jones) over the visible (Vis) and near-infrared (NIR) spectrum (400nm-1900nm). On the way to demonstrating the final prototype, we must meet the incremental metrics outlined in the table below. The ambitious goals of the HARDI program could be divided into two essentially independent projects: 1) development of a high sensitivity, Vis/NIR photodetector and 2) development of fabrication and integration technologies to enable the production of a high performance imaging array on a hemispherical substrate. To address the first goal, we developed a Vis/NIR photodetector based on carbon nanotubes and this work is summarized in Ref. [147]. The rest of this chapter focuses on the second goal – fabricating organic semiconductors on flexible and deformable substrates.

Table 7.1 – HARDI Program Metrics

Phase	Detector Area (μm^2)	Feature Size (μm)	Spectral Range (nm)	Radius of Curvature (cm)	Registration (μm)	Array Size
1	200	50	400-1200	5	5	10x10
2	50	20	400-1600	2.5	1	100x100
3	10	5	400-1900	1	0.5	1000x1000

7.2. Fabricating an Organic Sensor Array

We elected to use a transparent, thermo-formable plastic substrate for our hemispherical detector array. Using a transparent substrate provides the fewest constraints for the OPD design because the detector could be fabricated on either the inside or outside of the hemispherical substrate, allowing either top-illumination (light directly incident on the detector) or bottom-illumination (light passes through the substrate prior to reaching the detector) OPDs. Thermo-formed substrates would be faster to make and less expensive than machined glass, and is more suited for our patterning process than injection molded substrates. The ideal substrate would be transparent over the Vis/NIR range, mechanically rigid but easily deformed into our desired shape, and chemically resistant to any solvents that may be required for spin-casting an OPD. To meet these criteria, we chose to use a 1mm thick glycol-modified polyethylene terephthalate (PETg).

7.2.1. Patterning soft materials on a non-planar surface

Xin Xu, et al.[17] demonstrated a process for thermo-forming a flat PETg sheet into a hemisphere and, using the same mold, to directly pattern metal and ITO electrodes onto the hemispherical PETg. This patterning process relies on cold-welding and dry-etching in order to be compatible with organic films. Cold welding[211,212,213] is the formation of a metallic bond

between two smooth and clean metal surfaces. The bond is formed at low temperature by the applying pressure to form intimate contact between the two metal surfaces. This method creates a strong bond but is susceptible to roughness or chemical contamination of the surface, such as oxidation of the metal; therefore, cold weld bonds are most easily formed using a soft and chemically inert metal such as Au. Dry etching is a plasma etching process performed in a low vacuum environment. Specifically, Ar-ion etching is used, which is a purely physical etch that occurs when Ar^+ atoms are bombarded against the sample by the application of a high electric field. When the energetic Ar ions hit the sample surface, they sputter material off of the surface, resulting in etching of the surface. This etch is non-selective and will attack both the metal and organic layers. However, the etch is anisotropic and etching occurs fastest in the direction of the applied field; consequently, a thick metal mask can be used to protect regions of the organic layers where they are needed in the device.

The basic process for patterning involves four steps: 1) prepare the hemispherical substrate with a strike layer, 2) prepare the pattern in a planar elastomeric PDMS stamp, 3) transfer the pattern to the substrate, and 4) etch the strike layer to isolate the patterns. To prepare the hemispherical substrate, a vacuum mold is first machined out of Al. This mold will define the radius of the hemisphere and, in the case of an incomplete hemisphere, the depth of the hemispherical surface. Throughout the hemispherical region, there are small perforations machined through the Al mold, to allow drawing the flat PETg sheet into the hemispherical cavity of the mold by applying vacuum. Next, the substrate is thermo-formed by placing it on top of the mold and drawing it into the mold with the vacuum after the PETg is heated to its softening temperature of 140° C in an oven. Then the substrate is coated with a thin Au strike layer (~6 nm) – this strike layer will be used to bond the patterned metal to the PETg via a cold

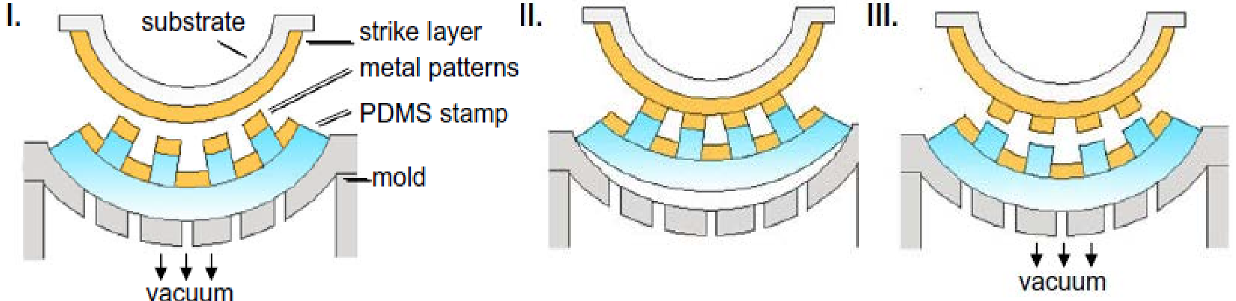

Figure 7.3 – Stamp Patterning Organics: Process sequence for fabricating a hemispherical FPA. (I) The hemispherical plastic substrate, coated initially with a metal strike layer, is placed in proximity to a patterned PDMS stamp of the same shape, deformed by vacuum in an aluminum mold. (II) The vacuum holding the PDMS stamp is released, allowing the stamp to snap into contact with the substrate surface. Metallic bonds are formed between metal patterns on the stamp and strike layer on the plastic dome. (III) The PDMS stamp is separated from the substrate by reapplication of vacuum, leaving behind the metal patterns on the hemisphere.

weld bond. Next, the desired pattern is formed as raised features on the PDMS stamp that is cast from a lithographically defined and micromachined Si mold. Then, a thick Au layer (~100 nm) is deposited onto the PDMS stamp.

The metal pattern is transferred from the PDMS stamp to the PETg substrate by the process shown in Fig. 7.3. First, the PDMS stamp is drawn into the Al mold by vacuum and the PETg substrate is placed into the mold above the PDMS stamp. Second, by turning off the vacuum and allowing the PDMS stamp to elastically relax, intimate contact is formed between the metal on the plateaus of the stamp and the uniform strike layer on the substrate. This relaxation provides enough force to form a cold-weld bond between the two metal layers. Third, the vacuum is re-applied to withdraw the PDMS stamp, and the cold-welded metal pattern is left behind on the substrate. Finally, the patterning is completed by etching the strike layer using an Ar-plasma etch in order to electrically isolate the patterns.

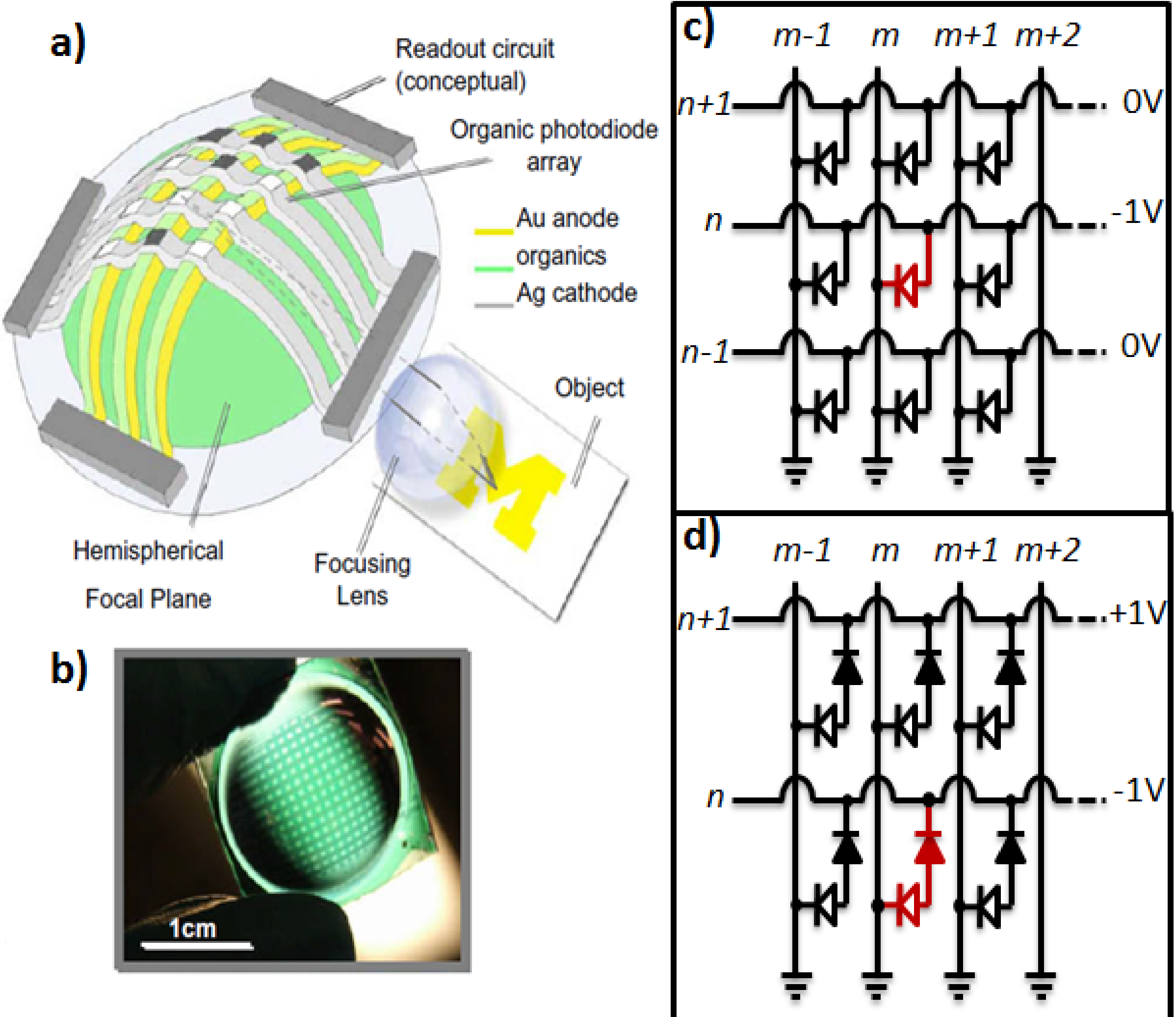

Figure 7.4 – Hemispherical Photodetector Array: (a) Schematic of the hemispherical organic photodetector focal plane array (FPA) and its incorporation into a simple imaging system. The lens produces an image of the object on the spherical focal plane, where an array of photodiodes has been defined. The readout circuits are commonly used in FPAs, but are not employed in our work. (b) Photograph of a completed hemispherical focal plane with a 11x13 array of $(500\ \mu m)^2$ photodetectors on a 1 cm radius plastic hemisphere. (c) Circuit diagram for a small region of a crosshatch photodiode array. The pixel at position $m \times n$ is the desired pixel to read and is highlighted in red. (d) Circuit diagram for a photodiode array incorporating a blocking diode to reduce leakage pathways in the circuit. The pixel to be read at site $m \times n$ is highlighted in red.

7.2.2. Crosshatch OPD Array

Using this metal patterning process, the simple cross-hatch OPD array shown in Fig. 7.4 can be easily fabricated onto the hemispherical substrate. Xin Xu, et al. demonstrated such a monolithically integrated OPD array on a hemispherical PETg substrate. The array had a strong visible response with a peak external quantum efficiency (EQE) of 20.5% at 605nm. At -1V a device in the array had a D^* of 1.25 x 10^{11} cm·Hz$^{1/2}$/W. A problem with this crosshatch diode array is that the dark current from a single pixel (addressed by a row and a column contact) is influenced by leakage pathways in the circuit. Indeed, when the non-addressed rows and columns are left floating, the dark current scales with the number of pixels on a row[18] – *i.e.* dark current scales as N in an $N \times N$ array. This results in a dramatic reduction of dynamic range for the sensor, and is a fundamental limitation for scaling this circuit architecture into a large array.

When the crosshatch diode array is biased as shown in Fig. 7.4(c), a reverse bias on row n is applied to every diode on that row. If the pixels on all other rows are OFF (i.e. no current is flowing through them), the current from each pixel can be read out independently through its corresponding column. For example, the highlighted pixel $n \times m$, is read by biasing row n at -1 volts and reading the current flowing through column m. This architecture works well if, and only if, the pixels are OFF on all rows except row n, otherwise you get leakage or crosstalk on each readout column due to the other pixels. However, a simple photodiode pixel is only OFF at zero volts if it is in the dark! If there is light on rows other than n, those pixels will also contribute to the photocurrent measured for pixel $n \times m$. This leads to large crosstalk and an unusable sensor. This problem can be mitigated either by 1) adding a mechanical and movable aperture to illuminate only the desired row during readout or 2) using a more complicated pixel

architecture. A mechanical aperture is an impractical solution; an improved pixel architecture is the obvious choice.

7.2.3. OPD Array with Blocking Diode

The leakage problem could be addressed by adding a reversed, blocking diode at each pixel as shown in Fig. 7.4(d). Ideally this blocking diode would have a very high rectification ratio and no photoresponse. If the pixel is reverse biased, the blocking diode is forward biased and is ON allowing the extraction of photocurrent produced by the photodiode. However if the pixel is forward biased, the blocking diode turns OFF minimizing current flow through the pixel. With this architecture, rows not being addressed are forward biased to minimize leakage current through those pixels and this leakage is only weakly dependent on the illumination on the photodiode. The OFF and ON behavior of a single pixel are shown in Fig. 7.5(c) for various illumination condictions. The advantage of this design is that the pixels are still two-terminal pixels and can use the simple crosshatch fabrication described above. The two diodes can be fabricated as a thin-film stack similar to the devices presented in chapter 3. This allows simple fabrication schemes for this architecture.

The limitation of this architecture is the reverse-bias leakage of a realistic blocking diode. This leakage can greatly reduce the sensitivity of a pixel in a sensor array. To demonstrate this effect we use an idealized model for the pixel as shown in Fig. 7.5(a). The behavior of the photodiode is assumed to follow:

$$J_1 = J_{s1}\left(\exp\left(\frac{qV_1}{n_1 kT}\right) - 1 + B_1 V_1\right) - J_{ph} \tag{7.1}$$

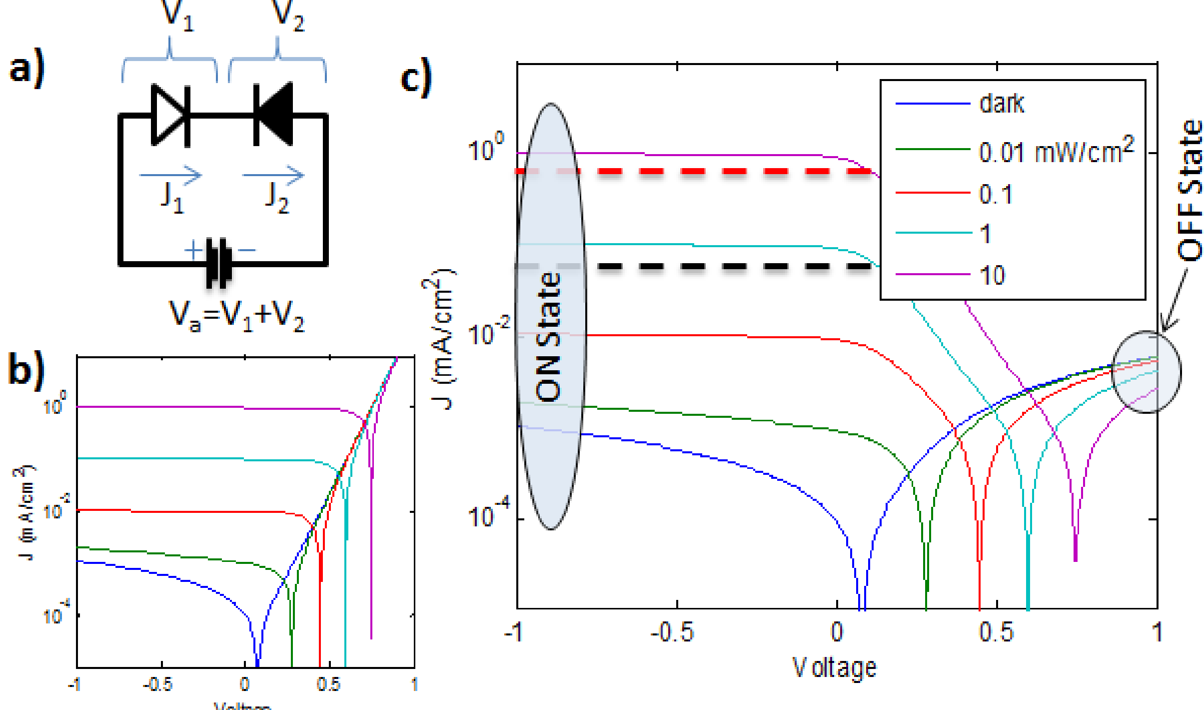

Figure 7.5 – Pixel with a Blocking Diode: (a) Circuit diagram for a pixel incorporating a blocking diode. (b) Simulated illuminated current density verse voltage (*J*-*V*) behavior for a single photodiode. Note that when the diode is forward biased it passes a large current independent of illumination. The color scheme and light intensities are the same as in part (c). (c) Simulated illuminated *J*-*V* for pixel with a blocking diode that shuts down the forward bias current.

where J_{s1} is the ideal diode saturation current, n_1 is the ideality factor, V_1 is the voltage across the photodiode, B_1 is a diode leakage parameter to approximate the interfacial dissociation kinetics (*c.f.* Chapter 3), and J_{ph}, the photocurrent, is assumed to be constant and given by 10% of the incident light intensity. The blocking diode is in reverse polarity and is assumed to follow:

$$-J_2 = J_{s2}\left(\exp\left(\frac{-qV_2}{n_2kT}\right) - 1 + B_2V_2\right) \quad (7.2)$$

where the parameters are similar to those defined above, but have values specific to the blocking diode. Equations 7.1 and 7.2 are coupled by the series circuit requirements that $J_1 = J_2$ and $V_1 + V_2 = V_a$, where V_a is the external bias applied across the pixel. We show the results of this model

for the single pixel under different illuminations in Fig. 7.5(c) using $J_{s2} = 10J_{s1} = 1\text{x}10^{-7}$ A/cm^2, $n_1 = n_2 = 2.5$, and $B_1 = B_2 = 100$ V^{-1}. This figure shows the low current OFF state for the pixel at +1 Volts, as well as the ON state at -1 Volts where the photocurrent is collected efficiently.

When this pixel is used in an array as shown in Fig. 7.4(d), the current measured from the mth column when addressing pixel $m \times n$ is given by

$$J(V, L) = J_{ON}^{m,n}(V, L) + (N - 1)J_{OFF}. \tag{7.3}$$

Here we assume that the OFF current from all the other pixels on the column is a constant (J_{OFF}), which is a good approximation as long as the illumination on the OFF pixels is not so high that the reverse bias across the blocking diode is significantly reduced. From Fig. 7.5(c) we take 10 mW/cm^2 to be the maximum intensity before the blocking diode performance degrades. Next we assume that the photocurrent from the ON pixel must be greater than $J_{ON}^{m,n}(-1, L) > (N - 1)J_{OFF}$ in order to have a sufficient signal to noise ratio for light detection. These upper and lower limits define the dynamic range of the sensor – obviously the lower limit is strongly dependent on the size of the array. For a 10x10 array, the photocurrent from a pixel must be greater than $9 \cdot J_{OFF}$; this lower limit is shown by the black dotted line in Fig. 7.5(c) and results in a dynamic range of ~50 or 6 bits. For a 100x100 array, the photocurrent from a pixel must be greater than $99 \cdot J_{OFF}$; this lower limit is shown by the red dotted line in Fig. 7.5(c) and results in a dynamic range of ~5 or 2 bits. These dynamic ranges can be improved by developing a better blocking diode than used in the simulation, but clearly this pixel cannot be scaled into a large, high-density and high sensitivity sensor array.

7.2.4. Passive Pixel Sensor

To overcome the limitations of the crosshatch diode array, we developed a one-transistor (1-T) passive pixel sensor (PPS). The pixel architecture is shown in Fig. 7.6(a). It incorporates an organic thin-film transistor (OTFT) to toggle the pixel between a low current OFF state and an ON state to read out the pixel photocurrent. We chose to use an OTFT because the same fabrication techniques outlined above can also be used to pattern the OTFT on the hemispherical substrate. Additionally, recent advances in OTFT technologies have demonstrated mobilities > 1 $cm^2/V \cdot s$ and ON/OFF ratios > 10^6, which should be adequate for use in megapixel sensor arrays. The design of the passive pixel architecture also utilizes the intrinsic capacitance of the thin-film photodiode to increase the pixel sensitivity. When the pixel is held in the OFF state, photocurrent is generated by the diode and accumulated on the pixel capacitance. This integrated photocurrent can then be read during a short readout time as the readout electronics cycle through all of the pixels in the sensor. This architecture presents significant fabrication challenges, but solving these challenges will pave the way toward fabricating a high-performance 3- or 4-T active pixel sensor.

Here, we demonstrate a boron subphthalocyanine chloride (SubPc)/C_{60} photodetector monolithically integrated in series with a top gate, pentacene OTFT switch for use as a passive pixel sensor[214] in imaging focal plane array applications that require a low OFF current[17,18]. The integrated structure is fabricated by sequential layer growth using vacuum thermal evaporation of the small molecular weight organic materials. The pixel is activated using the OTFT by applying a negative gate voltage which turns the transistor to the ON (i.e. conducting) state, permitting photocurrent from the OPD to be collected at the source. The device has an 8-bit dynamic range and allows for >400 kHz switching.

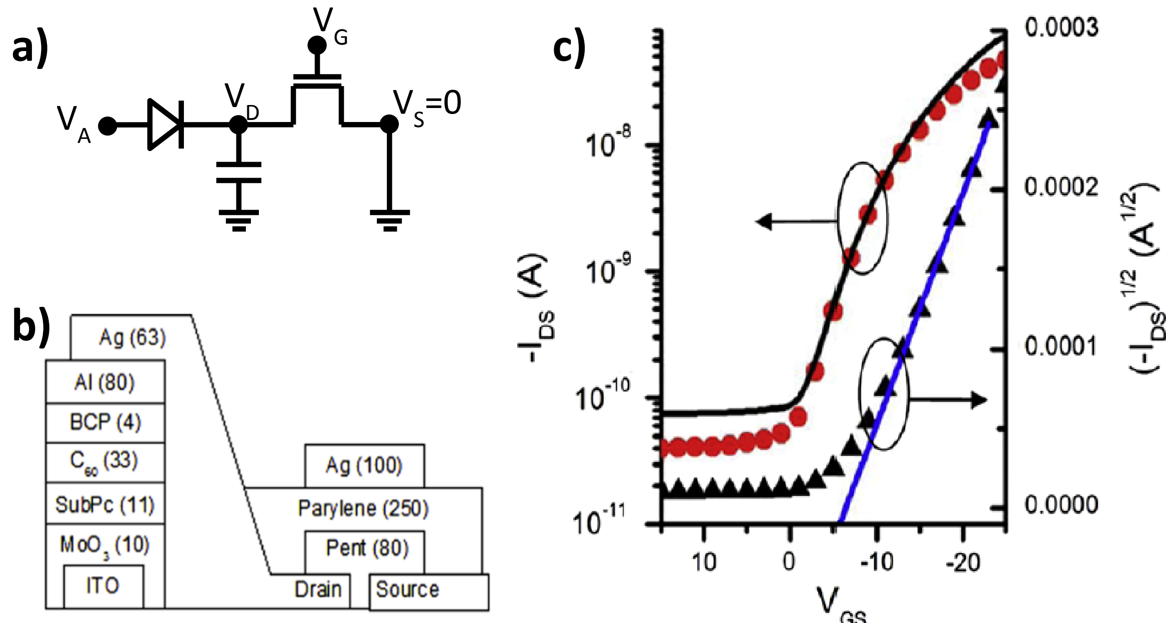

Figure 7.6 – Passive Pixel Sensor: (a) Equivalent circuit for the passive pixel consisting of an organic photodetector (OPD), an organic thin-film transistor (OTFT) and the intrinsic capacitance of the OPD. (b) Schematic cross-section of the integrated pixel structure. Layer thicknesses in parentheses are in nanometers. (c) Top gate pentacene OTFT transfer characteristic at a drain-source voltage of V_{DS} = 17.5 V (solid line) and 7.5 V (circles) for a 500 µm wide by 25 µm long channel. Also shown is the square root of drain-source current $(I_{DS})^{1/2}$, (triangles) with fit to pinch-off region (straight solid line).

A cross-section of the integrated circuit is shown in Fig. 7.6(b). The OPD was fabricated by vacuum thermal evaporation onto a commercially patterned 200 µm wide stripe of 100 nm thick, 20 Ω/sq. indium tin oxide (ITO) precoated on a glass substrate. Prior to organic thin film deposition, the substrate was solvent cleaned and UV ozone treated as described elsewhere[215]. All organic materials were purified by vacuum thermal gradient sublimation and were deposited at 1 Å/s in a vacuum chamber with a base pressure of 1×10^{-6} Torr unless otherwise stated. Prior to deposition of the photoactive layers, a 10 nm thick MoO_3 film was deposited onto the ITO at 0.2 Å/s as a hole transport and electron blocking layer that reduces photodetector dark current[216]. The active layers consisted of a 110 Å thick film of SubPc followed by a 325 Å thick film of C_{60}.

Subsequently, a 40 Å thick layer of exciton blocking and electron transporting bathocuproine was deposited[217]. The cathode, an 800 Å thick Al stripe that was either 100 or 500 μm wide, was deposited through a shadow mask aligned with the ITO anode across the anode stripe defining the detector area. The top gate OTFT was subsequently grown adjacent to the detector with the drain connected to the detector cathode, forming the passive pixel sensor circuit[214]. The OTFT layers were also grown by vacuum thermal evaporation except for the gate insulator. Here, parylene-C gate dielectric was deposited at room temperature after vaporization and pyrolysis to prevent any damage to the pentacene channel. The OTFT structure consists of (from substrate to top gate): a 625 Å thick Ag layer for the drain and source contacts deposited through a second, aligned mask, an 800 Å thick pentacene channel layer (deposited at 0.2 Å/s for the first 300 Å, and 0.5 Å/s for the remainder), and a 250 nm thick parylene-C insulator followed by a 1000 Å thick Ag top gate electrode. Channel widths of 100 μm and 500 μm were employed, each with gate lengths of 25 and 50 microns. During deposition the device was kept in vacuum or in an ultrahigh purity (<1 ppm O2 or H2O) N_2 glovebox except when exposed to air after the cathode, pentacene, and parylene-C deposition steps.

Independent steady state electrical characterizations of both the OTFT and OPD were obtained using a semiconductor parameter analyzer. The OPD was tested in the dark and under illumination at powers as high as 0.33 mW/cm^2, at a wavelength of λ = 578 nm using a Hg lamp with a notch filter. A quartz-tungsten lamp chopped at 190 Hz synchronized with a lock-in amplifier, and filtered by a monochromator was used to determine the detector spectral response. Optical power intensity was measured using a calibrated Si photodetector. The optical pulse response was measured using a N_2 pumped dye laser at λ = 581 nm with a pulse energy of 5 μJ

and duration of 1.5 ns. The switching response of the OTFT was measured using an oscilloscope and a pulse generator connected to the OTFT gate.

The OTFT with a gate width to length ratio of W/L = 20 for a gate width of W=500 μm had a drain-source current, I_{DS}, ON/OFF ratio of 700 when the gate-source voltage, V_{GS}, was varied from -25 V to +15 V (voltages are relative to the source at ground) and at a drain-source voltage of V_{DS} = -17.5 V. The OFF current was approximately I_{OFF} = 80 pA as shown in the transfer characteristics of Fig. 7.6(c). At low V_{DS}, I_{OFF} is reduced but more slowly than the reduction in the ON current resulting in a reduced ON/OFF ratio. Analysis of the transfer characteristics in the pinchoff regime yields a pentacene mobility of μ = 0.0025 cm^2/V·s and threshold voltage of V_{th} = 7 V according to: $I_{DS} = \frac{1}{2}\frac{W}{L}\mu C_i(V_{GS} - V_{th})^2$, where C_i = 8 nF/cm^2 is the capacitance of the parylene-C gate dielectric. The resistance of the OTFT, extracted from I_{DS} vs. V_{DS}, is 220 MΩ at V_{DS} = -5 V with V_{GS} = -20 V. The relatively high resistance and low mobility of the OTFT is due to the top gate, bottom-contact configuration, and air exposure between the pentacene and parylene depositions. Growth of the pentacene channel at elevated temperatures also is known to increase the hole mobility.[218]

The current–voltage (I–V) characteristic of a 200 μm × 500 μm OPD at a wavelength of λ = 578 nm is shown in Fig. 7.7(a), with the wavelength-dependent external quantum efficiency (EQE) shown in the inset. The SubPc response peak at λ = 580 nm and the broader C_{60} peak at λ = 450 nm are apparent.[219] Under reverse bias, the C_{60} peak increases significantly relative to that of SubPc due to increased photoconductivity in the thin film bulk (*c.f.* Chapter 4).[74,207]

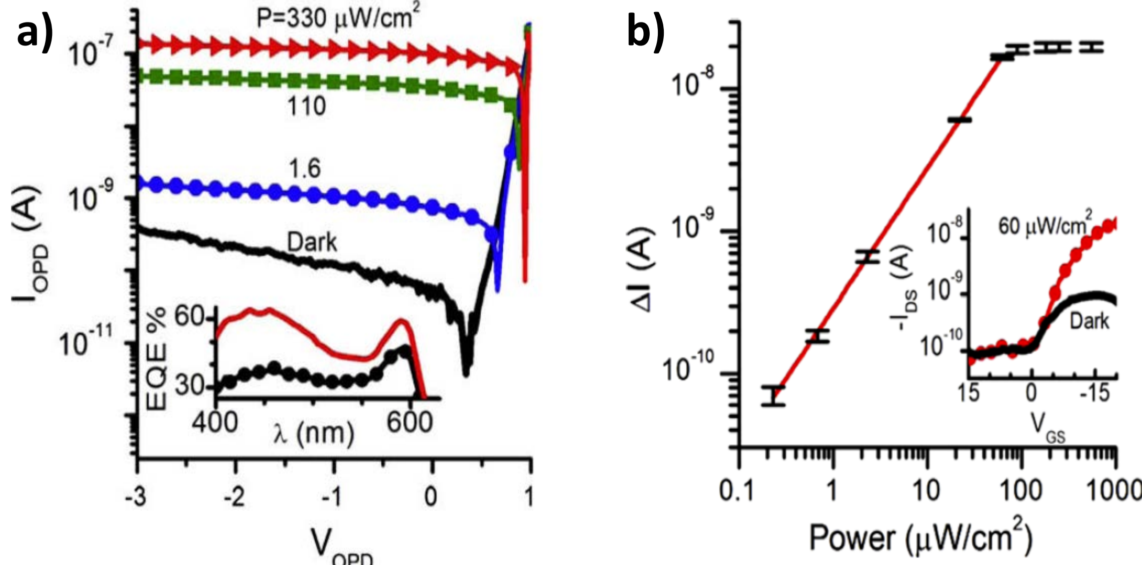

Figure 7.7 – Passive Pixel Sensor Response: (a) Steady state current-voltage (I_{OPD}-V_{OPD}) characteristics for a 200 μm x 500 μm SubPc/C_{60} based OPD in the dark (solid line) and illuminated at a wavelength of λ = 578 nm at 1.5 (circles), 110 (squares), and 330 μW/cm^2 (triangles). Inset: Spectral dependence of external quantum efficiency (EQE) of the OPD, at 0 V (solid line) and at -2.5 V (circles). (b) Power intensity dependent photocurrent of an integrated pixel with a 200 μm x 500 μm OPD, and a 500 μm wide x 25 μm long OTFT channel, illuminated at a wavelength of λ = 578 nm. The photocurrent, ΔI, is the illuminated current minus the dark current. The pixel is in the ON state, with a gate-source voltage of -20 V, and the anode-source voltage is V_{AS} = -5 V. The line is a linear fit of log(ΔI) to log(P) with a slope of 1.01 ± 0.02 and an intercept corresponding to a responsivity of 0.29 A/W. Inset: The anode-source current, I_{AS}, in the dark (solid line) and illuminated at 60 μW/cm^2 (circles) for V_{AS} = -5 V with V_{GS} varied from +15 V to -20 V.

The anode-source current, I_{AS}, of the integrated device is shown in the inset of Fig. 7.7(b) for V_{AS} = -5.0 V. In the ON state at V_{GS} = -20 V, the pixel provides an intensity dependent photocurrent that is suppressed in the OFF state. The ON state photocurrent is plotted in Fig. 7.7(b) as a function of power intensity and shows an 8-bit dynamic range of $DR = \Delta I_{max}/\Delta I_{min} = (I_{max} - I_{dark})/(I_{min} - I_{dark})$ = 300, where I_{max} is the current that is reduced by 1 dB from the linear response of current vs. incident optical power, I_{dark} is the OPD dark current, and I_{min} is the minimum current distinguishable from I_{dark}. This DR is lower than expected from the transfer

characteristic since V_{AS} = -5.0 V is restricted to low voltage to avoid damaging the OPD. The line is a fit of log(ΔI) to log(P) and yields a slope of 1.01 ± 0.02 and intercept of -6.54 ± 0.06, corresponding to a responsivity of 0.29 A/W at λ = 581 nm.

The response of the pixel to a 1.5 ns optical pulse at λ = 581 nm is shown in Fig. 7.8 with V_{GS} = -20 V and OPD anode to OTFT-source voltage, V_{AS}, of -5 V. The signal is measured on an oscilloscope with a 1 MΩ load that is much less than the channel resistance, and an exponential fit has a decay time of 60 ms. The response time of the OPD alone is approximately 10 ns,[147] and the long response time corresponds to discharge through the OTFT. Improving the mobility of the OTFT by improving molecular ordering of the pentacene film and preventing air exposure between the channel and gate insulator deposition steps can reduce the time required to extract photogenerated charge from the pixel. The electrical pulse response of the integrated device under illumination is shown in the inset of Fig. 7.8, with V_{AS} = -10 V and with a 50 ms long pulse of V_{GS} = -20 V applied to the transistor gate. A resistance–capacitance (RC) time of 1.3 μs is required to charge the OTFT using a 5 kΩ load, resulting in a switching frequency of 400 kHz.

The OPD has a linear response over more than 5 decades in power intensity, so the *DR* is limited by the performance of the OTFT which limits the photocurrent of the OPD at high light intensity. For small photocurrents, the OTFT operates in a linear, resistive regime where $V_{DS} \propto I_{DS}$, and all the photocurrent can be extracted through the transistor. For large currents, the OTFT saturates and the forward bias on the OPD is diminished since the total voltage across the circuit, $V_{AS} = V_{OPD} + V_{DS}$, is fixed. This restricts the photocurrent to the ON current of the OTFT. The OTFT ON current could realistically be improved toward reported values of 10^{-6} A by improving

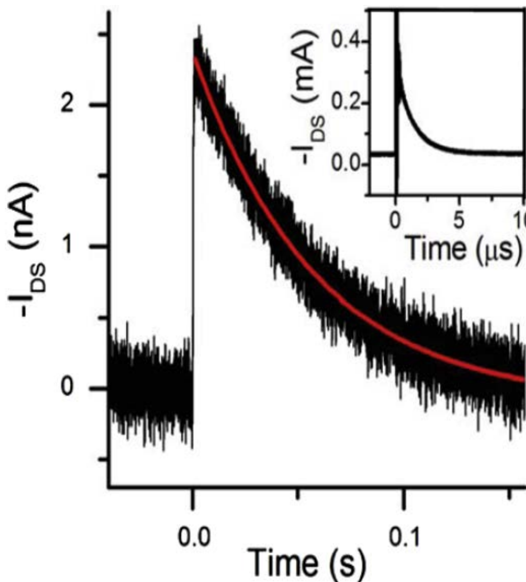

Figure 7.8 – OTFT Switching Speed: Optical pulse responsethrough a 1 MΩ load of an integrated pixel, with a 200 μm x 100 μm OPD and a 500 μm wide x 25 μm long OTFT channel. The optical pulse is 1.5 ns long with a pulse energy of 5 mJ centered at a wavelength of λ = 581 nm. The anode-source current, I_{AS}, decays exponentially with a 60 ms time constant, shown by the fit (red line). Inset: OTFT switching response of the pixel with 5 kΩ load due to a 800 ms long, gate-source voltage pulse of -20 V. The response time of 1.3 μs corresponds to a frequency response of > 400 kHz.

fabrication techniques.[220] This would result in a dynamic range of 13 bits for the same dark current.

This device has applications in systems that require low dark current, for example, sensors with multiple detectors sharing a common output as is typical of most imaging focal plane arrays. The integrated OTFT in the OFF state reduces the OPD dark current by a factor of 10, enabling the fabrication of a sensor comprised of 10 × 10 array blocks with integrated OFF currents comparable to that of a single detector. Optimization of the OTFT performance to reported OFF currents <4 pA characteristic of discrete, top gate pentacene OTFTs can extend array sizes to >100 × 100.[221] Since the vertical integration achieved using layer-by-layer growth requires no complex patterning processes, it preserves the potential low cost of organic

electronics. In addition, the room temperature processing including gate insulator deposition makes this process compatible with flexible plastic substrates.

In conclusion, we have demonstrated a monolithically integrated, small molecular weight OPD plus OTFT passive pixel sensor circuit with an 8-bit dynamic range, a switching time of >400 kHz, and an OFF current of <50 pA. This circuit has applications in focal plane detector arrays for high sensitivity imaging applications.

7.2.5. A 10×10 PPS Array

In the previous section, we demonstrated a discrete pixel consisting of an organic photodetector (OPD) integrated with an organic thin film transistor (OTFT).[222] Here, we demonstrate a 10×10 organic passive pixel sensor array that combines boron subphthalocyanine chloride (SubPc)/C_{60} photodetectors monolithically integrated with a top gate, pentacene transistor with parylene-C as the gate insulator. The integrated pixels have a dynamic range of 300 (corresponding to an approximately 8 bit resolution) and a 2.2 ms readout time that is adequate for a 30 frames per second (fps) video standard.

Each pixel in the array consists of an anode (A) and source (S) column, and a gate (G) row. When a gate row is at ground for integration, each pixel on that row stores photocurrent on the photodetector junction capacitance. When a negative gate voltage is applied, a row of transistors are switched to the ON (i.e. conducting) state, and the stored charge is then read out through the OTFT and collected at each source column.

We first pattern ten, 40 nm thick, 280 μm wide Au semitransparent anode stripes by shadowing mask. Next, a second mask is aligned to the anodes to pattern a 600 μm wide by 1.4 cm long photodetector over the anode stripes, using locating pins mounted into a substrate

holder. The OPD materials, consisting of a 10 nm thick MoO_3 electron blocking layer, a 11 nm thick boron subphthalocyanine chloride (SubPc) donor, a 32.5 nm thick C_{60} acceptor and a 10 nm bathocuproine (BCP) exciton blocking layer, are thermally evaporated at 300 μm distance from the OTFT channel region to prohibit the OPD leakage current from increasing the OFF state current of the OTFT. Next, a 100 nm thick Au and 15 nm thick MoO3 bi-layer is patterned using a third mask aligned to the deposited patterns to define the drain interconnects and source contacts. A 350 μm wide drain interconnect overlaps the anode column, forming a 280 μm × 350 μm OPD, and results in a L=80 μm TFT channel with a 250 μm wide by 1.7 cm long source column parallel to the anodes. Pentacene is then deposited at 0.2~0.5 Å/s to a thickness of 55 nm on top of drain/source contacts, followed by the deposition of a 370 nm thick parylene-C insulating layer over the entire surface. Finally, a 100nm thick by 280 μm wide (W) Ag gate row is deposited orthogonal to the anode and source stripes, and overlaps the channel region to result in an OTFT with a gate geometry of W/L=7/2 (see Fig. 7.9(a)).

The current-voltage characteristics of an OPD measured in the dark and under various illumination intensities at λ=578 nm are shown in Fig. 7.9(b), with a rectification ratio in the dark of ~10^4 at an operation voltage of V=±2 V. The photocurrent increases linearly with illumination intensity at λ=578 nm, resulting in a dynamic range >10^5 (i.e. >16 bits). The external quantum efficiency at zero bias of the OPD has a peak of 12.4% ±0.3% at a wavelength of λ=600 nm.

The drain-source current of the top-gate, bottom-contact pentacene TFT is measured at V_{DS} = -2V, -5V, -10V, showing an ON/OFF ratio of 100 when the gate-source voltage, V_{GS}, varies from +10 V to -40 V. The OTFT has an OFF current of 80 pA when V_{DS} = -2V. The mobility, μ, at V_{DS} = -10V is calculated to be 0.004 $cm^2/V\cdot s$ and the threshold voltage is V_{th} =

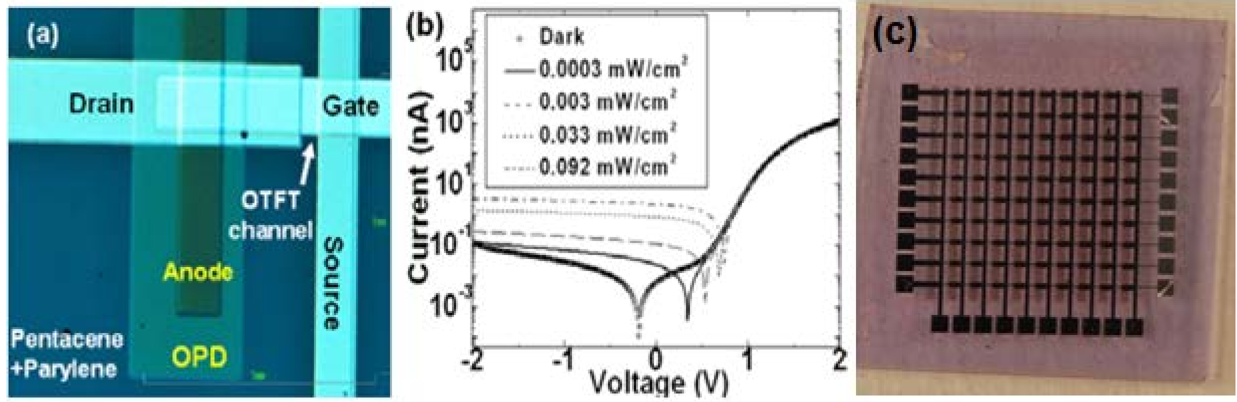

Figure 7.9 – 10x10 Passive Pixel Array: (a) Microscopic image of a single integrated pixel in a 10x10 array. (b) Current-Voltage characteristics of the OPD from -2 V to +2 V bias illuminated at λ = 578 nm at various intensities. (c) Photograph of the 10x10 array. Source and anode contacts form columns (the anode is transparent and not visible). The gate contacts are on the right, while the left contacts are connected to the drain/cathode of the first row (the interior drain/cathode do not have contact pads).

3.75 V. Since the transistor is grown in the top gate and bottom drain/source contact configuration, the mobility of the OTFT is about 25 times lower than an optimized bottom gate structure.[221]

The integrated pixel is characterized at an anode-source voltage, V_{AS}, of -2 V, with V_{GS} varied from +10V to -40V, as shown in Fig. 7.10(a). The source current significantly increases with light intensity when the gate is turned on, and remains in an OFF state when V_{GS} = 10V. The ON current of the integrated pixel shows a linear dependence on light intensity from 300 nW/cm^2, the lowest detectable power intensity, to 90 μW/cm^2 where the photocurrent deviates from linear behavior by ~1dB. This dynamic range of 300, corresponding to an 8-bit gray scale, is lower than that of the discrete OPD since the photocurrent is limited by the ON current of the OTFT. With an optimized pentacene TFT, the ON current may be increased by >10 times. [221]

The response of the integrated pixel to a -15 V, 99 ms long electrical pulse applied to the transistor gate using a 1 MΩ load is measured at V_{AS} = -5 V. A bi-exponential is required to fit

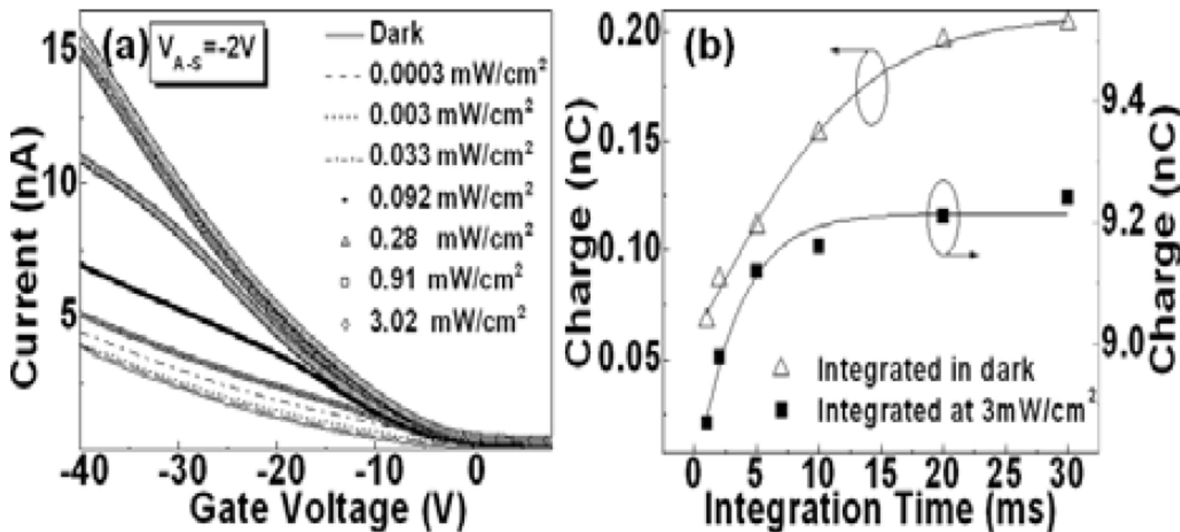

Figure 7.10 – Array Response: (a) Anode-source current of the integrated pixel illuminated at various intensities at λ = 578 nm and under various gate voltages, for anode-source bias V_{AS} = -2 V. (b) Total stored charge verse integration time in the dark (triangle), and at 3 mW/cm^2 illumination (square).

the pixel response. The first time constant, t_1=370 μs, is the switching time of the OTFT, determined by the resistance-capacitance (RC) time required to charge the gate-source capacitance, and to apply the gate-source voltage through the load. The corresponding switching frequency of >400 Hz is sufficient for operation at a 30 Hz frame rate, and can be increased to 67 kHz using a standard, 600Ω video load, albeit with a corresponding reduction in signal amplitude. The second decay time constant, t_2 =2.2 ms, corresponds to the discharge time through the OTFT to read out the stored charges on C_{OPD} during integration. This time is equal to $t_2 = R_{ON,TFT} \times C_{OPD}$. It is sufficiently fast for 15 rows to be sequentially output to achieve 30 Hz frame rate video standard. Since the readout time constant is determined by the ON resistance of the TFT, a mobility of 0.1 cm2/Vs from an optimized pentacene TFT is required to achieve 30 Hz frame rate for a 128×128 passive sensor array.[221] Alternatively, slower transistor response can be accommodated in large FPA's by employing parallel read out of smaller, segmented array blocks.

When the integration time is varied from 1 ms to 30 ms in the dark, the areas under the response curves indicate that the total stored charge increases until the OPD saturates at 30 ms (see Fig. 7.10(b)). When the illumination during integration is increased to 3mW/cm2, the integrated current is higher, which results in saturation of the OPD capacitor at a shorter time of ~ 10 ms.

In conclusion, we demonstrated a 10×10 passive pixel sensor array comprised of monolithically integrated organic photodiodes with pentacene TFTs. The 200 device FPA has an 8-bit dynamic range and a readout time of 2.2 ms, sufficient for achieving > 30 Hz frame rate. Due to the room temperature fabrication employing soft organic materials, it is feasible to realize such passive pixel sensor arrays on flexible plastic or curved surfaces with higher resolution (e.g. ~ 1 μm) by cold welding.[17,18] The mobility of the pentacene TFTs can also be improved by optimizing the growth conditions and gate dielectric properties. In this case, the ON resistance of the TFTs can be reduced by at least a factor of ten.

7.2.6. Scaling to High-Density Arrays

The shadow masking techniques used to fabricate the 10×10 PPS array are not sufficient to scale down to fabricate complex high density arrays. Complex high-density arrays require small features and small tolerances on the alignment registration between multiple patterning steps, both of these are challenging tasks for shadow masking. Additionally, established shadow mask techniques are not compatible with fabrication on non-planar surfaces. Here, we demonstrate techniques to pattern high-density devices using the stamp transfer patterning techniques introduced in Section 7.2.1.

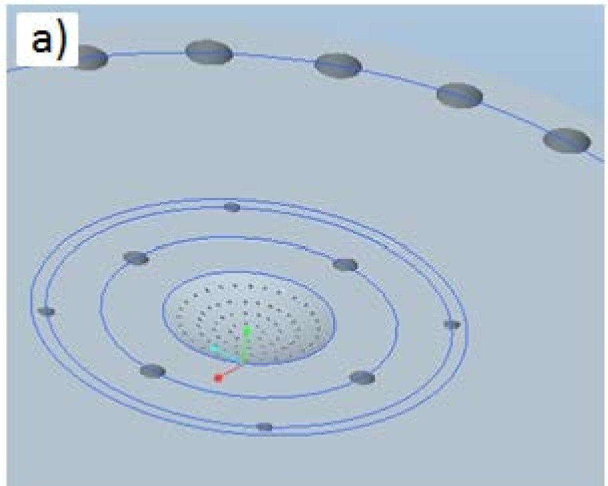

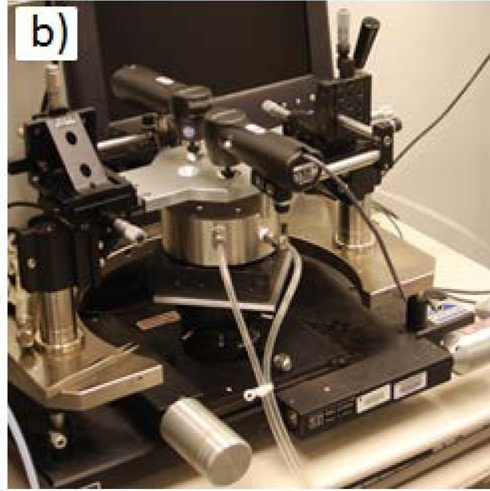

Figure 7.11 – Aligned Stamping: (a) CAD model of three stage vacuum chuck for aligned stamping. The first stage is the hemispherical cutout in the center used for forming and stamping on the hemispherical substrate. The second stage is the 4 large holes just outside of the hemisphere and is used for holding the stamp in place. The third stage is the outer set of 4 small holes used to hold the substrate in place after alignment. (b) Photograph of the alignment station used for aligned stamp-patterning.

To meet the HARDI goals, we must develop techniques to fabricate a 128x128 and ultimately a 1000x1000 pixel array on a 1cm radius hemisphere. This requires a pixel pitch of less than 250 μm and 30 μm respectively. To do this we extend the lithographically based stamping technique to perform aligned stamp patterning. To do this we designed a three-stage vacuum chuck and a modified probe station as shown in Fig. 7.11(a) and (b). The inner stage of the vacuum chuck is used to elastically deform the active region of a PDMS stamp into a hemisphere. The edges of the stamp are held in place on the vacuum chuck by the four large holes connected to the second stage of the chuck. The third stage of the chuck consists of the four small outer holes that will be used to hold the PET substrate in place after alignment has been performed.

Alignment fiducials are designed into every pattern that is stamped to enable alignment between successive stampings. The alignment between patterns is performed using the probe

station in Fig. 7.11(b). The center of the figure shows a cylindrical aluminum stamp chuck with two vacuum hoses attached to it. This chuck is fixed onto a 4-D stage that enables X,Y,Z translations and θ rotation. This allows four degrees of freedom for alignment of the stamp to the PET substrate that is suspended face-down above the chuck and is held in place by a fixed secondary vacuum chuck. Two microscope imagers on 3D stages are positioned above the secondary vacuum chuck looking through cut-outs and through the transparent PET substrate at the alignment marks of the pattern on the PET. By slowly raising the stamp to the substrate, the alignment marks on the stamp can be found and the stamp can be properly aligned to the substrate. The two are brought into contact, the third stage vacuum is turned on to hold the substrate to the vacuum chuck, and the substrate is released from the secondary vacuum chuck by turning its vacuum off. Now the assembly can be taken to the press to transfer flat patterns or the first stage vacuum can be turned off to allow the hemispherically deformed PDMS to elastically relax on the substrate and transfer the hemisphere region.

To fabricate a 128x128 passive pixel OPD and OTFT array, we design the mask patterns for this array shown in Fig. 7.12. The active region is a square with edge length of 1.7 cm and the pixel pitch is 135 μm. To facilitate making electrical contacts to the device, we fan the contacts out to a 4” pattern so we can easily probe the 128 source and anode columns and the 128 drain and gate contacts as shown in Fig. 7.12(a). Figure 7.12(b) shows the detail of the source fan out connecting to the source columns in the active region. The pixel layout is shown in Fig. 7.12(c) and (d). A 50 μm wide anode column runs parallel to a 20 μm wide source column. A 100x65 μm^2 drain/cathode overlaps the anode to define the width of both the OPD and the OTFT channel. The drain/cathode feature is designed on the same mask as the source to give reliable channel lengths free of registration errors. The gate pattern is shown in green in Fig. 7.12(d) and

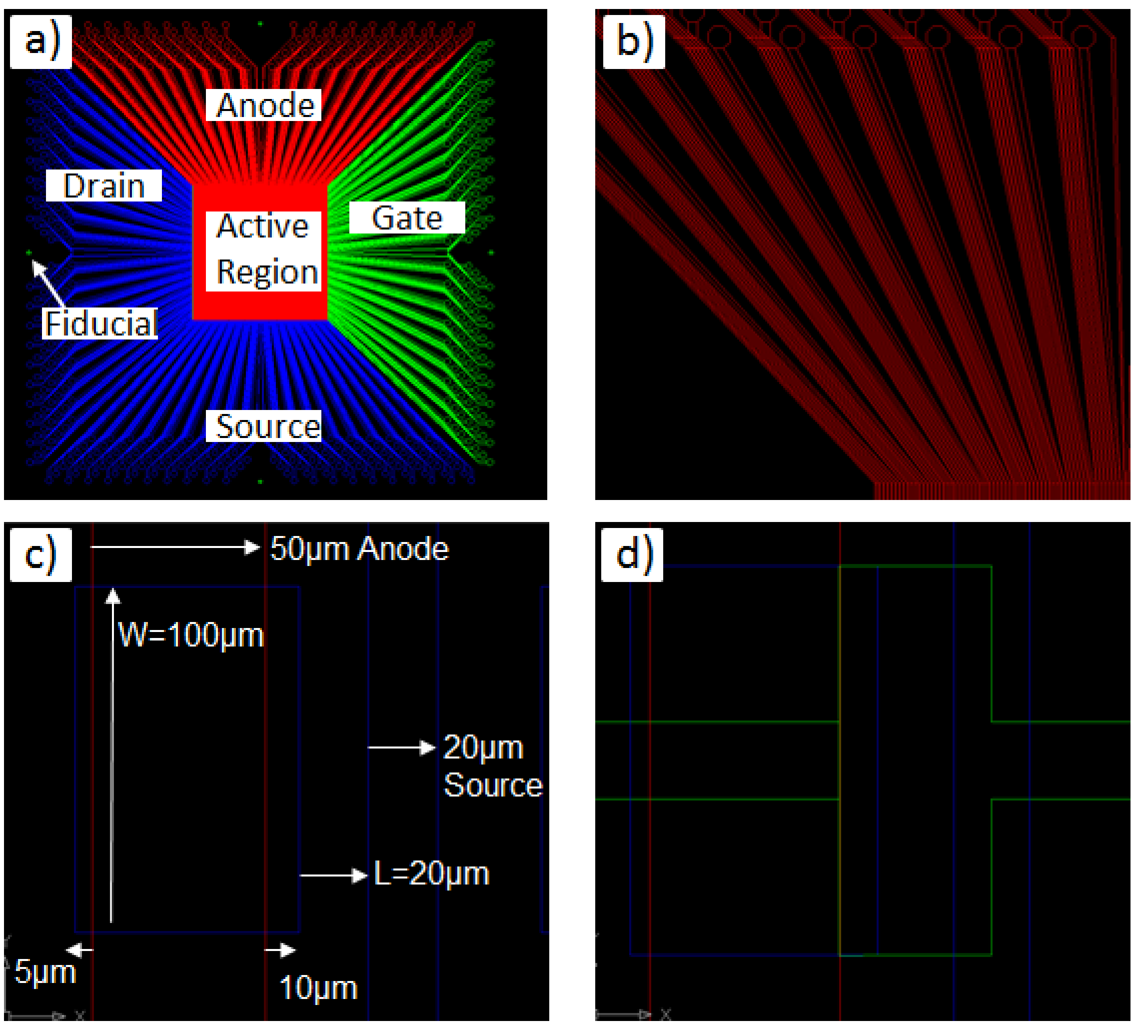

Figure 7.12 – 128x128 Passive Pixel Array Design: (a) Array patterns for a 128x128 passive pixel sensor utilizing an OPD and OTFT. This full view shows the fan out for contacting and addressing the ~16,000 pixels. The sensor area is the 1.7 x 1.7 cm^2 area at the center. (b) Detail of the fan out for the anode. (c) Detail of the anode and drain/source patterns and how they overlap. (d) Detail of the full pixel structure including the overlapping gate row.

consists of a wide region that completely overlaps the OTFT channel between the drain and source. The gates are interconnected along a row by a 20 µm wide interconnect.

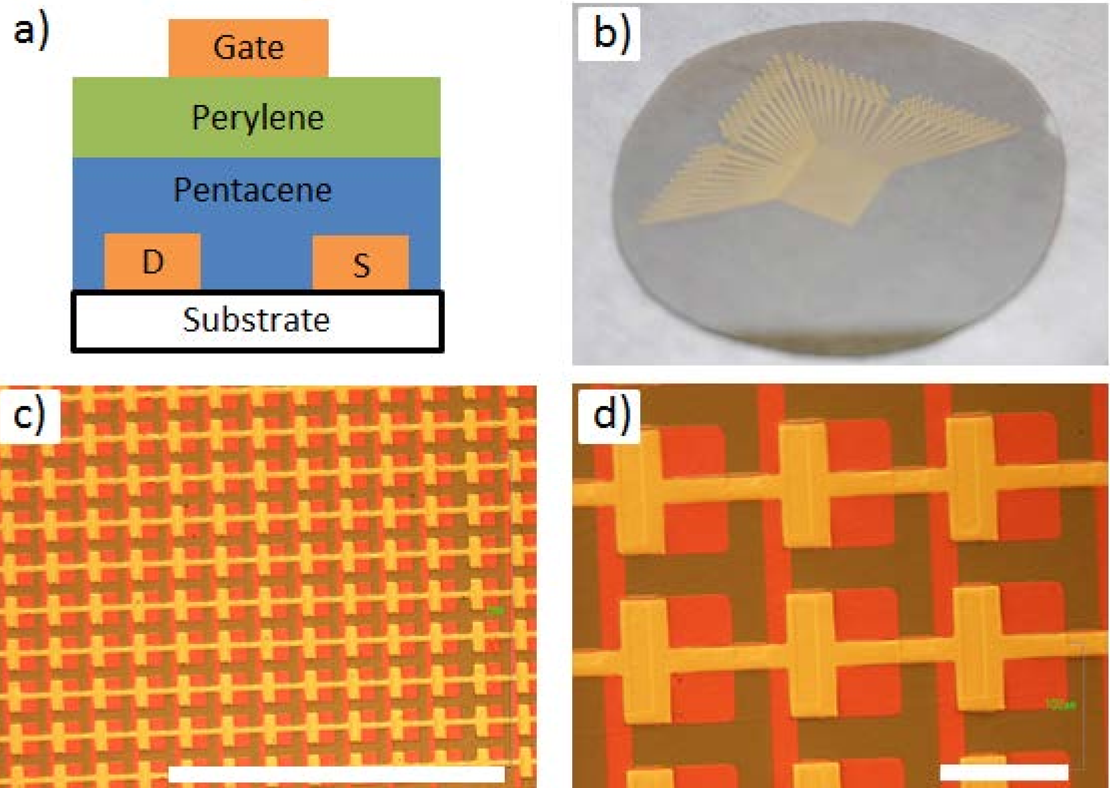

Figure 7.13 – OTFT Array Fabrication: (a) Structure of the top-gate bottom-contact organic thin-film transistor (OTFT). (b) Full view of a 4" circular, flat PET substrate with drain/source pattern and pentacene and perylene layers. (c) Microscope image of the sensor area after the gate pattern is applied by aligned stamping.. The process has high patterning yield and uniformity. (d) Close-up of six OTFT devices in the array. We achieve very accurate registration with < 1 μm error in the relative placement of the patterns.

To demonstrate high-resolution aligned patterning, we fabricated a 128x128 OTFT array on a flat PET substrate using the drain/source and gate patterns above. First we stamp the drain/source pattern onto PET. Then we deposit 80 nm of pentacene, a p-type organic transistor material, over the whole substrate. Next we deposit 250 nm of perylene-C as the gate dielectric. Then we deposit a Au strike layer and stamp the gate pattern aligned with respect to the drain/source. Etching the strike layer completes the array. The device structure is shown in Fig. 7.13(a) and Fig. 7.13(b) shows a photograph of the patterned drain/source contacts on PET. Microscope images of the completed array are shown in Fig. 7.13(c) and (d). The microscope

images show the high yield and high registration accuracy of the multilayer stamp-patterning process.

Using the OTFT structure above (c.f. Sect. 7.2.4) in a high density sensor array presents several challenges. The ON/OFF ratio of 10^3 characteristic of the transistor is satisfactory for an array of up to 1000x1000. However, the low mobility requires a large OTFT width in order to pass the photocurrent generated by the OPD. Scaling the OTFT to small channel lengths in order to increase the ON current of the transistor quickly begins to degrade the ON/OFF ratio resulting in poor OFF current leakage. For a 128x128 array, this requires that a large a fraction (more than 50%) of the pixel area be used for the transistor, and this reduces the sensitivity of the sensor. For a higher density array, shrinking the transistor by a factor of 10 while matching it to the photodetector output and maintaining a sufficient ON/OFF ratio becomes a formidable challenge. Scaling OTFTs down to the order of 10x10 μm is an interesting challenge rooted fundamentally in understanding the leakage processes present in OTFTs. While this understanding could provide a valuable technological advance, it is not practical to address this fundamental problem within the scope of the HARDI project. Instead, we leverage the novel techniques developed here, but change our process to utilize high performance inorganic transistors with our broadband organic detectors and fabricate a hybrid imaging array (c.f. Chapter 8.3).

7.3. Conclusions

In summary, we have developed techniques to fabricate a visible/near-infrared hemispherical imaging array. We have demonstrated sensitive, broad-band detection using organic photodetectors based on carbon nanotubes.[147] We have demonstrated high resolution

patterning techniques for organic semiconductors with precise registration between multilayer patterns enabling the fabrication of advanced devices. We have demonstrated crosshatch OPD arrays and single transistor, passive pixel sensor arrays. Now that we have the techniques to fabricate high-density devices, we begin to be limited by the performance of the OTFT. Due to the low conductivity of organic semiconductors, it is challenging to scale OTFTs to the small device size required for the HARDI program. To meet the HARDI program requirements, we replace the OTFT with a crystalline inorganic transistor and began developing a hybrid OI hemispherical imaging array. The current developments and the future work for this hybrid array are summarized in Chapter 8.3.

Chapter 8

Conclusions and Future Work

8.1. Conclusions

In the first chapter, we discussed why traditional inorganic semiconductor technologies are not well suited for two important classes of devices: large area optoelectronics and flexible electronics. Large area optoelectronics are necessary for applications such as solar cells and large format displays, while flexible electronics are desirable because they can be portable, lightweight, robust, and even inexpensive. The motivation of this work was to advance our understanding of organic electronics, because they are ideally suited both of these applications. We leveraged the knowledge and fabrication techniques developed for inorganic semiconductors in order to develop models to describe the operation of organic and hybrid organic/inorganic heterojunctions (OI-HJs) (Chapters 2-6) and to develop high-resolution fabrication techniques for flexible and non-planar devices (Chapter 7). An important consequence of this approach is that we identify how the disparate theories developed for inorganic versus organic semiconductors can be brought together and utilized in conjunction to design hybrid OI devices.

Hybrid OI devices have already demonstrated promising performance in dye-sensitized and III-V solar cells.[156,223] We anticipate that the theoretical foundations presented in this work will aid the development of even better performing devices. To carry this work forward, we are investigating OI-HJs using crystalline inorganics, where the inorganic properties can be very well controlled in order to validate the theoretical model and address important fundamental questions – for example, what is the minimum valence band to HOMO level discontinuity in order for interface recombination (*c.f.* Chapter 5) to dominate hole injection (*c.f.* Appendix A).

The fabrication techniques demonstrated here could enable high performance flexible and non-planar devices. Specifically, the development of hybrid organic and inorganic devices on flexible substrates provides the opportunity to utilize the optimal characteristics of both materials in a monolithically integrated device. In Section 8.3 we discuss the current development and future work required to demonstrate a flexible hybrid sensor array.

8.2. OI HJ with crystalline Inorganics

Using crystalline inorganics in an OI-HJ will enable us to explore the theory presented in Chapter 5 and characterize the transition between current conduction mechanisms outlined in Appendix A. The well-defined and controllable properties of crystalline inorganics provide an ideal platform to test the theory under various conditions – for example, one can use a set of organic materials with slightly different HOMO energy levels to explore the dynamics at the interface (similar to the method in Chapter 3). This detailed understanding of the recombination process is essential to optimizing devices for photovoltaic performance. Similarly, understanding the injection process over the OI barrier versus the interface recombination rate is necessary to optimize other device structures such as hybrid light-emitting diodes.

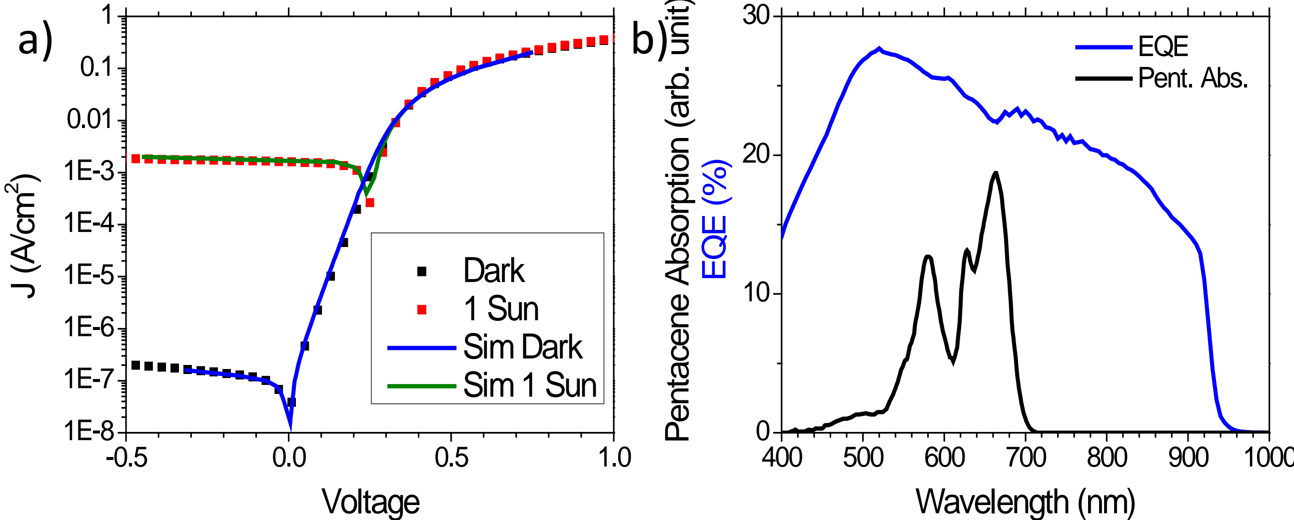

Figure 8.1 – Hybrid OI with Crystalline Inorganics: (a) Current density versus voltage characteristics of a InP (wafer, $n = 10^{18}\ cm^{-3}$) / InP ($1\ \mu m, n = 10^{16}\ cm^{-3}$) / Pentacene (20nm) / Au (20nm) device. The dark current (black symbols) and 1-sun illuminated current (red symbols) are shown along with fits to the theory presented in Chapter 5 (solid lines). (b) The external quantum efficiency for photon to electron conversion (EQE) is shown (blue line) along with the absorption spectrum of Pentacene (black line). Note that the EQE is dominated by InP photoresponse.

To begin this investigation we fabricated a 1 μm thick, lightly doped n-type ($10^{16}\ cm^{-3}$) InP active layer on an n^+ InP wafer. We completed the device fabrication by depositing 20nm of Pentacene followed by a semitransparent layer of Au (20 nm thick). Figure 8.1(a) shows the resulting current density versus voltage characteristics (symbols) in the dark and under 1-Sun illumination. The model presented in Chapter 5 shows a good fit to the dark and illuminated device characteristics (solid lines). The external quantum efficiency (EQE) for the device is shown in Fig. 8.1(b) along with the absorption spectrum of Pentacene. There is a slight reduction in the EQE at the pentacene absorption due to less efficient charge generation from the excitonic Pentacene layer than from direct carrier generation in the InP. Future experiments will test the model predictions over a wide-range of conditions including varied temperature, light intensity,

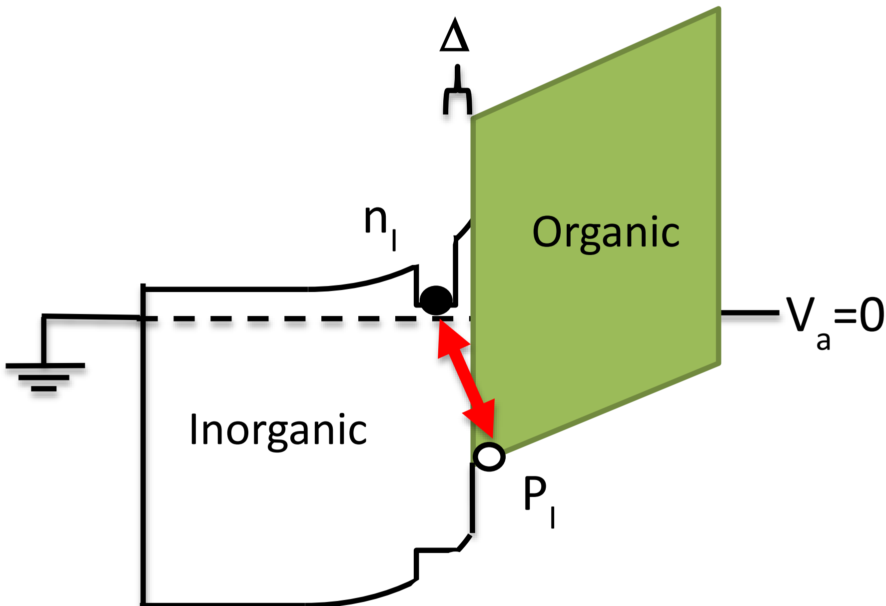

Figure 8.2 – Quantum Well at OI Heterojunction: A quantum well (QW) at the organic/inorganic heterojunction (OI-HJ) would provide an ability to control the formation of the hybrid charge transfer exciton (HCTE). Separating the QW by a distance Δ would reduce the electron and hole interaction across the interface, while the depth of the well can be used to tune the density of electrons in the inorganic at the OI-HJ.

and voltage. Additionally, capacitance-voltage measurements can be used to identify the charge distribution in the device to compare against model predictions.

The existence and properties of the hybrid charge transfer state (HCTE) can be studied utilizing the precision crystal growth available through molecular beam epitaxy (MBE). The HCTE is a novel state with unique properties due to the dissimilar characteristics of the constituent materials, and these properties may be suitable for novel applications. As an example experiment, the strength of the electron and hole interaction across the interface (*i.e.* the binding energy of the HCTE) could be tuned by growing a quantum well (QW) in the inorganic crystal adjacent to the OI-HJ. Figure 8.1 shows a sample structure for this experiment. The QW energy levels can be tuned via composition or width of the QW. A deeper QW would increase the number of electrons at the interface and enhance the formation of HCTEs. Alternatively the QW

can be separated from the OI-HJ by a small distance to directly control the HCTE binding energy.

8.3. Existence of Charge Transfer State: Monte Carlo Simulation

In Section 2.4 we discussed the two models for charge generation from an excitonic heterojunction. Even in a purely excitonic system, the role of a stable charge-transfer state is under debate – is it an intermediate step to generating free charge or is it so tightly bound that it exclusively leads to recombination? Addressing this question directly requires ultrafast spectroscopy to examine population of states and the temporal behavior of photocurrent under various conditions. I outlined an alternative statistical approach in Eqs. 2.22-2.23 using a simple one-step model. To be more realistic, a Monte Carlo approach similar to that done by Peumann, *et al.* could be performed, while taking these alternative pathways into consideration and accounting for the electric field profile through the device.

8.4. Hybrid Sensory Array

The scaling of organic transistors for use in a high-density sensor array is a very challenging prospect. However, recent demonstrations of epitaxial lift-off[12] techniques to produce thin and flexible inorganic devices suggest that we may be able to integrate high-performance inorganic transistors with our OPD array on a semi-rigid substrate. These technologies were developed to fabricate high-efficiency, more cost effective, and flexible III-V photovoltaics. The process begins by growing an epitaxial PV structure on top of a sacrificial layer that is grown on top of the substrate wafer. Then the epi is bonded (by cold-welding for example) to a flexible Kapton substrate resulting in the stack shown in Fig. 8.3(a). Next the sacrificial layer is removed by a chemically selective etch that does not disturb the epi. The result

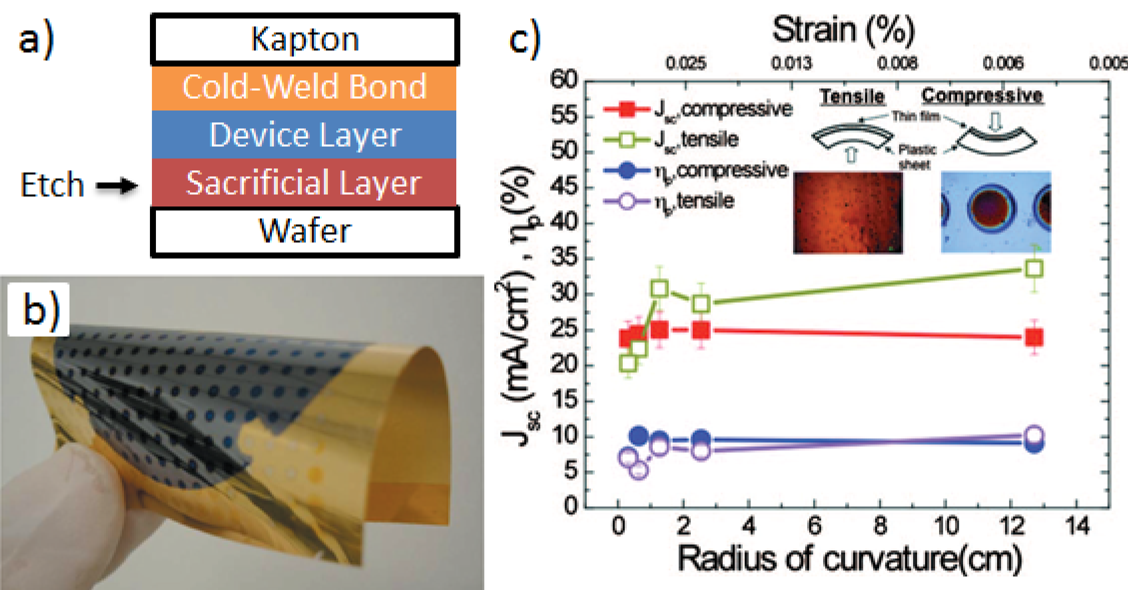

Figure 8.3 – Flexible Inorganics: (a) Structure of lift-off assembly after the wafer, complete with a sacrificial layer and device layer, are cold-weld bonded to a Kapton substrate. The sacrificial layer will be etched to release the device layer from the wafer. (b) Photograph of thin GaAs PV cells transferred to a flexible Kapton substrate. (c) Photovoltaic performance of flexible InP PV cells after being bent to the specified radius. Reproduced from Ref. 11.

is that the entire active region of the III-V based device (only a few microns thick) can be transferred to the plastic. Because the semiconductor device is so thin, it can be bent to < 1 cm radius of curvature without any loss in solar cell performance.[11] The flexible solar cell is shown in Fig. 8.3(b) and the device performance after bending at different radii is shown in Fig. 8.3(c).

8.4.1. III-V Transistor Fabrication

If we can integrate inorganic devices with our non-planar sensor array, we can utilize high-mobility and high ON/OFF ratio inorganic transistors that can easily be scaled to small sizes and replace our low mobility and large size OTFT. This would enable us to integrate the superior electronic properties of inorganic devices with the superior optical properties of our strongly absorbing and broadband organic photodetector.[147]

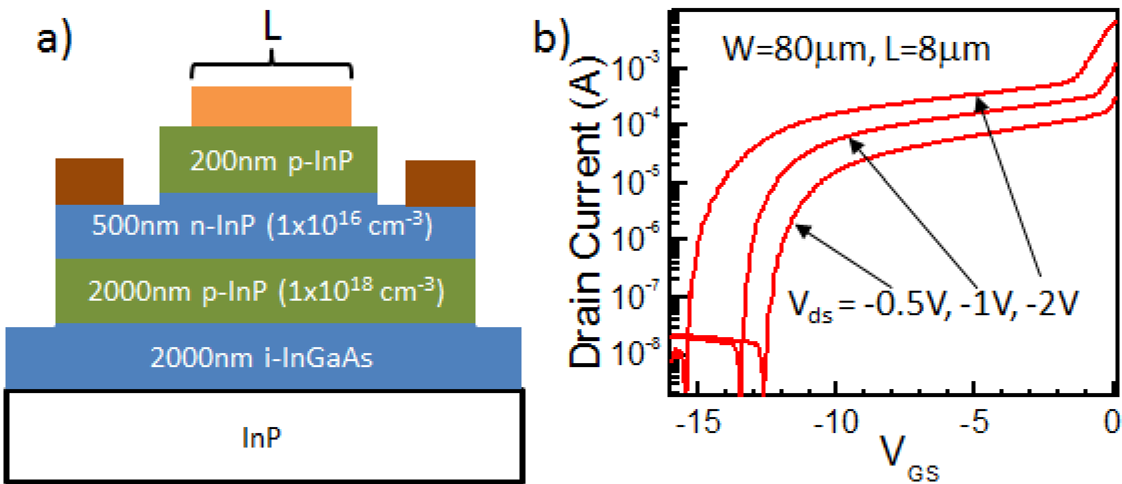

Figure 8.4 – InP JFET: (a) Structure of an InP junction field-effect transistor fabricated on an InP wafer. The drain and source contacts are shown in brown, while the gate contact is shown in orange. (b) Transfer characteristics for a JFET with an 80 μm wide x 8 μm long channel at various drain-source bias voltages (V_{ds}). When zero gate voltage (V_{GS}) is applied, the channel conducts freely, at large reverse bias the channel become fully depleted and can transport little current.

To demonstrate the utility of this novel design we fabricate an InP junction field-effect transistor (JFET). The finished device structure is shown in Fig. 8.4(a). On the InP wafer we grow a 2 μm thick InGaAs etch stop layer, followed by a 2 μm thick p-type InP carrier confinement layer, then a 0.5 μm thick n-type InP channel layer and a 0.2 μm highly doped p-type InP gate layer. The transfer characteristics of this device with an 80 μm wide by 8 μm long channel are shown in Fig. 8.4(b). At VDS = -2 V the device has an ON/OFF ratio > 10^4 and an ON current of ~ 1 mA. This device has not been optimized, most notably a mesa sidewall passivation by p-type diffusion doping would reduce surface recombination and enable > 10^5 ON/OFF ratio with a carrier mobility > 1000 cm^2/Vs.[224]

To geometrically optimize this structure, we design a series of devices varying the channel length and width, where Fig. 8.5 shows the mask designs for a channel length variation for 10 μm wide devices. The fabrication steps using these masks (without the contact fan-out)

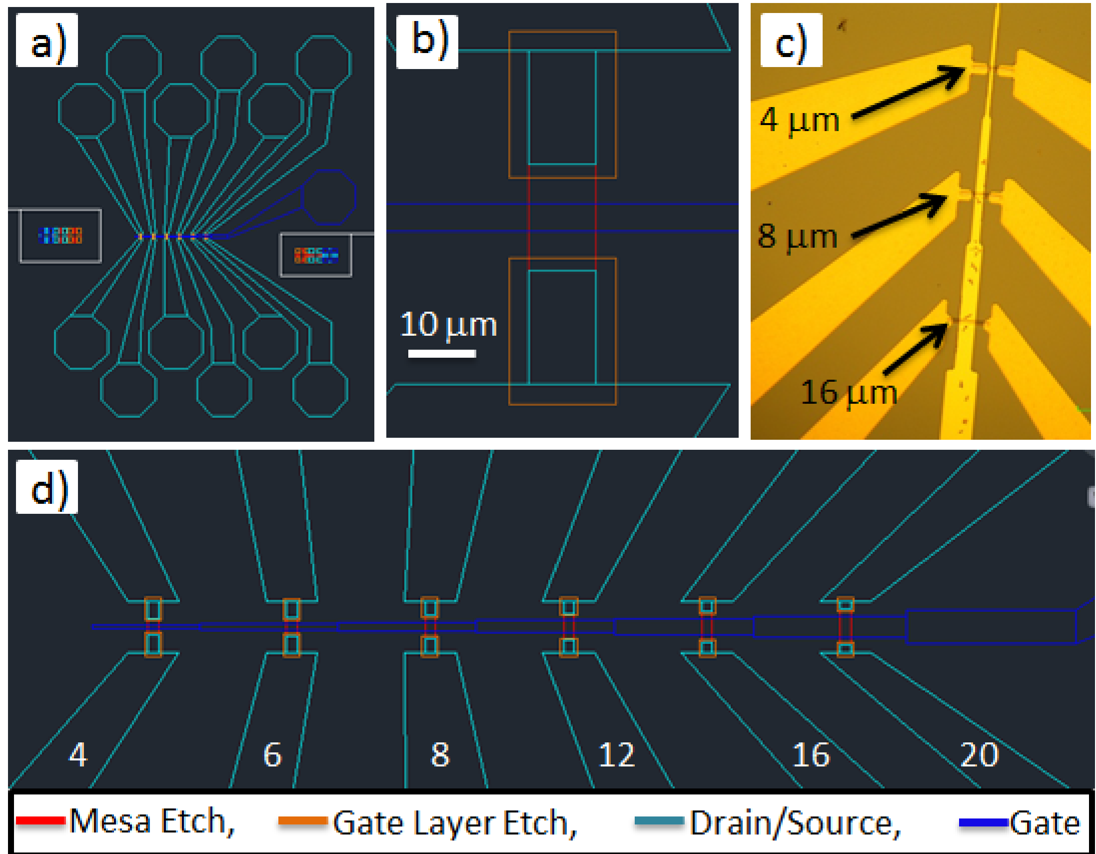

Figure 8.5 – JFET Design: (a), (b) and (d) show CAD designs for a transistor design study varying the channel length. The channel width is fixed at 10 μm and the mesa dimension is fixed at 10 μm by 40 μm. The channel length is varied from 4 μm to 20 μm as indicated in (d). (c) A microscope image of the completed devices.

are outlined in Fig. 8.6(a)-(d). In (a) the 10 mm x 40 mm mesa is define by etching through the InP epi layers to the InGaAs etch stop. In (b) the drain/source contact regions are revealed by etching away the p-type gate layer down into the n-type channel. Not visible, a sidewall passivation of silicon-nitride is deposited conformally and then etched aniostropically. This leaves an insulating layer of SiNx on the sidewalls so that the drain/source and gate contacts are only electrically in contact with the top surface of the mesa preventing leakage pathways. In (c) the drain/source contacts are deposited by lift-off techniques. In (d) the gate contact is deposited onto the p-type gate layer. An AFM of the completed structure is shown in Fig. 8.6(e) and (f).

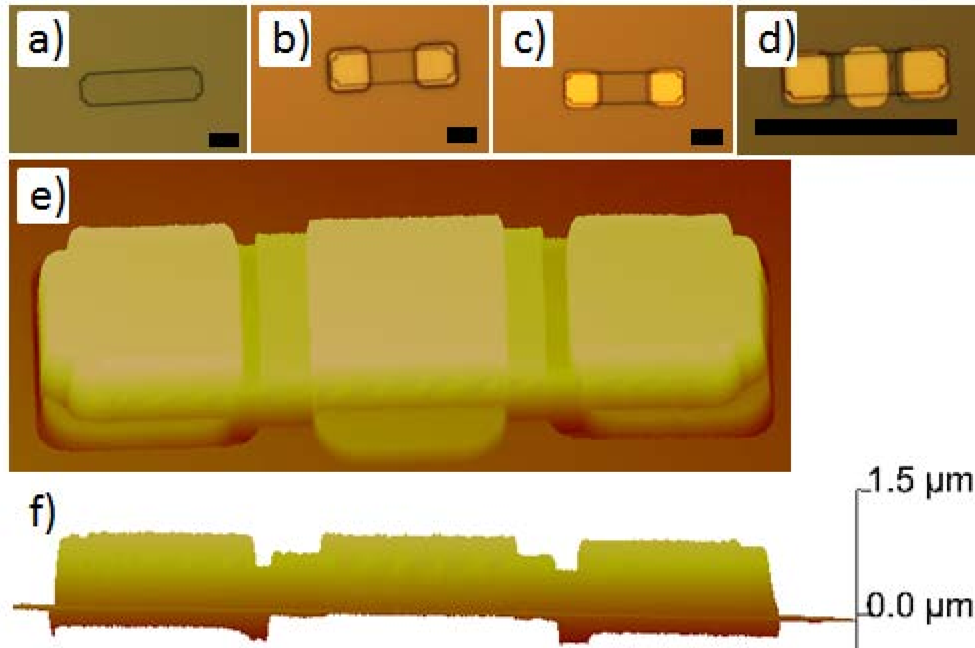

Figure 8.6 – JFET Fabrication: (a)-(d) show the fabrication steps for a JFET. (a) Mesa etch is performed to define the mesa area. (b)The drain/source contact regions are revealed by etching away the gate layer. Then sidewall passivation is performed. (c) Drain/source contacts are deposited. (d) The gate contact is deposited. (e) An AFM image of the completed device. (f) Profile of the completed device.

8.4.2. Array Transfer

We spent Sect. 7.2 developing techniques to pattern integrated organic devices directly on a hemispherical surface; this was relatively easy because we can deposit the organic semiconductors directly onto the plastic substrate – but how do we transfer inorganic devices onto a hemispherical surface? One possible route is fabricate devices on a wafer, release them, then pick-and-place them onto a 3D substrate. This could be done using a method similar to that demonstrate in Ref. [225]. However, this is impractical for a large, high density array that may consist of > 1 million devices and require registration < 1 μm. A better technique would take advantage of the massively parallelizable fabrication techniques enabled by standard photolithography – as we did with the stamping process in Sect. 7.2.

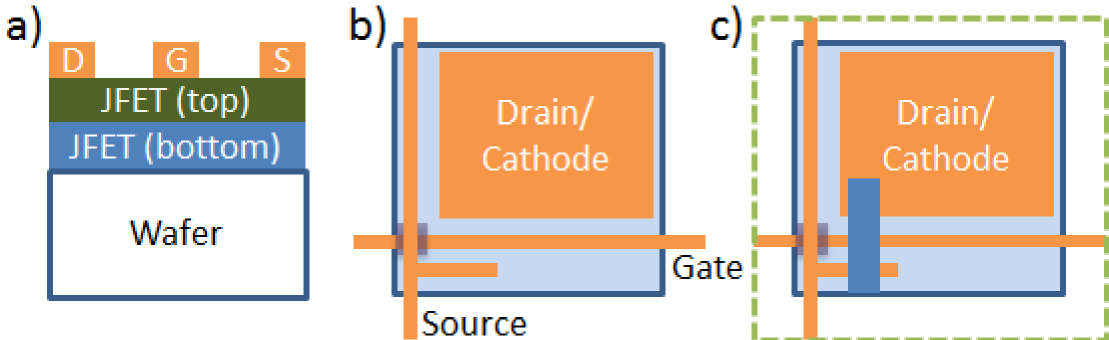

Figure 8.7 – Inorganic Array Transfer: (a) Schematic of a transistor fabricated on a wafer with drain, source and gate contacts. (b) Interconnects for a passive pixel sensor are patterned on a plastic substrate. Only a single pixel is shown, but the gate row and source column span the entire array. Note that a perylene insulating layer is patterned where the gate and source overlap to maintain isolation. (c) The transistor array is bonded to the plastic by cold-welding to the drain/cathode, gate and source interconnects. Once the devices are released from the wafer, we see the bottom of the transistor in blue. The organic photodetector materials and transparent anode contact can then be patterned.

Our solution is to fabricate the inorganic devices as an array on the wafer, and then transfer the entire array in a single step to a flat plastic substrate before 3D deformation. Subsequently we can deform the semi-rigid substrate and fabricate the OPD using the methods of Sect. 7.2. Because the inorganic device fabrication is performed on wafer, we can use the full suite of semiconductor fabrication tools (including a mask aligner, a stepper, e-beam lithography, diffusion furnaces, etc.) to fabricate very compact and high-performance transistors. This makes it practical to consider more advanced pixel architectures such as a four-transistor (4-T) active pixel complete with amplification, readout control, and a reset switch. For now, however, we still consider a simple, 1-T passive pixel sensor to demonstrate the transfer technology.

As an example of this method, we choose to fabricate the transistor array on the wafer with contacts, but without interconnects – a schematic of a single pixel of this array is shown in Fig. 8.7. Next we pattern a matching set of interconnects on a plastic (still PETg) substrate (see

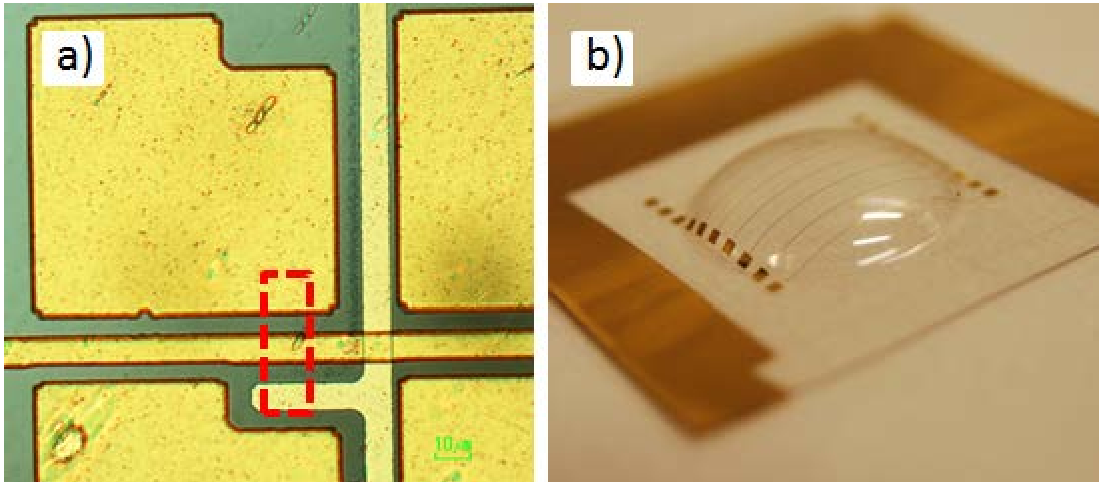

Figure 8.8 – Patterning PETg: (a) Au interconnects for a 128x128 passive pixel sensor patterned on a PETg substrate. When the array is completed a transistor will be bonded at the red box and the large pad will simultaneously function as the drain contact and the cathode of an organic photodetector. (b) 15 mm wide by 1.5 cm long Au lines were patterned onto a flat PETg substrate. The substrate was then deformed into a hemisphere without damaging the conductivity of the Au lines.

Fig. 8.7(a) and (b)) so that transistors are interconnected after we form a cold-weld bond between the device contacts and the interconnects on the PETg. Transfer is completed after releasing the inorganic devices from the wafer as shown in Fig. 8.7(c). The PETg can then be deformed into a hemisphere. Next the OPD can be deposited across the whole surface - the low conductivity of organic semiconductors will ensure minimal leakage laterally between the various interconnects and devices in the array. Finally the transparent, top, anode contact can be patterned as discussed in Sect. 7.2.1. Figure 8.8(a) shows Au interconnects prepared on a PETg substrate; the substrate is ready to have a transistor array bonded and this pixel's transistor would sit at the red box straddling the drain/cathode, gate, and source interconnects.

One requirement for this process to work is that we are able to deform the PETg without damaging the interconnects or transistors. We note that hemispherical deformation requires 2D stretching, which is much more demanding than the simple bend test demonstrated on thin-film

inorganics shown in Fig. 8.3. However, because the transistors are so small we expect that the stretching will still look like a1D bend, which the devices can withstand. The long, thin metal interconnects required to operate the sensor are more likely to break during the deformation process. To test this we pattern 15 μm wide x 1.5 cm long lines of Au on a PETg substrate. Then we deform the PETg into a hemisphere as shown in Fig. 8.8(b). We observe less than a 5% change in resistance across each wire demonstrating that we can non-destructively deform the interconnects.

The inorganic transfer shown in Fig. 8.3 has been demonstrated for large areas of epitaxy – an entire 2" wafer was transferred to the flexible Kapton substrate. Small devices are more likely to be damaged by the etchant during release from the wafer. This may be a problem if etching laterally as in Ref. [12], even with a high chemical selectivity such as HF etching AlAs 10^7 times faster than GaAs.[226,227] To mitigate this, we etch through the entire wafer using the sacrificial layer as an etch stop. We also protect the devices by surrounding them with a wide protection layer as shown in Fig. 8.9(a). When the devices are bonded to the plastic, the protection layer is also bonded and encapsulates the devices to protect them from the etchant as illustrated in Fig. 8.9(b). Once the wafer is etched, the sacrificial layer can be selectively etched to complete the transfer. Figure 8.9(c) shows a portion of a 10x128 array of 10 μm x 40 μm InGaAs mesas that were transferred to a flexible Kapton substrate with nearly 100% yield. Using this procedure it is quite simple to transfer to Kapton, however, Kapton cannot be thermoformed into a hemisphere by the method of Sect. 7.2.1. Kapton behaves well because it is very flat and is very resistant to the various etchants required for lift-off. PETg on the other hand proved much more challenging because it has a very rough surface making strong, leak-free cold welding difficult and PETg is less chemically resistant and it gets attacked by the etchants resulting in

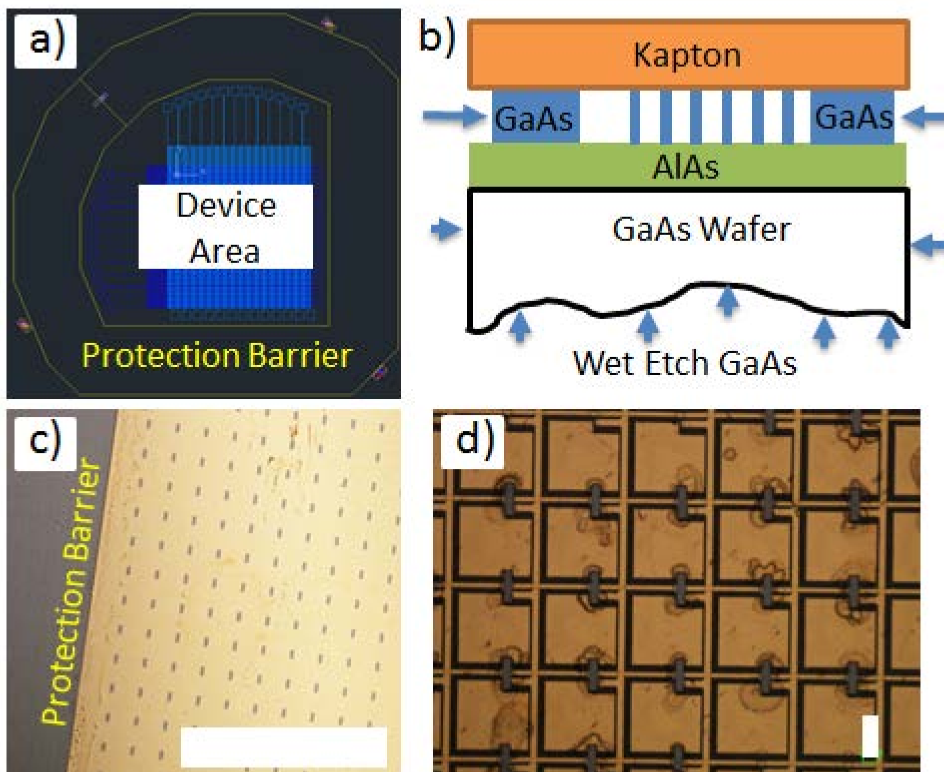

Figure 8.9 – GaAs Array Transfer: (a) CAD pattern for 128x128 transistor array incorporating a wide protection barrier surrounding the device area. Every tenth pixel has a large contact pad to facilitate testing. (b) Schematic cross-section of the array bonded to Kapton. The wide GaAs protection regions prevent the wafer etch from reaching the small GaAs devices in the interior. These wide regions take longer to etch laterally than the time required for the wafer etch. (c) InGaAs mesa devices transferred to a flexible Kapton substrate after the wafer has been removed by wet chemical etching. The width of the white scale bar is 1mm. (d) InP transistor array transferred to pre-patterned PETg substrate after wafer removal. There is some residue left from the wafer etch that must be cleaned prior to deposition of the organic photodetector. The width of the white scale bar is 20 µm.

delamination of the metal from the PETg surface. Figure 8.9(d) shows a sample array transfer to PETg which is characterized by low yield including failed transfers and damaged devices. Improving the yield of this process is a key factor for the success of this versatile fabrication technique, and this remains an area of active investigation.

Appendix

Appendix A

Alternate OI-HJ Configuration

The model discussed in Chapter 5 was developed to describe an n-P junction dominated by interfacial recombination according to the scheme of Fig. 5.1. It is straightforward to modify the model to describe other hybrid device architectures. Figure A1(a) shows the case of a Type-II n-P junction[38] with a small valence band offset (ΔE_v) such that current is dominated by injection from the organic HOMO into the inorganic valence band under forward bias. Carrier hopping in the organic (rather than band transport in the inorganic), suggests that the injection rate for a single carrier can be described by: $k_{hop} = \upsilon \exp(-\Delta E_v / k_B T)$,[64] where υ is the hopping attempt frequency. The forward bias current is then given by $J = q a_O P_{HJ} k_{hop}$. Under reverse bias, the current is limited by Shockley-Read-Hall (SRH) generation in the depletion region, or by minority carrier diffusion from the inorganic bulk. The current for this OI-HJ device is thus given by:

$$J = \upsilon q a_O P_c \exp\left(\frac{qV_O - \Delta E_v}{k_B T}\right) - \frac{q n_i W_D}{\tau} - q\sqrt{\frac{D_I}{\tau_I}}\frac{n_i^2}{N_D}. \tag{A1}$$

Here, we have used Eq. 5.6 for P_{HJ}. The intrinsic carrier density is $n_i = \sqrt{N_c N_v} \exp(-E_{g,I}/2k_B T)$, τ_g is the SRH generation rate, $W_D = \sqrt{2\varepsilon_I \varepsilon_0 V_I / q N_D}$ is the depletion

width, D_I is the minority carrier diffusion length, τ_I is the minority carrier lifetime and N_D is the ionized dopant density in the inorganic.

Figure A1(b) shows a Type-I n-N junction,[38] where current is limited by electron injection over the conduction band discontinuity (ΔE_c) at the interface under forward bias. This injection corresponds to thermionic emission into the organic from the inorganic. Assuming an ohmic contact at the anode/organic interface, the reverse bias current is limited by transport through the organic film. The resulting current is given by:

$$J = A^* T^2 \exp\left(-\frac{\Delta E_c}{k_B T}\right) \exp\left(\frac{qV_I}{k_B T}\right) - f(V_O), \tag{A2}$$

where A^* is the effective Richardson constant.[38] Here $f(V_O) = q\mu_O N V_O / W_O$ at low currents when ohmic conduction is dominant in the organic. In this case, N is the electron (i.e. negative polaron) density in the organic and is generally a function of position. At high bias and current densities, the current is limited by space-charge conduction where $f(V_O) = 9\varepsilon_O \mu_O V_O^2 / 8W_O^3$ in the absence of traps, or by trap-charge limited conduction in the presence of a large trap density where:[179]

$$f(V_O) = N_{LUMO} \mu_O q^{1-l_O} \left(\frac{\varepsilon_O \varepsilon_0 l_O}{H_O(l_O + 1)}\right)^{l_O} \left(\frac{2l_O + 1}{l_O + 1}\right)^{l_O+1} \frac{V_O^{l_O+1}}{W_O^{2l_O+1}}. \tag{A3}$$

In each of these cases, the current is coupled to charge transport as discussed in Sec. 5.2.2. This determines the voltage distributions V_O and V_I required to evaluate current density as a function of the applied voltage: $V_a = V_O + V_I$. Under forward bias, both devices in Fig. A1(a) and A1(b) behave as diodes (exhibiting exponential dependence of J vs. V). But the reverse (or leakage) characteristics deviate from a traditional Shockley diode behavior.

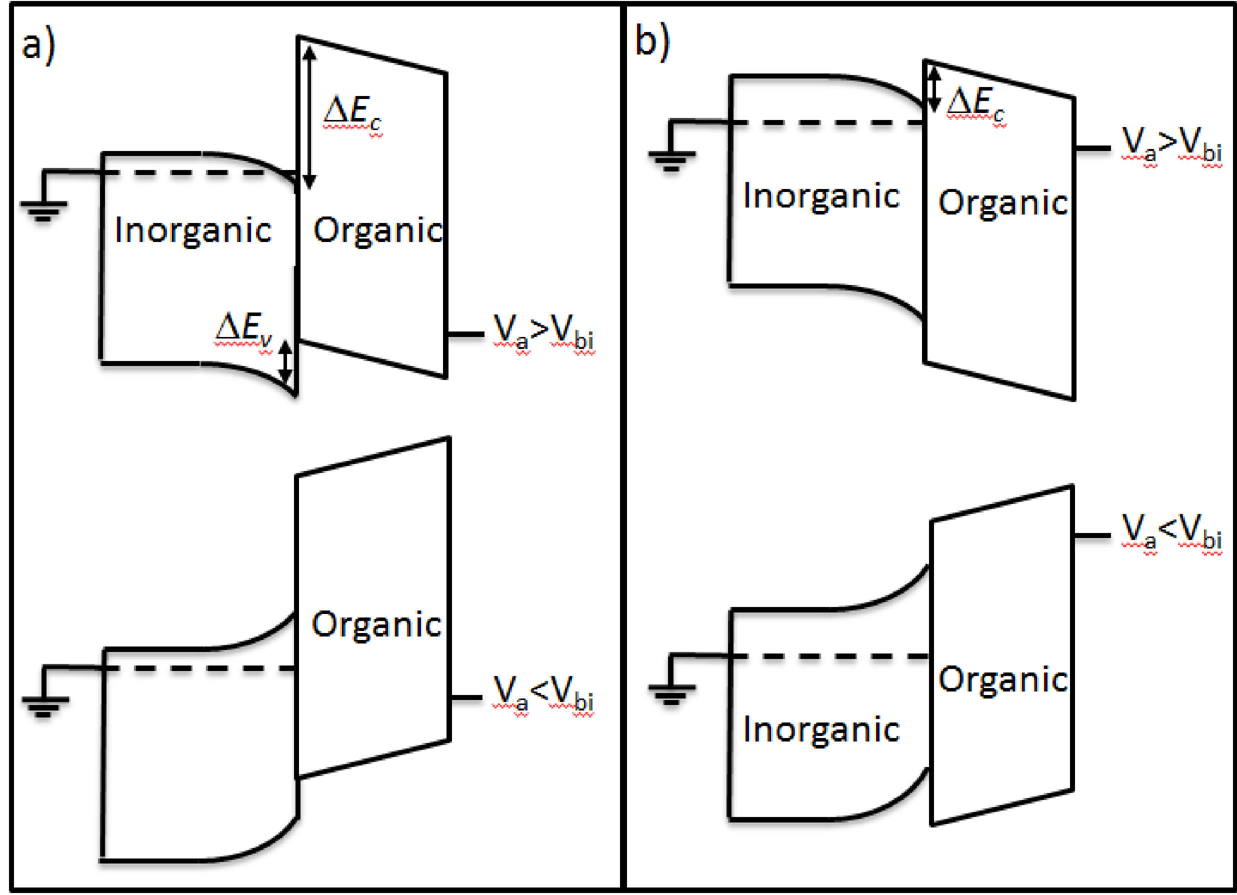

Figure A1: (a) Alternative current conduction pathways for a type-II n-P organic/inorganic heterojunction (OI-HJ) when the highest occupied molecular orbital (HOMO) to valence band discontinuity (ΔE_v) is small. Upon large forward bias (applied voltage is greater than the built-in voltage ($V_a > V_{bi}$), holes are injected as minority carriers into the inorganic valence band from the organic HOMO. These minority carriers ultimately recombine with free electrons. Upon reverse bias or moderate forward bias ($V_a < V_{bi}$), the current is dominated by Shockley-Read-Hall generation in the depletion region or minority carrier diffusion in the inorganic. (b) Current conduction pathway for a type-I n-N OI-HJ. Here, forward bias current is limited by thermionic emission into the organic from the inorganic over the lowest occupied molecular orbital (LUMO) to conduction band discontinuity (ΔE_c). Assuming an ohmic contact at the anode/organic interface, the reverse bias current is simply limited by drift or space charge limited current in the organic layer.

Bibliography

1. Gargini, P. A. Challenges for the Semiconductor Industry in the 21st Century. *ECS Trans.* **50,** 3–11 (2013).

2. Auth, C. *et al.* A 22nm high performance and low-power CMOS technology featuring fully-depleted tri-gate transistors, self-aligned contacts and high density MIM capacitors. in *2012 Symposium on VLSI Technology (VLSIT)* 131–132 (2012). doi:10.1109/VLSIT.2012.6242496

3. Rim, S.-B., Catrysse, P. B., Dinyari, R., Huang, K. & Peumans, P. The optical advantages of curved focal plane arrays. *Opt. Express* **16,** 4965–4971 (2008).

4. Samsung Electronics Corp. Flexible AMOLED Display - Hammer Test. at <http://www.youtube.com/watch?v=-k6r2HQY9Ws>

5. Park, J.-S. *et al.* Flexible full color organic light-emitting diode display on polyimide plastic substrate driven by amorphous indium gallium zinc oxide thin-film transistors. *Applied Physics Letters* **95,** 013503–013503 (2009).

6. Someya, T. A large-area, flexible pressure sensor matrix with field-effect transistors for artificial skin applications. *PNAS* **101,** 9966–9970 (2004).

7. Viventi, J., Kim, D., Moss, J. D., Rogers, J. A. & Litt, B. A Conformal, Bio-Interfaced Class of Silicon Electronics for Mapping Cardia Electrophysiology. *Sci. Transl. Med.* **2,**

8. Viventi, J. *et al.* Flexible, foldable, actively multiplexed, high-density electrode array for mapping brain activity in vivo. *Nat Neurosci* **14,** 1599–1605 (2011).

9. Rogers, J. A., Someya, T. & Huang, Y. Materials and Mechanics for Stretchable Electronics. *Science* **327,** 1603–1607 (2010).

10. Dinyari, R., Rim, S.-B., Huang, K., Catrysse, P. B. & Peumans, P. Curving monolithic silicon for nonplanar focal plane array applications. *Applied Physics Letters* **92,** 091114 (2008).

11. Shiu, K.-T., Zimmerman, J., Wang, H. & Forrest, S. R. Ultrathin film, high specific power InP solar cells on flexible plastic substrates. *Applied Physics Letters* **95,** 223503–223503 (2009).

12. Lee, K., Shiu, K.-T., Zimmerman, J. D., Renshaw, C. K. & Forrest, S. R. Multiple growths of epitaxial lift-off solar cells from a single InP substrate. *Applied Physics Letters* **97,** 101107–101107 (2010).

13. Ko, H. *et al.* Ultrathin compound semiconductor on insulator layers for high-performance nanoscale transistors. *Nature* **468,** 286–289 (2010).

14. Yang, Y. *et al.* Arrays of Silicon Micro/Nanostructures Formed in Suspended Configurations for Deterministic Assembly Using Flat and Roller-Type Stamps. *Small* **7,** 484–491 (2011).

15. Park, S.-I. *et al.* Printed Assemblies of Inorganic Light-Emitting Diodes for Deformable and Semitransparent Displays. *Science* **325,** 977–981 (2009).

16. Gu, G., Burrows, P. E., Venkatesh, S., Forrest, S. R. & Thompson, M. E. Vacuum-deposited, nonpolymeric flexible organic light-emitting devices. *Opt. Lett.* **22,** 172–174 (1997).

17. Xu, X., Davanco, M., Qi, X. & Forrest, S. R. Direct transfer patterning on three dimensionally deformed surfaces at micrometer resolutions and its application to hemispherical focal plane detector arrays. *Organic Electronics* **9,** 1122–1127 (2008).

18. Xu, X., Mihnev, M., Taylor, A. & Forrest, S. R. Organic photodetector arrays with indium tin oxide electrodes patterned using directly transferred metal masks. *Applied Physics Letters* **94,** 043313–043313 (2009).

19. Sekitani, T., Zschieschang, U., Klauk, H. & Someya, T. Flexible organic transistors and circuits with extreme bending stability. *Nature Materials* **9,** 1015–1022 (2010).

20. Zhou, L. *et al.* All-organic active matrix flexible display. *Applied Physics Letters* **88,** 083502–083502–3 (2006).

21. U.S. Energy Information Administration. *http://www.eia.gov/energy_in_brief/article/renewable_electricity.cfm*. (U.S. EIA Website, 2013).

22. Pauling, Linus. *The Nature of the Chemical Bond and the Structure of Molecules and Crystals*. (Cornell University Press, 1960).

23. Langmuir, I. THE ARRANGEMENT OF ELECTRONS IN ATOMS AND MOLECULES. *J. Am. Chem. Soc.* **41,** 868–934 (1919).

24. Ashcroft, N. W. & Mermin, D. N. *Solid State Physics*. (Cornell University, 1976).

25. Ewald, P. P. Die Berechnung optischer und elektrostatischer Gitterpotentiale. *Annalen der Physik* **369,** 253–287 (1921).

26. Singh, Jasprit. *Electronic and Optoelectronic Properties of Semiconductor Structures*. (Cambridge University Press, 2007).

27. Cho, A. Y. Growth of III–V semiconductors by molecular beam epitaxy and their properties. *Thin Solid Films* **100,** 291–317 (1983).

28. Dingle, R., Wiegmann, W. & Henry, C. H. Quantum States of Confined Carriers in Very Thin Al_{x}Ga_{1-x}As-GaAs-Al_{x}Ga_{1-x}As Heterostructures. *Phys. Rev. Lett.* **33,** 827–830 (1974).

29. Chang-Hasnain, C. J. Tunable VCSEL. *IEEE Journal of Selected Topics in Quantum Electronics* **6,** 978–987 (2000).

30. Bhattacharya, P. *Semiconductor Optoelectronic Devices*. (Prentice Hall, 1996).

31. Levine, B. F. Quantum #x2010;well infrared photodetectors. *Journal of Applied Physics* **74,** R1–R81 (1993).

32. Nguyen, L. D., Brown, A. S., Thompson, M. A. & Jelloian, L. M. 50-nm self-aligned-gate pseudomorphic AlInAs/GaInAs high electron mobility transistors. *IEEE Transactions on Electron Devices* **39,** 2007–2014 (1992).

33. Lubinsky, A. R., Duke, C. B., Lee, B. W. & Mark, P. Semiconductor Surface Reconstruction: The Rippled Geometry of GaAs(110). *Phys. Rev. Lett.* **36,** 1058–1061 (1976).

34. Sakamoto, T. *et al.* Phase-Locked Epitaxy Using RHEED Intensity Oscillation. *Japanese Journal of Applied Physics* **23,** L657–L659 (1984).

35. Nahory, R. E., Pollack, M. A., Johnston, W. D. & Barns, R. L. Band gap versus composition and demonstration of Vegard #x2019;s law for In1-xGaxAsyP1-y lattice matched to InP. *Applied Physics Letters* **33,** 659–661 (1978).

36. Williams, P. Secondary Ion Mass Spectrometry. *Annual Review of Materials Science* **15,** 517–548 (1985).

37. Hall, E. H. On a New Action of the Magnet on Electric Currents. *American Journal of Mathematics* **2,** 287–292 (1879).

38. Sze, S. M. & Ng, K. K. *Physics of Semiconductor Devices*. (Wiley, 2007).

39. Petroff, P. M., Miller, R. C., Gossard, A. C. & Wiegmann, W. Impurity trapping, interface structure, and luminescence of GaAs quantum wells grown by molecular beam epitaxy. *Applied Physics Letters* **44,** 217–219 (1984).

40. Chai, Y. G. & Chow, R. Source and elimination of oval defects on GaAs films grown by molecular beam epitaxy. *Applied Physics Letters* **38,** 796–798 (1981).

41. M. L. Cohen & J. R. Chelikowsky. *Electronic Structure and Optical Properties of Semiconductors*. (Springer-Verlag, 1988).

42. Søndergaard, R., Hösel, M., Angmo, D., Larsen-Olsen, T. T. & Krebs, F. C. Roll-to-roll fabrication of polymer solar cells. *Materials Today* **15,** 36–49 (2012).

43. Forrest, S. R. Ultrathin Organic Films Grown by Organic Molecular Beam Deposition and Related Techniques. *Chem. Rev.* **97,** 1793–1896 (1997).

44. Burrows, P. E. *et al.* Organic vapor phase deposition: a new method for the growth of organic thin films with large optical non-linearities. *Journal of Crystal Growth* **156,** 91–98 (1995).

45. Baldo, M. *et al.* Organic Vapor Phase Deposition. *Advanced Materials* **10,** 1505–1514 (1998).

46. Greene, F. D., Misrock, S. L. & Wolfe, J. R. The Structure of Anthracene Photodimers. *J. Am. Chem. Soc.* **77,** 3852–3855 (1955).

47. Reese, C. & Bao, Z. Organic single-crystal field-effect transistors. *Materials Today* **10,** 20–27 (2007).

48. Sherwood, J. N. & Thomson, S. J. Growth of single crystals of anthracene. *J. Sci. Instrum.* **37,** 242 (1960).

49. Podzorov, V., Sysoev, S. E., Loginova, E., Pudalov, V. M. & Gershenson, M. E. Single-crystal organic field effect transistors with the hole mobility #x223c;8 cm2/V #x2009;s. *Applied Physics Letters* **83,** 3504–3506 (2003).

50. Wei, G., Wang, S., Renshaw, K., Thompson, M. E. & Forrest, S. R. Solution-processed squaraine bulk heterojunction photovoltaic cells. *Acs Nano* **4,** 1927–1934 (2010).

51. Kim, C. S., Lee, S., Gomez, E. D., Anthony, J. E. & Loo, Y.-L. Solvent-dependent electrical characteristics and stability of organic thin-film transistors with drop cast bis(triisopropylsilylethynyl) pentacene. *Applied Physics Letters* **93,** 103302–103302–3 (2008).

52. Sirringhaus, H. *et al.* High-Resolution Inkjet Printing of All-Polymer Transistor Circuits. *Science* **290,** 2123–2126 (2000).

53. Gevorgyan, S. A. *et al.* An inter-laboratory stability study of roll-to-roll coated flexible polymer solar modules. *Solar Energy Materials and Solar Cells* **95,** 1398–1416 (2011).

54. Heliatek roll-to-roll fabrication. *Heliatek* at <http://www.heliatek.com/technologie/fertigung/?lang=en>

55. Walzer, K., Maennig, B., Pfeiffer, M. & Leo, K. Highly Efficient Organic Devices Based on Electrically Doped Transport Layers. *Chemical Reviews* **107,** 1233–1271 (2007).

56. Maennig, B. *et al.* Controlled p-type doping of polycrystalline and amorphous organic layers: Self-consistent description of conductivity and field-effect mobility by a microscopic percolation model. *Physical Review B* **64,** (2001).

57. Tang, C. W., VanSlyke, S. A. & Chen, C. H. Electroluminescence of doped organic thin films. *Journal of Applied Physics* **65,** 3610–3616 (1989).

58. Baldo, M. A. *et al.* Highly efficient phosphorescent emission from organic electroluminescent devices. *Nature* **395,** 151–154 (1998).

59. Forrest, S. R. The road to high efficiency organic light emitting devices. *Organic Electronics* **4,** 45–48 (2003).

60. Jeong, J. K. *et al.* 3.1: Distinguished Paper: 12.1-Inch WXGA AMOLED Display Driven by Indium-Gallium-Zinc Oxide TFTs Array. *SID Symposium Digest of Technical Papers* **39,** 1–4 (2008).

61. Miller, A. & Abrahams, E. Impurity conduction at low concentrations. *Physical Review* **120,** 745 (1960).

62. Hertel, D. & Bässler, H. Photoconduction in Amorphous Organic Solids. *ChemPhysChem* **9,** 666–688 (2008).

63. Gartstein, Y. N. & Conwell, E. M. High-field hopping mobility of polarons in disordered molecular solids. A Monte Carlo study. *Chemical Physics Letters* **217,** 41–47 (1994).

64. Bässler, H. Charge transport in disordered organic photoconductors a Monte Carlo simulation study. *physica status solidi (b)* **175,** 15–56 (1993).

65. Bouchaud, J.-P. & Georges, A. Anomalous diffusion in disordered media: statistical mechanisms, models and physical applications. *Physics reports* **195,** 127–293 (1990).

66. Pfister, G. Hopping transport in a molecularly doped organic polymer. *Phys. Rev. B* **16,** 3676–3687 (1977).

67. Marcus, R. A. & Sutin, N. Electron transfers in chemistry and biology. *Biochimica et Biophysica Acta (BBA)-Reviews on Bioenergetics* **811,** 265–322 (1985).

68. Kestner, N. R., Logan, J. & Jortner, J. Thermal electron transfer reactions in polar solvents. *The Journal of Physical Chemistry* **78,** 2148–2166 (1974).

69. Dexter, D. L. in *Luminescence of Crystals, Molecules, and Solutions* (Williams, F., Baron, B., Martens, M. & Varma, S. P.) 57–63 (Springer US, 1973). at <http://link.springer.com/chapter/10.1007/978-1-4684-2043-2_6>

70. Silbey, R. Electronic Energy Transfer in Molecular Crystals. *Annual Review of Physical Chemistry* **27,** 203–223 (1976).

71. Klessinger, M. & Michl, J. *Excited States and Photochemistry of Organic Molecules*. (VCH Publishers, 1995).

72. Powell, R. C. & Soos, Z. G. Singlet exciton energy transfer in organic solids. *Journal of Luminescence* **11,** 1–45 (1975).

73. Főrster, T. 10th Spiers Memorial Lecture. Transfer mechanisms of electronic excitation. *Discuss. Faraday Soc.* **27,** 7–17 (1959).

74. Peumans, P., Yakimov, A. & Forrest, S. R. Small molecular weight organic thin-film photodetectors and solar cells. *Journal of Applied Physics* **93,** 3693–3723 (2003).

75. Pettersson, L. A., Roman, L. S. & Inganas, O. Modeling photocurrent action spectra of photovoltaic devices based on organic thin films. *Journal of Applied Physics* **86,** 487–496 (1999).

76. Aldrich, C. & Bajaj, K. K. Binding energy of a Mott-Wannier exciton in a polarizable medium. *Solid State Communications* **22,** 157–160 (1977).

77. Mihailetchi, V., Koster, L., Hummelen, J. & Blom, P. Photocurrent Generation in Polymer-Fullerene Bulk Heterojunctions. *Physical Review Letters* **93,** (2004).

78. Giebink, N., Wiederrecht, G., Wasielewski, M. & Forrest, S. Ideal diode equation for organic heterojunctions. I. Derivation and application. *Physical Review B* **82,** (2010).

79. Giebink, N., Lassiter, B., Wiederrecht, G., Wasielewski, M. & Forrest, S. Ideal diode equation for organic heterojunctions. II. The role of polaron pair recombination. *Physical Review B* **82,** (2010).

80. Peumans, P. & Forrest, S. R. Separation of geminate charge-pairs at donor–acceptor interfaces in disordered solids. *Chemical Physics Letters* **398,** 27–31 (2004).

81. Deibel, C., Strobel, T. & Dyakonov, V. Role of the Charge Transfer State in Organic Donor–Acceptor Solar Cells. *Advanced Materials* **22,** 4097–4111 (2010).

82. Marsh, R. A., Hodgkiss, J. M. & Friend, R. H. Direct Measurement of Electric Field-Assisted Charge Separation in Polymer:Fullerene Photovoltaic Diodes. *Advanced Materials* **22,** 3672–3676 (2010).

83. Lee, J. *et al.* Charge Transfer State Versus Hot Exciton Dissociation in Polymer−Fullerene Blended Solar Cells. *J. Am. Chem. Soc.* **132,** 11878–11880 (2010).

84. Limpinsel, M., Wagenpfahl, A., Mingebach, M., Deibel, C. & Dyakonov, V. Photocurrent in bulk heterojunction solar cells. *Physical Review B* **81,** (2010).

85. Blom, P. W. M., Mihailetchi, V. D., Koster, L. J. A. & Markov, D. E. Device Physics of Polymer:Fullerene Bulk Heterojunction Solar Cells. *Advanced Materials* **19,** 1551–1566 (2007).

86. Barth, S., Hertel, D., Tak, Y.-H., Bässler, H. & Hörhold, H. H. Geminate pair dissociation in random organic systems. *Chemical physics letters* **274,** 165–170 (1997).

87. Clarke, T. M. & Durrant, J. R. Charge photogeneration in organic solar cells. *Chemical reviews* **110,** 6736–6767 (2010).

88. Etzold, F. *et al.* Ultrafast Exciton Dissociation Followed by Nongeminate Charge Recombination in PCDTBT:PCBM Photovoltaic Blends. *Journal of the American Chemical Society* **133,** 9469–9479 (2011).

89. Nelson, J. Diffusion-limited recombination in polymer-fullerene blends and its influence on photocurrent collection. *Phys. Rev. B* **67,** 155209 (2003).

90. Müller, J. G. *et al.* Ultrafast dynamics of charge carrier photogeneration and geminate recombination in conjugated polymer:fullerene solar cells. *Phys. Rev. B* **72,** 195208 (2005).

91. Bakulin, A. A. *et al.* The Role of Driving Energy and Delocalized States for Charge Separation in Organic Semiconductors. *Science* **335,** 1340–1344 (2012).

92. Kirchartz, T., Pieters, B. E., Taretto, K. & Rau, U. Electro-optical modeling of bulk heterojunction solar cells. *Journal of Applied Physics* **104,** 094513–094513 (2008).

93. Onsager, L. Deviations from Ohm's law in weak electrolytes. *The Journal of Chemical Physics* **2,** 599 (1934).

94. Onsager, L. Initial recombination of ions. *Physical Review* **54,** 554 (1938).

95. Braun, C. L. Electric field assisted dissociation of charge transfer states as a mechanism of photocarrier production. *The Journal of chemical physics* **80,** 4157 (1984).

96. Einstein, A. Über die von der molekularkinetischen Theorie der Wärme geforderte Bewegung von in ruhenden Flüssigkeiten suspendierten Teilchen. *Annalen der Physik* **322,** 549–560 (1905).

97. Wetzelaer, G. A. H., Koster, L. J. A. & Blom, P. W. M. Validity of the Einstein Relation in Disordered Organic Semiconductors. *Physical Review Letters* **107,** 066605 (2011).

98. Kusse, Bruce R. & Westwig, Erik A. *Mathematical Physics: Applied Mathematics for Scientists and Engineers*. (Wiley, 1998).

99. Peumans, P., Bulovic, V. & Forrest, S. R. Efficient, high-bandwidth organic multilayer photodetectors. *Applied Physics Letters* **76,** 3855–3857 (2000).

100. Burns, S. E. *et al.* Measurements of optical electric field intensities in microcavities using thin emissive polymer films. *Advanced Materials* **9,** 395–398 (1997).

101. Yoo, S. *et al.* Analysis of improved photovoltaic properties of pentacene/C60 organic solar cells: Effects of exciton blocking layer thickness and thermal annealing. *Solid-State Electronics* **51,** 1367–1375 (2007).

102. Huang, Y., Shi, L., Kim, E. S. & Seo, H. J. Site-selective spectroscopy and crystallographic sites of Eu3+ ions doped in Gd2BaZnO5. *Journal of Applied Physics* **105,** 013512–013512–5 (2009).

103. Bulović, V. *et al.* A surface-emitting vacuum-deposited organic light emitting device. *Applied Physics Letters* **70,** 2954–2954 (1997).

104. Peumans, P. & Forrest, S. R. Very-high-efficiency double-heterostructure copper phthalocyanine/C60 photovoltaic cells. *Applied Physics Letters* **79,** 126–128 (2001).

105. Hirose, Y. *et al.* Chemistry and electronic properties of metal-organic semiconductor interfaces: Al, Ti, In, Sn, Ag, and Au on PTCDA. *Phys. Rev. B* **54,** 13748–13758 (1996).

106. Kahn, A., Koch, N. & Gao, W. Electronic structure and electrical properties of interfaces between metals and π-conjugated molecular films. *Journal of Polymer Science Part B: Polymer Physics* **41,** 2529–2548 (2003).

107. Rand, B. P. *et al.* Organic Double-Heterostructure Photovoltaic Cells Employing Thick Tris(acetylacetonato)ruthenium(III) Exciton-Blocking Layers. *Advanced Materials* **17,** 2714–2718 (2005).

108. Eaton, D. R. The Nuclear Magnetic Resonance of Some Paramagnetic Transition Metal Acetylacetonates. *J. Am. Chem. Soc.* **87,** 3097–3102 (1965).

109. Glatthaar, M. *et al.* Efficiency limiting factors of organic bulk heterojunction solar cells identified by electrical impedance spectroscopy. *Solar Energy Materials and Solar Cells* **91,** 390–393 (2007).

110. Oey, C. C. *et al.* Polymer–TiO2 solar cells: TiO2 interconnected network for improved cell performance. *Nanotechnology* **17,** 706 (2006).

111. Kouskoussa, B. *et al.* On the improvement of the anode/organic material interface in organic solar cells by the presence of an ultra-thin gold layer. *physica status solidi (a)* **206,** 311–315 (2009).

112. Tremolet de Villers, B., Tassone, C. J., Tolbert, S. H. & Schwartz, B. J. Improving the Reproducibility of P3HT:PCBM Solar Cells by Controlling the PCBM/Cathode Interface. *J. Phys. Chem. C* **113,** 18978–18982 (2009).

113. Mazhari, B. An improved solar cell circuit model for organic solar cells. *Solar Energy Materials and Solar Cells* **90,** 1021–1033 (2006).

114. Godoy, A. *et al.* Effects of the buffer layer inserted between the transparent conductive oxide anode and the organic electron donor. *Solar Energy Materials and Solar Cells* **94,** 648–654 (2010).

115. Endo, A., Kajitani, M., Mukaida, M., Shimizu, K. & Satŏ, G. P. A new synthetic method for ruthenium complexes of β-diketones from 'ruthenium blue solution' and their properties. *Inorganica Chimica Acta* **150,** 25–34 (1988).

116. Endo, A. *et al.* Electrochemistry of Tris(β-diketonato)ruthenium(III) Complexes at Platinum Electrodes in Nonaqueous Solutions and Substituent Effects on Their Reversible Half-Wave Potentials. *Bulletin of the Chemical Society of Japan* **62,** 709–716 (1989).

117. Patterson, G. S. & Holm, R. H. Effects of chelate ring substituents on the polarographic redox potentials of tris(.beta.-diketonato)ruthenium(II,III) complexes. *Inorg. Chem.* **11,** 2285–2288 (1972).

118. Handy, R. F. & Lintvedt, R. L. Polarographic reduction potentials and substituent group electronic effects for a series of tris(1, 3, 5-diketonato)chromium(III) chelates in dimethyl sulfoxide and in dioxane-water. *Inorg. Chem.* **13,** 893–896 (1974).

119. Djurovich, P. I., Mayo, E. I., Forrest, S. R. & Thompson, M. E. Measurement of the lowest unoccupied molecular orbital energies of molecular organic semiconductors. *Organic Electronics* **10,** 515–520 (2009).

120. Schulze, K. *et al.* Efficient Vacuum-Deposited Organic Solar Cells Based on a New Low-Bandgap Oligothiophene and Fullerene C60. *Advanced Materials* **18,** 2872–2875 (2006).

121. Jin, H. *et al.* Polymer−Electrode Interfacial Effect on Photovoltaic Performances in Poly(3-hexylthiophene):Phenyl-C61-butyric Acid Methyl Ester Based Solar Cells. *J. Phys. Chem. C* **113,** 16807–16810 (2009).

122. Pope, M. & Swenberg, C. E. *Electronic processes in organic crystals and polymers.* (Oxford University Press, 1999).

123. Haddock, J. N., Zhang, X., Domercq, B. & Kippelen, B. Fullerene based n-type organic thin-film transistors. *Organic Electronics* **6,** 182–187 (2005).

124. Hamed, A., Sun, Y. Y., Tao, Y. K., Meng, R. L. & Hor, P. H. Effects of oxygen and illumination on the in situ conductivity of C_{60} thin films. *Phys. Rev. B* **47,** 10873–10880 (1993).

125. Kalb, W. L., Haas, S., Krellner, C., Mathis, T. & Batlogg, B. Trap density of states in small-molecule organic semiconductors: A quantitative comparison of thin-film transistors with single crystals. *Phys. Rev. B* **81,** 155315 (2010).

126. Hains, A. W., Liang, Z., Woodhouse, M. A. & Gregg, B. A. Molecular Semiconductors in Organic Photovoltaic Cells. *Chem. Rev.* **110,** 6689–6735 (2010).

127. Closs, G. L., Calcaterra, L. T., Green, N. J., Penfield, K. W. & Miller, J. R. Distance, stereoelectronic effects, and the Marcus inverted region in intramolecular electron transfer in organic radical anions. *J. Phys. Chem.* **90,** 3673–3683 (1986).

128. Lemmetyinen, H., Tkachenko, N. V., Efimov, A. & Niemi, M. Photoinduced intra- and intermolecular electron transfer in solutions and in solid organized molecular assemblies. *Phys. Chem. Chem. Phys.* **13,** 397–412 (2010).

129. Moser, J. E. & Grätzel, M. Observation of temperature independent heterogeneous electron transfer reactions in the inverted Marcus region. *Chemical Physics* **176,** 493–500 (1993).

130. Chen, H.-Y. *et al.* Polymer solar cells with enhanced open-circuit voltage and efficiency. *Nat Photon* **3,** 649–653 (2009).

131. Rand, B. P., Burk, D. P. & Forrest, S. R. Offset energies at organic semiconductor heterojunctions and their influence on the open-circuit voltage of thin-film solar cells. *Phys. Rev. B* **75,** 115327 (2007).

132. Schilinsky, P., Waldauf, C., Hauch, J. & Brabec, C. J. Simulation of light intensity dependent current characteristics of polymer solar cells. *Journal of Applied Physics* **95,** 2816–2819 (2004).

133. Lare, Y. *et al.* Influence of the exciton blocking layer on the stability of layered organic solar cells. *Journal of Physics and Chemistry of Solids* **72,** 97–103 (2011).

134. Renshaw, C. K., Schlenker, C. W., Thompson, M. E. & Forrest, S. R. Reciprocal carrier collection in organic photovoltaics. *Physical Review B* **84,** 045315 (2011).

135. Mandoc, M. M., Veurman, W., Koster, L. J. A., de Boer, B. & Blom, P. W. M. Origin of the Reduced Fill Factor and Photocurrent in MDMO-PPV:PCNEPV All-Polymer Solar Cells. *Advanced Functional Materials* **17,** 2167–2173 (2007).

136. Arkhipov, V. I. & Bässler, H. Exciton dissociation and charge photogeneration in pristine and doped conjugated polymers. *physica status solidi (a)* **201,** 1152–1187 (2004).

137. Cheyns, D. *et al.* Analytical model for the open-circuit voltage and its associated resistance in organic planar heterojunction solar cells. *Phys. Rev. B* **77,** 165332 (2008).

138. Day, J. *et al.* Photoconductivity in organic thin films: From picoseconds to seconds after excitation. *Journal of Applied Physics* **103,** 123715 (2008).

139. Reynaert, J., Arkhipov, V. I., Heremans, P. & Poortmans, J. Photomultiplication in Disordered Unipolar Organic Materials. *Advanced Functional Materials* **16,** 784–790 (2006).

140. Kersting, R. *et al.* Ultrafast Field-Induced Dissociation of Excitons in Conjugated Polymers. *Phys. Rev. Lett.* **73,** 1440–1443 (1994).

141. Arkhipov, V. I., Emelianova, E. V. & Bässler, H. Hot Exciton Dissociation in a Conjugated Polymer. *Phys. Rev. Lett.* **82,** 1321–1324 (1999).

142. Sugiyama, K., Ishii, H., Ouchi, Y. & Seki, K. Dependence of indium–tin–oxide work function on surface cleaning method as studied by ultraviolet and x-ray photoemission spectroscopies. *Journal of Applied Physics* **87,** 295–298 (2000).

143. Gebeyehu, D., Maennig, B., Drechsel, J., Leo, K. & Pfeiffer, M. Bulk-heterojunction photovoltaic devices based on donor–acceptor organic small molecule blends. *Solar Energy Materials and Solar Cells* **79,** 81–92 (2003).

144. Mihailetchi, V. D., Xie, H. X., de Boer, B., Koster, L. J. A. & Blom, P. W. M. Charge Transport and Photocurrent Generation in Poly(3-hexylthiophene): Methanofullerene Bulk-Heterojunction Solar Cells. *Advanced Functional Materials* **16,** 699–708 (2006).

145. Mikhnenko, O. V. *et al.* Temperature Dependence of Exciton Diffusion in Conjugated Polymers. *J. Phys. Chem. B* **112,** 11601–11604 (2008).

146. Sudha Devi, L. *et al.* Triplet energy transfer in conjugated polymers. I. Experimental investigation of a weakly disordered compound. *Phys. Rev. B* **78,** 045210 (2008).

147. Arnold, M. S. *et al.* Broad spectral response using carbon nanotube/organic semiconductor/C60 photodetectors. *Nano letters* **9,** 3354–3358 (2009).

148. Shockley, W. The theory of p-n junction semiconductors and p-n junction transistors. *Bell System Technical Journal* **28,** 435 (1949).

149. Forrest, S. R. The path to ubiquitous and low-cost organic electronic appliances on plastic. *Nature* **428,** 911–918 (2004).

150. Nelson, S. F., Lin, Y.-Y., Gundlach, D. J. & Jackson, T. N. Temperature-independent transport in high-mobility pentacene transistors. *Applied Physics Letters* **72,** 1854–1856 (1998).

151. Zang, D. Y., So, F. F. & Forrest, S. R. Giant anisotropies in the dielectric properties of quasi-epitaxial crystalline organic semiconductor thin films. *Applied Physics Letters* **59,** 823–825 (1991).

152. Haddon, R. C. *et al.* Conducting films of C60 and C70 by alkali-metal doping. *Nature* **350,** 320–322 (1991).

153. Blochwitz, J. *et al.* Interface electronic structure of organic semiconductors with controlled doping levels. *Organic Electronics* **2,** 97–104 (2001).

154. So, F. F. & Forrest, S. R. Organic-on-inorganic semiconductor photodetector. *IEEE Transactions on Electron Devices* **36,** 66–69 (1989).

155. Forrest, S. R. & So, F. F. Organic-on-inorganic semiconductor heterojunctions: Energy-band discontinuities, quasi-Fermi levels, and carrier velocities. *Journal of applied physics* **64,** 399–409 (1988).

156. Li, N., Lee, K., Renshaw, C. K., Xiao, X. & Forrest, S. R. Improved power conversion efficiency of InP solar cells using organic window layers. *Applied Physics Letters* **98,** 053504–053504–3 (2011).

157. Vlachopoulos, N., Liska, P., Augustynski, J. & Graetzel, M. Very efficient visible light energy harvesting and conversion by spectral sensitization of high surface area polycrystalline titanium dioxide films. *J. Am. Chem. Soc.* **110,** 1216–1220 (1988).

158. Hagfeldt, A., Boschloo, G., Sun, L., Kloo, L. & Pettersson, H. Dye-sensitized solar cells. *Chemical Reviews* **110,** 6595–6663 (2010).

159. Sargent, E. H. Colloidal quantum dot solar cells. *Nat Photon* **6,** 133–135 (2012).

160. Mcdonald, S. A. *et al.* Solution-processed PbS quantum dot infrared photodetectors and photovoltaics. *Nature materials* **4,** 138–142 (2005).

161. Coe-Sullivan, S., Woo, W.-K., Steckel, J. S., Bawendi, M. & Bulović, V. Tuning the performance of hybrid organic/inorganic quantum dot light-emitting devices. *Organic Electronics* **4,** 123–130 (2003).

162. Huynh, W. U. Hybrid Nanorod-Polymer Solar Cells. *Science* **295,** 2425–2427 (2002).

163. Agranovich, V. M., Gartstein, Y. N. & Litinskaya, M. Hybrid Resonant Organic–Inorganic Nanostructures for Optoelectronic Applications. *Chemical Reviews* **111,** 5179–5214 (2011).

164. Wenus, J. *et al.* Hybrid organic-inorganic exciton-polaritons in a strongly coupled microcavity. *Phys. Rev. B* **74,** 235212 (2006).

165. Slootsky, M., Liu, X., Forrest, S. R. & Menon, V. M. Formation of hybrid polaritons in an organic-inorganic microcavity at room temperature. in *CLEO: 2013 Technical Digest* **QMD3,** 7 (2013).

166. Kröger, M. *et al.* Role of the deep-lying electronic states of MoO3 in the enhancement of hole-injection in organic thin films. *Applied Physics Letters* **95,** 123301–123301–3 (2009).

167. Qi, X., Li, N. & Forrest, S. R. Analysis of metal-oxide-based charge generation layers used in stacked organic light-emitting diodes. *Journal of Applied Physics* **107,** 014514–014514–8 (2010).

168. Lassiter, B. E., Zimmerman, J. D., Panda, A., Xiao, X. & Forrest, S. R. Tandem organic photovoltaics using both solution and vacuum deposited small molecules. *Applied Physics Letters* **101,** 063303–063303–4 (2012).

169. Forrest, S. R., Kaplan, M. L. & Schmidt, P. H. Organic-on-inorganic semiconductor contact barrier diodes. I. Theory with applications to organic thin films and prototype devices. *Journal of applied physics* **55,** 1492–1507 (1984).

170. Forrest, S. R., Kaplan, M. L. & Schmidt, P. H. Organic-on-inorganic semiconductor contact barrier diodes. II. Dependence on organic film and metal contact properties. *Journal of Applied Physics* **56,** 543–551 (1984).

171. Méndez, H., Thurzo, I. & Zahn, D. R. T. Experimental study of charge transport mechanisms in a hybrid metal/organic/inorganic device. *Physical Review B* **75,** 045321 (2007).

172. Forrest, S. R., Kaplan, M. L., Schmidt, P. H., Feldmann, W. L. & Yanowski, E. Organic-on-inorganic semiconductor contact barrier devices. *Applied Physics Letters* **41,** 90 (1982).

173. Forrest, S. R., Kaplan, M. L., Schmidt, P. H. & Parsey, J. M. Organic-on-GaAs contact barrier diodes. *Journal of Applied Physics* **58,** 867 (1985).

174. Yella, A. *et al.* Porphyrin-sensitized solar cells with cobalt (II/III)–based redox electrolyte exceed 12 percent efficiency. *Science* **334,** 629–634 (2011).

175. Xiao, X., Zimmerman, J. D., Lassiter, B. E., Bergemann, K. J. & Forrest, S. R. A hybrid planar-mixed tetraphenyldibenzoperiflanthene/C70 photovoltaic cell. *Applied Physics Letters* **102,** 073302–073302–4 (2013).

176. Avasthi, S. *et al.* Silicon surface passivation by an organic overlayer of 9,10-phenanthrenequinone. *Applied Physics Letters* **96,** 222109–222109–3 (2010).

177. Sieval, A. B. *et al.* Silicon Surface Passivation by Organic Monolayers: Minority Charge Carrier Lifetime Measurements and Kelvin Probe Investigations. *J. Phys. Chem. B* **107,** 6846–6852 (2003).

178. Chasse, T., Wu, C.-I., Hill, I. G. & Kahn, A. Band alignment at organic-inorganic semiconductor interfaces: α-NPD and CuPc on InP (110). *Journal of applied physics* **85,** 6589–6592 (1999).

179. Mark, P. & Helfrich, W. Space-Charge-Limited Currents in Organic Crystals. *Journal of Applied Physics* **33,** 205–215 (1962).

180. Van de Lagemaat, J. & Frank, A. J. Effect of the Surface-State Distribution on Electron Transport in Dye-Sensitized TiO2 Solar Cells: Nonlinear Electron-Transport Kinetics. *J. Phys. Chem. B* **104,** 4292–4294 (2000).

181. Hirae, S., Hirose, M. & Osaka, Y. Energy distribution of trapping states in polycrystalline silicon. *Journal of Applied Physics* **51,** 1043–1047 (1980).

182. Peter, L. M., Li, J. & Peat, R. Surface recombination at semiconductor electrodes: Part I. Transient and steady-state photocurrents. *Journal of electroanalytical chemistry and interfacial electrochemistry* **165,** 29–40 (1984).

183. Wannier, G. H. The structure of electronic excitation levels in insulating crystals. *Physical Review* **52,** 191 (1937).

184. So, F. F. & Forrest, S. R. Evidence for exciton confinement in crystalline organic multiple quantum wells. *Physical review letters* **66,** 2649 (1991).

185. Fleming, R. J. Upper Limit of Electron Effective Mass in Organic Semiconductors. *The Journal of Chemical Physics* **56,** 4911 (1972).

186. De Wijs, G. A., Mattheus, C. C., de Groot, R. A. & Palstra, T. Anisotropy of the mobility of pentacene from frustration. *Synthetic metals* **139,** 109–114 (2003).

187. Debye, P. Reaction rates in ionic solutions. *Transactions of the Electrochemical Society* **82,** 265–272 (1942).

188. Mott, N. F. & Gurney, R. W. *Electronic Processes in Ionic Crystals*. (Clarendon Press, 1940).

189. Lüssem, B., Riede, M. & Leo, K. Doping of organic semiconductors. *physica status solidi (a)* **210,** 9–43 (2013).

190. Kido, J. & Matsumoto, T. Bright organic electroluminescent devices having a metal-doped electron-injecting layer. *Applied Physics Letters* **73,** 2866–2868 (1998).

191. Anthopoulos, T. D. & Shafai, T. S. Oxygen induced p-doping of #x3b1;-nickel phthalocyanine vacuum sublimed films: Implication for its use in organic photovoltaics. *Applied Physics Letters* **82,** 1628–1630 (2003).

192. Schafferhans, J., Baumann, A., Wagenpfahl, A., Deibel, C. & Dyakonov, V. Oxygen doping of P3HT:PCBM blends: Influence on trap states, charge carrier mobility and solar cell performance. *Organic Electronics* **11,** 1693–1700 (2010).

193. Schottky, W. Halbleitertheorie der Sperrschicht. *Naturwissenschaften* **26,** 843–843 (1938).

194. Tong, X., Wang, N., Slootsky, M., Yu, J. & Forrest, S. R. Intrinsic burn-in efficiency loss of small-molecule organic photovoltaic cells due to exciton-induced trap formation. *Solar Energy Materials and Solar Cells* **118,** 116–123 (2013).

195. Hwang, J., Wan, A. & Kahn, A. Energetics of metal–organic interfaces: new experiments and assessment of the field. *Materials Science and Engineering: R: Reports* **64,** 1–31 (2009).

196. Greiner, M. T. *et al.* Universal energy-level alignment of molecules on metal oxides. *Nature materials* **11,** 76–81 (2011).

197. Hendry, E., Wang, F., Shan, J., Heinz, T. F. & Bonn, M. Electron transport in TiO~ 2 probed by THz time-domain spectroscopy. *PHYSICAL REVIEW-SERIES B-* **69,** 081101–R (2004).

198. Yagi, E., Hasiguti, R. R. & Aono, M. Electronic conduction above 4 K of slightly reduced oxygen-deficient rutile TiO_ \${\$2-x\$}\$. *Physical Review B* **54,** 7945 (1996).

199. Hsiao, P.-T., Tung, Y.-L. & Teng, H. Electron Transport Patterns in TiO2 Nanocrystalline Films of Dye-Sensitized Solar Cells. *The Journal of Physical Chemistry C* **114,** 6762–6769 (2010).

200. Diebold, U. The surface science of titanium dioxide. *Surface Science Reports* **48,** (2003).

201. Tong, X., Bailey-Salzman, R. F., Wei, G. & Forrest, S. R. Inverted small molecule organic photovoltaic cells on reflective substrates. *Applied Physics Letters* **93,** 173304–173304–3 (2008).

202. Sarma, R. & Saikia, D. Low-Cost Bilayer Electrode for Pentacene-Based OTFTs. *IEEE Electron Device Letters* **32,** 209–211 (2011).

203. Sun, X. W. *et al.* Inverted tandem organic solar cells with a MoO3/Ag/Al/Ca intermediate layer. *Applied Physics Letters* **97,** 053303–053303–3 (2010).

204. Zhao, B.-X., Zhou, J.-C. & Rong, L.-Y. Microstructure and optical properties of TiO< sub> 2</sub> thin films deposited at different oxygen flow rates. *Transactions of Nonferrous Metals Society of China* **20,** 1429–1433 (2010).

205. Tavares, C. J. *et al.* Reactive sputtering deposition of photocatalytic TiO< sub> 2</sub> thin films on glass substrates. *Materials Science and Engineering: B* **138,** 139–143 (2007).

206. Hertel, D. & Bässler, H. Photoconduction in amorphous organic solids. *ChemPhysChem* **9,** 666–688 (2008).

207. Renshaw, C. K., Zimmerman, J. D., Lassiter, B. E. & Forrest, S. R. Photoconductivity in donor-acceptor heterojunction organic photovoltaics. *Physical Review B* **86,** 085324 (2012).

208. Keun Kim, S., Kim, W.-D., Kim, K.-M., Seong Hwang, C. & Jeong, J. High dielectric constant TiO2 thin films on a Ru electrode grown at 250 #x2009; #xb0;C by atomic-layer deposition. *Applied Physics Letters* **85,** 4112–4114 (2004).

209. Fröhlich, K. *et al.* Growth of High-Dielectric-Constant TiO2 Films in Capacitors with RuO2 Electrodes. *Electrochem. Solid-State Lett.* **11,** G19–G21 (2008).

210. Jin, F., Tong, H., Shen, L., Wang, K. & Chu, P. K. Micro-structural and dielectric properties of porous TiO2 films synthesized on titanium alloys by micro-arc discharge oxidization. *Materials Chemistry and Physics* **100,** 31–33 (2006).

211. Kim, C., Burrows, P. E. & Forrest, S. R. Micropatterning of Organic Electronic Devices by Cold-Welding. *Science* **288,** 831–833 (2000).

212. Kim, C., Shtein, M. & Forrest, S. R. Nanolithography based on patterned metal transfer and its application to organic electronic devices. *Applied Physics Letters* **80,** 4051–4053 (2002).

213. Kim, C. & Forrest, S. r. Fabrication of Organic Light-Emitting Devices by Low-Pressure Cold Welding. *Advanced Materials* **15,** 541–545 (2003).

214. Renshaw, D., Denyer, P. B., Wang, G. & Lu, M. ASIC image sensors. in *, IEEE International Symposium on Circuits and Systems, 1990* 3038–3041 vol.4 (1990). doi:10.1109/ISCAS.1990.112652

215. Salzman, R. F. *et al.* The effects of copper phthalocyanine purity on organic solar cell performance. *Organic Electronics* **6,** 242–246 (2005).

216. Li, N., Lassiter, B. E., Lunt, R. R., Wei, G. & Forrest, S. R. Open circuit voltage enhancement due to reduced dark current in small molecule photovoltaic cells. *Applied Physics Letters* **94,** 023307 (2009).

217. Vogel, M., Doka, S., Breyer, C., Lux-Steiner, M. C. & Fostiropoulos, K. On the function of a bathocuproine buffer layer in organic photovoltaic cells. *Applied Physics Letters* **89,** 163501 (2006).

218. Gundlach, D. J., Lin, Y.-Y., Jackson, T. N., Nelson, S. F. & Schlom, D. G. Pentacene organic thin-film transistors-molecular ordering and mobility. *IEEE Electron Device Letters* **18,** 87–89 (1997).

219. Gommans, H. *et al.* On the Role of Bathocuproine in Organic Photovoltaic Cells. *Advanced Functional Materials* **18,** 3686–3691 (2008).

220. Kalb, W. L., Mattenberger, K. & Batlogg, B. Oxygen-related traps in pentacene thin films: Energetic position and implications for transistor performance. *Phys. Rev. B* **78,** 035334 (2008).

221. Newman, C. R., Chesterfield, R. J., Panzer, M. J. & Frisbie, C. D. High mobility top-gated pentacene thin-film transistors. *Journal of Applied Physics* **98,** 084506 (2005).

222. Renshaw, C. K., Xu, X. & Forrest, S. R. A monolithically integrated organic photodetector and thin film transistor. *Organic Electronics* **11,** 175–178 (2010).

223. Grätzel, M. Dye-sensitized solar cells. *Journal of Photochemistry and Photobiology C: Photochemistry Reviews* **4,** 145–153 (2003).

224. Forrest, S. R., Cohen, M. J., Lange, M. J., Kim, D.-S. & others. Very low leakage JFET for monolithically integrated arrays. (1999).

225. Meitl, M. A. *et al.* Transfer printing by kinetic control of adhesion to an elastomeric stamp. *Nature Materials* **5,** 33–38 (2005).

226. Clawson, A. R. Guide to references on III–V semiconductor chemical etching. *Materials Science and Engineering: R: Reports* **31,** 1–438 (2001).

227. Williams, K. R., Gupta, K. & Wasilik, M. Etch rates for micromachining processing-Part II. *Microelectromechanical Systems, Journal of* **12,** 761–778 (2003).